Distribution Agreement

In presenting this thesis or dissertation as a partial fulfillment of the requirements for an advanced degree from Emory University, I hereby grant to Emory University and its agents the non-exclusive license to archive, make accessible, and display my thesis or dissertation in whole or in part in all forms of media, now or hereafter known, including display on the world wide web. I understand that I may select some access restrictions as part of the online submission of this thesis or dissertation. I retain all ownership rights to the copyright of the thesis or dissertation. I also retain the right to use in future works (such as articles or books) all or part of this thesis or dissertation.

Signature:

_____	_____
Xinlin Lu	Date

Polyoxometalate-based Catalysts for Oxidation Reactions: Redox-buffering Catalysts and Alkane Dehydrogenating Nanoparticles

By

Xinlin Lu
Doctor of Philosophy

Chemistry

_____
Craig L. Hill, Ph.D.
Advisor

_____
Cora MacBeth, Ph.D.
Committee Member

_____
Yonggang Ke, Ph.D.
Committee Member

Accepted:

_____
Kimberly Jacob Arriola, Ph.D.
Dean of the James T. Laney School of Graduate Studies

_____
Date

Polyoxometalate-based Catalysts for Oxidation Reactions: Redox-buffering Catalysts and Alkane Dehydrogenating Nanoparticles

By

Xinlin Lu

Bachelor of Engineering. East China University of Science and Technology, 2015

Master of Science. University of Akron, 2017

Advisor: Craig L. Hill, Ph.D.

An abstract of

A dissertation submitted to the Faculty of the

James T. Laney School of Graduate Studies of Emory University

in partial fulfillment of the requirements for the degree of

Doctor of Philosophy

in Chemistry

2023

Abstract

Polyoxometalate-based Catalysts for Oxidation Reactions: Redox-buffering Catalysts and Alkane Dehydrogenating Nanoparticles

By

Xinlin Lu

Polyoxometalate (POM)-catalyzed oxidation reactions have been studied for over a century. Systems include thermal, photo or photoelectron-activation and are conducted both homogeneously and heterogeneously. However, with the rapid growth of POM synthetic chemistry, a significant number of new POM molecules and POM-based materials have been designed and prepared in the last few decades. While a great number of different oxidation reactions catalyzed by POMs and POM-based materials have been reported, fundamental studies focusing on understanding the functioning of these catalysts by thermodynamic and kinetic tools are limited. Therefore, this dissertation focuses on the design of new POM-based catalytic systems and materials while simultaneously studying their mechanisms in detail. Chapter 2, describes a two-component catalytic system based on the tetrabutylammonium salt of $[PMo_6V_6O_{40}]^{9-}$, $TBA_4H_5[PMo_6V_6O_{40}]$ (**PV_6Mo_6**), and $Cu(ClO_4)_2$, I discovered that exhibits a strong synergistic effect between **PV_6Mo_6** and Cu(II) ion with respect to activity. Detailed kinetic and electrochemical studies have been performed and reveal a new POM-based self-redox buffering oxidation mechanism. Chapter 3 extends study of the redox buffering effect associated with TBA salts of $PV_xMo_{12-x}O_{40}^{(3+x)-}$ (**PVMo**) and focuses on the impact of vanadium atom number (x = 0-4, and 6). Detailed electrochemistry studies give the basic electrochemical performances of **PVMo** in acetonitrile and facilitate calculation of key redox buffering parameters, such as the number of buffer steps and the number of electrons transferred at each buffer step. Further kinetic studies show that vanadium atoms have much faster electron-transfer rates than molybdenum atoms in the **PVMo** complexes. This implies that the redox buffering effect of **PVMo** is more pronounced when a larger number of vanadium atoms reside in the POM. The third project involves formulation of the homogeneous **PVMo**/Cu(II) system as a more utilitarian heterogeneous one by inserting the POMs into the metal-organic framework (MOF), HKUST-1, making POM@HKUST. Studies show that the reactivity synergism still exists between Cu(II) in the nodes of HKUST-1 and **PVMo**(x = 1-3) but not for the corresponding transition-metal-substituted polytungstates **XPW_{11}** (X = V, Co, Zn and Co). In addition, synergism in activity also leads to synergism in stability by fast electron transfer between the POM and the MOF framework. For the **XPW_{11}**@HKUST, the Cu(II) nodes decompose to Cu(I) structures discovered by X-ray photoelectron spectroscopy (XPS). Finally, the fourth project describes the synthesis and photochemical activity of $Na_4W_{10}O_{32}$-stabilized Pt(0) nanoparticles (NPs). These NPs show efficient activity for photodehydrogenation of alkanes to alkanes with quantum yields around 0.10, turnover numbers around 100, and high selectivity (ca. 80%) to the non-thermodynamic 1-alkenes. The NPs are stable and reusable for several runs of reactions.

Polyoxometalate-based Catalysts for Oxidation Reactions: Redox-buffering Catalysts and Alkane Dehydrogenating Nanoparticles

By

Xinlin Lu

Bachelor of Engineering. East China University of Science and Technology, 2015

Master of Science. University of Akron, 2017

Advisor: Craig L. Hill, Ph.D.

A dissertation submitted to the Faculty of the

James T. Laney School of Graduate Studies of Emory University

in partial fulfillment of the requirements for the degree of

Doctor of Philosophy

in Chemistry

2023

Acknowledgement

I would like to thank my advisor Dr. Craig Hill for accepting me in his group when I had a hard time and felt confused about my academic future. Thanks for his constant support throughout my whole Ph.D. time, for his always kindness and compassionate mentor. I want to special thanks to Dr. Yurii Geletii for all his help and guidance, without him I could not have accomplished any of my projects. Whenever I have a question, Yurii has always showed me patience and given me insightful answers. I would like to thank former members of the lab: Dr. Kevin P. Sullivan, Dr. Qiushi (Benjamin) Yin, Dr. Daniel L. Collins-Wildman, and Dr. Meilin Tao, who gave me substantial help and advice on both science and real life. I want to thank the current members of the group: Zhiyao (Philip) Zhu, Victoria G. Snider, and Ting Cheng, who are my closest friends and support me with their kindness and friendships.

I would like to thank committee members, Dr. Cora MacBeth and Dr. Yonggang Ke, for providing me with valuable feedback and insightful comments on my annual reports and oral defense. I want to acknowledge Dr. John Bacsa for giving me great help with collecting X-ray diffraction data and teaching me related knowledge. I want to particularly thank my master's degree advisor Dr. Stephen Z.D. Cheng and mentor Dr. Wei Zhang for opening the gate of real science for me and teaching me the skills and knowledge to let me be able to continue as a Ph.D. student.

I would like to thank all the support from my family. My mother, Cuili Lou, encourages me to be a scientist and gives me all her support and love. My father, Xuezhong Lu, gave me all his support throughout my college years and studies aboard. I hope all these years I did not let them down.

I want to thank my wife, Jieqiong Fang, without whom I could not achieve any of these successes and without whom any of my accomplishments would be meaningless. She accompanies and supports me through every difficult time and gives me the love one needs to retain for a lifetime.

Table of Contents

Table of Contents

List of Figures

Abbreviations and Symbols

A	absorbance
ATR	attenuated total reflectance
BTC	1,3,5-Benzenetricarboxylic acid (trimesic acid)
BE	bulk electrolysis
CV	cyclic voltammetry
CAN	cerium ammonium nitrate, Ce(IV)
DLS	dynamic light scattering
DMA	*N,N*-dimethylacetamide
EDX	energy dispersive X-ray spectroscopy
ET	Electron transfer
FT-IR	Fourier transform infrared spectroscopy
Fc	ferrocene
Fc^+	ferrocenium ion
GC	gas chromatography
IVCT	intervalence charge-transfer
MOF	metal-organic framework
OT	oxygen transfer
PCET	Proton-coupled electron transfer
POM	polyoxometalate
PVMo	TBA salts of $PV_nMo_{12-n}O_{40}^{(3+n)-}$ (n = 0-6)
PVW	TBA salts of $PV_nW_{12-n}O_{40}^{(3+n)-}$ (n = 0-6)
RDE	rotating disk electrode
RPM	revolutions per minute
RLS	rate-limiting step
RSH	thiol substrates (2-mercaptoethanol)
RSSR	disulfate (bis(2-hydroxyethyl) disulfide)
RHE	reversible hydrogen electrode

SEM	scanning electron microscope
SWV	square pulse wave voltammetry
TBA	tetrabutylammonium
TEM	transmission electron microscope
TGA	thermogravimetric analysis
TON	turnover number
TOF	turnover frequency
UV-Vis	ultraviolet-visible spectroscopy
XPS	X-ray photoelectron spectroscopy
XRD	X-day diffraction
XPW_{11}	Transition-metal-substituted polytungstates
Å	angstrom (10^{-10} meters)
A	electrode surface area, $cm^2\ s^{-1}$
C_0	bulk concentration of POM, mol cm^{-3}
D	Diffusion coefficient of POM, $cm^2\ s^{-1}$
E	potential of an electrode versus a reference, mV
E_i	standard reduction potential of POM_i species, mV
$E_{1/2}$	half wave potential, mV
E^0	formal potential of some species, mV
ΔE^0	the change of Gibb's free energy (expressed by electrochemical solution potential), mV
$\Delta E(t)$	the change of solution electrochemical potential of the reaction, mV
ΔE_f^0	standard Gibb's energies of formation (expressed in potential), mV
F	Faraday's constant, C
I	current
i_L	limiting current, A
K	equilibrium constant
n	number of transferred electrons in the redox reaction
n_{app}	apparent reduction state of POM

N_A	Avogadro's number
Q	number of coulombs
R	gas constant, J mol^{-1} K^{-1}
T	temperature, K
t	time, s
α_i	concentration ratio of POM_i species
λ	reorganization energy for electron transfer
ω	angular frequency of rotation, s^{-1}
k_{app}	apparent rate constant
$k_{1/2}$	$t_{1/2} = 1/k_{1/2}$, $t_{1/2}$ is the halflife

Chapter 1:

Introduction to Polyoxometalate-based Materials for Catalytic Oxidation Reactions

1.1 Overview of Polyoxometalates

Polyoxometalates (POMs) are a class of inorganic compounds that were first synthesized by Berzelius in 1824. Enlightened structure theory was generated since then by researchers such as Werner and Pauling.[1,2] However, the correct structure of the heteropoly acid $H_3PW_{12}O_{40}$ was not unveiled until 1933 by Keggin due to previous limitations of x-ray diffraction techniques.[1,2] From that time on, thousands of POMs with different structures were synthesized and characterized. POMs can incorporate many elements into their broad range of structures that induce a range of physical and chemical properties facilitating POM applications in catalysis,[3–5] energy,[6–9] nanomaterials[10–13] and biomedicine.[14–18] In this work, we will focus on a few POM structures, including Keggin, decatungstate and Weakley-type (sandwich-like) POMs. The oxidation catalytic activity, redox properties and photoactivity are discussed. In addition, POM-stabilized nanostructures and POMs captured in metal-organic framework (POM@MOF) materials will be addressed.

1.1.1 Polyoxometalate Structures

Polyoxometalates (POMs) are polyanionic molecular metal oxides and are an assembly of metal addenda atoms bridged by oxygen atoms. When POMs are constituted only by addenda metals, they can be classified as isopolyanions, formula: $[M_xO_y]^{n-}$, where M is a metal such as W(VI), Mo(VI) and V(V). If the POMs have an additional heteroatom, they are classified as heteropolyanions, formula $[X_zM_xO_y]^{n-}$, where X is heteroatom, such as P, Si, S, Al and Co. POM structural families range from the simplest with only six addenda metals, the Lindqvist structure, formula: $[M_6O_{19}]^{n-}$ to the huge 'blue lemon' structure, Mo_{368}.[19] Here we only focus on a few common POM structures that show distinct redox, photoactive and oxidative properties (Figure 1.1). Lindqvist and decatungstate structural families are examples of isopolyanions, while Keggin,

Wells−Dawson and Anderson structures are examples of heteropolyanions. A detailed discussion of the Keggin structure is given below.

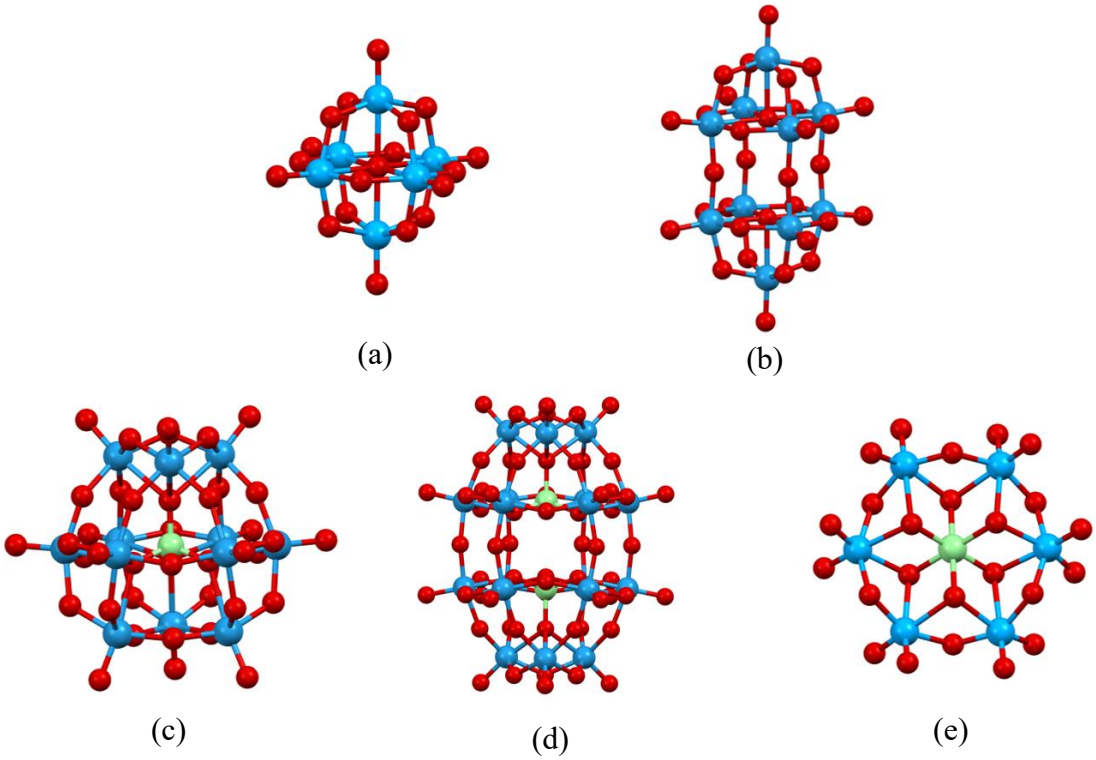

Figure 1.1. Ball-and-stick structures of POMs. (a) Lindqvist structure, $[M_6O_{19}]^{n-}$; (b) Decatungstate $[W_{10}O_{32}]^{4-}$; (c) Keggin structure $[XM_{12}O_{40}]^{n-}$; (d) Wells−Dawson structure $[X_2M_{18}O_{62}]^{n-}$; (e) Anderson structure $[XM_6O_{24}]^{n-}$. Blue: addenda atom; red: oxygen; green: heteroatom.

The Keggin structure with its general chemical formula of $[XM_{12}O_{40}]^{n-}$ (Figure 1.1c), is constituted by a tetrahedral heteroatom surrounded by distorted octahedral MO_6 addenda. Each MO_6 addenda has edge-shared oxygens with a neighboring metal and one unshared terminal oxygen. The Keggin structural family exists as five isomers that differ by sequentially rotating by 60° one of the $\{M_3O_{13}\}$ triads from α to form β, γ, δ, and ε complexes (Figure 1.2). This isomerism not only affects the stability of both fully oxidized states and reduced Keggin polyanions but also the redox potentials of addenda metal.[20] For example, the stability order of fully oxidized Keggin

complexes is α > β > γ > δ > ε for addenda metals in the hexavalent state, e.g. W(VI) or Mo(VI), and the reducibility order is usually α < β < γ.[21]

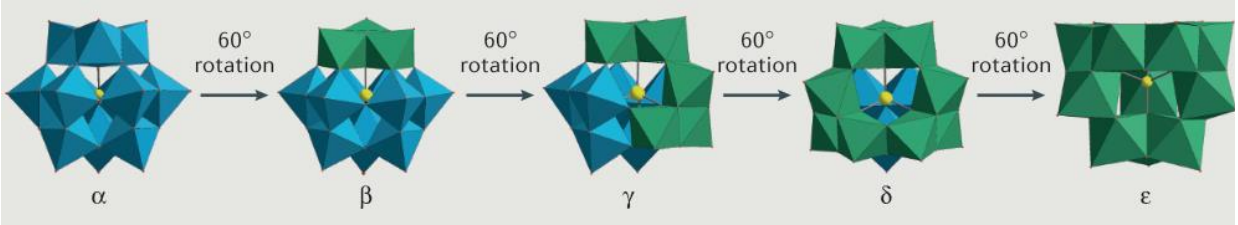

Figure 1.2. Isomers of Keggin structure $[XM_{12}O_{40}]^{n-}$. Reproduced with permission from Springer Nature © 2018.[20]

The most studied Keggin complexes are based on M = Mo(VI), W(VI) and/or V(V) addenda (all d^0 metal centers), with heteroatoms, X = P and Si. Moreover, two or more different addenda metals can exist in one Keggin polyanion to form mixed-addenda structures. Phosphovanadomolybdates $PV_xMo_{12-x}O_{40}^{(3+x)-}$ (x = 1-6) (**PVMo**) and phosphovanadotungstates $PV_xW_{12-x}O_{40}^{(3+x)-}$ (x = 1-6) (**PVW**) are commonly used as oxidative catalysts due to the strong oxidative ability of V(V) centers, and $H_5PV_2Mo_{10}O_{40}$ is the single most studied POM due to its high stability and vanadium positive potentials.[5,22] Both **PVMo** and **PVW** have a series of positional isomers based on the relative positions of the V atoms. For example, $[PV_2Mo_{10}]^{5-}$ has 66 degeneracies of 5 overall isomers with different free energies (Figure 1.3).[23,24] Generally, the **PVW** complexes are configurationally stable, meaning their isomers do not readily interconvert under their synthetic conditions. In contrast, the **PVMo** complexes during synthesis, and in solution in general, interconvert fairly readily and are thus usually present as the mixture of the above positional isomers.[25,26]

Figure 1.3. Different positional isomers of the $[PV_2Mo_{10}]^{5-}$ and their calculated free energies in acetonitrile. Reproduced with permission from ref. 5. Copyright © 2018, American Chemical Society.

In addition to the positional isomers noted above, solutions of **PVMo** and **PVW** are mixtures of compositional isomers, i.e., components with different x in $PV_xMo_{12-x}O_{40}^{(3+x)-}$ or $PV_xW_{12-x}O_{40}^{(3+x)-}$. These two types of isomerism, facile for **PVMo** system, render these mixtures very complex.[27] While the less labile **PVW** do not dissociate free vanadium, VO_2^+ in aqueous solutions at ambient laboratory temperatures, the more labile **PVMo** in acidic aqueous solutions do dissociate VO_2^+, and this dissociation increases with increasing numbers of vanadium centers in the **PVMo**. Dissocation of VO_2^+ from the POM can impact catalysis because the former can also be redox-active and catalytically non-innocent. As a consequence, quantifying properties, including catalytic mechanisms of the **PVMo** system requires distinguishing whether the POM, freely-diffusing vanadate, or both is/are the actual catalyst.[22] We answer this question for our system in the following studies.

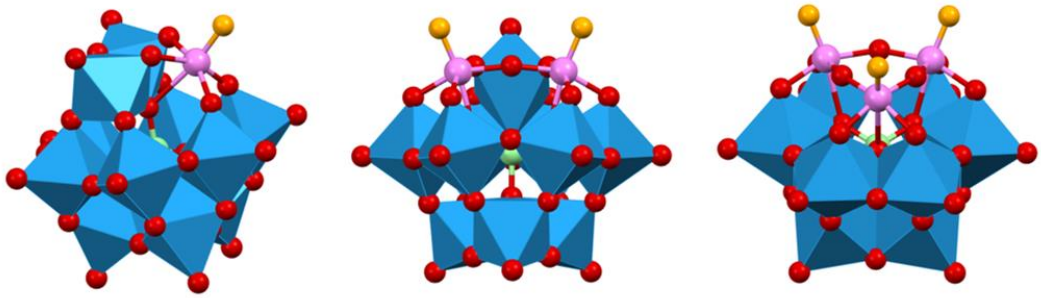

(a) (b) (c)

Figure 1.4. The polyhedral structure of (a) mono-, (b) di-, and (c) tri-transition metal substituted Keggin POMs. Blue: MO_6 addenda; pink: transition metal M'; orange: solvent molecule or specific organic ligand; red: oxygen.

By increasing the pH of the plenary Keggin POM aqueous solutions, the lacunary structures that remove 1-3 addenda metal are formed.[28] The lacunary structures have exposed basic oxygens and chelate transition-metal or noble-metal cations such as M' = Co, Ni, Mn, Fe, Ru, and many others. Depending on the number of removed addenda, the resulting defect Keggin POM can bind one, two or three new metals (Figure 1.4). The lacunary POM can be treated as a weak-field ligand that induces a small d-orbital splitting of the new, inserted transition metals.[3,29] In contrast to the addenda atoms which have terminal oxygen(s), the transition metals usually have a solvent molecule as the external non-bridging ligand. For example, when synthesized from the aqueous conditions, polyoxotungstates can form monomeric species $\{M'(H_2O)(XW_{11}O_{39})\}$. The liable solvent ligand, "H_2O" in the above formula, can be replaced by an organic substrate during catalytic turnover thus providing accessibility to the reactive centers.[3,29] The solvent ligand can also be replaced by certain organic ligands which introduce further functional groups and interesting properties.[30,31]

1.1.2 Polyoxometalates Redox Properties

Three types of POMs were classified by Pope et al.[2,32] based on their redox properties. Type I has one terminal oxygen atom per addendum metal atom and transfers electron reversibly. Examples are the Keggin and Wells-Dawson structures (Figure 1.1c,d). Type II has two terminal oxygen atoms per addendum metal atom and transfers electrons irreversibly. The Anderson structural family is an example (Figure 1.1e). Type III has the mixtures type I and type II addenda. The difference in redox properties between type I and II POM centers is largely attributed to the position of the LUMOs. For type I, the LUMO is nonbinding and mainly derives from the metal-centered d_{xy} orbital, while the LUMO for type II is metal-oxygen antibonding.[2,32] A further classification to type VI based on different polyhedral structures has been given by Fabre and Falaise et al.[29] The electrochemical behavior of heteropolyanions is very complex; here we summarize six factors that have strong effects based on Keggin structure.[21,33]

(1) The potentials of different addenda metals in POMs fall in the sequence V > Mo > W in both aqueous and organic solvents. The sequence is followed for the mixed-addenda Keggin complexes.[21] For example, in the much-studied POM, $[PV_2W_{10}]^{5-}$, the first two-electron reduction involves the V but not the W atoms.

(2) Keggin POM undergo several one-electron reductions in solutions in which no protonation can happen, such as neutral aqueous and most organic solvents. In acidic aqueous conditions (pH < 1), the two one-electron waves convert into one two-electron wave and shift to more positive potentials by a proton-coupled electron transfer (PCET) process.[34] In organic solvents, the addition of a strong acid, such as CF_3SO_3H, results in similar behavior.[35–39]

(3) When no PCET process can occur, the first and second formal potentials of the one-electron processes, E_0^1 and E_0^2, decrease linearly and depend on the overall ionic charges on POM. This change is about 180 mV and 500 mV per ionic charge in aqueous solution and organic solvent respectively. For the heteropolytungstates ($[XW_{12}]^{n-}$) and heteropolymolybdates ($[XMo_{12}]^{n-}$), this trend is independent of the heteroatoms. More precisely, the heteroatom effect on the POM potential is small compared to the ionic charge effect. In addition, the E_0 values of the redox couples with the same ionic charge are very similar and independent of the number of electrons added to POM (Figure 1.5).[40] In combination with the fact that two-electron-reduced Keggin complexes are diamagnetic (the electrons are antiferromagnetic coupled), these potential shift findings suggest that the two electrons added to the Keggin unit LUMO are paired but have very weak interactions. Different electronic structures of Keggin POMs are noted by different groups.[41–43]

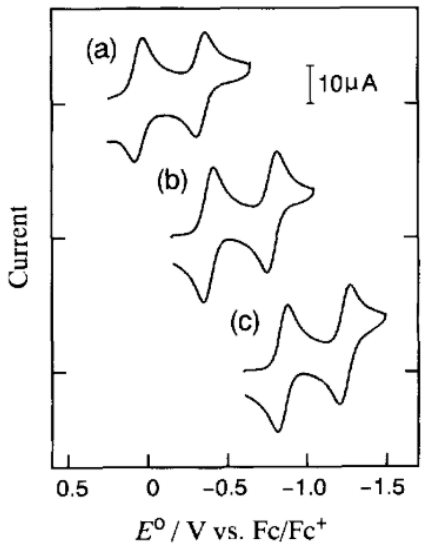

Figure 1.5. Cyclic voltammograms of (a) α-$[SMo_{12}O_{40}]^{2-}$, (b) α-$[PMo_{12}O_{40}]^{3-}$ and (c) α-$[SiMo_{12}O_{40}]^{4-}$ in 1,2-dichloroethane with 0.05 M tetrabutylammonium perchlorate ($TBAClO_4$) as electrolyte. Reproduced with permission from ref. 38. Copyright © 1995 Published by Elsevier B.V.

The significance of the ionic charge effect is dependent on the size of POM. The E_0^1 of the Preyssler-type POM ($[M^{n+}P_5W_{30}O_{110}]^{n-15}$) is only around 41 mV per ionic charge in aqueous solution. This can be explained by the charge density: larger POMs disperse charge more effectively than smaller ones. The Preyssler and Keggin polyanions have respective volumes of 1600 $Å^3$ and 590 $Å^3$.[29,44]

(4) Although the heteroatoms have a much smaller effect on the potential than the overall ionic charge on POM, they still can shift the redox potentials of the addenda metals. Nadjo et al.[45] showed that the E^0 values shift more negative with smaller heteroatoms. The size difference causes the electrostatic potential that is generated by heteroatom unit XO_4 to be slightly different. Eda, et al.[36,39] on the other hand, concluded that heteroatom difference significantly impacts the μ_4-O-M bond length in Keggin polyanions, and that this factor largely dictates the degree of electron depopulation of addenda metal by the highly electronegative oxygen atoms. The μ_4-O-M bond lengths can be described by bond valence(s). In our work, we extend the bond valence theory to our systems.

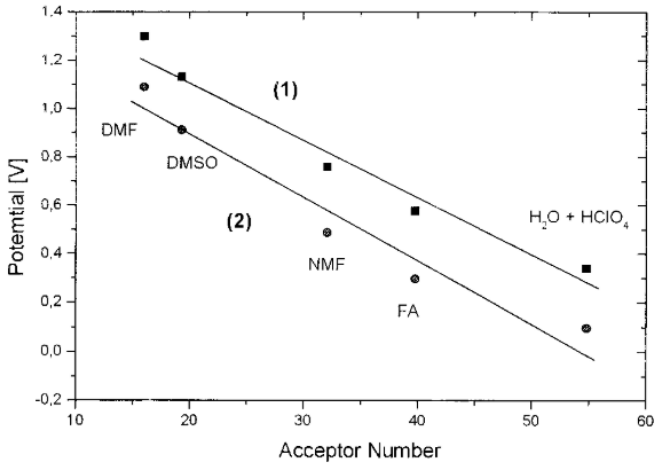

Figure 1.6. Relationship between the first formal potential of POM, E_0^1, and the acceptor number of the solvent. (1) α-$K_4SiW_{12}O_{40}$ and (2) α-$K_6P_2Mo_{18}O_{62}$. Reproduced with permission from ref. 19. Copyright © 1998, American Chemical Society.

(5) Different solvents can shift the formal potential of POM addenda metals. This can be described either by introducing a solvation energy term in the overall thermodynamics,[40] or using acceptor number which describes the Lewis acidity of the solvents (Figure 1.6).[46] In addition to all factors described above, the counter-cations and electrolytes also impact POM redox behaviors via cation-POM ion-pairing.[40,47]

Understanding electrochemical behavior of POMs not only impacts their catalytic,[5] electrochemical,[7,29] energy,[48] and material science,[49,50] properties, but also helps us to understand and establish the foundation for interpreting NMR spectroscopy, spin coupling, electron transfer mechanisms and magnetic behavior.[1,2,51] We perform electrochemical studies on polyvanadomolybdates, $PV_xMo_{12-x}O_{40}^{(3+x)-}$ (x = 1-6), which is addressed in Chapters 2 and 3.

1.1.3 Reduced Polyoxometalates, Mixed-Valence Species

Reduced POMs or mixed-valence POMs are electron-rich molecules that have potential applications in many electric devices and materials, is a topic recently reviewed by Rompel et al.[20] This is a very substantial field, thus here we only give a short summary of reduced Keggin POM properties that focus on understanding their intramolecular processes and corresponding UV-Vis spectroscopy, because we performed a multitude of titration and UV-Vis spectral interpretations in this dissertation.

The reduced heteropolytungstates ($[XW_{12}]^{n-}$) and heteropolymolybdenums ($[XMo_{12}]^{n-}$) have been very well studied.[1,2,51] $[XW_{12}]^{n-}$ can accept up to 6 electrons, and when 1-4 electrons are accepted, a deep blue color is observed which has led to the name ‘heteropoly blues’ given to these reduced POMs. The ‘blue electrons’ are delocalized over all 12 W addenda metals on the NMR and EPR time scales. The delocalization is through thermally-activated electron hopping or ground-state π-electron delocalization. The blue color comes from intervalence electron-transfer

(IVCT) transitions in the near-IR region (centered around 700-800 nm) that are characteristic of class II mixed-valence behavior from the original theory by Robin and Day.[52] The delocalization is through the bridging oxygens, i.e. the W(V)-O-W(VI) units. Oxygens proximal to the reduced tungstens have higher electron density. This makes these oxygens easier to protonate, if H^+ is available, and also increases the bond strength which makes the reduced $[XW_{12}]^{n-}$ a bit more stable than the corresponding fully oxidized species.[53–55]

The six-electron reduced $[XW_{12}]^{n-}$ have a deep brown color, hence they are called 'heteropoly browns'. The brown species, $[XW_3^{IV}W_9^{VI}]^{(6+n)-}$, result from disproportionation of $[XW_6^{V}W_6^{VI}]^{(6+n)-}$ (blue). The two electrons in W^{IV} are localized as confirmed by ^{183}W spectroscopy.[56] In contrast to heteropoly blues where the bridging oxygens are most negative and thus the thermodynamically favored sites for protonation, the terminal oxygens are the ones protonated on the W^{IV} centers forming terminal H_2O ligands in the heteropoly browns. The latter protonations hinder intramolecular electron transfer, and thus these heavily reduced Keggin POMs do not exhibit IVCT bands and are Robin and Day class I complexes.[29] A special case is $[H_2W_{12}O_{40}]^{6-}$ that can take up 32 electrons with accompanying protonation in acidic aqueous solution, and thus constitutes an exceptional electron reservoir.[57,58] The conventional thermodynamic alpha isomer of $[XMo_{12}]^{n-}$ is the most reducible POM and is capable of accepting 12 electrons; this remains a heteropoly blue, i.e. one with only delocalized electrons.[59]

For mixed-addenda Keggin, **PVW**, and **PVMo**, the reduced electrons are localized on V atoms.[34] This generates V^{IV}-to-W^{VI} or V^{IV}-to-Mo^{VI} IVCT bands typically centered around 550-650 nm. When there are additional vanadium centers substituted in the POM, a V^{IV}-to-V^{V} IVCT band around 1000 nm may be observed.[60,61] The overall UV-Vis spectra of reduced **PVW** and **PVMo** may also contain d-d transitions of V and Mo in combination with three different IVCT

bands that collectively make the spectra very complex. We have made a careful assignment of the different numbers of electrons in reduced **PVMo** based on several titration methods (Chapters 2 and 3).

1.2 Polyoxometalate-catalyzed Reactions

POMs are effective catalysts for many reactions due to their superior Brønsted acidity, extensive redox properties, and photoactivity.[4,5,22] POMs with different counterions are very soluble in aqueous and polar organic solvents which facilitates many homogeneous catalytic reactions.[4] In addition, many of their salts with or without solid supports can be used as heterogeneous catalysts.[62] POM structures correlate with many POM properties. In Keggin complexes with H^+ as counterions (heteropolyacids), the terminal oxygens have multiple bond character and are strongly polarized toward the interior of the POM. That is, these oxygens strongly donate electron density due to the empty d orbitals of addenda metal.[1] A consequence of this polarization is that the terminal POM oxygens are very weak bases. This is the origin of the very strong Brønsted acidity of heteropolyacids; many of them have lower pKa (measured in organic solvents) than mineral inorganic acids such as H_2SO_4 and HCl. Many organic reactions facilitated by acidic conditions are efficiently catalyzed by heteropolyacids, including esterification, condensation, and hydration.[22] The interior polarization of POMs and consequent very low negative charge density on the oxygens also leads to very small POM solvation energies and lattice energies which in turn significantly impact POM solubility, lability and stability. [1]

The oxidative catalytic and photocatalytic reactions will be discussed briefly in the following sections that focus on oxidation reactions catalyzed by Keggin POMs, especially **PVMo**, and photodriven reactions catalyzed by decatungstate.

1.2.1 Polyoxometalate-catalyzed Oxidation Reactions

Aerobic oxidation reactions are widespread in nature, and two different families of enzymes, oxygenases and oxidases exist. Oxygenases are subclassified into monooxygenases and dioxygenases. Monooxygenases transfer one oxygen atom from O_2 to the substrate and reduce the other one to H_2O using sacrificing reducing agents (Figure 1.7a). One the other hand, dioxygenases split the O-O bond and transfer both atoms to the substrate. Oxidases directly transfer electrons to oxygen and generate H_2O or H_2O_2 without O atom transfer.[63–65] These mechanisms apply to POM-catalyzed oxidation reactions. Overall, POM catalyzed oxidations can proceed by oxygen atom transfer (OT) and electron transfer (ET) reactions.

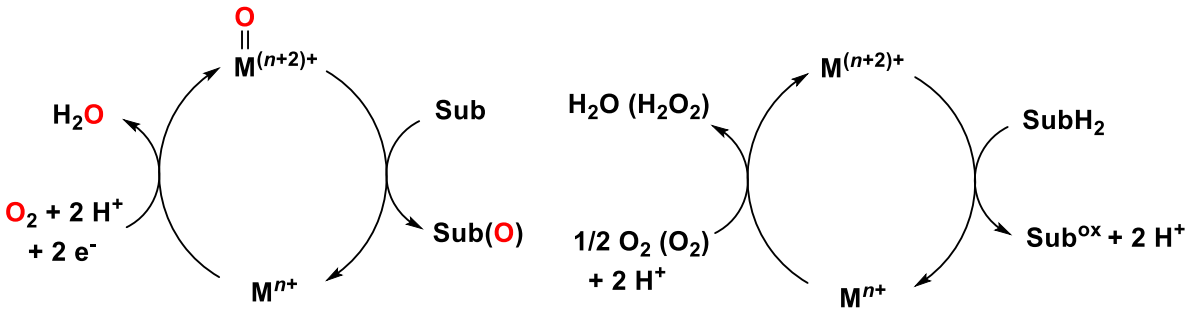

Figure 1.7. Simplified catalytic cycles of aerobic oxidations. (a) Monooxygenase pathways; (b) dioxygenase pathways.

OT reactions catalyzed by POMs have been studied by several groups,[66–74] and can be further classified as follows:

(1) POMs receive an oxygen atom from oxygen donors such as iodosylbenzene (PhIO) or pentafluoroiodosylbenzene (PFIB), and then transfer this oxygen to the substrate. Transition-metal-substituted POMs, $[M'XW_{11}O_{39}]^{n-}$, M' = Co(II), Mn(II), Fe(II) and Cr(V) can catalyze hydrocarbon oxidation by this mechanism as established by Hill and co-workers.[67–69]

(2) Heteropoly Browns can directly remove oxygen atoms from the substrate, for example, from Me_2SO to form Me_2S.[66] This results, in part, from the fact that the terminal ligand on the W(IV) addenda is not a terminal oxo but frequently a terminal aqua ligand as discussed above.

(3) Mars-van Krevenlen type, electron transfer-oxygen transfer reactions (ET-OT), that have been established by Neumann et al.[72–74] This mechanism is established for direct reaction of $H_5PV_2Mo_{10}O_{40}$ with hydrocarbons (such as anthracene),[72,74] carbon-carbon bond cleavage reactions[73] and carbon-metal bond activations in conjunction with homogeneous catalysis by this POM.[73,75] A simplified ET-OT mechanism involves POM accepting one electron from the substrate forming an intermediate complex, then POM transferring one of its terminal oxygens to the substrate.

Electron transfer reactions (ET) catalyzed by POMs strongly depend on the POM's oxidative ability, in another words, its redox potential (thermodynamics). When the proton source is available, proton-coupled electron transfer (PCET) occurs.[76,77] Polyvanadomolybdates (**PVMo)**,[5,22] phosphovanadotungstates (**PVW**),[4,62] and transition-metal-substituted Keggin complexes[3] are usually efficient oxidation catalysts and several of these POMs can catalyze oxidation of hydrocarbons, alcohols, amines and phenols.

The POMs reduced by reaction with substrates can be reoxidized by O_2. This is a fundamental and very important process. In oxygen reduction to H_2O, an overall four-electron process, or reduction to H_2O_2, a two-electron process, each step has different formal potential, E^0, and can couple with proton transfer (Figure 1.8).[78] Reduced POMs are usually O_2 activation catalysts that can generally be differentiated as inner-sphere and outer-sphere based on the electron transfer mechanism. A considerable amount of research has been done on this topic; here, we give only a short introduction relevant to the work in this dissertation.

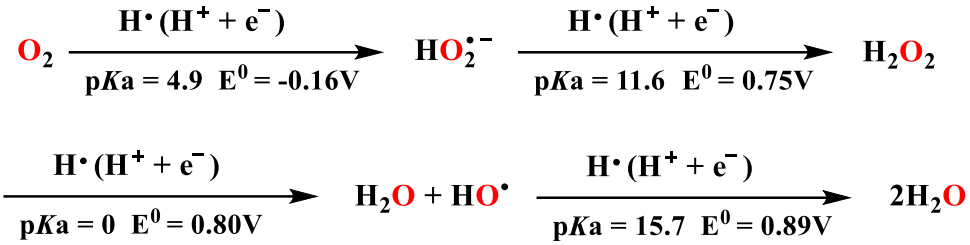

Figure 1.8. Energetics of the stepwise $4H^+/4e^-$ reduction of dioxygen to water. Data from ref. 76.

Inner-sphere electron transfer happens when the electron donor (D) and electron acceptor (A) form an intermediate chemical complex, i.e.. a transient bond. Due to the strong interaction and close distance between D and A, inner-sphere ET usually exhibits faster kinetics, k_{et}, than outer-sphere ET. The reaction of reduced polyoxomolybdates (e.g., PMo_{12})[79,80] and vanadopolymolybdates (e.g., PV_2Mo_{10})[81,82] with O_2 have been suggested to proceed via an inner-sphere electron transfer mechanism. Neumann et al.[81,82] proposed the same mechanism for reaction involving PV_2Mo_{10}: One of the V(IV)-O bond breaks generating a coordination site on the V(IV). Dioxygen then attacks the V(IV) site forming a peroxo intermediate which then reacts with a V(IV) in another POM generating a transient dimer. Finally, the dimer decomposes to two reoxidized POMs and H_2O (Figure 1.9). These processes are consistent with liable Mo-O and V-O bonds. Reoxidation of reduced polyoxomolybdates and vanadomolbydates by O_2 forming a peroxo intermediate with substrate, therefore, behaves like a radical scavenger that changes the otherwise autoxidation mechanism to an oxidative dehydrogenation one.[79,83] On the other hand, both vanadium and transition-metal-substituted Keggin POMs generate peroxo radicals and exhibit autooxidation mechanisms for some oxidations including alkene epoxidation and formaldehyde oxidation.[84–87]

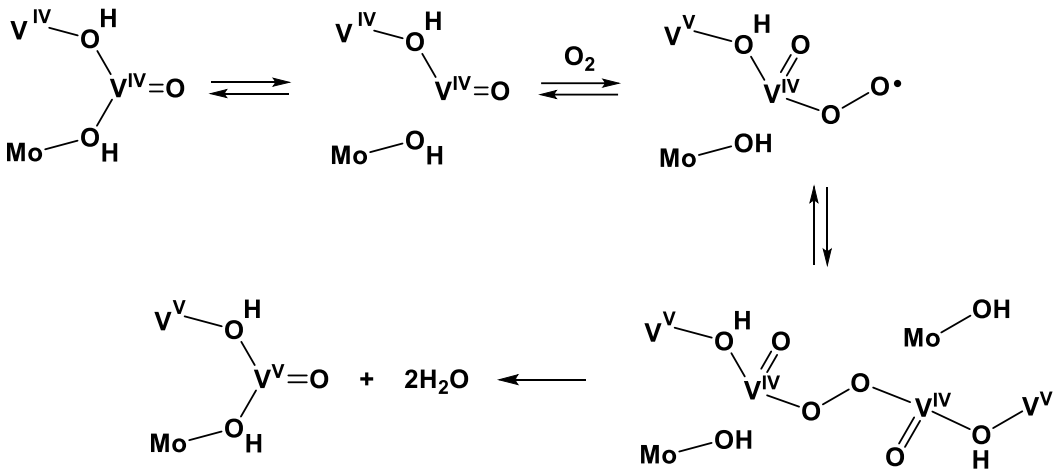

Figure 1.9. Inner-sphere electron transfer mechanism for reoxidation $[PV_2Mo_{10}]^{6-}$ by O_2. Adapted with permission from ref. 79. Copyright © 1992, American Chemical Society

Reoxidization of reduced polyoxotungstates by O_2 has been proved to proceed via an outer-sphere electron transfer mechanism.[88–93] Keggin POMs have well-defined spherical structures with each metal fully coordinated by terminal and shared oxygen atoms that limit access of electron acceptors or donors to the metal centers. These properties of POMs in concert with the relatively low charge densities and the internal structural and charge polarization argue for the likelihood of outer-sphere electron transfer mechanisms.[5] Outer-sphere electron transfer was initially formulated by Marcus et al.[94] Marcus theory extended the Debye colliding-sphere model to describe the diffusion-controlled electron transfer process between two molecules (Figure 1.10 bottom).[5] The mechanisms and kinetics of the theory were very well established based on transition state theory (Figure 1.10 top). It is important to note that Marcus theory describes electron transfer between precursor and successor complexes but not between reactant and product.[95]

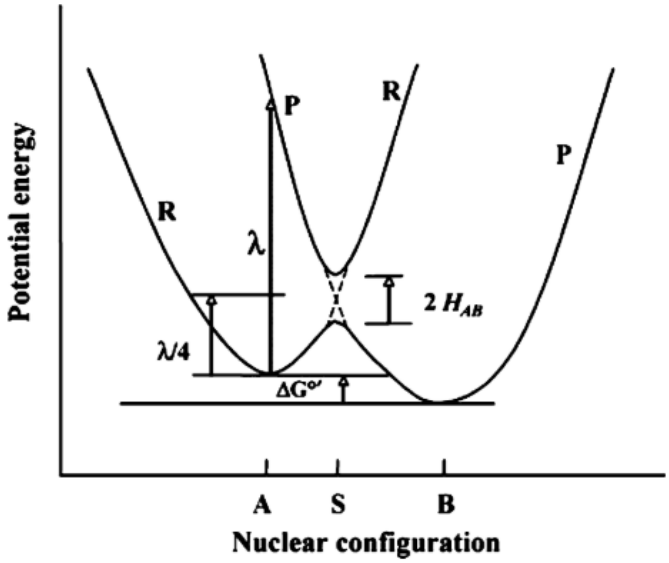

$$D^n + A^m \rightleftharpoons [\,D^n, A^m\,] \overset{k_{et}}{\rightleftharpoons} [\,D^{(n+1)}, A^{(m-1)}\,] \rightleftharpoons D^{(n+1)} + A^{(m-1)}$$

Reactant, R **Precursor, A** **Successor, B** **Product, P**

Figure 1.10. Top: Outer-sphere electron transfer potential energy surfaces between reactants, R, products, P. The positions of the precursor and successor complexes are labeled A and B, respectively, and electron transfer occurs at position S. H_{AB} is the electronic matrix element that describes the splitting of the potential surfaces. $\Delta G^{0\prime}$ is the corrected Gibbs free energy. Bottom: electron transfer precursor and successor intermediates based on Debye's colliding-sphere model. Reproduced with permission from ref. 5. Copyright © 2018, American Chemical Society.

According to Marcus equation, eq 1.1, and Eyring equation, eq 1.3, one can establish the relationship between free energy, $\Delta G^{0'}$, and electron transfer kinetics, k_{et}, eq 1.4.[95]

$$\Delta G^{\neq} = \frac{z_1 z_2 e^2}{D r_{12}} \exp(-\chi r_{12}) + \frac{\lambda}{4}\left(1 + \frac{\Delta G^{0\prime}}{\lambda}\right)^2 \qquad (1.1)$$

$\Delta G^{\neq}$ is free energy of activation. Where z_1 and z_2 are charges on electron donor and acceptor and r_{12} is distance between them. D is the dielectric constant of solvent; e is electron charge and χ is reciprocal Debye radius. λ is reorganization energy and $\Delta G^{0\prime}$is corrected Gibbs free energy.

$$\Delta G^{0\prime} = \Delta G^{0} + (z_1 - z_2 - 1)\frac{e^2}{Dr_{12}}\exp(-\chi r_{12}) \quad (1.2)$$

$$k_{et} = \kappa Z \exp(-\Delta G^{\neq}/RT) \quad (1.3)$$

$$RT \ln Z - RT \ln k_{et} = W(r) + \frac{\lambda}{4} + \frac{\Delta G^{0'}}{2} + \frac{(\Delta G^{0'})^2}{4\lambda} \quad (1.4)$$

Where k_{et} is electron transfer rate constant, s^{-1}, κ is transmission coefficient and Z is the collision frequency, $M^{-1}\ s^{-1}$. W(r) is the work term that equals the first term and factor of eq 1.1.

All the variables in eq 1.4 can be calculated or experimentally measured except reorganization energy, λ, which is often hard to determine. Reorganization energy is related to the energy required to transit from precursor to successor complexes and has a dominant effect on the electron transfer rate. Self-exchange rate of donor and acceptor, k_{11} and k_{12} (intramolecular electron transfer), eq 1.5-1.6, and correlated Marcus cross relation (eq 1.8-1.10) can be further applied to calculate k_{12} (k_{et}), thus λ_{12} by eq 1.4.[5]

$$^1D^n + {}^2D^{n-1} \rightleftharpoons {}^1D^{n-1} + {}^2D^n \qquad k_{11}, \lambda_{11} \quad (1.5)$$

$$^1A^m + {}^2A^{m-1} \rightleftharpoons {}^1A^{m-1} + {}^2A^m \qquad k_{22}, \lambda_{22} \quad (1.6)$$

$$D^{n-1} + A^m \rightleftharpoons A^{m-1} + D^n \qquad k_{12}, \lambda_{12} \quad (1.7)$$

$$k_{12} = (k_{11}k_{22}k_{12}f_{12})^{0.5}C_{12} \quad (1.8)$$

Where

$$\ln f_{12} = \frac{1}{4}\frac{(\ln K_{12} + \frac{W_{12} - W_{21}}{RT})}{\ln(\frac{k_{11}k_{22}}{Z^2} + \frac{W_{11} - W_{22}}{RT})} \quad (1.9)$$

$$C_{12} = exp[-(W_{12} + W_{12} - W_{12} - W_{12})/RT] \quad (1.10)$$

Where W_{ij} (i, j = 1 or 2) are Coulombic work terms of all four species.

For the reoxidation of reduced POM (D) by O_2 (A), the self-exchange rate of POM, k_{11}, can be measured experimentally by ^{31}P NMR by correlating intramolecular electron transfer rate to NMR signal broadness that has been established by Baker et al.[96,97] Further, Geletii and Weinstock et al.[88] used the α-$Al^{III}W_{12}O_{40}^{5-}$/$\alpha$-$Al^{III}W_{12}O_{40}^{6-}$ redox couple as a probe and ^{17}Al NMR to measure the self-exchange rate of the POM. Self-exchange rate of $O_2/O_2^{\bullet-}$, k_{22}, was measured by Lind and Merényi.[98] Since the Marcus cross relation is based on the assumption that the electron donor and acceptor are spherical and have the same size, and a lot of work based on organic or organometallic electron donors reoxidized by O_2 have produced very different kinetic results using the original Marcus cross relation.[5,95] Weinstock later modified the Marcus cross relation by considering the different reactant size.[99] On the other hand, λ can be calculated by Sutin's semiclassical model.[100]

By using these factors (k and λ) and established experimental methods, a few polyoxotungstates (α-$X^{n+}W_{12}O_{40}^{(9-n)-}$, X^{n+} = Al^{3+},Si^{4+}, and P^{5+}) were proved to undergo outer-sphere electron transfer.[91,92] Other evidence such as ^{17}O NMR labeling experiments were given by Hill et al.[89] In addition, the reoxidation of reduced polyoxotungstates by O_2 has been shown to be first-order dependent on [POM_{red}] and [O_2] and generate H_2O_2 as product, eq 1.11.[91]

$$2POM_{red} + O_2 + 2H^+ \rightarrow 2POM_{ox} + H_2O_2 \qquad (1.11)$$

The reduction of O_2 to $O_2^{\bullet-}$coupled with H^+ has two pathways: a sequential electron and proton transfer (ET-PT) mechanism[91] and a concerted proton-electron transfer (CPET) (or a proton-coupled electron transfer (PCET)) mechanism.[93] We have discussions on inner-sphere versus outer-sphere electron transfer mechanisms based on our systems in Chapters 2 and 3.

1.2.2 Polyoxometalate Photoactivities

$H_3PW_{12}O_{40}$ was shown to be photoactive over a century ago; however, systematic studies of POM photochemistry were conducted in the 1980s by Hill,[101–104] Yamase,[105–110] Papaconstantinou[111–113] and others. Polyoxotungstates and polyoxomolybdates with Keggin, Wells-Dawson, and decatungstate structures have been the main focus of this research. These POMs show high extinction coefficients for O → M ligand-to-metal charge transfer (LMCT) absorption bands in the UV region of the spectrum. Considerable effort has been put into shiftting the electronic absorption spectra of POMs into the visible region. Three general approaches to do this have been established: (1) Engineering the LMCT band into the visible region by introducing mixed-addenda metals, such as V,[114,115] or inserting transition metals (M') to introduce M'-to-POM charge transfer.[116] (2) Using photosensitizers, such as Ru(II) or Ir(III) complexes, a POM mixed system,[6] or use of photosensitizers as counterions.[117] (3) Using organic photosensitzer molecules to build organic-inorganic hybrid POM materials.[118,119] In addition, the photoactivity of polyoxovanadates (POVs) has been a recent focus because of their LMCT absorbance bands are in the visible.[120–122] In Chapter 5, we examine key features of POM photochemistry with a focus on decatungstate.

In the presence of primary and secondary alcohols, ethers, ketones and aldehydes, heteropolytungstates, such as $[PW_{12}O_{40}]^{3-}$, $[P_2W_{18}O_{62}]^{6-}$ and $[W_{10}O_{32}]^{4-}$ undergo photoredox reactions.[109,123] The photoreduced POMs are heteropoly blues with their associated and characteristic delocalized electrons as addressed above. The mechanism for the $[PW_{12}O_{40}]^{3—}$ catalyzed photo-oxidation of a representative organic substrate, a primary acohol, is summarized in eqs 1.12-1.13.

$$H_3PW_{12}O_{40} + RCH_2OH \xrightarrow{hv} H_5PW_{12}O_{40} + RCHO \quad (1.12)$$

$$H_5PW_{12}O_{40} + 1/2O_2 \rightarrow H_3PW_{12}O_{40} + H_2O \quad (1.13)$$

Yamase et al.[105] found that $[W_{10}O_{32}]^{5-}$ can photocatalytic dehydrogenate alcohols under N_2. At the same time, Hill et al.[124] documented that $[PW_{12}O_{40}]^{3-}$ can catalyze the same reaction. Shortly after this, Hill et al.[103,125,126] discovered that $[W_{10}O_{32}]^{5-}$ and $[PW_{12}O_{40}]^{3-}$ can catalyze photo-dehydrogenation of alkanes to alkenes and H_2 under Ar or N_2. The reaction mechanism was studied in detail by Renneke and Hill et al.[101,126] Several strong lines of evidence establish that alkyl radicals are involved in the process, and that photoexcited POMs abstract hydrogen: eqs 1.14-1.18 describe the mechanism:

$$W_{10}O_{32}^{4-} + hv \rightarrow W_{10}O_{32}^{4-*} \quad (1.14)$$

$$W_{10}O_{32}^{4-*} + RH \rightarrow HW_{10}O_{32}^{4-} + R^{\bullet} \quad (1.15)$$

$$2HW_{10}O_{32}^{4-} \rightarrow W_{10}O_{32}^{4-} + H_2 \quad (1.16)$$

$$2R^{\bullet} \rightarrow \text{alkene} + \text{alkane} \quad (1.17)$$

POM-photocatalyzed alkane dehydrogenation generates thermodynamic or non-thermodynamic alkene products dictated by the conditions, eqs 1.18-1.20. The product selectivity depends on whether the intermediate alkyl radicals are oxidized or not by the POM, eqs 1.18 versus1.19, therefore, the redox potential of POM is important in regulating the reaction selectivity. Further study showed that the acidity of the medium also has a strong effect on reaction rate and product selectivity by influencing the POM potential in both ground and excited states. [101,103]

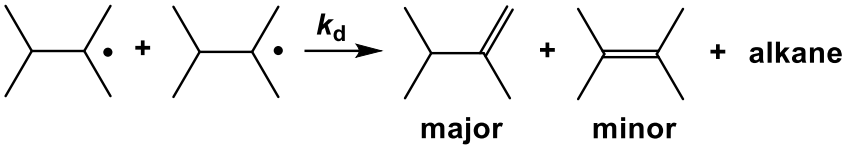

(1.18)

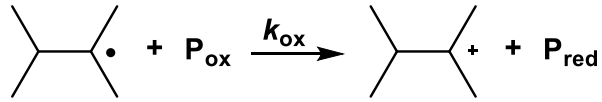

(1.19)

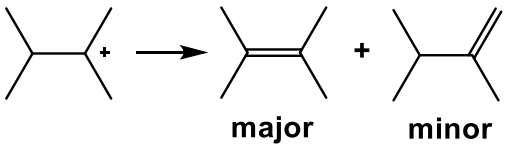

(1.20)

Decatungstate, $[W_{10}O_{32}]^{5-}$, usually displays the highest quantum efficiencies and reaction conversion of all POMs for hydrocarbon dehydrogenation.[127] Subsequent research established that $[W_{10}O_{32}]^{5-}$ can catalyze the alkylation and vinylation of alkanes,[128] as well as the radical carbonylation of alkanes.[129] Recently, $[W_{10}O_{32}]^{5-}$ has been widely used in C-H functionalization reactions, and studies have attempted to distinguish hydrogen atom transfer (HAT) processes from single electron transfer (SET) ones.[130]

The crystal and electronic structures of $[W_{10}O_{32}]^{5-}$ have been studied by Yamasa, et al.[131–133] The one- or two-electron reduced forms of decatungstate have a deep blue color from broad bands around 650 nm and 1130 nm that are class-II and class-III intervalence charge transfer (IVCT) bands based on the Robin-Day classification. The class-III IVCT band derives mainly from the fully delocalized electrons on the eight equatorial WO_6 octahedra.[133] Several theoretical calculations further support the delocalization of reduced electrons.[134,135] One the other hand, considerable effort has been made to characterize the nature of the excited states of $[W_{10}O_{32}]^{5-}$ by transient laser spectroscopy.[136–139] The initial event generates a singlet excited state (S_1) via a O → M ligand-to-metal charge transfer (LMCT) transition. Flash excitation pump-probe experiments show that an intermediate triplet state (T) with the life time around $\tau = 55 \pm 20$ ns is formed (Figure

1.11).[138] This triplet state is the chemically active species that features a terminal oxygen with radical character that undergoes hydrogen atom transfer (HAT), i.e. abstracts a hydrogen atom from the organic substrate.[130]

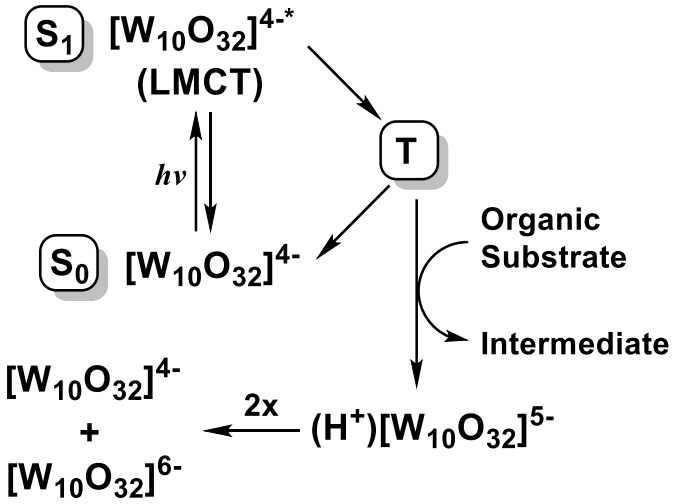

Figure 1.11. Simplified diagram of decatungstate photophysical steps.

1.3 Polyoxometalate-based Materials

Due to the collective, attractive properties of POMs described above and their consequent applications, there has been a great deal of fairly recent research on the design and synthesis of POM-based heterogeneous materials. Such materials have significant applications in catalysis, sustainable and clean energy conversion and storage, molecule storage and separation, sensors, and biomedicine.[29,48,140–148] Different strategies have been used to incorporate POMs into or as functional materials:

(1) Immobilization of POMs on surfaces or in porous materials by covalent bond formation ("grafting"), electrostatic forces or host-guest capture involving multiple non-covalent interactions. The supports for these heterogeneous systems can be carbon materials, such as reduced graphene

oxide (rGO)[149] and carbon nanotubes (CNTs);[150–152] semiconductor surfaces;[153–158] polymers;[157] porous materials such as nickel foam, silica, zeolites, metal-organic frameworks (MOFs),[160–162] and covalent organic frameworks (COFs).[163]

(2) Organic functionalized-POM polymer networks[164] or super-assembly nanostructures.[165,166] By introducing different organic functional groups, materials can achieve electron or proton conductivity, and photoactivity in visible spectral range.[167] The POM itself can also form supramolecular assemblies, by using polymolybdates or polyvanadates as building blocks. Different nanostructure morphologies can be obtained such as nanosheets, nanowires, micelles, and many others.[12]

(3) POMs can stabilize metal(0) nanostructures including noble metals such as Au, Pt and Pd. Therefore, these materials have the potential to catalyze a variety of different reactions.[10–12] Recently, POM-stabilized metal oxides have been designed and synthesized. These nanosystems have shown great catalytic activity in the oxygen evolution reaction (OER), hydrogen evolution reaction (HER), and CO_2 reduction.[168–172]

In this dissertation we discuss in detail POMs captured in MOF materials, and POM-stabilized metal(0) materials, and the projects related to this are addressed in Chapters 4 and 5.

1.3.1 Polyoxometalates Captured in Metal-Organic Frameworks (MOFs)

Loading homogeneous POMs on highly porous or high specific surface area supports can convert them into stable heterogeneous catalysts which facilitates easier product separation and more facile recyclability. Metal-Organic Frameworks (MOFs) are a class of materials with highly porous 3D networks constituted by organic linkers and inorganic nodes.[173–175] MOFs have very large surface area, tunable pore size, and designable functionalities that make them attractive in

many fields.[176–180] There are two classes of POM-based MOF materials: (1) POMOFs: POMs are used as inorganic nodes or pillars coordinated with organic linkers, and thus the POMs are part of the MOF frameworks. (2) POM@MOF: POMs are captured in the pores of MOF frameworks noncovalently (Figure 1.12).[176,181]

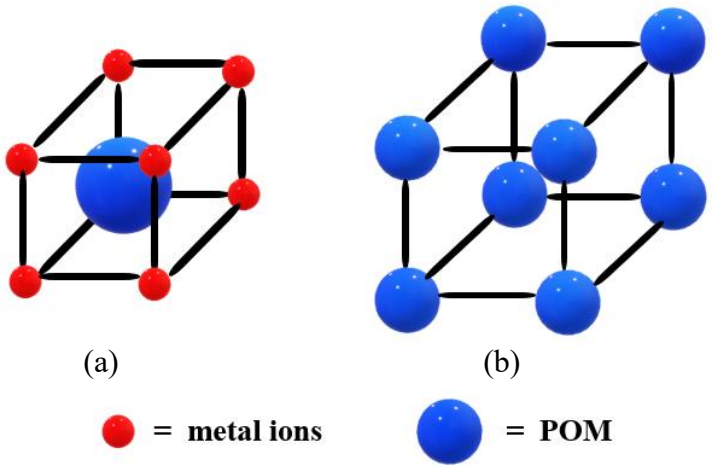

Figure 1.12. Illustration of (a) POM@MOF and (b) POMOF structures.

Chapter 4 addresses POM@MOF materials, and therefore, we focus on this type of material here. Many MOFs with POMs incorporated into their pores have been reported, including MIL, UiO, HKUST-1, NU-1000 and ZIFs.[162] These POM@MOFs feature complementary MOF pore sizes and POM sizes. Keggin type, Wells-Dawson type and sandwich type POMs are used mostly commonly in POM@MOF materials due to their relatively smaller size, stability and attractive catalytic properties. Of these, POM@MIL-101 and POM@HKUST-1 are studied in this work.

Férey et al.[182] synthesized the Cr-based highly stable and giant-cage MOF named MIL-101. MIL-101 has two pores with internal free diameters of 29 and 34 Å, respectively, and both can capture POMs (Figure 1.13).[183] Various Keggin complexes, such as $[PW_{12}O_{40}]^{3-}$, $[PMo_{12}O_{40}]^{3-}$, $[PV_2Mo_{10}O_{40}]^{5-}$, and Wells-Dawson derivatives have captured in MIL-101 pores.[184–191] However,

due to the relatively large pore size compared to the Keggin structure (~11.5 Å polyanion diameter), leaching of pore-incorporated POMs is observed, and normally only one POM per pore is stable in MIL-101.[185] One of the strategies to reduce POM leaching is to use amine-functionalized MIL-101 that introduces positive charges (ammonium catons below pH ~10) that bind the polyanionic POMs electrostatically.[192] Whereas MIL-101 has terephthalate as a linker, MIL-100 has benzene-1,3,5-tricarboxylate as a linker. The latter has two pores of 24 Å and 29 Å which have often been used to capture POMs. The inorganic nodes can be Fe(III) and Al(III) in addition to Cr(III).[193] POM@MIL-101(or 100) materials can catalyze several reactions including oxidation of alkanes, alkenes, alcohols and sulfides; oxidative desulfurization; condensation and esterification.[194,195] $H_3PMo_{12}O_{40}$@MIL-100(Fe) shows interesting photoactivity upon excitation of the carboxylate oxygen-to-Fe(III) LMCT band at 320nm.[196]

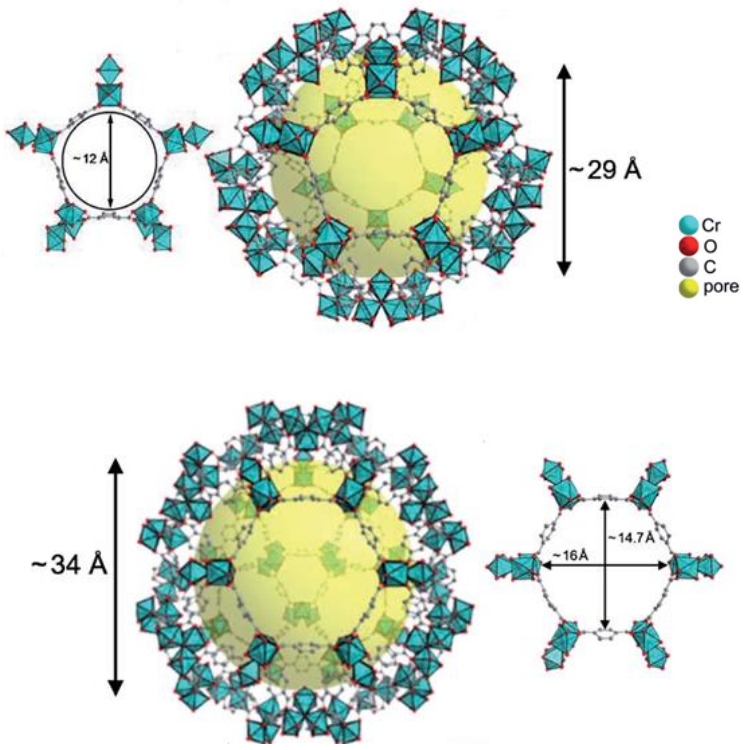

Figure 1.13. Illustration of MIL-101(Cr) MOF framework. Adapted from ref. 181 with permission from The Royal Society of Chemistry.

A significant finding was the facile incorporation of Keggin-type POMs into the pores of HKUST-1 (MOF-199).[162] HKUST-1, named after Hong Kong University of Science and Technology) uses 1,3,5-benzenetricarboxylic acid (BTC) as organic linker and Cu^{2+} as inorganic nodes.[197] The two large pores in HKUST-1 have sizes of 10 and 13 Å, respectively. Considering the Keggin has around 1 nm in diameter, HKUST-1 can accommodate one Keggin unit within its larger pore (Figure 1.14).[198] Since the accessible window to the larger pore is around 11 Å, Keggin POMs residing in HKUST-1 pores after hydrothermal synthesis cannot easily leak out as in the case of POM@MIL-101 materials.[199] Cu(II), Ru(III), Mo(III), Zn(III), Ni(III), Fe(III) and Cr(III) have been used as inorganic nodes in HKUST-1,[200] however, only Cu(II)-BTC HKUST-1 has been used to capture POMs.

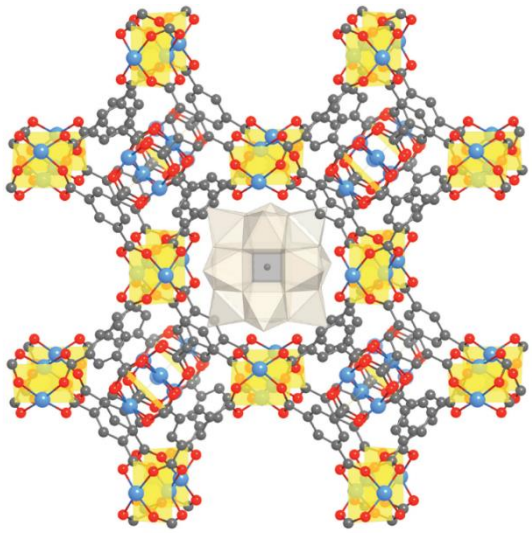

Figure 1.14. X-ray crystal structure of POM@HKUST-1 (ball and stick). Atoms: gray, C; red, O; and blue, Cu. The Keggin POM is present in white polyhedral notation and the copper(II) acetate cluster linkers are yellow cubes. Reproduced with permission from ref. 196. Copyright © 2011, American Chemical Society.

Yamase et al.[201] synthesized the first POM@HKUST-1 using a one-pot hydrothermal synthesis that generates POM and MOF at the same time from the initial raw materials. The Keggin

complexes, $H_4SiMo_{12}O_{40}$, $H_3PW_{12}O_{40}$ and $H_3PMo_6W_6O_{40}$ were generated *in situ* inside the pores of HKUST-1. Subsequently, Su et al.[199] used a different synthetic method to insert pre-formed Keggin POMs during hydrothermal synthesis. A series of Keggin complexes has been successful inserted into the pores of the MOF, NENU 1-6 (Northeast Normal University) during synthesis. Hill et al.[198] incorporated the transition-metal-substituted Keggin, $[CuPW_{11}O_{39}]^{5-}$ into HKUST-1 and found a synergistic effect between this MOF and POM with respect to both catalytic activity (H_2S and thiol oxidation) and stability. To date, there have been many studies of POM@HKUST-1 materials that focus on catalytic oxidative desulfurization, oxidation of olefins, benzene, and thiols.[202–209]

1.3.2 Polyoxometalate-stabilized Nanoparticles

POM polyions have been found to serve as protecting ligands for metal(0) nanoparticles (POM-M(0) NPs), and as such, help control NP size and morphology.[210] Noble metals such as Pd(0), Pt(0), Ir(0), Rh(0), Au(0), Ag(0) and Ru(0) as well as the 3d transition metals, Cu(0) and Co(0) can be stabilized by a variety of POMs.[10,12,211] Recently, Weinstock et al. synthesized POM stabilized metal oxides, such as TiO_2,[168] Co_3O_4,[171] and hematite,[170] as well as ferric oxide-hydroxide (FeOOH).[172] Our work in Chapter 5 involves POM stabilized Pt(0) for photo-driven catalytic reactions.

Finke et al, first synthesized POM-stabilized Ir(0) and Rh(0) nanoparticles by H_2-reduction of POM-supported Ir(I) and Rh(I) complexes, such as $(Bu_4N)_5Na_3[(1,5\text{-cyclooctadiene})Ir^{I}P_2W_{15}Nb_3O_{62}]$.[211–213] An exemplary POM-M(0) NP synthesis: treatment of metal salts in the POM solution by a reducing agent such as H_2, $NaBH_4$ or Zn(0). The other two successful syntheses of these systems are the following: (1) Use of the reduced POM as both the

reducing and stabilizing agent; in this case, the POM can be reduced by chemical, photochemical and electrolysis methods.[214–216] (2) Use of the ligand-exchange reaction method.[217,218]

The mechanism of metal(0) NP protection has been discussed by many groups. Indirect evidence for this protection and proof that the POM resides on the NP surfaces has used data from elemental analysis, UV-Vis absorption bands and zeta potentials. Weinstock et al. used cryo-TEM to directly observe a monolayer of POM ligand on the surface of the NPs (Figure 1.15).[12,210,219] The Gouy-Chapman-Stern model was invoked to describe the NPs: the POM ligand shell is negatively charged with the counter-cations tightly packed within the Stern layer. More precisely, the counterions (such as K^+) are extensively integrated into the POM monolayer to meet the energetic requirement from the electrostatic work and account for the space between POM molecules in cryo-TEM images.[210,219]

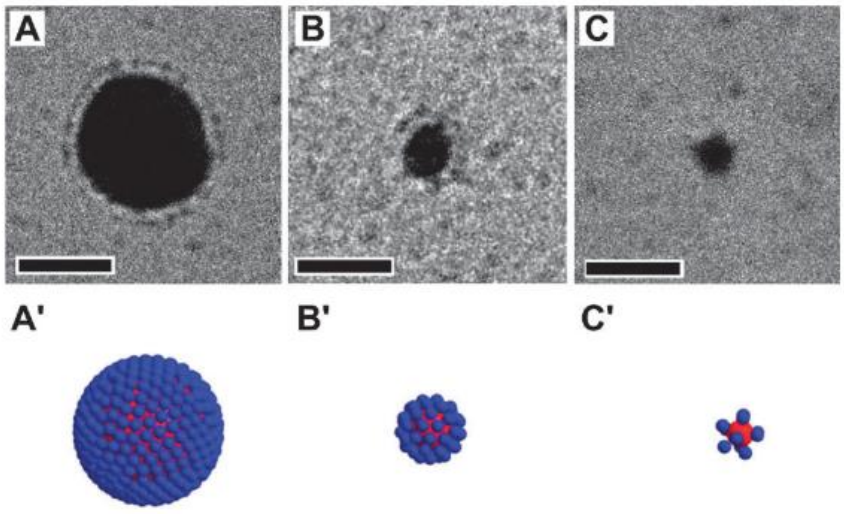

Figure 1.15. Cryo-TEM images and illustrations of α-$AlW_{11}O_{39}^{9-}$-stabilized Au(0) nanoparticles with core diameters of (A, A') 14 nm A; (B, B') 5.4 nm; and (C, C') 3 nm. Bars = 10 nm. Reproduced with permission from ref. 208. Copyright © 2008, American Chemical Society.

Langmuir isotherms have been used to describe the equilibrium and stability of POM monolayers on metal(0) surfaces using monolayer stability constant, K, as a parameter.[219] The counter-cations and overall charges on the POMs have a huge effect on the stability of the NPs. The NPs are more stable with larger alkali-metal cations (due to strong ion pairing), and the monolayer stability constant, K, increases linearly with increasing charge density on the POM.[12,210,219] The size and morphology of NPs can be regulated by factors such as temperature; concentration and structure of POM polyanion; electrochemical potential of the POM; and the type and concentration of reducing-agent used.[220–222]

1.4 Scope of Current Work

In the following chapters, both homogeneous and heterogeneous catalytic systems for thermal and photoactivated oxidation reactions have been developed. Chapter 2 is based on the tetrabutylammonium salt of hexavanadopolymolybdate $TBA_4H_5[PMo_6V_6O_{40}]$ (**PV_6Mo_6**) and $Cu(ClO_4)_2$ as a two-component homogeneous catalytic system, **PV_6Mo_6**/Cu(II), for the aerobic oxidative deodorization of thiols in acetonitrile. A strong synergistic effect between **PV_6Mo_6** and Cu(II) ion on catalytic activity is observed. Detailed kinetics studies by UV-Vis and stopped-flow spectroscopy methods along with thermodynamic data from electrochemistry methods reveal the function of the Cu(II) and **PV_6Mo_6** components in the system. In addition, $TBA_4H_5[PW_6V_6O_{40}]$ (**PV_6W_6**) does not function as self-redox buffer and has very slow electron transfer rates compared to **PV_6Mo_6**. The difference between two POMs is attributed to inner-sphere versus outer-sphere electron transfer mechanisms operable during catalytic turnover.

Chapter 3 is a close examination of the **PV_6Mo_6**/Cu(II) redox buffering system. The impact of vanadium atom number (x = 0-4, and 6) in TBA salts of $PV_xMo_{12-x}O_{40}^{(3+x)-}$ (**PVMo**) on this multicomponent catalytic system is discussed. Thorough electrochemical studies of all **PVMo** are

conducted to understand their electrochemical behavior in acetonitrile. All **PVMo** can transfer multiple electrons depending on the solution electrochemical potentials, and as a consequence, all **PVMo** have redox buffer abilities. Further stopped-flow kinetics studies in both acetonitrile and aqueous buffer solutions show that the vanadium atoms in **PVMo** have much faster electron transfer rate than the molybdenum atoms.

In Chapter 4, POM@MOF materials that are based on HKUST-1, i.e. POM@HKUST composites, are synthesized. $PV_xMo_{12-x}O_{40}^{(3+x)-}$ (x = 1-3) and transition-metal-substituted polytungstates, $\mathbf{XPW_{11}}$ (X = V, Co, Zn and Co) were incorporated into the pores of HKUST-1. Their catalytic activity for aerobic thiol oxidation and stability are studied. The reactivity synergism in homogeneous solution between POM and Cu(II) ion still exists in these analogous heterogeneous catalysts, **PVMo**@HKUST, but this synergism does not exist in the corresponding polytungstates, $\mathbf{XPW_{11}}$@HKUST. Moreover, the POM-MOF synergy is not only for catalytic activity but also for stability. In contrast to the **PVMo**@HKUST systems, the $\mathbf{XPW_{11}}$@HKUST systems decompose completely under the same aerobic oxidation conditions. Further, X-ray photoelectron spectroscopy (XPS) reveals the limit of electron transfer between the polytungstate units, $\mathbf{XPW_{11}}$, and the Cu(II) nodes in HKUST-1.

In chapter 5, we report the photochemical synthesis of $Na_4W_{10}O_{32}$-stabilized (~20 nm) Pt(0) nanoparticles (NPs) and that these nanoparticles (W_{10}-PtNPs) efficiently catalyze the photodehydrogenation of alkanes at room temperature, a process that is endothermic and endoergic in the dark, and for which $W_{10}O_{32}^{4-}$ salts or Pt(0) particles alone are completely inactive. These W_{10}-PtNPs exhibit high efficiency (quantum yields ~0.10 and turnover numbers ~100) and high selectivity (~80%) for alkene photodehydrogenation and can be isolated and reused.

1.5 References

1 L. C. W. Baker and D. C. Glick, *Chem. Rev.*, 1998, **98**, 3–49.

2 M. T. Pope and A. Müller, *Angew. Chemie Int. Ed. English*, 1991, **30**, 34–48.

3 C. L. Hill and C. M. Prosser-McCartha, *Coord. Chem. Rev.*, 1995, **143**, 407–455.

4 S. S. Wang and G. Y. Yang, *Chem. Rev.*, 2015, **115**, 4893–4962.

5 I. A. Weinstock, R. E. Schreiber and R. Neumann, *Chem. Rev.*, 2018, **118**, 2680–2717.

6 H. Lv, Y. V. Geletii, C. Zhao, J. W. Vickers, G. Zhu, Z. Luo, J. Song, T. Lian, D. G. Musaev and C. L. Hill, *Chem. Soc. Rev.*, 2012, 41, 7572–7589.

7 M. R. Horn, A. Singh, S. Alomari, S. Goberna-Ferrón, R. Benages-Vilau, N. Chodankar, N. Motta, K. Ostrikov, J. Macleod, P. Sonar, P. Gomez-Romero and D. Dubal, *Energy Environ. Sci.*, 2021, **14**, 1652–1700.

8 N. Li, J. Liu, B. Dong and Y. Lan, *Angew. Chemie Int. Ed.*, 2020, **59**, 20779–20793.

9 G. Zhang and Y. Wang, *Polyoxometalates*, 2023, 9140020.

10 B. Keita, T. Liu and L. Nadjo, *J. Mater. Chem.*, 2009, **19**, 19–33.

11 L. S. Ott and R. G. Finke, *Coord. Chem. Rev.*, 2007, **251**, 1075–1100.

12 Y. Wang and I. A. Weinstock, *Chem. Soc. Rev.*, 2012, **41**, 7479–7496.

13 D. L. Long, R. Tsunashima and L. Cronin, *Angew. Chemie - Int. Ed.*, 2010, **49**, 1736–1758.

14 J. T. Rhule, C. L. Hill, D. A. Judd and R. F. Schinazi, *Chem. Rev.*, 1998, **98**, 327–357.

15 M. Aureliano, N. I. Gumerova, G. Sciortino, E. Garribba, C. C. McLauchlan, A. Rompel and D. C. Crans, *Coord. Chem. Rev.*, 2022, **454**, 214344.

16 M. Aureliano, N. I. Gumerova, G. Sciortino, E. Garribba, A. Rompel and D. C. Crans, *Coord. Chem. Rev.*, 2021, **447**, 214143.

17 A. Bijelic, M. Aureliano and A. Rompel, *Chem. Commun.*, 2018, **54**, 1153–1169.

18 A. Bijelic, M. Aureliano and A. Rompel, *Angew. Chemie - Int. Ed.*, 2019, **58**, 2980–2999.

19 A. Müller and P. Gouzerh, *Chem. Soc. Rev.*, 2012, **41**, 7431–7463.

20 N. I. Gumerova and A. Rompel, *Nat. Rev. Chem.*, 2018, **2**, 112.

21 M. Sadakane and E. Steckhan, *Chem. Rev.*, 1998, **98**, 219–237.

22 I. V. Kozhevnikov, *Chem. Rev.*, 1998, **98**, 171–198.

23 Michael T. Pope* Thomas F. Scully, *Inorg. Chem.*, 1975, **14**, 1974–1975.

24 H. Hirao, D. Kumar, H. Chen, R. Neumann and S. Shaik, *J. Phys. Chem. C*, 2007, **111**, 7711–7719.

25 P. J. Domaille and G. Watunya, *Inorg. Chem.*, 1986, **25**, 1239–1242.

26 P. J. Domaille, *J. Am. Chem. Soc.*, 1984, **106**, 7677–7687.

27 M. T. Pope, S. E. O'Donnell and R. A. Prados, *J. Chem. Soc. Chem. Commun.*, 1975, **2**, 22–23.

28 M. T. Pope, *Polyoxometalate Mol. Sci.*, 2003, 3–31.

29 B. Fabre, C. Falaise and E. Cadot, *ACS Catal.*, 2022, **12**, 12055–12091.

30 A. Dolbecq, E. Dumas, R. Mayer and P. Mialane, *Chem. Rev.*, 2010, **110**, 6009–6048.

31 A. Proust, B. Matt, R. Villanneau, G. Guillemot, P. Gouzerh and G. Izzet, *Chem. Soc. Rev.*, 2012, **41**, 7605–7622.

32 M. T. Pope, *Inorg. Chem.*, 1972, **11**, 1973–1974.

33 T. Ueda, *ChemElectroChem*, 2018, **5**, 823–838.

34 J. J. Altenau, M. T. Pope, R. A. Prados and H. So, *Inorg. Chem.*, 1975, **14**, 417–421.

35 and A. G. W. Peter J. S. Richardt,† Robert W. Gable,† Alan M. Bond, *Inorganics*, 2019, **7**, 703–709.

36 S. Himeno and M. Takamoto, *J. Electroanal. Chem.*, 2002, **528**, 170–174.

37 K. Maeda, S. Himeno, T. Osakai, A. Saito and T. Hori, *J. Electroanal. Chem.*, 1994, **364**,

149–154.

38 S. X. Guo, A. W. A. Mariotti, C. Schlipf, A. M. Bond and A. G. Wedd, *Inorg. Chem.*, 2006, **45**, 8563–8574.

39 J. I. Nambu, T. Ueda, S. X. Guo, J. F. Boas and A. M. Bond, *Dalt. Trans.*, 2010, **39**, 7364–7373.

40 K. Maeda, H. Katano, T. Osakai, S. Himeno and A. Saito, *J. Electroanal. Chem.*, 1995, **389**, 167–173.

41 X. López, J. J. Carbó, C. Bo and J. M. Poblet, *Chem. Soc. Rev.*, 2012, **41**, 7537–7571.

42 N. Suaud, A. Gaita-Ariño, J. M. Clemente-Juan, J. Sánchez-Marín and E. Coronado, *J. Am. Chem. Soc.*, 2002, **124**, 15134–15140.

43 K. Eda and T. Osakai, *Inorg. Chem.*, 2015, **54**, 2793–2801.

44 M. H. Chiang, M. R. Antonio and L. Soderholm, *Dalt. Trans.*, 2004, 3562–3567.

45 I. M. Mbomekallé, X. López, J. M. Poblet, F. Sécheresse, B. Keita and L. Nadjo, *Inorg. Chem.*, 2010, **49**, 7001–7006.

46 B. Keita, D. Bouaziz and L. Nadjo, *J. Electrochem. Soc.*, 1988, **135**, 87–91.

47 T. Konishi, K. Kodani, T. Hasegawa, S. Ogo, S. X. Guo, J. F. Boas, J. Zhang, A. M. Bond and T. Ueda, *Inorg. Chem.*, 2020, **59**, 10522–10531.

48 *Angew. Chemie - Int. Ed.*, 2020, **59**, 20779–20793.

49 E. Coronado and C. J. Gómez-García, *Chem. Rev.*, 1998, **98**, 273–296.

50 D. L. Long, R. Tsunashima and L. Cronin, *Angew. Chemie - Int. Ed.*, 2010, **49**, 1736–1758.

51 N. I. Gumerova and A. Rompel, *Nat. Rev. Chem.*, , DOI:10.1038/s41570-018-0112.

52 M. B. Robin and P. Day, *Adv. Inorg. Chem. Radiochem.*, 1968, **10**, 247–422.

53 G. M. Varga, E. Papaconstantinou and M. T. Pope, *Inorg. Chem.*, 1970, **9**, 662–667.

54 M. T. Pope and G. M. Varga, *Inorg. Chem.*, 1966, **5**, 1249–1254.

55 N. Casañ-Pastor, P. Gomez-Romero, G. B. Jameson and L. C. W. Baker, *J. Am. Chem. Soc.*, 1991, **113**, 5658–5663.

56 K. Piepgrass and M. T. Pope, *J. Am. Chem. Soc.*, 1987, **109**, 1586–1587.

57 J. P. Launay, *J Inorg Nucl Chem*, 1976, **38**, 807–816.

58 S. P. E. Smith and J. B. Christian, *Electrochim. Acta*, 2008, **53**, 2994–3001.

59 J. N. Barrows and M. T. Pope, *Intramolecular Electron Transfer and Electron Delocalization in Molybdophosphate Heteropoly Anions*, 1989.

60 C. Daniel and H. Hartl, *J. Am. Chem. Soc.*, 2009, **131**, 5101–5114.

61 E. Cadot, M. Fournier, A. Tézé and G. Hervé, *Inorg. Chem.*, 1996, **35**, 282–288.

62 Noritaka Mizuno and Makoto Misono, *Chem. Rev.*, 1998, **98**, 199–217.

63 S. S. Stahl, *Angew. Chemie - Int. Ed.*, 2004, **43**, 3400–3420.

64 A. J. Hickman and M. S. Sanford, *Nature*, 2012, **484**, 177–185.

65 S. D. McCann and S. S. Stahl, *Acc. Chem. Res.*, 2015, **48**, 1756–1766.

66 K. Piepgrass and M. T. Pope, *J. Am. Chem. Soc.*, 1989, **111**, 753–754.

67 C. L. Hill and R. B. Brown, *J. Am. Chem. Soc.*, 1986, **108**, 536–538.

68 A. M. Khenkin and C. L. Hill, *J. Am. Chem. Soc.*, 1993, **115**, 8178–8186.

69 M. Faraj and C. L. Hill, *J. Chem. Soc. Chem. Commun.*, 1987, 1487–1489.

70 R. Neumann and M. Dahan, *Nature*, 1997, **388**, 353–355.

71 R. Neumann and M. Dahan, *J. Am. Chem. Soc.*, 1998, **120**, 11969–11976.

72 Alexander M. Khenkin and Ronny Neumann*, *Angew. Chemie - Int. Ed.*, 2000, **39**, 4088–4090.

73 A. M. Khenkin and R. Neumann, *J. Am. Chem. Soc.*, 2008, **130**, 14474–14476.

74 A. M. Khenkin, L. Weiner, Y. Wang and R. Neumann, *J. Am. Chem. Soc.*, 2001, **123**, 8531–8542.

75 A. M. Khenkin, I. Efremenko, J. M. L. Martin and R. Neumann, *J. Am. Chem. Soc.*, 2013, **135**, 19304–19310.

76 R. Neumann and M. Levin, *J. Org. Chem.*, 1991, 56, 5707–5710.

77 R. Neumann and M. Levin, *J Am Chem Soc*, 1992, **114**, 7278–7286.

78 R. Trammell, K. Rajabimoghadam and I. Garcia-Bosch, *Chem. Rev.*, 2019, **119**, 2954–3031.

79 A. M. Khenkin and R. Neumann, *J. Am. Chem. Soc.*, 2001, **123**, 6437–6438.

80 A. Hiskia and E. Papaconstantinou, *Inorg. Chem.*, 1992, **31**, 163–167.

81 R. Neumann and M. Levin, *J. Am. Chem. Soc.*, 1992, **114**, 7278–7286.

82 R. Neumann and A. M. Khenkin, *Chem. Commun.*, 2006, 2529–2538.

83 A. M. Khenkin and R. Neumann, *Inorg. Chem.*, 2000, **39**, 3455–3462.

84 O. A. Kholdeeva, V. A. Grigoriev, G. M. Maksimov, M. A. Fedotov, A. V. Golovin and K. I. Zamaraev, *J. Mol. Catal. A Chem.*, 1996, **114**, 123–130.

85 Y. Nishiyama, Y. Nakagawa and N. Mizuno, *Angew. Chemie - Int. Ed.*, 2001, **40**, 3639–3641.

86 L. Chen, K. Zhu, L. H. Bi, A. Suchopar, M. Reicke, G. Mathys, H. Jaensch, U. Kortz and R. M. Richards, *Inorg. Chem.*, 2007, **46**, 8457–8459.

87 S. Shinachi, M. Matsushita, K. Yamaguchi and N. Mizuno, 2005, **233**, 81–89.

88 Y. V. Geletii, C. L. Hill, A. J. Bailey, K. I. Hardcastle, R. H. Atalla and I. A. Weinstock, *Inorg. Chem.*, 2005, **44**, 8955–8966.

89 D. C. Duncan and C. L. Hill, *J. Am. Chem. Soc.*, 1997, **119**, 243–244.

90 M. Kim, I. A. Weinstock, Y. V. Geletii and C. L. Hill, *ACS Catal.*, 2015, **5**, 7048–7054.

91 Y. V. Geletii, C. L. Hill, R. H. Atalla and I. A. Weinstock, *J. Am. Chem. Soc.*, 2006, **128**, 17033–17042.

92 Y. V. Geletii and I. A. Weinstock, *J. Mol. Catal. A Chem.*, 2006, **251**, 255–262.

93 O. Snir, Y. Wang, M. E. Tuckerman, Y. V. Geletii and I. A. Weinstock, *J. Am. Chem. Soc.*, 2010, **132**, 11678–11691.

94 R. A. Marcus, *Angew. Chemie Int. Ed. English*, 1993, **32**, 1111–1121.

95 I. A. Weinstock, *Chem. Rev.*, 1998, **98**, 113–170.

96 M. Kozik, C. F. Hammer and L. C. W. Baker, *J. Am. Chem. Soc.*, 1986, **108**, 7627–7630.

97 M. Kozik and L. C. W. Baker, *J. Am. Chem. Soc.*, 1990, **112**, 7604–7611.

98 J. Lind, X. Shen, G. Merényi and B. Jonsson, *J. Am. Chem. Soc.*, 1989, **111**, 7654–7655.

99 I. A. Weinstock, *Inorg. Chem.*, 2008, **47**, 404–406.

100 N. Sutin, *Acc. Chem. Res.*, 1982, **15**, 275–282.

101 R. F. Renneke, M. Kadkhodayan, M. Pasquali and C. L. Hill, *J. Am. Chem. Soc.*, 1991, **113**, 8357–8367.

102 R. C. Chambers and C. L. Hill, *Inorg. Chem.*, 1989, 28, 2509–2511.

103 R. F. Renneke and C. L. Hill, *Angew. Chemie Int. Ed. English*, 1988, **27**, 1526–1527.

104 D. C. Duncan, T. L. Netzel and C. L. Hill, *Inorg. Chem.*, 1995, **34**, 4640–4646.

105 T. Yamase, N. Takabayashi and M. Kaji, *J. Chem. Soc. Dalt. Trans.*, 1984, 793–799.

106 Toshihiro Yamase and Moriyasu Sugeta, *J. CHEM. SOC., Dalt. TRANS*, 1993, 759–765.

107 Toshihiro Yamase, *J. Chem. Soc., Dalt. Trans.*, 1982, 1987–1991.

108 T. Yamase and M. Suga, *J. Chem. Soc. Dalt. Trans.*, 1989, 661–669.

109 T. Yamase, *Chem. Rev.*, 1998, **98**, 307–325.

110 T. Yamase, *Catal. Surv. from Asia*, 2003, **7**, 203–217.

111 E. Papaconstantinou, *Chem. Soc. Rev.*, 1989, **18**, 1–31.

112 P. Argitis and E. Papaconstantinou, *J. Photochem.*, 1985, **30**, 445–451.

113 A. Ioannidis and E. Papaconstantinou, *Inorg. Chem.*, 1985, **24**, 439–441.

114 C. Li, K. Suzuki, N. Mizuno and K. Yamaguchi, *Chem. Commun.*, 2018, **54**, 7127–7130.

115 P. Argitis and E. Papaconstantinou, *Inorg. Chem.*, 1986, **25**, 4386–4389.

116 K. Suzuki, F. Tang, Y. Kikukawa, K. Yamaguchi and N. Mizuno, *Angew. Chemie*, 2014, **126**, 5460–5464.

117 N. Fay, V. M. Hultgren, A. G. Wedd, T. E. Keyes, R. J. Forster, D. Leane and A. M. Bond, *Dalt. Trans.*, 2006, 4218–4227.

118 J. M. Cameron, D. J. Wales and G. N. Newton, *Dalt. Trans.*, 2018, **47**, 5120–5136.

119 B. Matt, X. Xiang, A. L. Kaledin, N. Han, J. Moussa, H. Amouri, S. Alves, C. L. Hill, T. Lian, D. G. Musaev, G. Izzet and A. Proust, *Chem. Sci.*, 2013, **4**, 1737–1745.

120 J. Forster, B. Rösner, M. M. Khusniyarov and C. Streb, *Chem. Commun.*, 2011, **47**, 3114–3116.

121 A. Seliverstov and C. Streb, *Chem. Commun.*, 2014, **50**, 1827–1829.

122 A. Seliverstov and C. Streb, *Chem. - A Eur. J.*, 2014, **20**, 9733–9738.

123 C. Tanielian, *Coord. Chem. Rev.*, 1998, **178**–**180**, 1165–1181.

124 C. L. Hill and D. A. Bouchard, *J. Am. Chem. Soc.*, 1985, **107**, 5148–5157.

125 R. F. Renneke and C. L. Hill, *J. Am. Chem. Soc.*, 1988, **110**, 5461–5470.

126 R. F. Renneke, M. Pasquali and C. L. Hill, *J. Am. Chem. Soc.*, 1990, **112**, 6585–6594.

127 C. L. Hill, *Synlett*, 1995, **02**, 127–132.

128 B. S. Jaynes and C. L. Hill, *J. Am. Chem. Soc.*, 1993, **115**, 12212–12213.

129 B. S. Jaynes and C. L. Hill, *J. Am. Chem. Soc.*, 1995, **117**, 4704–4705.

130 D. Ravelli, S. Protti and M. Fagnoni, *Acc. Chem. Res.*, 2016, **49**, 2232–2242.

131 T. Yamase, *J. Chem. Soc. Dalt. Trans.*, 1987, 1597–1604.

132 Y. Sasaki, T. Yamase, Y. Ohashi and Y. Sasada, *Bull. Chem. Soc. Jpn.*, 1987, 60, 4285–4290.

133 T. Yamase and E. Ishikawa, *Inorg. Chem.*, 2022, **61**, 13743–13755.

134 H. Duclusaud and S. A. Borshch, *J. Am. Chem. Soc.*, 2001, **123**, 2825–2829.

135 D. Ravelli, D. Dondi, M. Fagnoni, A. Albini and A. Bagno, *Phys. Chem. Chem. Phys.*, 2013, **15**, 2890–2896.

136 D. C. Duncan and C. L. Hill, *Inorg. Chem.*, 1996, **35**, 5828–5835.

137 I. Texier, J. A. Delaire and C. Giannotti, *Phys. Chem. Chem. Phys.*, 2000, **2**, 1205–1212.

138 V. De Waele, O. Poizat, M. Fagnoni, A. Bagno and D. Ravelli, *ACS Catal.*, 2016, **6**, 7174–7182.

139 D. C. Duncan and M. A. Fox, *J. Phys. Chem. A*, 1998, **102**, 4559–4567.

140 A. R. Bagheri, N. Aramesh, J. Chen, W. Liu, W. Shen, S. Tang and H. K. Lee, *Anal. Chim. Acta*, 2022, **1209**, 339509.

141 Rongji Liu* and Carsten Streb*, *Adv. Energy Mater.*, 2021, **11**, 2101120.

142 Y. Ji, L. Huang, J. Hu, C. Streb and Y. Song, *Energy Environ. Sci.*, 2015, **8**, 776–789.

143 Y. Zhang, J. Liu, S. L. Li, Z. M. Su and Y. Q. Lan, *EnergyChem*, 2019, **1**, 100021.

144 Y. V. Geletii, Q. Yin, Y. Hou, Z. Huang, H. Ma, J. Song, C. Besson, Z. Luo, R. Cao, K. P. O'Halloran, G. Zhu, C. Zhao, J. W. Vickers, Y. Ding, S. Mohebbi, A. E. Kuznetsov, D. G. Musaev, T. Lian and C. L. Hill, *Isr. J. Chem.*, 2011, **51**, 238–246.

145 C. Freire, D. M. Fernandes, M. Nunes and V. K. Abdelkader, *ChemCatChem*, 2018, **10**, 1703–1730.

146 S. M. Lauinger, Q. Yin, Y. V. Geletii and C. L. Hill, *Polyoxometalate Multielectron Catalysts in Solar Fuel Production*, Elsevier Inc., 1st edn., 2017, vol. 69.

147 Y. Chen, F. Li, S. Li, L. Zhang and M. Sun, *Inorg. Chem. Commun.*, 2022, **135**, 109084.

148 A. Dolbecq, P. Mialane, B. Keita and L. Nadjo, *J. Mater. Chem.*, 2012, **22**, 24509–24521.

149 R. Liu, G. Zhang, H. Cao, S. Zhang, Y. Xie, A. Haider, U. Kortz, B. Chen, N. S. Dalal, Y. Zhao, L. Zhi, C. X. Wu, L. K. Yan, Z. Su and B. Keita, *Energy Environ. Sci.*, 2016, **9**,

1012–1023.

150 F. M. Toma, A. Sartorel, M. Iurlo, M. Carraro, P. Parisse, C. MacCato, S. Rapino, B. R. Gonzalez, H. Amenitsch, T. Da Ros, L. Casalis, A. Goldoni, M. Marcaccio, G. Scorrano, G. Scoles, F. Paolucci, M. Prato and M. Bonchio, *Nat. Chem.*, 2010, **2**, 826–831.

151 J. W. Jordan, J. M. Cameron, G. A. Lowe, G. A. Rance, K. L. Y. Fung, L. R. Johnson, D. A. Walsh, A. N. Khlobystov and G. N. Newton, *Angew. Chemie - Int. Ed.*, , DOI:10.1002/anie.202115619.

152 J. W. Jordan, G. A. Lowe, R. L. McSweeney, C. T. Stoppiello, R. W. Lodge, S. T. Skowron, J. Biskupek, G. A. Rance, U. Kaiser, D. A. Walsh, G. N. Newton and A. N. Khlobystov, *Adv. Mater.*, , DOI:10.1002/adma.201904182.

153 J. M. Gurrentz and M. J. Rose, *J. Phys. Chem. C*, 2021, **125**, 14287–14298.

154 S. M. Lauinger, B. D. Piercy, W. Li, Q. Yin, D. L. Collins-Wildman, E. N. Glass, M. D. Losego, D. Wang, Y. V. Geletii and C. L. Hill, *ACS Appl. Mater. Interfaces*, 2017, **9**, 35048–35056.

155 S. M. Lauinger, J. M. Sumliner, Q. Yin, Z. Xu, G. Liang, E. N. Glass, T. Lian and C. L. Hill, *Chem. Mater.*, 2015, **27**, 5886–5891.

156 M. Sarnowska, K. Bienkowski, P. J. Barczuk, R. Solarska and J. Augustynski, *Adv. Energy Mater.*, 2016, **6**, 1–6.

157 J. Tourneur, B. Fabre, G. Loget, A. Vacher, C. Mériadec, S. Ababou-Girard, F. Gouttefangeas, L. Joanny, E. Cadot, M. Haouas, N. Leclerc-Laronze, C. Falaise and E. Guillon, *J. Am. Chem. Soc.*, 2019, **141**, 11954–11962.

158 M. Laurans, K. Trinh, K. Dalla Francesca, G. Izzet, S. Alves, E. Derat, V. Humblot, O. Pluchery, D. Vuillaume, S. Lenfant, F. Volatron and A. Proust, *ACS Appl. Mater. Interfaces*, 2020, **12**, 48109–48123.

159 V. G. Snider, R. Alshehri, R. M. Slaugenhaupt and C. L. Hill, *ACS Appl. Mater. Interfaces*, 2021, **13**, 51519–51524.

160 Q. Wang and D. Astruc, *Chem. Rev.*, , DOI:10.1021/acs.chemrev.9b00223.

161 D. Y. Du, J. S. Qin, S. L. Li, Z. M. Su and Y. Q. Lan, *Chem. Soc. Rev.*, 2014, **43**, 4615–4632.

162 Y. Liu, C. Tang, M. Cheng, M. Chen, S. Chen, L. Lei, Y. Chen, H. Yi, Y. Fu and L. Li, *ACS Catal.*, 2021, **11**, 13374–13396.

163 H. Ma, B. Liu, B. Li, L. Zhang, Y. G. Li, H. Q. Tan, H. Y. Zang and G. Zhu, *J. Am. Chem. Soc.*, 2016, **138**, 5897–5903.

164 K. P. Sullivan, W. A. Neiwert, H. Zeng, A. K. Mehta, Q. Yin, D. A. Hillesheim, S. Vivek, P. Yin, D. L. Collins-Wildman, E. R. Weeks, T. Liu and C. L. Hill, *Chem. Commun.*, 2017, **53**, 11480–11483.

165 H. Liu, J. Luo, W. Shan, D. Guo, J. Wang, C. H. Hsu, M. Huang, W. Zhang, B. Lotz, W. Bin Zhang, T. Liu, K. Yue and S. Z. D. Cheng, *ACS Nano*, 2016, **10**, 6585–6596.

166 H. Liu, C. H. Hsu, Z. Lin, W. Shan, J. Wang, J. Jiang, M. Huang, B. Lotz, X. Yu, W. Bin Zhang, K. Yue and S. Z. D. Cheng, *J. Am. Chem. Soc.*, 2014, **136**, 10691–10699.

167 J. M. Cameron, G. Guillemot, T. Galambos, S. S. Amin, E. Hampson, K. Mall Haidaraly, G. N. Newton and G. Izzet, *Chem. Soc. Rev.*, 2022, **51**, 293–328.

168 M. Raula, G. Gan Or, M. Saganovich, O. Zeiri, Y. Wang, M. R. Chierotti, R. Gobetto and I. A. Weinstock, *Angew. Chemie*, 2015, **127**, 12593–12598.

169 B. Chakraborty and I. A. Weinstock, *Coord. Chem. Rev.*, 2019, **382**, 85–102.

170 B. Chakraborty, G. Gan-Or, Y. Duan, M. Raula and I. A. Weinstock, *Angew. Chemie - Int. Ed.*, 2019, **58**, 6584–6589.

171 G. Zhang, M. Baranov, F. Wang, J. M. Poblet, S. Kozuch, N. Leffler, A. I. Shames, J. M. Clemente-Juan, A. Neyman and I. A. Weinstock, *J. Am. Chem. Soc.*, 2021, **143**, 20769–20778.

172 B. Chakraborty, G. Gan-Or, M. Raula, E. Gadot and I. A. Weinstock, *Nat. Commun.*, , DOI:10.1038/s41467-018-07281-z.

173 J. L. C. Rowsell and O. M. Yaghi, *Microporous Mesoporous Mater.*, 2004, **73**, 3–14.

174 I. Ahmed and S. H. Jhung, *Mater. Today*, 2014, **17**, 136–146.

175 J. E. Mondloch, O. Karagiaridi, O. K. Farha and J. T. Hupp, *Acc. Chem. Res.*, 2010, **43**, 1166–1175.

176 Q. Wang and D. Astruc, *Chem. Rev.*, 2020, **120**, 1438–1511.

177 S. Dang, Q. L. Zhu and Q. Xu, *Nat. Rev. Mater.*, , DOI:10.1038/natrevmats.2017.75.

178 H. Furukawa, K. E. Cordova, M. O'Keeffe and O. M. Yaghi, *Science (80-.).*, , DOI:10.1126/science.1230444.

179 Norbert Stock* and Shyam Biswas, *Chem. Rev.*, 2012, **112**, 933–969.

180 J. Lee, O. K. Farha, J. Roberts, K. A. Scheidt, S. T. Nguyen and J. T. Hupp, *Chem. Soc. Rev.*, 2009, **38**, 1450–1459.

181 J. X. Liu, X. B. Zhang, Y. L. Li, S. L. Huang and G. Y. Yang, *Coord. Chem. Rev.*, 2020, **414**, 213260.

182 G. Férey, C. Mellot-Draznieks, C. Serre, F. Millange, J. Dutour, S. Surblé and I. Margiolaki, *Science (80-.).*, 2005, **309**, 2040–2042.

183 M. Y. Zorainy, M. Gar Alalm, S. Kaliaguine and D. C. Boffito, *J. Mater. Chem. A*, 2021, **9**, 22159–22217.

184 † Diana M. Fernandes,† André D. S. Barbosa,† João Pires,‡ Salete S. Balula,† Luís Cunha-Silva,*,† and Cristina Freire*, *ACS Appl. Mater. Interfaces*, 2013, **5**, 13382–13390.

185 N. V. Maksimchuk, O. A. Kholdeeva, K. A. Kovalenko and V. P. Fedin, *Isr. J. Chem.*, 2011, **51**, 281–289.

186 N. V. N. Maksimchuk, M. N. Timofeeva, M. S. Melgunov, A. N. A. Shmakov, Y. A. Chesalov, D. N. D. Dybtsev, V. P. Fedin and O. A. Kholdeeva, *J. Catal.*, 2008, **257**, 315–323.

187 N. V Maksimchuk, K. A. Kovalenko, S. S. Arzumanov, Y. A. Chesalov, M. S. Melgunov, A. G. Stepanov, V. P. Fedin and O. A. Kholdeeva, *Inorg. Chem.*, 2010, **49**, 2920–2930.

188 Q. Deng, G. Nie, L. Pan, J. J. Zou, X. Zhang and L. Wang, *Green Chem.*, 2015, **17**, 4473–

4481.

189 J. Juan-Alcañiz, E. V. Ramos-Fernandez, U. Lafont, J. Gascon and F. Kapteijn, *J. Catal.*, 2010, **269**, 229–241.

190 N. V. N. Maksimchuk, M. N. Timofeeva, M. S. Melgunov, A. N. A. Shmakov, Y. A. Chesalov, D. N. D. Dybtsev, V. P. Fedin and O. A. Kholdeeva, *J. Catal.*, 2008, **257**, 315–323.

191 M. Zhang, A. M. Zhang, X. L. X. L. X. Wang, Q. Huang, X. Zhu, X. L. X. L. X. Wang, L. Z. Dong, S. L. Li and Y. Q. Lan, *J. Mater. Chem. A*, 2018, **6**, 8735–8741.

192 D. Julião, A. D. S. Barbosa, A. F. Peixoto, C. Freire, B. De Castro, S. S. Balula and L. Cunha-Silva, *CrystEngComm*, 2017, **19**, 4219–4226.

193 T. Steenhaut, Y. Filinchuk and S. Hermans, *J. Mater. Chem. A*, 2021, **9**, 21483–21509.

194 J. Sun, S. Abednatanzi, P. Van Der Voort, Y. Y. Liu and K. Leus, *Catalysts*, 2020, **10**, 578.

195 Y. Ren, M. Wang, X. Chen, B. Yue and H. He, *Materials (Basel).*, 2015, **8**, 1545–1567.

196 R. Liang, R. Chen, F. Jing, N. Qin and L. Wu, *Dalt. Trans.*, 2015, **44**, 18227–18236.

197 S. S. Y. Chui, S. M. F. Lo, J. P. H. Charmant, A. G. Orpen and I. D. Williams, *Science (80-.).*, 1999, **283**, 1148–1150.

198 J. Song, Z. Luo, D. K. Britt, H. Furukawa, O. M. Yaghi, K. I. Hardcastle and C. L. Hill, *J. Am. Chem. Soc.*, 2011, **133**, 16839–16846.

199 C. Y. Sun, S. X. Liu, D. D. Liang, K. Z. Shao, Y. H. Ren and Z. M. Su, *J. Am. Chem. Soc.*, 2009, **131**, 1883–1888.

200 C. R. W. and M. Dincă, *Dalt. Trans.*, 2012, **41**, 7782–7791.

201 L. Yang, H. Naruke and T. Yamase, *Inorg. Chem. Commun.*, 2003, **6**, 1020–1024.

202 X. Xu, S. Chen, Y. Chen, H. Sun, L. Song, W. He and X. Wang, *Small*, 2016, **12**, 2982–2990.

203 Y. Gao, Z. Lv, R. Gao, G. Zhang, Y. Zheng and J. Zhao, *J. Hazard. Mater.*, 2018, **359**,

258–265.

204 Y. Liu, S. Liu, S. Liu, D. Liang, S. Li, Q. Tang, X. Wang, J. Miao, Z. Shi and Z. Zheng, *ChemCatChem*, 2013, **5**, 3086–3091.

205 S. W. Li, J. R. Li, Q. P. Jin, Z. Yang, R. L. Zhang, R. M. Gao and J. she Zhao, *J. Hazard. Mater.*, 2017, **337**, 208–216.

206 X. Zhong, Y. Lu, F. Luo, Y. Liu, X. Li and S. Liu, *Chem. - A Eur. J.*, 2018, **24**, 3045–3051.

207 H. Yang, J. Li, H. Zhang, Y. Lv and S. Gao, *Microporous Mesoporous Mater.*, 2014, **195**, 87–91.

208 H. Yang, J. Li, L. Wang, W. Dai, Y. Lv and S. Gao, *Catal. Commun.*, 2013, **35**, 101–104.

209 E. Rafiee and N. Nobakht, *J. Mol. Catal. A Chem.*, 2015, **398**, 17–25.

210 A. Neyman, L. Meshi, L. Zeiri and I. A. Weinstock, *J. Am. Chem. Soc.*, 2008, **130**, 16480–16481.

211 R. G. Finke and S. Özkar, *Coord. Chem. Rev.*, 2004, 248, 135–146.

212 Y. Lin and R. G. Finke, *J. Am. Chem. Soc.*, 1994, **116**, 8335–8353.

213 J. D. Aiken and R. G. Finke, *J. Am. Chem. Soc.*, 1999, **121**, 8803–8810.

214 G. Maayan and R. Neumann, *Chem. Commun.*, 2005, 4595–4597.

215 T. Hsu-Yao, K. P. Browne, N. Honesty and Y. J. Tong, *Phys. Chem. Chem. Phys.*, 2011, **13**, 7433–7438.

216 A. Troupis, A. Hiskia and E. Papaconstantinou, *Angew. Chemie - Int. Ed.*, 2002, **41**, 1911–1914.

217 A. Z. Ernst, L. Sun, K. Wiaderek, A. Kolary, S. Zoladek, P. J. Kulesza and J. A. Cox, *Electroanalysis*, 2007, **19**, 2103–2109.

218 Y. Wang, A. Neyman, E. Arkhangelsky, V. Gitis, L. Meshi, I. A. Weinstock, V. Uni and B. S. V, 2009, 17412–17422.

219 Y. Wang, A. Neyman, E. Arkhangelsky, V. Gitis, L. Meshi and I. A. Weinstock, *J. Am.*

Chem. Soc., 2009, **131**, 17412–17422.

220 C. R. Graham, L. S. Ott and R. G. Finke, *Langmuir*, 2009, **25**, 1327–1336.

221 J. A. Widegren, J. D. Aiken, S. Özkar and R. G. Finke, *Chem. Mater.*, 2001, **13**, 312–324.

222 S. Zoladek, I. A. Rutkowska, K. Skorupska, B. Palys and P. J. Kulesza, *Electrochim. Acta*, 2011, **56**, 10744–10750.

Chapter 2:

Catalytic System for Aerobic Oxidation That Simultaneously Functions as Its Own Redox Buffer

Abstract

The control of solution electrochemical potential as well as pH impacts products in redox reactions, but the former gets far less attention. Redox buffers facilitate maintenance of potentials and have been noted in diverse cases, but they have not been a component of catalytic systems. We report a catalyst system that contains its own built-in redox buffer. Two highly synergistic components (a) the tetrabutylammonium salt of hexavanadopolymolybdate $TBA_4H_5[PMo_6V_6O_{40}]$ (**PV_6Mo_6**) and (b) $Cu(ClO_4)_2$ in acetonitrile catalyze the aerobic oxidative deodorization of thiols by conversion to the corresponding non-odorous disulfides at 23 ^oC (each catalyst alone is far less active). For example, the reaction of 2-mercaptoethanol with ambient air gives a TON = 3×10^2 in less than one hour with a TOF = 6×10^{-2} s^{-1} with respect to **PV_6Mo_6**. Multiple electrochemical, spectroscopic and other methods establish that (1) **PV_6Mo_6,** a multistep and multielectron redox buffering catalyst, controls the speciation and the ratio of Cu(II)/Cu(I) complexes and thus keeps the solution potential in different narrow ranges by involving multiple POM redox couples, and simultaneously functions as an oxidation catalyst that receives electrons from the substrate, (2) Cu catalyzes two processes simultaneously, oxidation of the RSH by **PV_6Mo_6** and reoxidation of reduced **PV_6Mo_6** by O_2, and (3) the analogous polytungstate-based system, $TBA_4H_5[PW_6V_6O_{40}]$ (**PV_6W_6**) has nearly identical cyclic voltammograms (CV) as **PV_6Mo_6** but has almost no catalytic activity: it does not exhibit self-redox buffering.

2.1 Introduction

Redox buffers maintain the solution electrochemical potential in narrow range by controlling the concentration of oxidized and reduced forms of redox couples in analogy with

conventional acid-base buffers that maintain solution pH by controlling the concentration of the two forms of an acid-base couple. The fundamental equations for acid-base buffering, including but not limited to the Henderson-Hasselbach equation, and redox buffering have analogous forms.[1,2] Redox buffering has been used to optimize performance in solid contact ion-selective electrodes,[3,4] and functions as a key component in copper-catalyzed benzylic C-H bond functionalization.[5] It is also a natural component in biological redox systems where the potential and more than one oxidation state of the redox-active species reversibly interconvert. Thiol-disulfide (RSH/RSSR) equilibria including the glutathione couple, GSH/GSSG are exemplary.[6–12] However, the formulation of a catalyst that has a built-in self-buffering capability has not been specifically reported to our knowledge.

Polyoxometalates (POMs) are attractive because they have extensive and tunable redox properties and are already successful catalysts for several commercialized organic oxidation processes. The Keggin polytungstic acids along with $PV_nMo_{12-n}O_{40}$ and the binary systems $PV_nMo_{12-n}O_{40}$/Pd (n = 1-6) are the most thoroughly studied POM catalysts.[13] Metals other than Pd have been evaluated with polyvanadomolybdates and found to be minimally reactive (e.g. Ru, Ir) or stoichiometric (Tl). $PV_nMo_{12-n}O_{40}$/Pd (n = 1-6) has been used for oxidation of ethylene, alkenes and alcohols,[14–16] and can replace the corrosive chloride in the long-used Hoechst-Wacker process that uses $CuCl_2$ and $PdCl_2$. Our group[17] and those of Matveev,[16] Kozhevnikov[13,14] and Neumann[15,18,19] reviewed organic substrate oxidations, including ones based on O_2 as the terminal oxidant, catalyzed by POMs, including $PV_nMo_{12-n}O_{40}$/Pd systems, while Misono and Mizuno[20–22] reviewed industrial POM-catalyzed oxidations some time ago. Thiol oxidations are also important in organic chemistry,[23,24] physiological processes[25–27] and environmental science.[28–30] Numerous catalytic and stoichiometric systems are known to

selectively oxidize thiols in context with either deodorization or synthesis, including nanoparticle systems,[31,32] POMs,[33–39] metal-organic frameworks (MOFs),[30,40,41] strong stoichiometric oxidants,[42–48] and noble metals.[49–53] Most of these systems do not use O_2 as terminal oxidant. In addition, most are slow, require elevated temperatures, and form side products.

The system we report here, the first POM and non-noble metal two-component catalytic system: tetrabutylammonium salt of hexavanadopolymolybdate $TBA_4H_5[PMo_6V_6O_{40}]$ (PV_6Mo_6) and $Cu(ClO_4)_2$ catalyzes our target reaction in this study: the aerobic oxidative deodorization of thiols, RSH, by conversion to the desired nearly odorless disulfide, RSSR, eq 2.1. Cu has been chosen because it efficiently catalyzes the oxidation of reduced POMs by O_2,[54] and is a known catalyst of aerobic thiol oxidation.[25,55–57] Remarkably, this PV_6Mo_6/Cu catalytic system functions as its own redox buffer which maintains optimal conditions for the highest turnover rate.

$$RSH + ¼\ O_2 \rightarrow ½\ RSSR + ½\ H_2O \qquad (2.1)$$

2.2 Experimental

2.2.1 General Materials and Methods

All chemicals were purchased from commercial sources and used without further purification. $TBA_6PV_3W_9O_{40}$, $TBA_4H_5PW_6V_6O_{40}$, $TBA_3H_3V_{10}O_{28}$ were synthesized according to the literature methods.[58,59] The FT-IR spectra were collected on a Nicolet TM 600 FT-IR spectrometer by the attenuated total reflectance (ATR) sampling technique. UV−vis spectra were measured with an Agilent 8453 spectrophotometer equipped with a diode array detector using a 1.0 cm optical path length quartz cuvette. ^1H and ^{31}P nuclear magnetic resonance (NMR) spectra were acquired on a Varian INOVA 400 spectrometer. The kinetics were followed by an SF-61 stopped-flow instrument (Hi-Tech Scientific, U.K.). Elemental analyses (N and P) were

conducted by Galbraith Laboratories (Knoxville, TN). The thermogravimetric (TGA) data were collected on a Mettler Toledo TGA instrument.

2.2.2 Electrochemistry

Cyclic voltammograms (CVs) and bulk electrolysis data were obtained using a BAS CV-50W electrochemical analyzer and conducted at room temperature (25 ± 2 °C). CVs were recorded in a standard three-electrode electrochemical cell with a glassy carbon disk working electrode, a platinum wire counter electrode and a Ag/Ag^+ (0.01 M $AgNO_3$ in CH_3CN) reference electrode using 0.1 M tetrabutylammonium hexafluorophosphate (n-Bu_4NPF_6) as the supporting electrolyte. The scan rate used in voltametric experiments was 100 mV s^{-1}. The measured potential was converted to the Fc/Fc^+ scale using data measured from CV for 1.0 mM ferrocene (Fc). A reticulated vitreous carbon working electrode was used as a working electrode in bulk electrolysis and the working and counter electrode were separated by porous glass sinters. Each electrolysis was conducted at the desired constant potential until the current dropped to <10% of the initial value, then aliquots were withdrawn and the UV-Vis spectra were recorded under Ar. The electrolysis was then resumed at the more negative potential.

Number of electrons transferred during bulk electrolysis was calculated by Faraday's law of electrolysis $Q = nFN$, where Q is the number of coulombs, $F = 96485\ C\ mol^{-1}$ is Faraday's constant, N is the moles of substrate electrolyzed and n is the stoichiometric number of electrons consumed.

Rotating disk electrode (RDE) voltammetry was conducted on a Wavedriver 10 potentiostat/galvanostat (Pine Research Instrumentation) using a standard three electrode setup with a 3 mm diameter glassy carbon disk working electrode, a Ag/Ag^+ (0.01 M $AgNO_3$ in

CH_3CN) reference electrode, and a platinum wire counter electrode. The rotation speed was controlled by a Model AFMSRCE ring-disk electrode system (Pine Research Instrumentation).

RDE data were analyzed by Levich plots (limiting current i_L versus $\omega^{1/2}$, where ω is the rotation speed) using the Levich equation $i_L = 0.62nFAD^{2/3}\omega^{1/2}v^{-1/6}C_0$, where n is the number of transferred electrons in the redox reaction, $F = 96485\ C\ mol^{-1}$ is Faraday's constant, A is the area of electrode surface, v is the kinematic viscosity of the 0.1 M *n*-Bu_4NPF_6 acetonitrile solution and C_0 is the bulk concentration of POM.

2.2.3 Synthesis of TBA salts of $PMo_{12-n}V_nO_{40}^{(3+n)-}$ (n = 1-6)

$H_3PMo_{12}O_{40}$, $H_4PVMo_{11}O_{40}$, $H_5PV_2Mo_{10}O_{40}$, $H_6PV_3Mo_9O_{40}$, $(NH_4)_7PV_4Mo_8O_{40}$ and $(NH_4)_5H_4PMo_6V_6O_{40}$ were synthesized according to the literature methods.[60–63] The tetra-*n*-butylammonium (TBA) salts of POMs were precipitated from aqueous solutions with TBA bromide. $TBA_3PMo_{12}O_{40}$ (**PMo_{12}**) was prepared in 0.1 M $HClO_4$, while $TBA_4PVMo_{11}O_{40}$ (**$PVMo_{11}$**) and $TBA_4HPV_2Mo_{10}O_{40}$ (**PV_2Mo_{10}**) were prepared in 0.1 M sulfate buffer at pH 2.0. $TBA_4H_2PV_3Mo_9O_{40}$ (**PV_3Mo_9**), $TBA_4H_3PV_4Mo_8O_{40}$ (**PV_4Mo_8**) and $TBA_4H_5PMo_6V_6O_{40}$ (**PV_6Mo_6**) were prepared directly in DI water. TBA salts of the POMs were recrystallized twice in acetonitrile. Their purity was confirmed by FT-IR spectroscopy: IR (ATR) **PMo_{12}**: 1059, 949, 872 and 782 cm^{-1}. **$PVMo_{11}$**: 1078, 1054, 982, 938, 865 and 787 cm^{-1}. **PV_2Mo_{10}**: 1077, 1063, 1048, 984, 935, 867, 780 cm^{-1}. **PV_3Mo_9**: 1077, 1062, 1048, 1004, 966, 935, 870 and 777 cm^{-1}. **PV_4Mo_8**: 1064, 1001, 961, 936, 876 and 765 cm^{-1}. **PV_6Mo_6**: 1062, 1001, 955, 933, 876 and 765 cm^{-1}. The number of TBA counterions was characterized by TGA.

2.2.4 Conditions for Catalytic Reactions

Quantification of RSH. The RSH concentration was determined using Ellman's reagent (5,5-dithiobis(2-nitrobenzoic acid) (DTNB)).[37] DTNB quickly reacts with thiols through the following reaction to form 2-nitro-5-thiobenzoic acid (TNB), which absorbs in the UV-vis region at λ_{max} = 412 nm ($\varepsilon = 13.1 \pm 0.9 \times 10^3$ M^{-1} cm^{-1}).

In a typical reaction, 0.1 mL of DTNB stock solution (5 mg/mL in methanol) was added to 5 mL of a 50 mM phosphate buffer solution (pH 7.4). This solution was used as a blank for UV-vis measurements. Then, 10 µL aliquot of the reaction solution was added and the absorbance at 412 nm was measured.

Oxidation of RSH. In a typical reaction, **PV_6Mo_6** (0.1 mM), $Cu(ClO_4)_2$ (0.5 mM) and 2-mercaptoethanol (30 mM) were stirred in acetonitrile under air in air-conditioned room at 25 ± 2 ^oC. The aliquots of the solution were withdrawn every several minutes and monitored as discussed above.

Reduction State of PV_6Mo_6 under Steady State Conditions. In a typical experiment, **PV_6Mo_6** (0.1 mM) and $Cu(ClO_4)_2$ (0.5 mM) were stirred in acetonitrile purged with air in a 1.0 cm optical path length quartz cuvette at 25±2 ^oC. The changes in the UV-Vis spectra of the solution in the course of the reaction were monitored after adding the 2-mercaptoethanol (30 mM). The absorption was then converted to the apparent extinction coefficient using the Beer–Lambert law.

Stopped-Flow Measurements. The rates of $PV_nMo_{12-n}O_{40}^{(3+n)-}$ reduction by 2-mercaptoethanol at different concentrations of $Cu(ClO_4)_2$ [Cu(II)] were measured under argon by

recording changes in visible spectra using the stopped-flow technique. In a typical experiment, one feeding syringe was filled with the de-aerated stock acetonitrile solution of POM and Cu(II). The second syringe was filled with the de-aerated acetonitrile solution of 2-mercaptoethanol. In all stopped-flow kinetic measurements, the concentrations of POM, Cu(II) and 2-mercaptoethanol in the reaction mixture were two times lower than those in the feeding syringes.

Reoxidation of Reduced POMs by O_2. PV_6Mo_6 was reduced by 3 equivalents (6-electron reduction) of ascorbic acid and kept under argon. Reoxidation was followed by UV-vis absorbance on 550 nm. In a typical experiment, after adding the Cu(II) stock solution to the 6-electron reduced POM solution in a 1.0 cm optical path length quartz cuvette, the O_2 was purged through the solution, and the absorbance was monitored as a function of time.

Reaction Stoichiometry Determination. The stoichiometry was determined by monitoring the oxygen consumption using a pressure monometer. In a typical experiment, **PV_6Mo_6** (0.1 mM), $Cu(ClO_4)_2$ (0.8 mM) and 2-mercaptoethanol (15 mM, 30 mM) was stirred in acetonitrile (30 mL) in a double-neck, jacketed glass flask (90 mL). The pressure monometer was connected to the flask and the system was airtight. The pressure drop due to the oxygen consumption was read by pressure monometer in mm Hg units. The volume of head space was 57 mL, and the solution volume was 30 mL.

2.3 Results and Discussion

2.3.1 Characterization of TBA salts of $PMo_{12-n}V_nO_{40}^{(3+n)-}$ (n = 1-6)

FT-TR spectra of TBA salts of $PMo_{12-n}V_nO_{40}^{(3+n)-}$ (n = 1-6, **PVMo**) are shown in Figure 2.1. The bands around 1480-1370 cm^{-1} can be assigned to C-H bending from the TBA counterion. The peaks in the range of 1070-1030 cm^{-1} are assigned to P-O vibrations. The splitting from a

signal peak is due to the positional isomers of the multi-vanadium Keggin complexes. The substitution of vanadium decreases the degree of structural symmetry. Peaks in the range of 1000-910 cm^{-1} are assigned to M-O vibrations (where M = V or Mo), and peaks around 870 and 780 cm^{-1} are assigned to inter-octahedral M-O-M and intra-octahedral M-O-M vibrations respectively.[61,63,64]

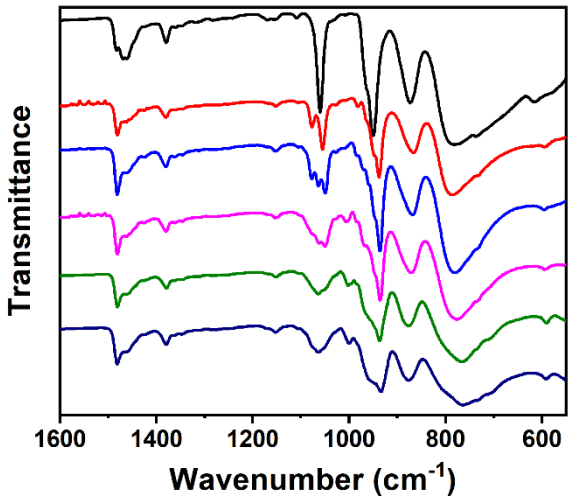

Figure 2.1. FT-IR (ATR) spectra. $TBA_3PMo_{12}O_{40}$ (black), $TBA_4PVMo_{11}O_{40}$ (red), $TBA_4HPV_2Mo_{10}O_{40}$ (blue), $TBA_4H_2PV_3Mo_9O_{40}$ (pink), $TBA_4H_3PV_4Mo_8O_{40}$ (green) and $TBA_4H_5PMo_6V_6O_{40}$ (TBA_4H_5**PV_6Mo_6**; dark blue).

The UV-Vis spectra of **PVMo** are given in Figure 2.2. The ligand-to-metal charge-transfer (LMCT) band of V(V) center is around 350-500 nm, which indicates the substitution of Mo(VI) with V(V). The intensity of this band increases with the increasing number of vanadium atoms in POM.[59] Therefore, the absorbance increases in the order of : **$PVMo_{11}$** < **PV_2Mo_{10}** < **PV_3Mo_9** < **PV_4Mo_8** < **PV_6Mo_6**.

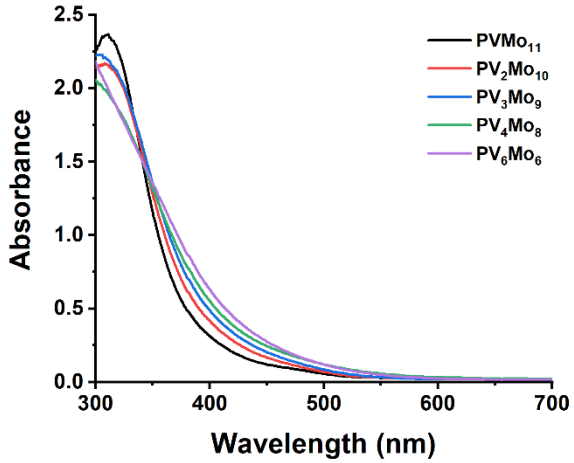

Figure 2.2. UV-Vis spectra of TBA salts of $PV_nMo_{12-n}O_{40}^{(3+n)-}$.

The number of TBA counterions of the most effective catalyst in this paper, $TBA_4H_5PMo_6V_6O_{40}$, **PV_6Mo_6**, was determined by elemental analyses: N/P = 4.05. The number of TBA counterions for all the $PMo_{12-n}V_nO_{40}^{(3+n)-}$ isomers was confirmed by TGA (Figure 2.3), 36.37%, 36.7%, 36.91% 38.5% and 38.31% weight loss for $TBA_4PVMo_{11}O_{40}$, $TBA_4HPV_2Mo_{10}O_{40}$, $TBA_4H_2PV_3Mo_9O_{40}$, $TBA_4H_3PV_4Mo_8O_{40}$ and $TBA_4H_5PMo_6V_6O_{40}$, respectively. None of these POMs show marked loss of hydration water molecules. The slow weight loss after 400 °C is due to the thermal instability of the **PVMo** structure at and above this temperature.

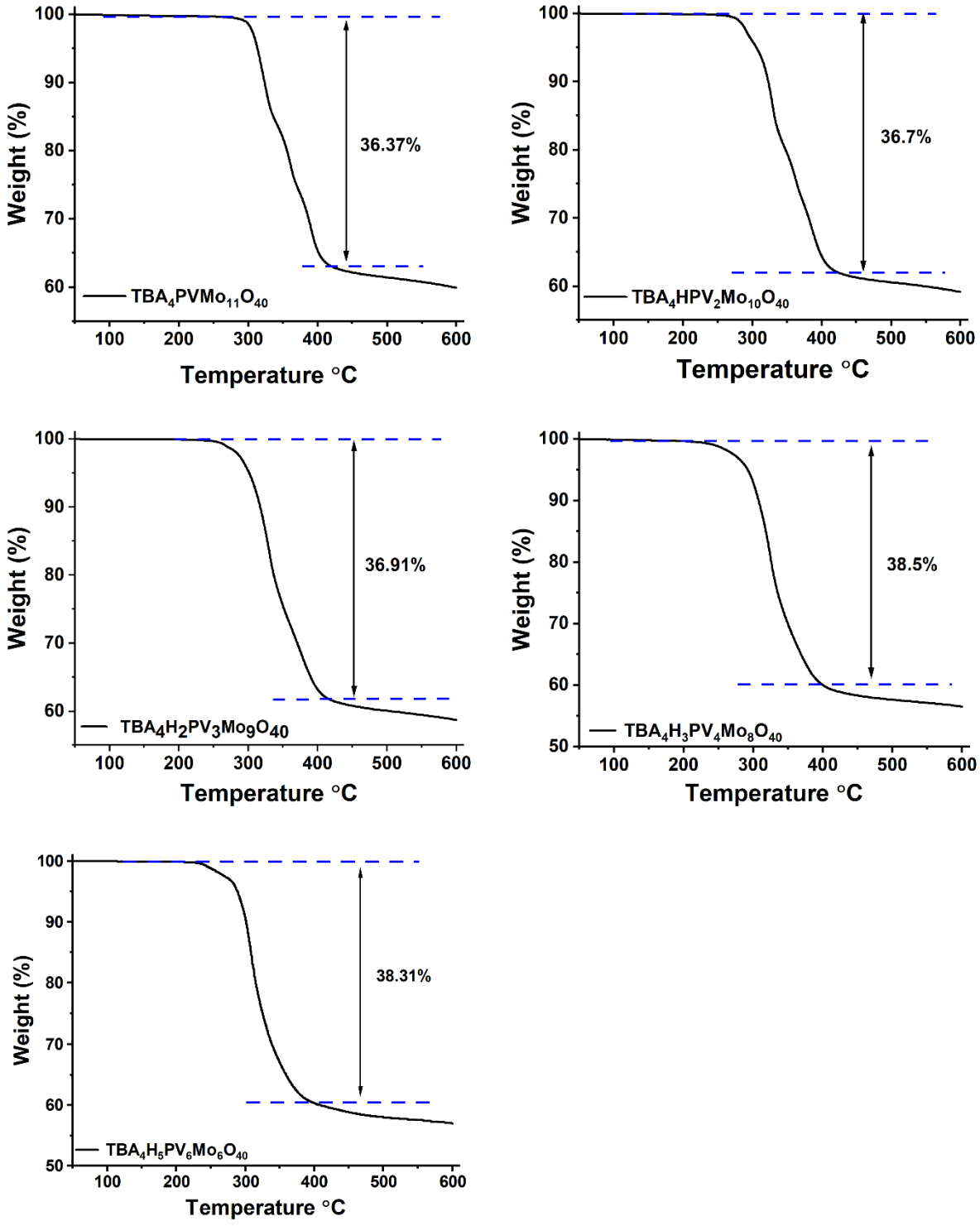

Figure 2.3. Thermogravimetric analysis (TGA) data of TBA salts of $PV_nMo_{12-n}O_{40}^{(3+n)-}$.

2.3.2 Reaction Stoichiometry and Product Detection

We seek a catalyst for eq 2.1 that is fast, selective for non-odorous disulfide product, and works with ambient air (O_2) at room temperature. We used 2-mercaptoethanol as the thiol for in depth studies because its reaction, eq 2.1, is facile to quantify. The reaction stoichiometry was measured by following the consumption of O_2 that described in experimental section, and the consumption curves are shown in Figure 2.4. The pressure dropped by 68 mm Hg when the RSH concentration was 30 mM, 0.895 mmol. The molar ratio between consumed RSH and consumed oxygen calculated from eq 2.2 and eq 2.3 was 4.06 ± 0.08. Similarly, the pressure dropped by 35 mm Hg in the reaction of RSH (15 mM, 0.447 mmol) when the molar ratio of RSH to oxygen was 3.96 ± 0.08, which can be calculated from eq 2.4 and eq 2.5. In addition, the pressure drop was 35 mm Hg at 15 mM RSH, roughly a half the 68 mm Hg drop at 30 mM RSH, which confirms the stoichiometry of the reaction.

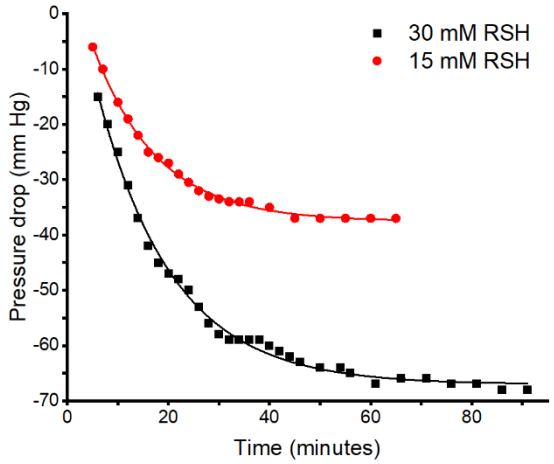

Figure 2.4. Oxygen consumption curve. Solid points: real experimental data. Solid line: exponential fitting curve.

$\Delta 68$ mmHg = $\Delta 9.57$ kpa (2.2)

$$\Delta pv = \Delta nRT \; ; \; \Delta n = \frac{9.57 \text{ kpa} \times 0.057 \text{ L}}{8.3145 \times (24 + 273.15)} = 2.24 \times 10^{-4}; \; \frac{8.95 \times 10^{-4}}{2.24 \times 10^{-4}} = 4.06 \qquad (2.3)$$

$$\Delta 35 \text{ mmHg} = \Delta 4.93 \text{ kpa} \qquad (2.4)$$

$$\Delta n = \frac{4.93 \text{ kpa} \times 0.057 \text{ L}}{8.3145 \times (24 + 273.15)} = 1.13 \times 10^{-4}; \; \frac{4.47 \times 10^{-4}}{1.13 \times 10^{-4}} = 3.96 \qquad (2.5)$$

The formation of the single product, bis(2-hydroxyethyl) disulfide (RSSR) was confirmed by ^{1}H NMR, Figure 2.5. Thus, the overall reaction can be described by eq 2.1.

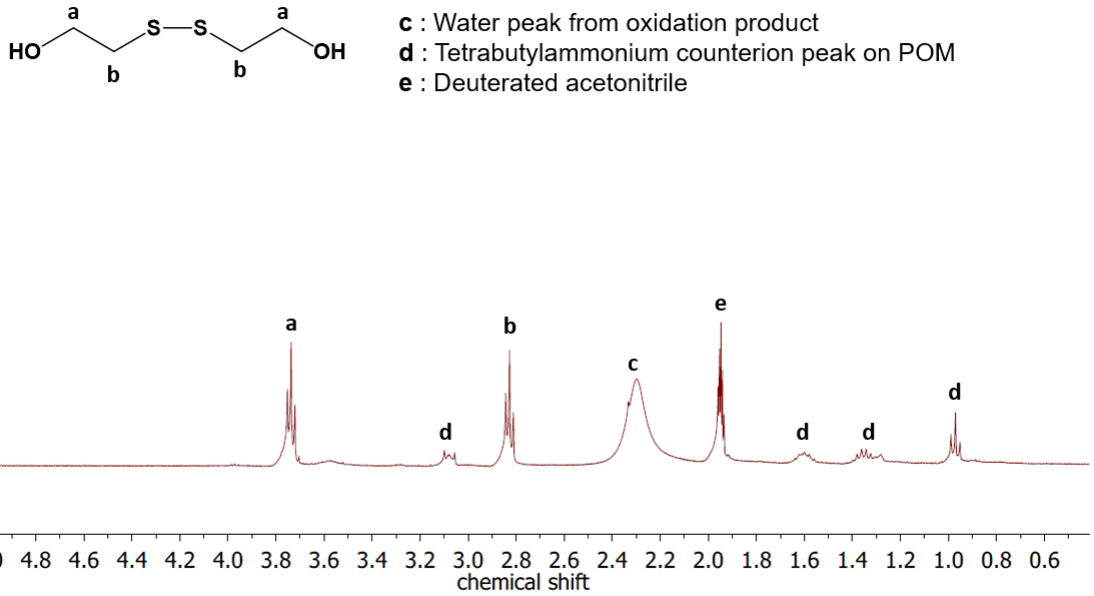

Figure 2.5. ^{1}H NMR of the solution at the end of the reaction: confirmation that the product of 2-mercaptoethanol oxidation is bis(2-hydroxyethyl) disulfide. Conditions: **PV_6Mo_6** (0.1 mM), $Cu(ClO_4)_2$ (0.8 mM) and 2-mercaptoethanol (30 mM) stirred in deuterated acetonitrile (5 mL) under air.

2.3.3 Catalytic Activity and Synergistic Effect

Table 2.1 summarizes the activity of $Cu(ClO_4)_2$ and multi-vanadium-substituted polytungstates and polymolybdate Keggin POMs for the oxidation of 2-mercaptoethanol (RSH)

by air in acetonitrile at ambient temperature. PV_6Mo_6 + Cu (**PV_6Mo_6**/Cu) is the most active catalyst, achieving a turnover number (TON) of 3×10^2 in 90 minutes.

Table 2.1. Air-based Oxidation of 30 mM 2-Mercaptoethanol Catalyzed by Different POM Systems[a]

Catalyst[e]	Cu concentration[a], mM	Conversion[b] %	TON×10^{-2}[c]	TOF×10^3, s^{-1} [d]
$Cu(ClO_4)_2$	0.5	9	0.03	0.6
PV_3W_9	0.5	13	0.42	7.8
PV_6W_6	0.5	16	0.57	11
$V_{10}O_{28}$	0.5	12	0.36	6.7
PMo_{12}	0.5	9	0.03	0.6
PV_6Mo_6	0.5	90	2.9	53
$PVMo_{11}$	0.8	10	0.30	5.6
PV_2Mo_{10}	0.8	12	0.36	6.7
PV_3Mo_9	0.8	16	0.48	8.9
PV_4Mo_8	0.8	86	2.6	48
PV_6Mo_6	0.8	100	3.0	56
PV_6Mo_6[f]	0.5	60	3.0	55

[a] Conditions: POM (0.1 mM), 2-mercaptoethanol (30 mM), acetonitrile (5 mL) at room temperature under air. [b] Conversion was measured after 90 min. [c] Turnover number (TON = moles of 2-mercaptoethanol consumed per mol of POM) was measured after 90 min. [d] Turnover Frequency, TOF = TON/(Reaction time). [e] For the POM chemical formulas see the POM synthesis section in the SI. [f] 50 mM 2-mercaptoethanol.

One of the most interesting findings is the dramatic synergism of catalytic activity of $Cu(ClO_4)_2$ and $PMo_{12-n}V_nO_{40}^{(3+n)-}$ (n = 1 - 4, 6): the activity of the mixture of two catalysts is much higher than a sum of their individual activities (Figure 2.6). In order to explain this phenomenon, we have studied the function of POM and Cu by kinetics and electrochemical

methods and probed the processes constituting the reaction mechanism. The system with the highest catalytic activity, Cu/**PV_6Mo_6**, was chosen for these studies.

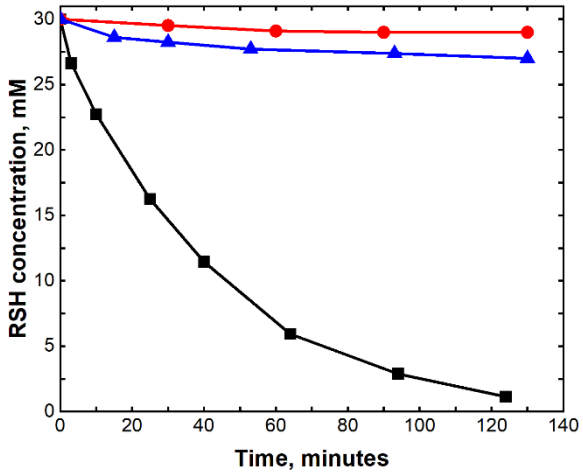

Figure 2.6. Kinetics of 30 mM 2-mercaptoethanol oxidation by air (1 atm, 24 ºC) in acetonitrile catalyzed by 0.1 mM **PV_6Mo_6** (red), by 0.5 mM $Cu(ClO_4)_2$ (blue), and by a combination of 0.1 mM **PV_6Mo_6** + 0.5 mM $Cu(ClO_4)_2$ (black).

2.3.4 Evidence of Non-dissociation of Free Vanadium, VO_2^+

Based on results in Table 1, the catalytic activity of molybdates increases as the number of vanadium atoms in the POM increases. The effect of substituted vanadium atoms on catalytic activity has been shown by several studies.[59,65–70] Two mechanisms are generously applied to explain the activity tendency: 1. When the complete POM structure performs as an active center, the activity is controlled by V(V/VI) redox potential and POM structure.[59,67] Some work observed peroxo vanadium complex of divanadium-substituted polyoxotungstates as acetive center with H_2O_2.[71,72] 2. It is known that polyvanadium-substituted heteropolyacids can dissociate free vanadium in acidic aqueous solution. Some studies show that the dissociated VO_2^+ species are active centers.[65,68,73,74] One example is the oxidation of 2,3,6-trimethylphenol (TMP) by O_2 in AcOH-H_2O catalyzed by $H_{3+n}PMo_{12-n}V_nO_{40}$.[65] They assumed that the active

species is vanadate, VO_2^+, and its dissociation from the parent POM, $PMo_{12-n}V_nO_{40}^{(3+n)-}$, is more pronounced with increasing numbers of vanadium atoms. If the free vanadate is the active center, the catalytic activity of POM should be similar to that of the same concentration of vanadate. Therefore, we compared the activity of sodium metavanadate alone ($NaVO_3$) and the mixture of $NaVO_3$ with **PV_6Mo_6** (Figure 2.7). $NaVO_3$ alone was catalytically inactive, and there was no difference in activity between POM with and without $NaVO_3$. These two arguments strongly suggest that free monomeric vanadium species are not involved in the catalysis under these conditions.

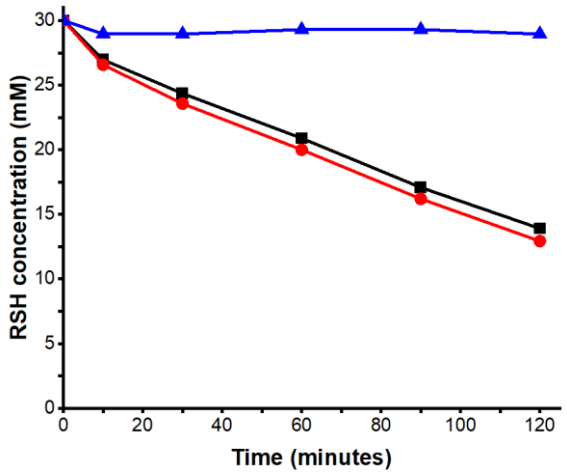

Figure 2.7. Kinetics of 2-mercaptoethanol oxidation by air. Black curve: **PV_6Mo_6** (0.1 mM) with $Cu(ClO_4)_2$ (0.5 mM); red curve: **PV_6Mo_6** (0.1 mM), $NaVO_3$ (0.1 mM) with $Cu(ClO_4)_2$ (0.5 mM). Blue curve: $NaVO_3$ (0.5 mM) with $Cu(ClO_4)_2$ (0.5 mM). Conditions: 2-mercaptoethanol (30 mM) in acetonitrile (5 mL). $NaVO_3$ was dissolved in hot DI water to make a stock solution. Stock solution (50 μL) was added to the acetonitrile solution resulting in 0.1 mM $NaVO_3$. Since $NaVO_3$ does not dissolve in acetonitrile, an aqueous stock solution of $NaVO_3$ with the required concentration was added to the acetonitrile solution.

Furthermore, the ^{31}P NMR of a mixture of **PV_6Mo_6** and **$PVMo_{11}$** shows only stack peaks of these two POMs but not a redistribution of isomers. Aging the **PV_6Mo_6** overnight does not show

additional NMR peaks (Figure 2.8). These results suggest that **PV_6Mo_6** is thermodynamically stable in acetonitrile over the reaction timescale. Reduction generates paramagnetic V(IV) which cannot be observed by NMR. However, we were able to observe the fairly constant reduced states of the POM under turnover conditions by UV-Vis spectroscopy (*vide infra*). V(IV) has a totally different UV-Vis absorption band than the V(IV)-to-Mo(VI) intervalence charge transfer (IVCT) band in the Keggin POM. If free vanadium outside the POM is dominant during the catalytic reaction, it is impossible for us to observe the fairly constant reduction states based on the V(IV)-to-Mo(VI) IVCT band. Therefore, we make an assumption here that vanadium outside the POM is not significant in this system. The difference in our multi-component catalyst system here and the classic studies of Kozhevnikov in aqueous media is not surprising because the solvation energy of VO_2^+ in acetonitrile is much lower than in water, and thus VO_2^+ dissociation from the polyanion in CH_3CN is much less favorable. This is consistent with Kozhevnikov's results: changing the solvent to acetonitrile shuts down the catalytic activity.[65]

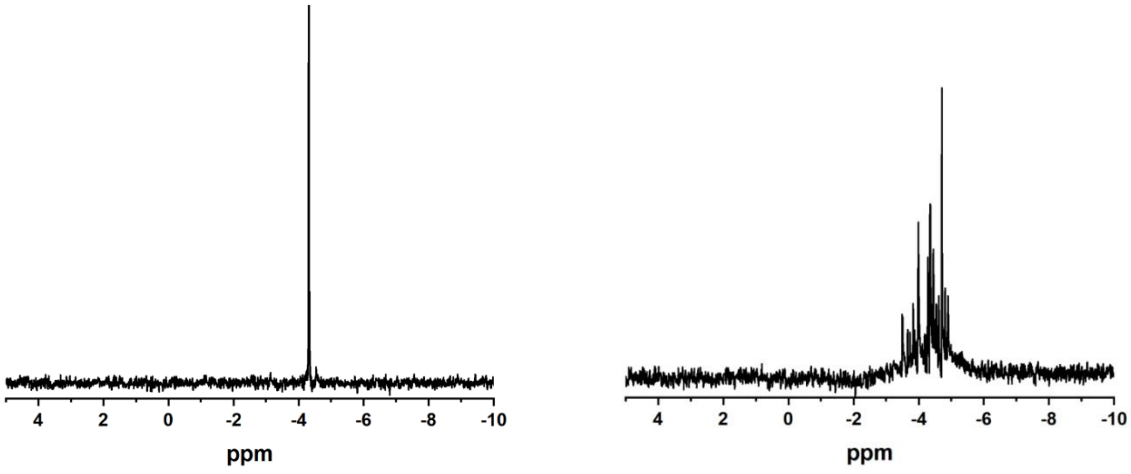

(a) (b)

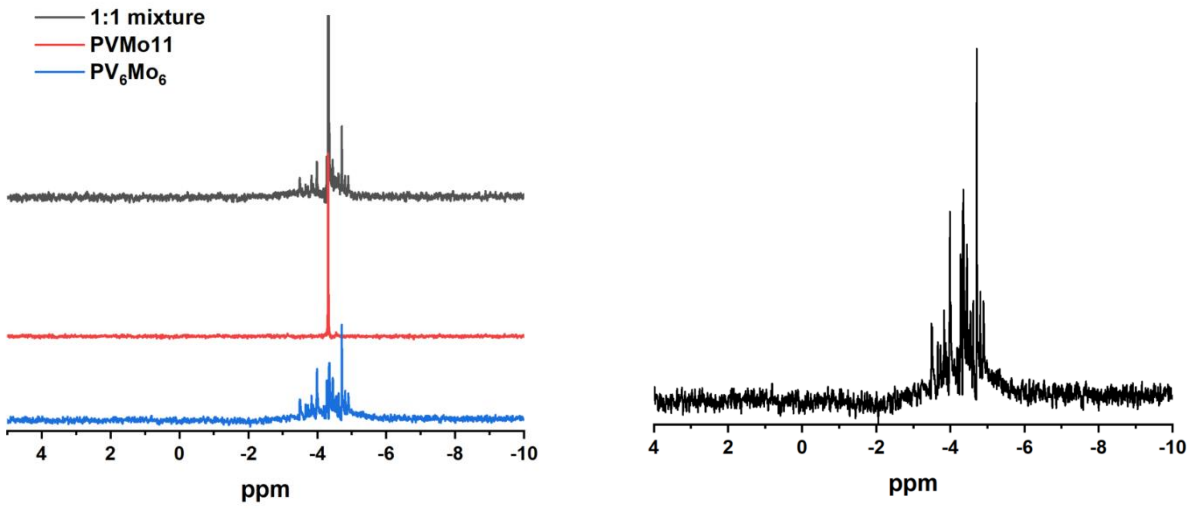

Figure 2.8. ^{31}P NMR spectra in acetonitrile-d_3 with respect to 85% H_3PO_4 (0 ppm) (a) **$PVMo_{11}$**; (b) **PV_6Mo_6**; (c) 1:1 mixture of **$PVMo_{11}$** and **PV_6Mo_6**; (d) **PV_6Mo_6** after aging overnight.

2.3.5 Features of the catalytic aerobic oxidation of 2-mercaptoethanol

Figure 2.9a shows that there is negligible inhibition of the rate by the accumulating product, the disulfide, RSSR. Moreover, we found no significant effect of either water or ionic strength on the rates (Figures 2.9b and 2.9c). Therefore, no extra water nor other salts were added in our experiments. The kinetics of 2-mercaptoethanol oxidation depends on concentrations of RSH, POM, Cu and O_2, which makes it extremely hard to quantitively analyze. Therefore, we analyzed our kinetics data semi-quantitively as described below.

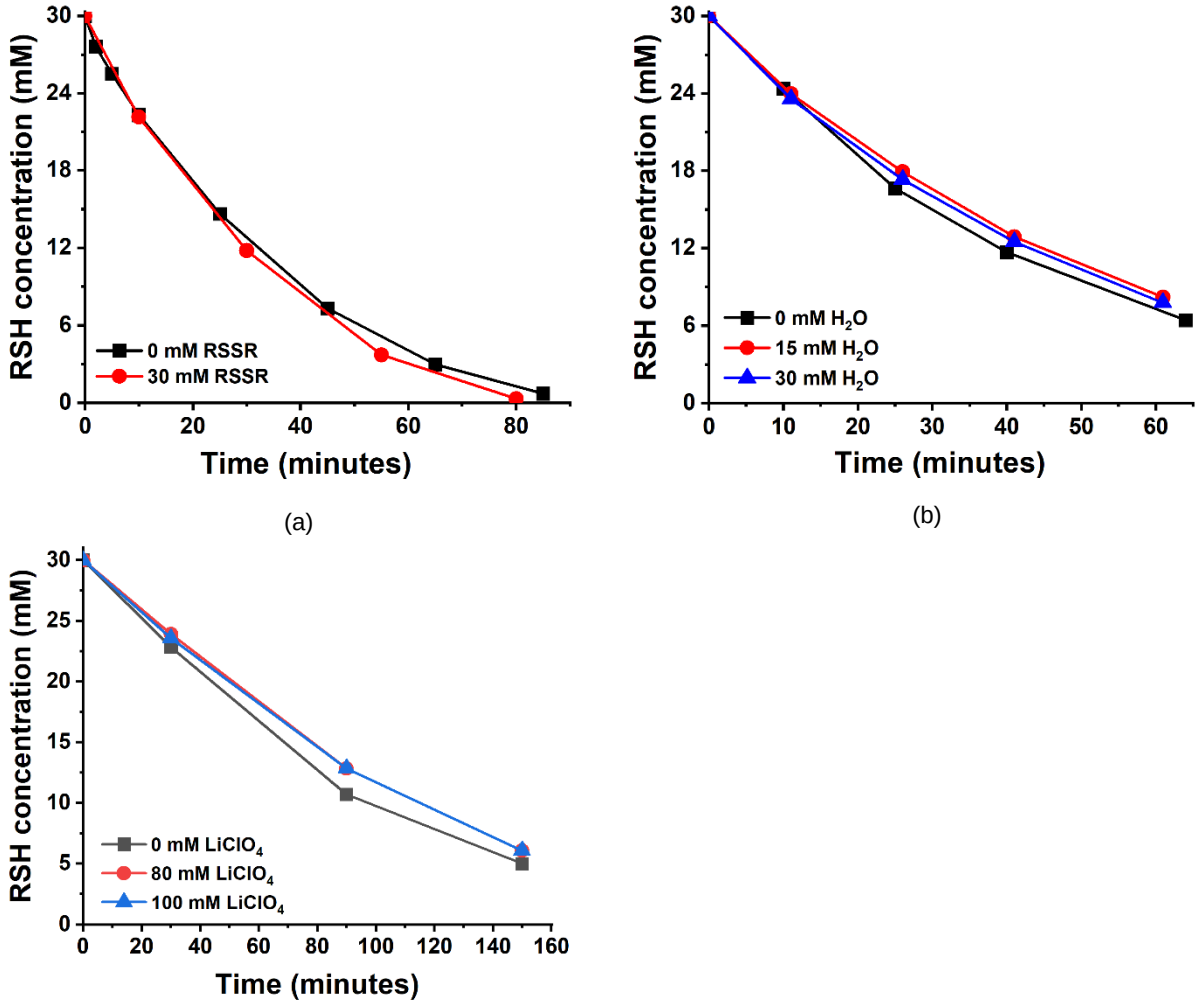

Figure 2.9. Effects of the reaction products and ionic strength on kinetics of 2-mercaptonethanol oxidation by air. (a) **RSSR effect: PV_6Mo_6** (0.1 mM), $Cu(ClO_4)_2$(0.5 mM) and 2-mercaptoethanol (30 mM). Black curve: bis(2-hydroxyethyl) disulfide (RSSR) (0 mM initial concentration); red curve: RSSR (30 mM initial concentration). (b) **H_2O effect: PV_6Mo_6** (0.1 mM), $Cu(ClO_4)_2$ (0.5 mM) and 2-mercaptoethanol (30 mM). Black curve: H_2O (0 mM); red curve: H_2O (15 mM); blue curve: H_2O (30 mM). (c) **Ionic strength effect by varying $LiClO_4$ concentration: PV_6Mo_6** (0.2 mM), $Cu(ClO_4)_2$ (0.5 mM) and 2-mercaptoethanol (30 mM). Black curve: $LiClO_4$ (0 mM); red curve: $LiClO_4$ (80 mM); Blue: $LiClO_4$ (100 mM).

After some optimization, we chose the following range of initial concentrations (in mM) for our detailed studies: 20-50 for RSH, 0.025-0.8 for POM, **PV_6Mo_6**, and 0.1-1.0 for Cu(II). The approach to measure the initial rates did not work effectively, because of low accuracy in

measurement of initial rates. Under the conditions in Figure 2.10a, the consumption of RSH fits well to the exponential curve, $[RSH] = [RSH]_o exp(-k_{app}t)$. However, the values of k_{app} depends on $[RSH]_0$ (Figure 2.10b), which intrinsically contradicts the exponential law. We found that all kinetic curves can be fitted to the mechanism, which includes a combination of the zero and the first order pathways: $[RSH] = [RSH]_o\{exp(-k_0t) - k_1t\}$. If the contribution of the zero order is comparable with that of the first order, the question arises how to quantify the catalytic activity of such systems. Therefore, we measured the time required to reach 50% conversion of RSH, $t_{1/2} = 1/k_{1/2}$. If the first order pathway is dominant, then $k_{1/2} = ln(2)k_0 \approx 1.45\ k_0$. The difference between k_{app} and k_0 is small, but results in the weak dependence k_{app} on $[RSH]_0$. The difference between $1.45\ k_0$ and $k_{1/2}$ is commonly small as shown on Figure 2.10c. All these make it reasonable to use $k_{1/2}$ as a measure of catalytic activity.

The highest TON and TOF were achieved at 0.1 mM **PV_6Mo_6** and 0.5 mM Cu(II) (Table 2.1). Therefore, we have chosen these concentrations as the starting points for detailed studies. An increase of $[RSH]_0$ from 20 to 50 mM results in a weak decrease in k_{app}, while k_0 remains almost constant (Figure 2.10b). The dependence of catalytic activity on Cu(II) expressed as $k_{1/2}$ has an S-shape (Figure 2.10c). The two $k_{1/2}$ values agree with each other indicating that the first order pathway dominates during this Cu concentration range. Moreover, we found an unusual dependence on POM initial concentration, Figure 2.10d. We measured the time required to reach 50% conversion of RSH, $t_{1/2} = 1/k_{1/2}$ and use $k_{1/2}$ to quantify the reaction rate. The activity increases with [POM], in the range 0-0.1 mM and at 0.3-0.8 mM $[PV_6Mo_6]_0$. In the middle concentration range of 0.1-0.3 mM, $k_{1/2}$ shows a negative dependence on $[PV_6Mo_6]_0$. The replacement of air with pure O_2 does not change the rate at low $[PV_6Mo_6]_0 < 0.1$ mM but increases the rate at higher concentrations (Figure 2.10d, red). At 0.8 mM $[PV_6Mo_6]_0$ and 0.5

mM $Cu(ClO_4)_2$ the rate is 2.5-fold higher under air. This kinetic behavior was hard to understand until we managed to determine the reduction state, n, of the POM under turnover conditions. The change in POM concentration changes not only the quantity of catalyst in solution, but also the distribution of POM reduction states, and thus the solution potential. These facts, in turn, explain the unusual kinetic dependencies. The reduction state curve (blue) and $k_{1/2}$ exhibit a similar trend suggesting they correlate with each other. The measurement of the POM apparent reduction state, n, and the relationship between n and $k_{1/2}$ are described below.

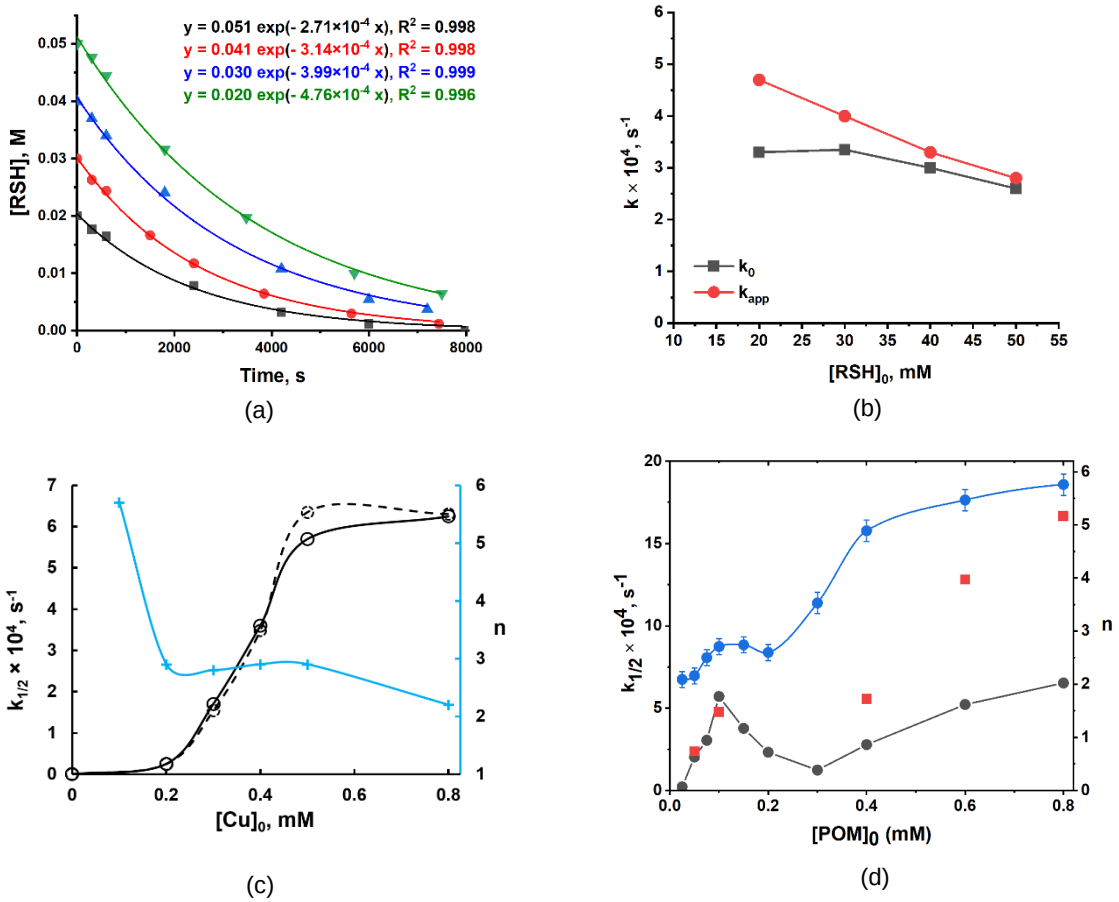

Figure 2.10. (a) Kinetics of RSH consumption versus time. Solid lines: the fitting to the equation $[RSH] = [RSH]_0\exp(-k_{app}t)$. Conditions: $\mathbf{PV_6Mo_6}$ (0.1 mM) and $Cu(ClO_4)_2$ (0.5 mM). (b) red: k_{app}; black: k_0 from fitting to the equation $[RSH] = [RSH]_0(\exp(-k_0t) - k_1t)$; (c) 0.1 mM $\mathbf{PV_6Mo_6}$ and 30 mM RSH, black solid and dashed: $k_{1/2}$ and $1.45k_0$, respectively; blue: the reduction state of $\mathbf{PV_6Mo_6}$ expressed in n. (d) Dependence of $k_{1/2}$ and n as a function of initial POM concentration. Conditions: 0.5 mM $Cu(ClO_4)_2$ and 30 mM RSH under air (black) and O_2 (red); the reduction state of $\mathbf{PV_6Mo_6}$ expressed in n (blue).

2.3.6 Electrochemistry

Electrochemical studies reveal some reaction thermodynamics. The cyclic voltammograms (CVs) of PV_6Mo_6, Figure 2.11a, show three reversible peaks of the same height and a fourth peak that is high, broad, and quasi-reversible. The differences between two successive $E^o_{1/2}$ are about 500 mV. For comparison, these peak-to-peak separations in water are 180-220 mV and in general depend on the dielectric constant of the solvent (37 and 81 for acetonitrile and water, respectively).[75]

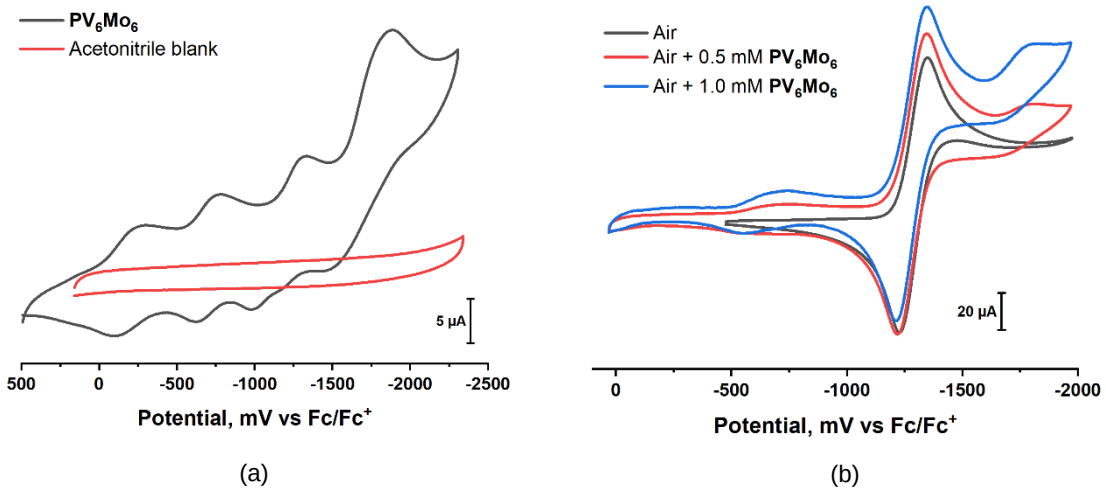

Figure 2.11. (a) Black: cyclic voltammograms (CV) of 0.5 mM **PV_6Mo_6** on glassy carbon electrode in acetonitrile under argon. Red: CV of acetonitrile blank. (b) CV of air-saturated acetonitrile. Black: 0 mM **PV_6Mo_6**; Red: 0.5 mM **PV_6Mo_6**; Blue: 1.0 mM **PV_6Mo_6**. Conditions: 100 mM *n*-Bu_4NPF_6, scan rate = 100 mV s^{-1}, T = 298 K.

The CV of an air-saturated solution shows a reversible peak overlapping with the third peak of POMs (Figure 2.11b). The CV of air-saturated solution taken in the presence of 1.0 mM **PV_6Mo_6** is the same as in the absence of the POM and is assigned to the one-electron-reduction product of O_2, superoxide. The ratio of cathodic to anodic currents of these peaks is close to 1. The reversibility of this peak indicates that the reaction product, $O_2^{\bullet -}$, is relatively stable under

these conditions, and that the addition of protonated **PV_6Mo_6** does not affect the lifetime of $O_2^{\bullet -}$ (the ratio of the cathodic to the anodic current remains equal to 1). Based on these data, we can conclude that the protonated POM, in acetonitrile, unlike water, is not strong enough to protonate superoxide. It is well known in aqueous media, that protonated superoxide, $HO_2^{\bullet}$, rapidly forms dioxygen and hydrogen peroxide.[76] These findings are consistent with the fact that the H^+ in the protonated **PV_6Mo_6** in acetonitrile does not dissociate and thus the POM is not a strong acid under these conditions.

In order to confirm the number of electrons involved in the redox reactions we performed bulk electrolysis of **PV_6Mo_6** at controlled potentials (Figure 2.12, Table 2.2). The chronocoulometric results show that all three peaks for **PV_6Mo_6** are one-electron. The electrolysis at -2000 mV does not have an identifiable endpoint and therefore is not informative. The spectra of solutions after electrolysis are the same as those after titration by ascorbic acid (Figure 2.15, see below).

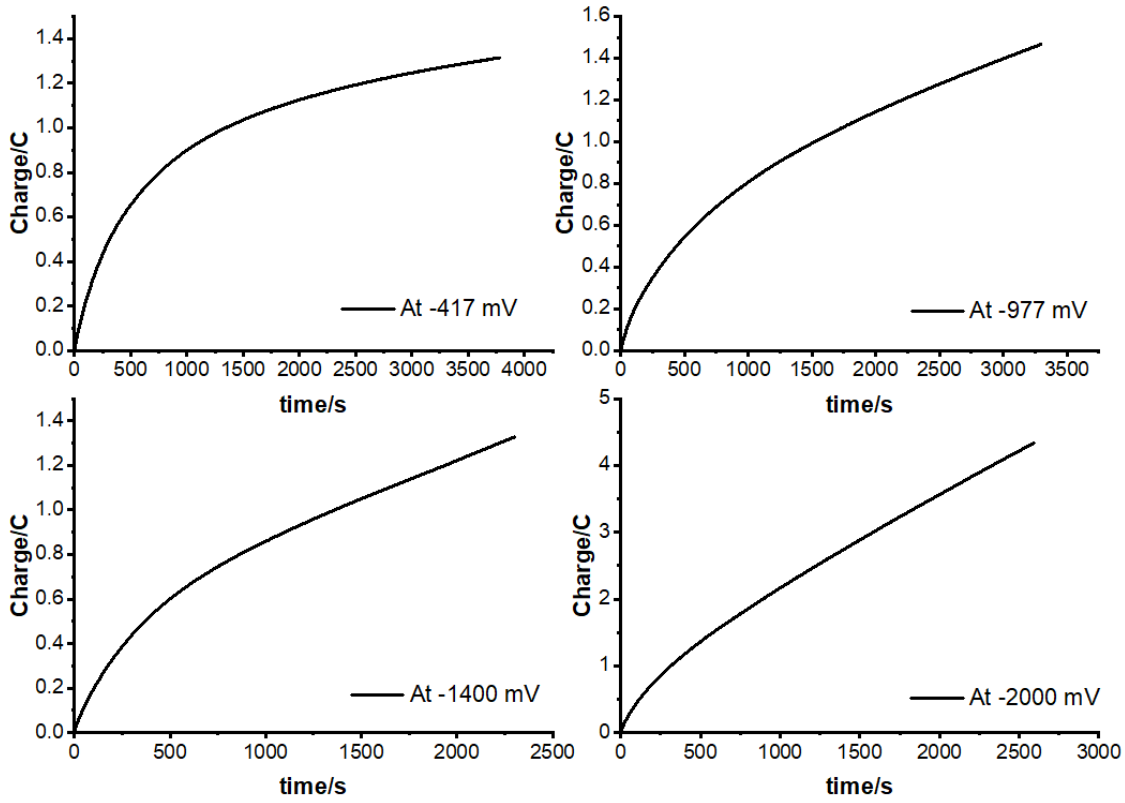

Figure 2.12. Charge vs time curves from the bulk electrolysis of **PV_6Mo_6**. Conditions: **PV_6Mo_6** (0.5 mM), *n*-Bu_4NPF_6 (100 mM) in acetonitrile (30 mL), at 25±2 ºC under argon. See Table 2.2 below.

Table 2.2. Bulk electrolysis of PV_6Mo_6 at constant potentials in acetonitrile.[a]

Potential/mV vs Fc/Fc^+	Number of coulombs	Number of electrons accumulated by POM[b]	Ending current ratio/%
-417	1.32	1	1.8
-977	1.46	2	4.4
-1400	1.4	3	5
-2000	2.8	5	12

[a] Conditions: **PV_6Mo_6** (0.5 mM), *n*-Bu_4NPF_6 (100 mM), acetonitrile (30 ml), at room temperature under argon. [b] Total number of electrons transferred, calculated according to Faraday's law of electrolysis.

In addition, rotating disk electrode (RDE) voltammetry was used to determine the number of electrons in the fourth peak (Figure 2.13). The $E_{1/2}$ of four processes in RDE are consistent with CV data (Table 2.3) and independent of rotation rate. The Levich plot (i_L vs $\omega^{1/2}$) for all four processes are

linear, indicating mass transport control. The relative ratio of limiting currents is I: II: III: IV = 1: 1.1: 1.1: 4±0.5.

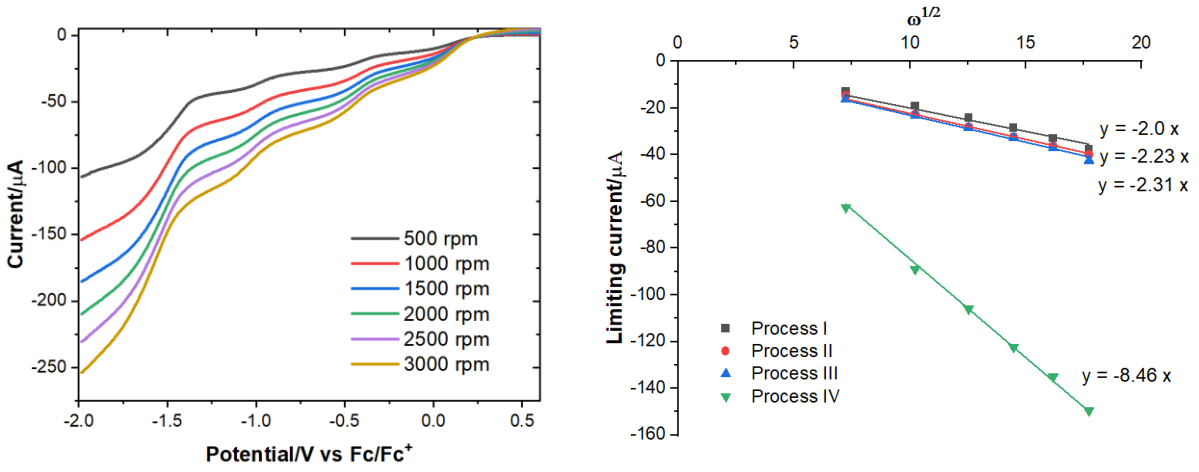

Figure 2.13. (a) Rotating disk electrode voltametric raw data at different electrode rotation speeds from 500 rpm to 3000 rpm. (b) Levich plot for all four processes. Conditions: **PV_6Mo_6** (0.5 mM), *n*-Bu_4NPF_6 (100 mM), acetonitrile (20 ml), at room temperature under argon, scan rate 5 mV s^{-1}.

Table 2.3. $E_{1/2}$ from rotating disk electrode voltametric measurements.[a]

	Process I	Process II	Process III	Process IV
$E_{1/2}$/mV vs Fc/Fc^+	-202	-721	-1285	-1810

[a] $E_{1/2}$ was measured by averaging all rotation speeds. Conditions: **PV_6Mo_6** (0.5 mM), *n*-Bu_4NPF_6 (100 mM), acetonitrile (20 ml), at room temperature under argon, scan rate = 5 mV s^{-1}

2.3.7 Measurements of PV_6Mo_6 reduction state under turnover conditions

The apparent reduction state of **PV_6Mo_6** during the reaction can be defined as the average number of electrons, n, transferred to the POM (eq 2.6 and 2.7, see below). To measure the **PV_6Mo_6** apparent reduction state in the course of the reaction, the UV-Vis absorbance at 550 nm was monitored as a function of time. Figure 2.14a shows examples of the POM at high reduction state (n = 5.9) remains almost constant (steady state) to about 75% conversion of RSH, then

slowly decreases. Figure 2.14b is an example of **PV_6Mo_6** remaining almost constant in the low reduction state (n = 2.2) until reaction completion. The initial reduction process is very fast and has been studied separately (see below). Thus, we have focused on steady reduction states for all measurements under turnover conditions.

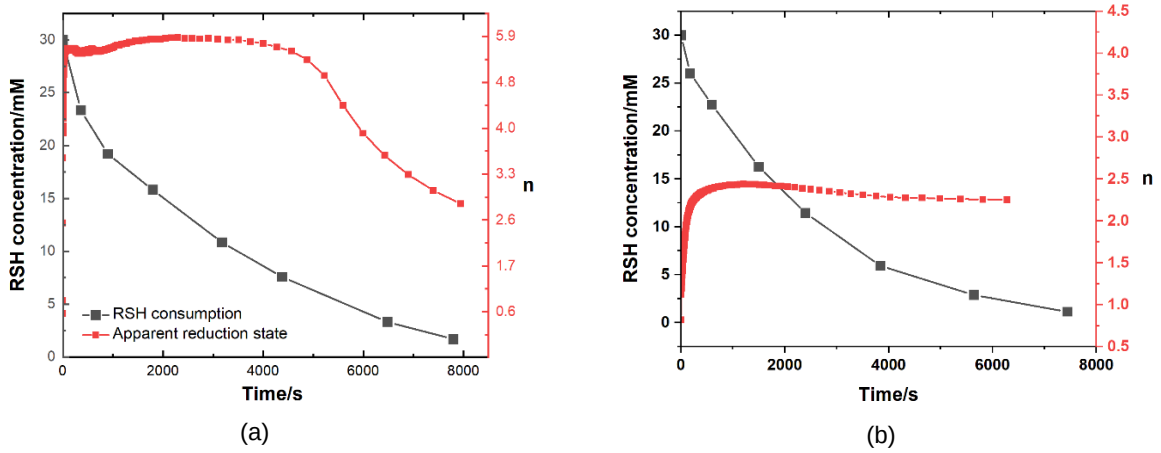

Figure 2.14. Black: The kinetics of 2-mercaptoethanol (30 mM) oxidation in the presence of $Cu(ClO_4)_2$ (0.5 mM), (a) PV_6Mo_6 (0.6 mM), (b) PV_6Mo_6 (0.1 mM). Red: Apparent reduction state, n, of PV_6Mo_6 at 550 nm.

To establish the correlation between n, and the absorbance, we titrated the fully oxidized **PV_6Mo_6** by ascorbic acid (Figure 2.15). In water, the removal of the first electron from ascorbic acid is a reversible pH-dependent process producing the ascorbate radical. However, oxidation of ascorbate radical includes an irreversible non-redox transformation.[77,78] The irreversibility of this step is the key property of ascorbic acid making it a very strong 2-electron stoichiometric reducing agent. Spectral changes and the formally calculated extinction coefficient at 550 nm in the process of titrating **PV_6Mo_6** with freshly prepared ascorbic acid are shown in Figure 2.15. Subsequently, we titrated the fully reduced POM with the strong one-electron oxidant Ce(IV) (cerium ammonium nitrate or "CAN"). The titration curves of the reduced POMs reproduce the

lines for reductions by ascorbic acid and confirm that ascorbic acid functions in these acetonitrile solutions as a two-electron reductant as in water. Thus, **PV_6Mo_6** can be reversibly reduced by 6 electrons under these conditions.

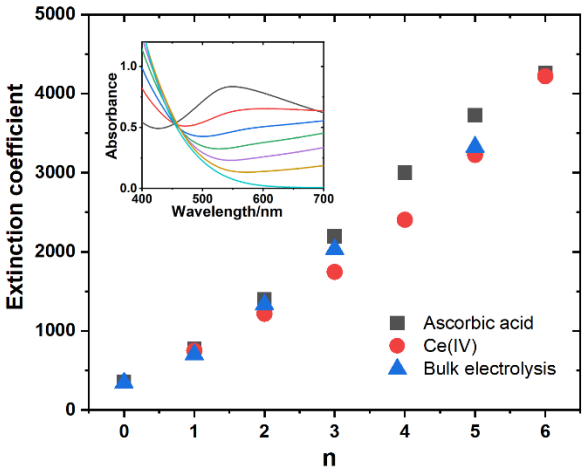

Figure 2.15. Dependence of apparent extinction coefficient of **PV_6Mo_6** at 550 nm on the number of electrons, n, transferred from ascorbic acid (black squares), after re-oxidation by CAN (red circles) and after bulk electrolysis (blue triangles); Inset: UV-Vis spectrum of ascorbic acid titration; The size of the icons in 3a is equal to the error bars.

Finally, the number of electrons, n, transferred to POM in the range 1-5 is linearly dependent on absorbance at 550 nm normalized by the **PV_6Mo_6** concentration (apparent extinction coefficient). This calibration has been used to convert the absorbance to n (Figure 2.16a). The UV-Vis spectra from 400-1100 nm are given in Figure 2.16b.

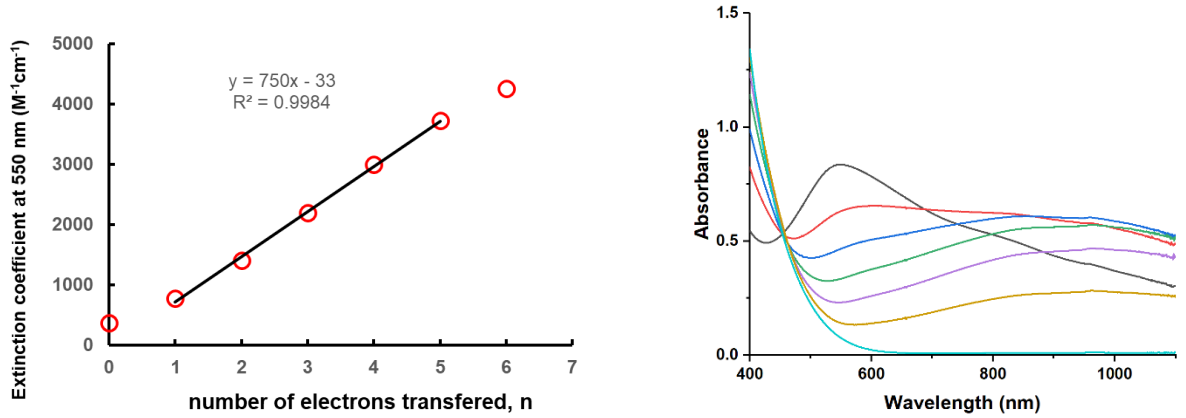

(a) (b)

Figure 2.16. (a) Titration of $\mathbf{PV_6Mo_6}$ by ascorbic acid in acetonitrile under Ar. (b) Extended UV-Vis spectra resulting from ascorbic acid titration.

A broad band centered around 1000 nm gradually increases and reaches a plateau from n = 1 to 5 and decreases at n=6. In addition, another band increases linearly from n = 1 to 6. To assign the bands, we start from the UV-Vis spectra of reduced $\mathbf{PVMo_{11}}$ in acetonitrile. Bulk electrolysis titration of $\mathbf{PVMo_{11}}$ in acetonitrile is given in Figure 2.17a. The one-electron-reduced $\mathbf{PVMo_{11}}$ has a broad absorbance centered around 650 nm that can be assigned as the V^{IV}-to-Mo^{VI} intervalence charge-transfer (IVCT) band.[79,80] The two-electron-reduced $\mathbf{PVMo_{11}}$ has a high-extinction-coefficient absorbance centered around 700 nm which can be assigned to Mo^{VI}-to-Mo^{V} IVCT band.[81,82] Further, the one- and two-electron-reduced forms of $\mathbf{PV_2Mo_{10}}$, exhibit a broad absorption centered around 600 that can be assigned as a V^{IV}-to-Mo^{VI} IVCT band, and a shoulder absorption centered around 850 nm that can be assigned as a V(IV) d-d transition (Figure 2.17b).[79] Compared with $\mathbf{PVMo_{11}}$ and $\mathbf{PV_2Mo_{10}}$, the broad band around 1000 nm for the one- to four-electron-reduced forms of $\mathbf{PV_6Mo_6}$ where n = 1-4 is tentatively assigned as a V^{IV}-to-V^{V} IVCT band.[36] One strong argument for this assignment is that this absorption band disappears when n=6, where all V(V) atoms have been reduced to V(IV). In addition, the V(IV) d-d

transition should also have a contribution of around 850 nm. The absorption around 550-600 nm that linearly increases can thus be assigned as a V^{IV}-to-Mo^{VI} IVCT band. No high extinction coefficient Mo^{VI}-to-Mo^{V} IVCT band at 700 nm was observed when n = 6, suggesting all 6 electrons result in reduction of V^{V} to V^{IV}.

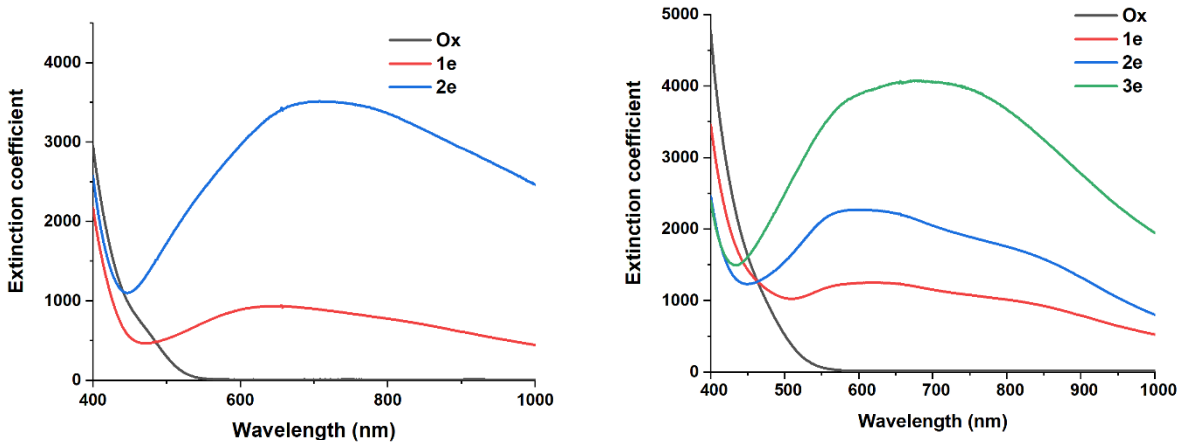

Figure 2.17. UV-Vis spectra from bulk electrolysis titration of (a) **$PVMo_{11}$**; (b) **PV_2Mo_{10}**.

2.3.8 Redox buffering by PV_6Mo_6

The POM distribution in different reduction states depends on chemical solution potential E and is described by eq 2.6, where E_i is the standard reduction potential of a $(PV_6Mo_6)_i/(PV_6Mo_6)_{i+1}$ couple measured electrochemically

$$\alpha_i = (\alpha_{i-1}10^{(Ei\ -E)/60})/(\sum_{i=0}^{i=6} \alpha i\ ) \quad (2.6)$$

The apparent reduction state of POM, n, is calculated by eq 2.7, and the results are given in Figure 2.18a.

$$n = \sum_0^6 i(\alpha i) \quad (2.7)$$

The speciation of highly reduced **PV_6Mo_6** (n > 3) depends on reduction potentials E_5 and E_6, which are not known. Exemplary results assuming $E_5 = E_6 = -1500$ mV are given in Figure 2.18b.

The reduction states of **PV_6Mo_6** measured under different reaction conditions all fall into the range of n = 2 to 3 and 3 to 6 which correspond to the potential range of E = -(1180-1340) and -(1600-1680) mV, respectably.

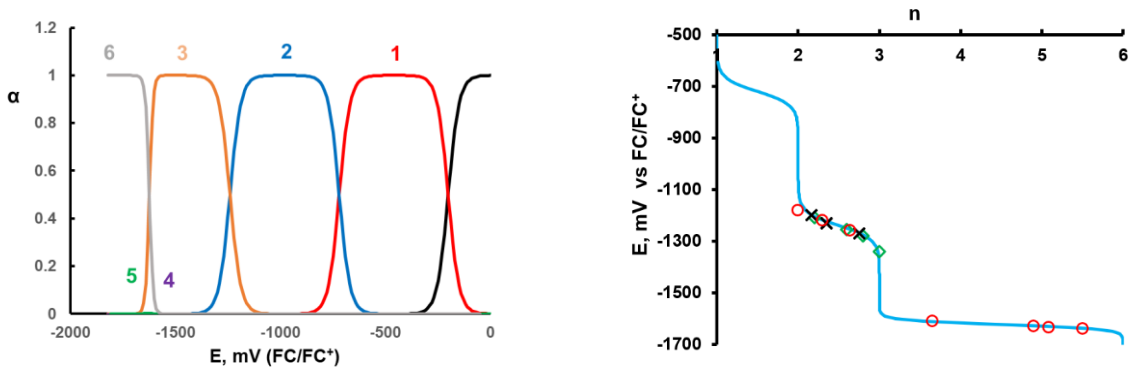

(a) (b)

Figure 2.18. (a) The distribution diagram of the reduced forms of **PV_6Mo_6** as a function of chemical solution potential. (b) The theoretical values of chemical solution potentials as function of the reduction state of **PV_6Mo_6** (blue line), and the experimental values for i) 0.1 mM **PV_6Mo_6**, 0.5 mM $Cu(ClO_4)_2$ and different $[RSH]_0$ (data from Figure 2.19; green diamonds); ii) 0.1 mM **PV_6Mo_6**, 30 mM RSH and different $Cu(ClO_4)_2$ (data from Figure 2.10c; black crosses); iii) 0.5 mM $Cu(ClO_4)_2$, 30 mM RSH and different concentrations of **PV_6Mo_6** (data from Figure 2.10d; red circles).

The apparent reduction state of **PV_6Mo_6**, n, under turnover conditions depends on the initial concentrations of Cu(II), POM and RSH (Figures 2.10c, d and 2.19), but remains almost constant under steady state conditions. The dependence of n on chemical solution potential E is shown on Figure 2.18b. All the measured reduction states under different conditions have been placed on the curve revealing that all these values fall into two potential ranges: E = -(1180-1340) and E = -(1600-1680) mV. Thus, a correlation is evident between the thermodynamic parameter, n, and the reaction rate, $k_{1/2}$ in Figure 2.10d. The first positive $[POM]_0$ dependence range 0-0.1 mM is when E = -(1180-1340) mV and the second positive $[POM]_0$ dependence range 0.3-0.8 mM is when E = -(1600-1680) mV. The middle negative dependence on $[POM]_0$ is the transition

between them. **PV_6Mo_6** resides in different reduction states corresponding to different solution electrochemical potential ranges. $k_{1/2}$ has two distinct positive $[POM]_0$ dependence ranges indicating different rate-limiting steps during the overall reaction induced by solution potential changes. The rate-limiting step may involve reoxidation of Cu(I) by O_2 as we observe different $[O_2]$ dependencies in the two ranges (Figure 2.10d). The low POM concentration range (0-0.1 mM) does not respond to $[O_2]$ change suggesting the rate-limiting step in this range does not involve reoxidation by O_2. While the reaction rate under pure O_2 in the high POM concentration range (0.3-0.8 mM) is 2.5-fold higher than under air indicating the rate-limiting step does involve O_2. Since under O_2, the reaction is not 5 times faster than under air, there is no conventional single well-defined rate-limiting step in this concentration regime.

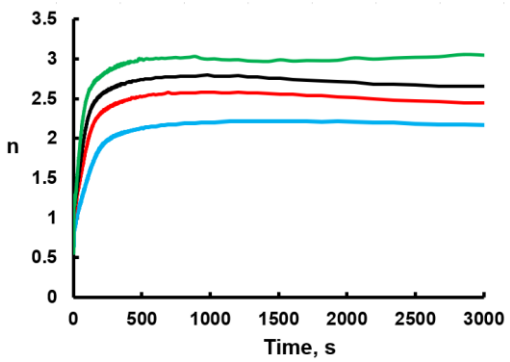

Figure 2.19. Change of apparent reduction state of **PV_6Mo_6** as a function of time during thiol oxidation by air with 0.1 mM **PV_6Mo_6** and 0.5 mM $Cu(ClO_4)_2$, [RSH] = 20 (blue), 30 (red), 40 (black), and 50 mM (green).

The change of Gibb's free energy (expressed by electrochemical solution potential, ΔE in mV) in the course of the reaction of thiol oxidation, eq 2.1 is

$$\Delta E(t) = \Delta E^0 + 60mV \log\left(\frac{[RSSR]^{\frac{1}{2}}}{[RSH]}\right) \quad (2.8)$$

$$\Delta E^0 = \frac{1}{2}\Delta E_f^0\,(H_2O) + \frac{1}{2}\Delta E_f^0\,(RSSR) - \frac{1}{4}\Delta E_f^0\,(O_2) - \Delta E_f^0\,(RSH) \quad (2.9)$$

where ΔE_f^0 are the standard Gibb's energies of formation.

The electrochemical solution potential in the catalytic reaction is eq 2.10.

$$\Delta E_c\,(t) = \Delta E^0 + 60mV \log\left(\frac{[RSSR]^{\frac{1}{2}}}{[RSH]}\right) - 60mV \left\{\log\left(\frac{[POM(n)]}{[POM(n+1)]}\right) + \log\left(\frac{[Cu(II)^*]}{[Cu(I)^*]}\right)\right\} \quad (2.10)$$

Since the ratio [POM(n)]/[POM(n+1)] remains constant under steady state conditions, the contribution to ΔE_c (t) of the [Cu(II)*]/[Cu(I)*] redox couple becomes important. [Cu(II)*] and [Cu(I)*] are the total concentrations of all Cu(II) and Cu(I) complexes present.

2.3.9 Thermodynamics, speciation, and catalytic cycle of copper complexes

Copper speciation in acetonitrile has been studied previously. Copper(I) is strongly complexed by acetonitrile, and the stable salt $[Cu(NCCH_3)_4](ClO_4)$ has been prepared.[83] Copper(II) exists in acetonitrile as a hexacoordinated distorted octahedron.[84] Both Cu(II) and Cu(I) can bind RSH and form polymeric structures.[26,85] When the acetonitrile solution contains water, Cu(II) should bind two RSH per ion and Cu(I) should bind an average of one RSH per ion,[26,85] eqs 2.11, 2.12 and 2.14. That Cu(II) can bind two equivalents of RSH in acetonitrile is proved using cyclic voltammetry and titration methods (Figure 2.20a, b). The CVs of Cu(II) with adding RSH are presented in Figure 2.20a, the peak at 675 mV has an anodic-cathodic peak potential separation of 130 mV and the ratio of currents is close to 1 in the positive potential domain. This peak is assigned to the reversible Cu(II)/Cu(I). The potential is on the high side of the range for this couple in other complexes, but in agreement with the literature value 950 mV versus SCE. The large difference between anodic and cathodic potentials is consistent with a sluggish electron transfer from Cu to the electrode. In the negative potential domain, the CVs are difficult to interpret due to deposition of Cu(0) and adsorption of RSH on electrode. With two

equivalents of RSH, the Cu(II)/Cu(I) peak totally disappears, which proves the formation of a complex between Cu and RSH. The newly generated peaks at negative potential may belong to the complexes Cu(II)RSH and $Cu(II)(RSH)_2$. One of the peaks around +1000mV is the RSH peak confirmed by comparing with the CV of RSH alone. Based on our data we suggest the following reaction mechanism:

$$Cu(II) + RSH \rightleftarrows Cu(II)(RS^-) + H^+ \quad (2.11)$$

$$Cu(II)(RS^-) + RSH \rightleftarrows Cu(II)(RS^-)_2 + H^+ \quad (2.12)$$

$$Cu(II)(RS^-)_2 + POM(n) \rightleftarrows Cu(I)(RS\bullet)_2 + POM(n+1),\ n = 0\text{-}5 \quad (2.13)$$

$$Cu(I)(RS\bullet)_2 \rightleftarrows Cu(I) + RSSR \quad (2.14)$$

$$Cu(II) + POM(n+1) \rightarrow Cu(I) + POM(n)) \quad n = 5\text{-}1 \quad (2.15)$$

$$Cu(I) + 1/2O_2 + 2H^+ \rightarrow [Cu(II)\text{-}O\bullet] \rightarrow Cu(II) + H_2O \quad (2.16)$$

All reactions, except in eqs 2.14-2.15 are reversible. Two important experiments are required before discussing the mechanism. The overall reaction mechanism includes the POM(n)/POM(n+1) distribution, and the multistep reaction of O_2 with Cu(I), which, collectively, are too complicated to analyze. Thus, we separate the overall process into the reaction under Ar with RSH (POM(n) $\rightarrow$ POM(n+1)) and the reaction with O_2 but no RSH (POM(n+1) $\rightarrow$ POM(n)) to understand the function of copper.

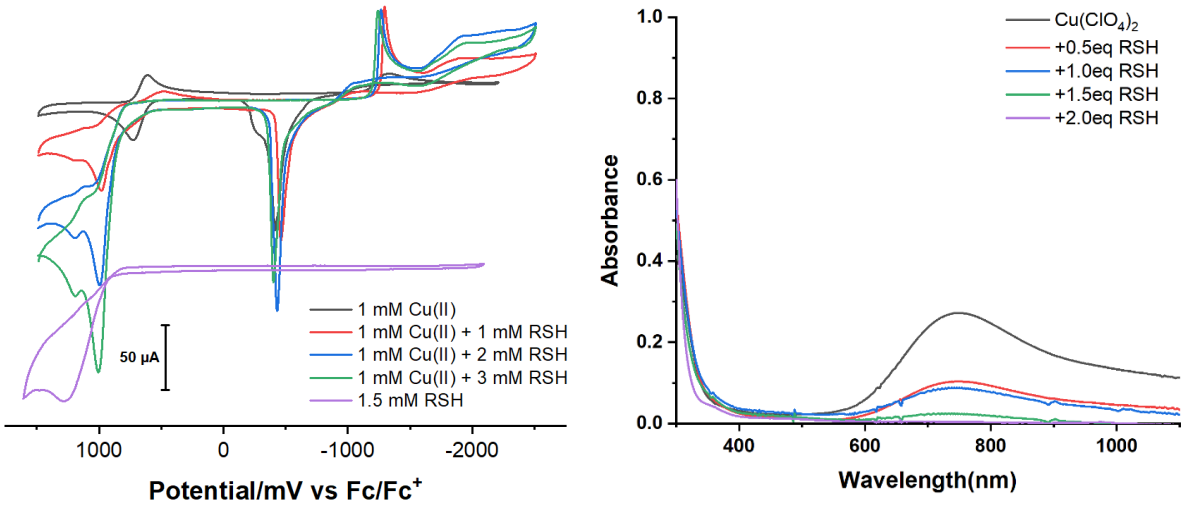

(a) (b)

Figure 2.20. (a) Cyclic voltammograms (CV) of 1.0 mM $Cu(ClO_4)_2$ with different concentrations of 2-mercaptoethanol. Conditions: 100 mM *n*-Bu_4NPF_6, scan rate 100 mV s^{-1}, T = 298 K. (b) 2-mercaptoethanol titration $Cu(ClO_4)_2$ in acetonitrile. Experiment done in a 10mL UV-Vis cuvette with 0.1mM $Cu(ClO_4)_2$ in 25mL acetonitrile. Titration is monitored at 750nm peak of Cu^{2+} ion.

2.3.10 Cu(II) catalysis of PV_6Mo_6 reduction by RSH under Ar

The data in Figure 2.19, which reflect turnover conditions, show that the reduction state of **PV_6Mo_6**, n, quickly increases with time and reaches the plateau within 5 min. In order to study this initial process, we excluded re-oxidation by replacing air with Ar and looked at the kinetics of changing n by following the absorbance at 550 nm. This reaction appeared to be extremely efficiently catalyzed by micromolar amounts of $Cu(ClO_4)_2$, Figure 2.21a. During the initial fast step, **PV_6Mo_6** is reduced by 2-3 electrons by 25-50 mM RSH (Figure 2.21b), which is consistent with the mechanism in eqs 2.11-2.14. Without O_2, the regeneration of Cu(II) is very likely eqs 2.17-2.18.[45,46]

$$Cu(I) + RSH \rightleftarrows Cu(I)(RS^-) + H^+ \quad (2.17)$$

$$Cu(I)(RS^-) + POM(n) \rightarrow Cu(II)(RS^-) + POM(n+1) \quad (2.18)$$

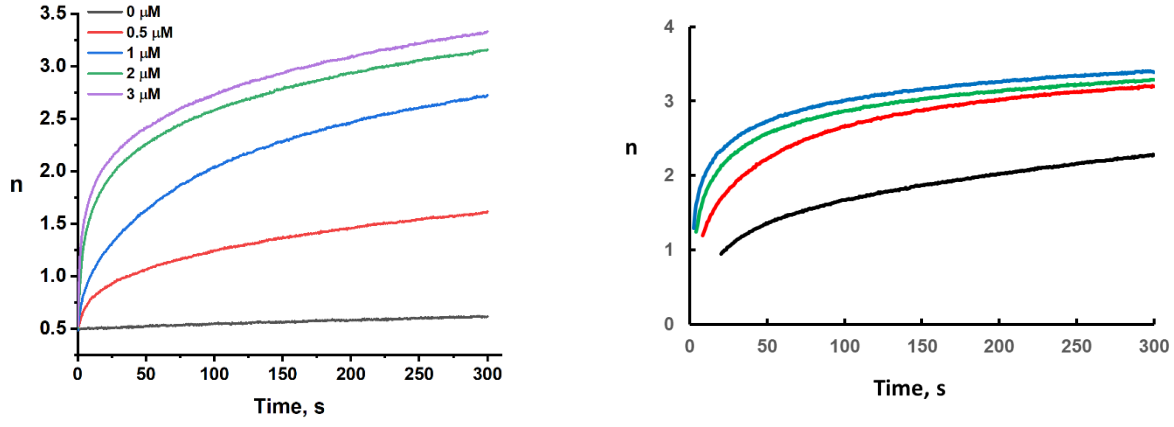

Figure 2.21. (a) Effect of Cu(II) concentration on $\mathbf{PV_6Mo_6}$ reduction by 2-mercaptoethanol in acetonitrile followed at 550 nm (expressed in the number of electrons acquired, n). Conditions: $\mathbf{PV_6Mo_6}$ (0.5mM), 2-mercaptoethanol (25mM), under argon. (b) The kinetics of 0.5 mM $\mathbf{PV_6Mo_6}$ reduction (expressed in the number of electrons acquired, n) by 12.5 (black), 25 (red), 37.5 (green), and 50 mM (blue) of RSH in the presence of 1.0 μM $Cu(ClO_4)_2$ under Ar.

Earlier, we found that submicromolar amounts of Cu(II) are always present in water[86–88] Here we use the same method to prove that no RSH oxidation takes place with the POM alone without Cu(II). Neocuproine, 2,9-dimethyl-1,10-phenanthroline (DMP), was employed to chelate the trace amount of Cu(II); around 10 μM of DMP completely stops the reaction (Figure 2.22). This further confirms that the Cu(II)/RSH complex and not RSH is the reducing species, and the entire reduction process under turnover conditions can be described by eqs 2.11-2.14.

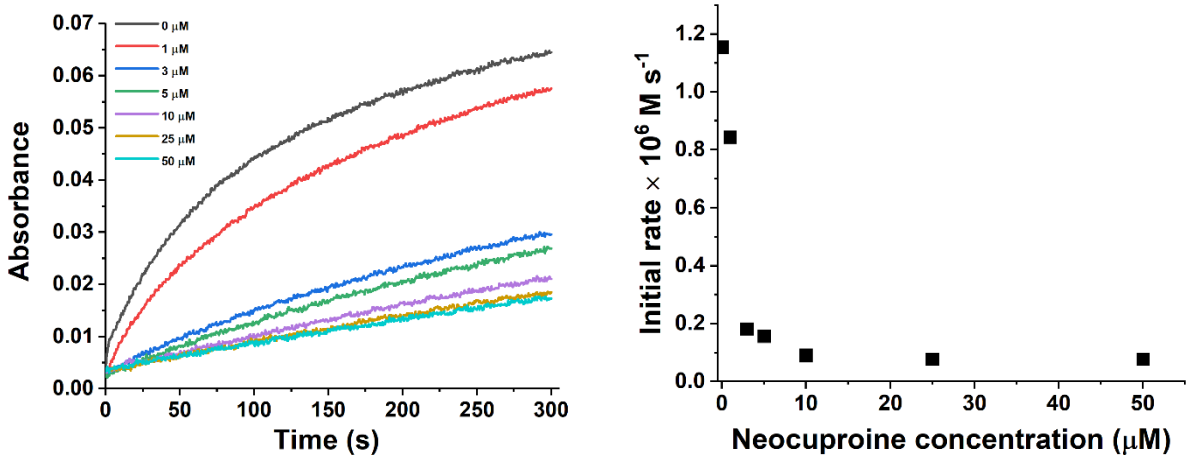

(a) (b)

Figure 2.22. (a) Stopped-flow kinetics data for **PV_6Mo_6** reduction by 2-mercaptoethanol at different neocuproine concentrations. (b) Initial rates versus neocuproine concentration. Conditions: **PV_6Mo_6** (0.4 mM), 2-mercaptoethanol (50 mM), acetonitrile, under argon.

2.3.11 Reaction of reduced PV_6Mo_6 with O_2 catalyzed by Cu(II)

In previous work, we found that re-oxidation of 1-electron reduced POMs, α-$AlW_{12}O_{40}^{6-}$, α-$SiW_{12}O_{40}^{5-}$, and α-$PW_{12}O_{40}^{4-}$, is catalyzed by copper[54,86,88,89] In this study, **PV_6Mo_6** was reduced by 6 electrons with 3 equivalents of ascorbic acid under Ar. Subsequently, the reduced **PV_6Mo_6** was reoxidized by purging O_2 in the presence of different concentrations of $Cu(ClO_4)_2$. We found that the oxidation of the reduced **PV_6Mo_6** by O_2 is also catalyzed by small amounts of copper in the absence of RSH (Figure 2.23). The short induction period is caused by the presence of a small amount of unreacted ascorbic acid. In contrast to the previous study in aqueous condition,[90] Cu(II) in acetonitrile is a strong oxidant relative to reduced **PV_6Mo_6**.

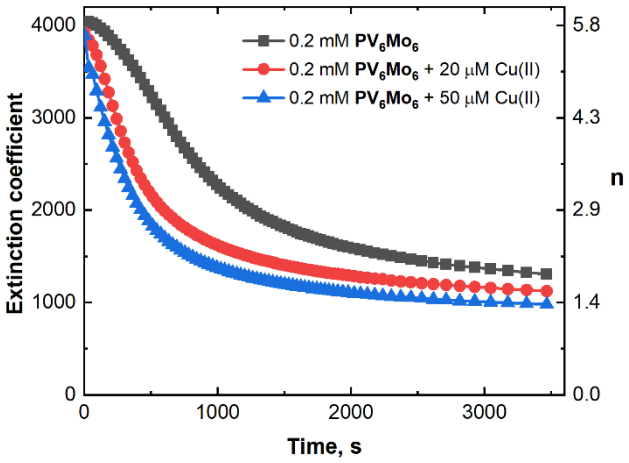

Figure 2.23. Effect of Cu(II) concentration on reduced $\mathbf{PV_6Mo_6}$ (0.2 mM solution) by O_2-based oxidation, followed by the decrease of absorbance at 550 nm. The 6-electron reduced $\mathbf{PV_6Mo_6}$ was obtained by adding 3 equivalents of ascorbic acid (6 electrons transferred).

The standard reduction potential E_0 of Cu(II)/Cu(I) couple measured by CV is unusually high, 675 mV (Figure 2.20a), which is consistent with the literature value 950 mV versus SCE.[91] Although reduced POM alone can react with O_2, this process is far slower when the catalyst, copper, is also present. Therefore, the copper-catalyzed POM reoxidation process can be described by eqs 2.15-2.16 (see discussion below for the reaction of Cu(I) and O_2). This result and CV study (Figure 2.24) prove that Cu(I) can react with O_2 in acetonitrile to regenerate Cu(II). Thus, Cu(II) has a remarkable ability to catalyze two distinct processes, the reduction of POMs by thiol and re-oxidation of the resulting reduced POMs by O_2.

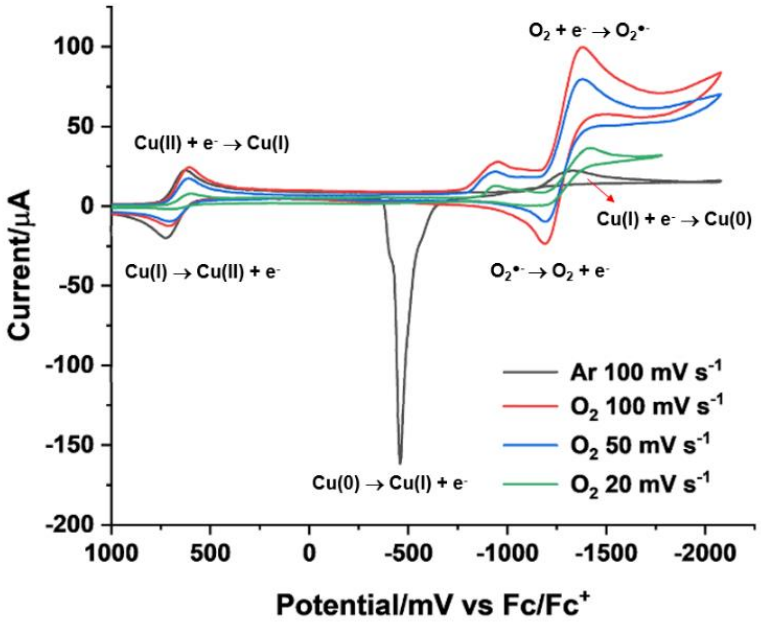

Figure 2.24. CV of 1 mM $Cu(ClO_4)_2$ under argon and O_2 with different scan rates. Conditions: 100 mM *n*-Bu_4NPF_6, T = 298 K.

The standard reduction potential of the Cu(II)/Cu(I) couple, E_0, is very high in acetonitrile, 675 mV vs. Fc^+/Fc, and the direct reaction of Cu(I) with O_2 to form superoxide is thus thermodynamically very unfavorable. The oxidation of Cu(I) likely proceeds through the formation of an intermediate Cu(I)…O_2 complex, which reacts with a second Cu(I) to form an unstable di-copper peroxo-intermediate. The homolysis of O-O bond results in formation of two formally Cu(III) intermediates, which we write as [Cu(II)-O•]. Recent multi-edge X-ray absorption spectroscopic (XAS) and density functional theory (DFT) studies put into question the existence of Cu(III) species in most coordination environments.[92] This oxidized Cu center would oxidize the reduced POMs by one electron and generate Cu(II).[93] Cu(II), as a strong one-electron oxidant, oxidizes a second reduced POM, regenerating Cu(I).

Additional electrochemical measurements provide further evidence for the general processes of the mechanism. Figure 2.24 shows CVs of Cu under Ar and O_2 at different scan

rates. The anodic and cathodic current ratio i_a / i_c of the Cu(II)/Cu(I) peak decreases with decreasing scan rate. The anodic current approaches 0 at 20 mV s^{-1}. This indicates that Cu(I) will be consumed by O_2 when reaction time increases. Furthermore, the symmetric anodic peak belonging to the absorbed Cu(I)/Cu(0) peak disappears when O_2 is present.[94,95] These results strongly suggest the Cu(I) forms a complex with O_2. This mechanism does not require the presence of RSH in solution, which is in agreement with experimental data in Figure 2.23.

2.3.12 Overall mechanism under turnover conditions

Given the current level of knowledge of POM speciation in the presence of Cu and also substrate (RSH), it is not feasible to construct a quantitative mechanism scheme incorporating all active species during catalytic turnover (POM, Cu, RSH, O_2). However, Scheme 2.1 shows the key pathways consistent with all our data in this study and with the equations above.

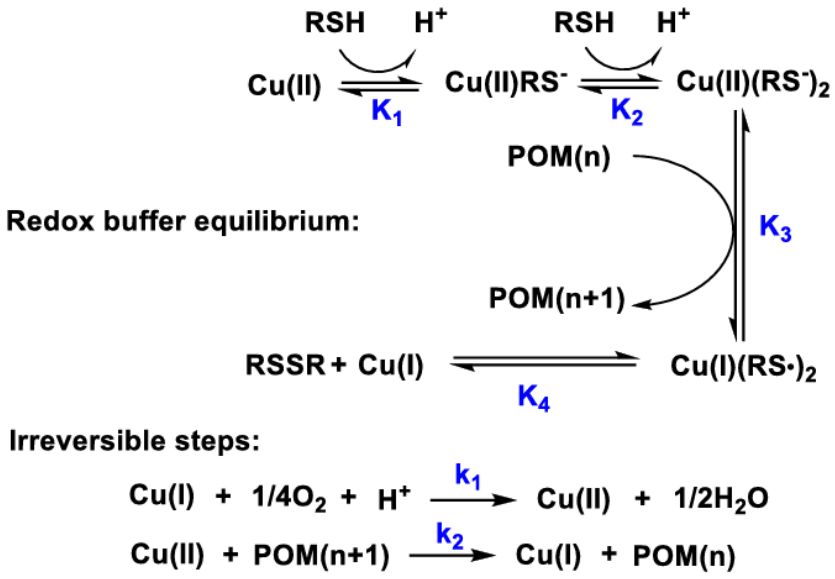

Scheme 2.1. Catalytic cycle of Cu(II)/Cu(I) couple

Most of the experiments were conducted with a RSH/Cu concentration ratio of 60, and we proved that RSH alone cannot reduce POM. Therefore, we considered $Cu(II)(RS^-)_2$ as the only

active reducing agent for simplicity.[46,48] We assume that the dissociation of thiolate complex Cu(II)(RS^-) into Cu(I) and RS• is unfavorable, and that eq 2.14 driven by S-S bond formation is dominant. The regeneration of Cu(II) occurs either by reaction of Cu(I) with O_2, eq 2.16, or by reaction of Cu(I)(RS^-) with POM(n), eqs 2.17-2.18. We should note that the reaction under Ar catalyzed by micromolar Cu is different with the overall reaction under turnover conditions catalyzed by millimolar Cu. The overall reaction under turnover condition consumes O_2 (Figure 2.4) and has trace conversion under Ar. Therefore, in aerobic turnover conditions, eq 2.16 is the dominate pathway to regenerate Cu(II): eqs 2.17-2.18 can be neglected.

The full analysis of the catalytic cycle is very complicated. For simplicity we assume that all reactions between copper, POM and RSH/RSSR are in thermodynamic equilibrium, except the irreversible reactions of Cu(I) with O_2 and Cu(II) with the reduced forms of POM. The presence of catalyst does not change the overall reaction thermodynamics. Since [POM(n)]/[POM(n+1)] remains constant under steady state conditions, the speciation and ratio of Cu(II)/Cu(I) should change. The ratio of oxidized to reduced POM, [POM(n)]/[POM(n+1)], controls the distribution of the Cu complexes. This is an internal redox buffer. This is similar to a conventional buffer where the ratio of protonated to deprotonated forms controls the pH. Since **PV_6Mo_6** can keep solution electrochemical potential changes in different narrow ranges by involving multiple redox couples (Figure 2.18), *it is a multistep and multielectron redox buffer*.[1,2] This thermodynamic approach does not address specific kinetic or mechanistic issues.

2.3.13 Difference in activity and redox buffering ability of PV_6Mo_6 versus PV_6W_6

Oxidation of RSH proceeds much faster in the presence of **PV_6Mo_6** than in the presence of **PV_6W_6** (Table 2.1), yet their reduction potentials are almost the same (Figure 2.25a). We compared the kinetics of **PV_6W_6** and **PV_6Mo_6** reduction by 25 mM RSH under Ar catalyzed by 2

μM Cu(II) (Figure 2.25b). Half of the initial **PV_6W_6** is reduced in 450 seconds, while the same process requires less than 1 second for PV_6Mo_6.

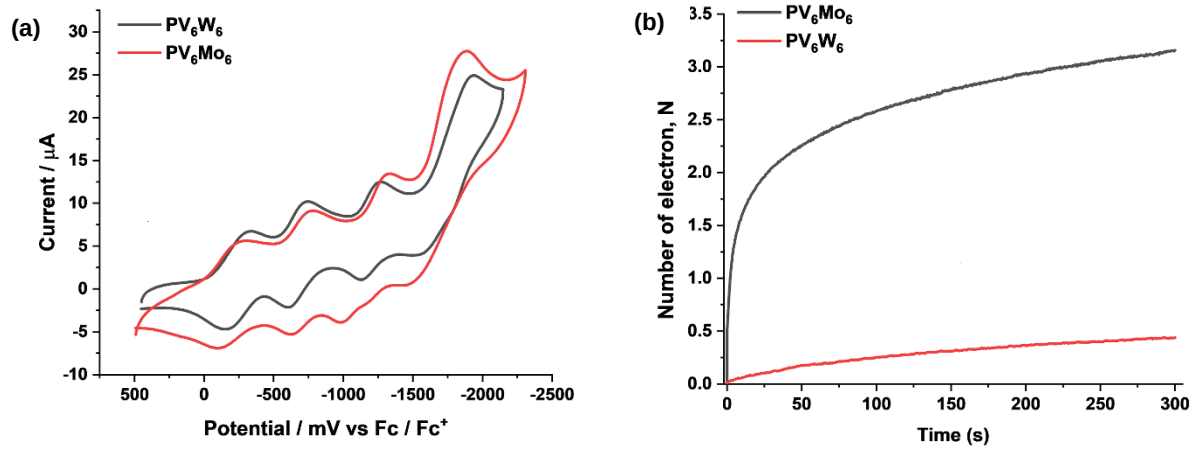

Figure 2.25. (a) Cyclic voltammograms of 0.5 mM **PV_6Mo_6** and **PV_6W_6** on glassy carbon electrode in acetonitrile under argon. (b) Kinetics of **PV_6W_6** and **PV_6Mo_6** reduction by 25 mM RSH under Ar catalyzed by 2 μM Cu(II).

Under turnover conditions (Figure 2.26), **PV_6W_6** is reduced by one electron in 200 seconds independent of thiol concentration, [RSH]. Over approximately the same length of time, **PV_6Mo_6** is reduced by 2.2-3.0 electrons at a rate dependent on [RSH]. Thus, **PV_6W_6** is unable to reach higher reduction states and thus does not exhibit a redox buffer capability like the **PV_6Mo_6**. Since both POMs have almost the same CV behavior, the huge difference in catalytic activity and reduction states cannot be explained based on thermodynamics.

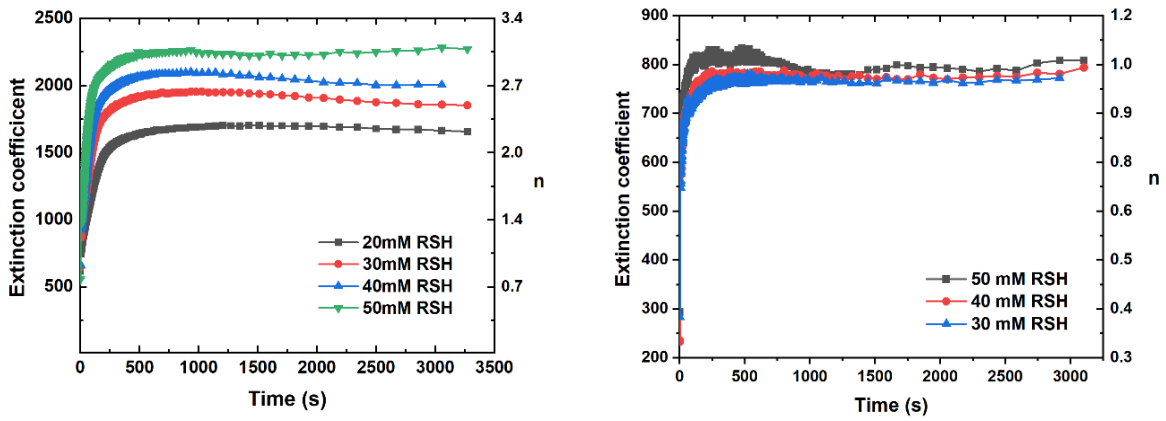

(a) (b)

Figure 2.26. Apparent reduction state of (a) $\mathbf{PV_6Mo_6}$ and (b) $\mathbf{PV_6W_6}$ depends on RSH concentration. Conditions: POM (0.1 mM), Cu(II) (0.5 mM) under air in acetonitrile.

Figure 2.27 shows that Cu can catalyze the RSH reduction of $\mathbf{PV_6W_6}$ under Ar, but only by a maximum of 1 electron. $-d[n]_0/dt$ was calculated from Figure 2.25b, and found to be 0.47 and 8.6×10^{-4}, s^{-1} for $\mathbf{PV_6Mo_6}$ and $\mathbf{PV_6W_6}$ respectively. This three-orders-of-magnitude rate difference clearly cannot be explained by an outer-sphere electron transfer mechanism operative in all cases given that these two reduced POMs have the same negative charges and nearly identical sizes.[88,89,96,97] Indeed, previous studies show that heteropolytungstates are more likely to undergo outer-sphere electron transfer mechanisms.[88,89,98] Neumann[99,100] provided evidence for a generic inner-sphere electron transfer mechanism between O_2 and $\mathbf{PV_2Mo_{10}}$, and a Mars-van Krevelen-type electron transfer-oxygen transfer reaction mechanism for aerobic oxidations catalyzed by $\mathbf{PV_2Mo_{10}}$.[101–103] The $\mathbf{PV_2Mo_{10}}$ reacts via inner-sphere mechanisms in these oxidations, a point consistent with the hydrolytically labile Mo-O bonds.[104] Thus, we attribute the huge activity difference and reduction state behavior difference between $\mathbf{PV_6Mo_6}$ and $\mathbf{PV_6W_6}$ to the electron transfer mechanism difference, inner-sphere versus outer-sphere electron transfer, respectively.

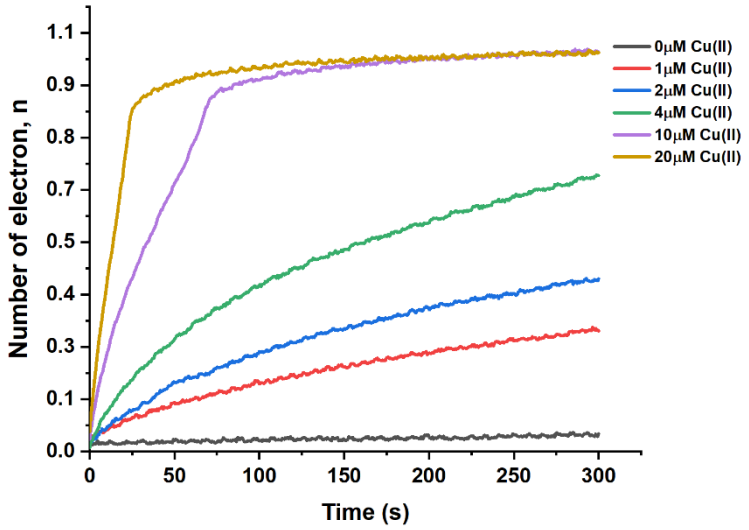

Figure 2.27. Cu(II) dependence of $\mathbf{PV_6W_6}$ reduction by RSH under Ar. Conditions: 25 mM RSH, 0.5 mM $\mathbf{PV_6W_6}$ in acetonitrile in room temperature.

One possibility is that $\mathbf{PV_6Mo_6}$ and $\mathbf{PV_6W_6}$ have different types of interaction with Cu(II) ions in acetonitrile. Figure 2.28a shows that after half equivalent of Cu(II), the ^{31}P NMR spectrum of $\mathbf{PV_6Mo_6}$ totally disappears. The addition of 0.25 equiv of Cu(II) into $\mathbf{PVMo_{11}}$ solution generates a broad peak that shifts 2.09 ppm (Figure 2.28b). Bajpe et al.[105] showed that adding $Cu(NO_3)_2$ shifts the ^{31}P, ^{183}W, and ^{17}O NMR peaks of heteropolyacids (HPAs), such as $H_3PMo_{12}O_{40}$ and $H_3PW_{12}O_{40}$, in an acidic buffer. In their work, they observed clear ^{31}P NMR peaks after the addition of Cu(II) ions and did not observe peak broadening. They proposed that the NMR peak shift is caused by the interaction between Cu(II) ions and the terminal oxygens of the Keggin polyanion.[105] In the medium used for our catalytic studies here, acetonitrile, the strong perturbation of ^{31}P NMR peaks suggests a very strong interaction between paramagnetic Cu(II) and vanadopolymolybdates. We established that $\mathbf{PVW_{11}}$ and $\mathbf{PV_6W_6}$, unlike the corresponding vanadopolymolybdate analogues, show no peak shift and broadening after adding Cu(II) in acetonitrile (Figure 2.28c, d). These results and those of Bajpe et al.[105] are consistent with different Cu(II) speciation and POM association chemistry in acetonitrile versus water.[106]

We postulate that the dramatic effect of Cu(II) on the ^{31}P NMR spectra of **PVMo** in acetonitrile likely involves coordinate-covalent bond formation between POM oxygens and Cu(II), which in turn involves some displacement of acetonitrile ligands on Cu(II) by POM oxygen. This is a contact ion pair or, conveniently, an inner-sphere interaction. In contrast, there is likely little or no formation of Cu(II)−**PVW** oxygen covalent (dative) bonds, thus far less influence of the S = 1/2 copper centers on the central phosphorus atom and its NMR properties.

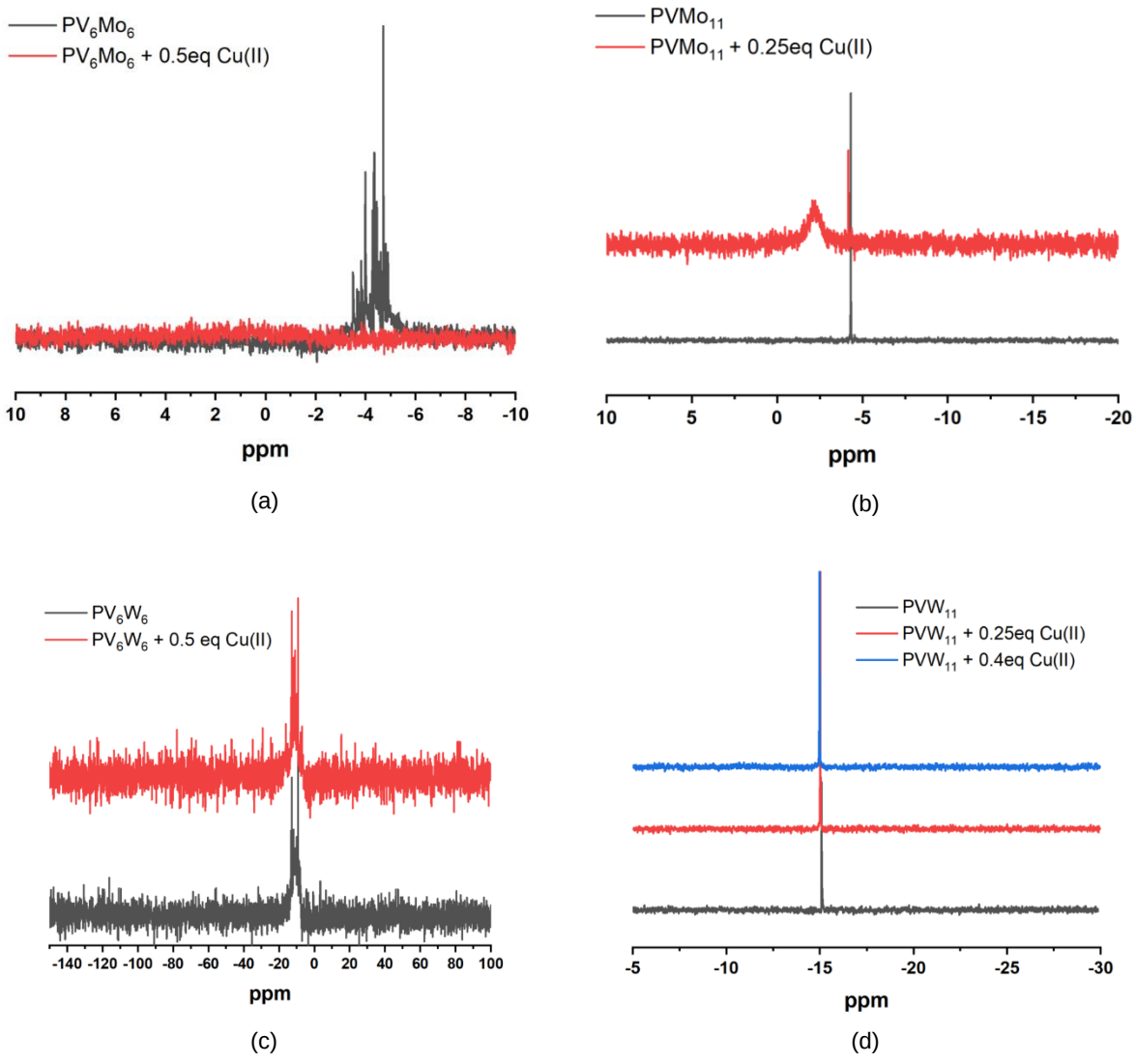

Figure 2.28. ^{31}P NMR spectra in acetonitrile-d_3 with respect to 85% H_3PO_4 (0 ppm) of (a) **PV_6Mo_6** before and after adding Cu(II); (b) **$PVMo_{11}$** before and after adding Cu(II); (c) **PV_6W_6** before and after adding Cu(II); (d) **PVW_{11}** before and after adding Cu(II).

2.4 Conclusions

(1) Polyvanadomolybdates and Cu(II) form a highly synergistic catalyst for the aerobic deodorization of a representative thiol, 2-mercaptoethanol (RSH), by oxidation to the corresponding non-odorous disulfide. Either the polyvanadomolybdate or Cu alone is almost inactive. Other d-electron transition metals, with the exception of Pd, in combination with polyvanadomolybdates, are not effective aerobic oxidation catalysts.

(2) We have identified the key steps in the optimal system, $TBA_4H_5PMo_6V_6O_{40}$ (**PV_6Mo_6**) + Cu(II). Significantly, **PV_6Mo_6** maintains the electrochemical potential of the solution in certain narrow ranges by controlling the speciation and concentration ratio of Cu(II)/Cu(I) during catalytic turnover and as such constitutes a redox buffer. Under turnover conditions, several redox couples of the POM are clearly involved. This is quite distinct from the numerous other studies of organic substrate oxidations catalyzed by POMs. This phenomenon has not been previously noted in the voluminous hydrolytic and catalytic oxidation chemistry of polyvanadophosphates.

(3) Also unique to our knowledge, the Cu functions as a dual catalyst in the **PV_6Mo_6**/Cu(II)/air oxidation system: Cu catalyzes reduction of the POM by the substrate, RSH, and it also catalyzes oxidation of the reduced POM by O_2/air.

(4) **PV_6W_6** does not have the redox buffer capability like **PV_6Mo_6**. As a consequence, the latter therefore shows no catalytic activity. Since both POM systems have almost the same electrochemical behavior, the huge electron transfer rate difference between them and Cu-complexes is attributed to inner-sphere versus outer-sphere electron transfer mechanisms.

2.5 References

1 R. De Levie, *J. Chem. Educ.*, 1999, **76**, 574–577.

2 D. W. King, *J. Chem. Educ.*, 2002, **79**, 1135–1140.

3 X. V. Zhen, C. R. Rousseau and P. Bühlmann, *Anal. Chem.*, 2018, **90**, 11000–11007.

4 X. U. Zou, J. H. Cheong, B. J. Taitt and P. Bühlmann, *Anal. Chem.*, 2013, **85**, 9350–9355.

5 J. A. Buss, A. Vasilopoulos, D. L. Golden and S. S. Stahl, *Org. Lett.*, 2020, **22**, 5749–5752.

6 R. E. Hansen, D. Roth and J. R. Winther, *Proc. Natl. Acad. Sci. U. S. A.*, 2009, **106**, 422–427.

7 G. G. Martinovich, I. V. Martinovich, S. N. Cherenkevich and H. Sauer, *Cell Biochem. Biophys.*, 2010, **58**, 75–83.

8 M. M. Lyles and H. F. Gilbert, *Biochemistry*, 1991, **30**, 613–619.

9 A. J. Meyer and R. Hell, *Photosynth. Res.*, 2005, **86**, 435–457.

10 C. Hwang, A. J. Sinskey and H. F. Lodish, *Science (80-.).*, 1992, **257**, 1496–1502.

11 A. J. Meyer, T. Brach, L. Marty, S. Kreye, N. Rouhier, J. P. Jacquot and R. Hell, *Plant J.*, 2007, **52**, 973–986.

12 F. Q. Schafer and G. R. Buettner, *Free Radic. Biol. Med.*, 2001, **30**, 1191–1212.

13 I. V. Kozhevnikov, *Chem. Rev.*, 1998, **98**, 171–198.

14 I. V. Kozhevnikov, *J. Mol. Catal. A Chem.*, 1997, **117**, 151–158.

15 I. A. Weinstock, R. E. Schreiber and R. Neumann, *Chem. Rev.*, 2018, **118**, 2680–2717.

16 I. V Kozhevnikov and K. I. Matveev, *Russ. Chem. Rev.*, 1982, **51**, 1075–1088.

17 C. L. Hill and C. M. Prosser-McCartha, *Coord. Chem. Rev.*, 1995, **143**, 407–455.

18 R. Neumann, *Inorg. Chem.*, 2010, **49**, 3594–3601.

19 R. Neumann and A. M. Khenkin, *Chem. Commun.*, 2006, 2529–2538.

20 Noritaka Mizuno and Makoto Misono, *Chem. Rev.*, 1998, **98**, 199–217.

21 T. Okuhara, N. Mizuno and M. Misono, *Adv. Catal.*, 1996, **41**, 113–252.

22 M. Misono, T. Okuhara and N. Mizuno, *Stud. Surf. Sci. Catal.*, 1989, **44**, 267–278.

23 F. Dénès, M. Pichowicz, G. Povie and P. Renaud, *Chem. Rev.*, 2014, **114**, 2587–2693.

24 A. R. Hajipour, S. E. Mallakpour and H. Adibi, *J. Org. Chem.*, 2002, **67**, 8666–8668.

25 A. V. Kachur, C. J. Koch and J. E. Biaglow, *Free Radic. Res.*, 1998, **28**, 259–269.

26 V. Vortisch, P. Kroneck and P. Hemmerich, *J. Am. Chem. Soc.*, 1976, **98**, 2821–2826.

27 P. W. Albro, J. T. Corbett and J. L. Schroeder, *J. Inorg. Biochem.*, 1986, **27**, 191–203.

28 S. M. S. Chauhan, A. Kumar and K. A. Srinivas, *Chem. Commun.*, 2003, 2348–2349.

29 L. Xu, E. Boring and C. L. Hill, *J. Catal.*, 2000, **195**, 394–405.

30 J. Song, Z. Luo, D. K. Britt, H. Furukawa, O. M. Yaghi, K. I. Hardcastle and C. L. Hill, *J. Am. Chem. Soc.*, 2011, **133**, 16839–16846.

31 A. Corma, T. Ródenas and M. J. Sabater, *Chem. Sci.*, 2012, **3**, 398–404.

32 A. Dhakshinamoorthy, S. Navalon, D. Sempere, M. Alvaro and H. Garcia, *ChemCatChem*, 2013, **5**, 241–246.

33 P. Sami, K. Venkateshwari, N. Mariselvi, A. Sarathi and K. Rajasekaran, *Transit. Met. Chem.*, 2010, **35**, 137–142.

34 G. A. Ayoko and M. A. Olatunji, *Polyhedron*, 1983, **2**, 577–582.

35 P. Sami, N. Mariselvi, K. Venkateshwari, A. Sarathi and K. Rajasekaran, *J. Chem. Sci.*, 2010, **122**, 335–340.

36 P. Sami, T. D. Anand, M. Premanathan and K. Rajasekaran, *Transit. Met. Chem.*, 2010, **35**, 1019–1025.

37 B. Botar, Y. V. Geletii, P. Kögerler, D. G. Musaev, K. Morokuma, I. A. Weinstock and C. L. Hill, *J. Am. Chem. Soc.*, 2006, **128**, 11268–11277.

38 T. Shanmugaprabha, K. Selvakumar, K. Rajasekaran and P. Sami, *Transit. Met. Chem.*, 2016, **41**, 77–85.

39 R. Hekmatshoar, S. Sajadi, M. M. Heravi and F. F. Bamoharram, *Molecules*, 2007, **12**, 2223–2228.

40 X. Xu, S. Chen, Y. Chen, H. Sun, L. Song, W. He and X. Wang, *Small*, 2016, **12**, 2982–2990.

41 A. Dhakshinamoorthy, M. Alvaro and H. Garcia, *Chem. Commun.*, 2010, **46**, 6476–6478.

42 B. Saha, M. Hung and D. M. Stanbury, *Inorg. Chem.*, 2002, **41**, 5538–5543.

43 S. Mandal, R. N. Bose, J. W. Reed and E. S. Gould, *Inorg. Chem.*, 1996, **35**, 3159–3162.

44 S. Goswami, N. Shaikh, A. Panja and P. Banerjee, *Int. J. Chem. Kinet.*, 2004, **36**, 129–137.

45 S. K. Ghosh, S. K. Saha, M. C. Ghosh, R. N. Bose, J. W. Reed and E. S. Gould, *Inorg. Chem.*, 1992, **31**, 3358–3362.

46 S. P. Ghosh, S. K. Saha, R. N. Bose, J. W. Reed, M. C. Ghosh and E. S. Gould, *Inorg. Chem.*, 1993, **32**, 2261–2264.

47 X. Wang and D. M. Stanbury, *Inorg. Chem.*, 2008, **47**, 1224–1236.

48 M. Hung and D. M. Stanbury, *Inorg. Chem.*, 2005, **44**, 3541–3550.

49 J. Sun and D. M. Stanbury, *Dalt. Trans.*, 2002, 785–791.

50 N. Bhattarai and D. M. Stanbury, *Inorg. Chem.*, 2012, **51**, 13303–13311.

51 Q. Wang, W. L. Man, W. W. Y. Lam, S. M. Yiu, M. K. Tse and T. C. Lau, *Inorg. Chem.*, 2018, **57**, 5850–5858.

52 Y. Hu and D. M. Stanbury, *Inorg. Chem.*, 2016, **55**, 7797–7803.

53 T. Shi, J. Berglund and L. I. Elding, *Inorg. Chem.*, 1996, **35**, 3498–3503.

54 M. Kim, I. A. Weinstock, Y. V. Geletii and C. L. Hill, *ACS Catal.*, 2015, **5**, 7048–7054.

55 G. A. Bagiyan, I. K. Koroleva, N. V. Soroka and A. V. Ufimtsev, *Russ. Chem. Bull.*, 2003, **52**, 1135–1141.

56 G. A. Bagiyan, I. K. Koroleva, N. V. Soroka and A. V. Ufimtsev, *Kinet. Catal.*, 2004, **45**, 372–380.

57 M. G. Gantman, I. G. Tarkhanova and Y. G. Kolyagin, *J. Sulfur Chem.*, 2016, **37**, 501–514.

58 V. W. Day, W. G. Klemparer and D. J. Maltbie, *J. Am. Chem. Soc.*, 1987, **109**, 2991–3002.

59 W. Guo, Z. Luo, H. Lv and C. L. Hill, *ACS Catal.*, 2014, **4**, 1154–1161.

60 T. Yokota, S. Fujibayashi, Y. Nishiyama, Y. Ishii and S. Sakaguchi, *J. Mol. Catal. A Chem.*, 1996, **114**, 113–122.

61 M. Hamamoto, K. Nakayama, Y. Nishiyama and Y. Ishii, *J. Org. Chem.*, 1993, **58**, 6421–6425.

62 G. A. Tsigdinos, *Ind. Eng. Chem. Prod. Res. Dev.*, 1974, **13**, 267–274.

63 G. A. Tsigdinos and C. J. Hallada, *Inorg. Chem.*, 1968, **7**, 437–441.

64 B. M. Alston, P. A. I. Cooper and P. R. J. Nichols, .

65 O. A. Kholdeeva, A. V. Golovin, R. I. Maksimovskaya and I. V. Kozhevnikov, *J. Mol. Catal.*, 1992, **75**, 235–244.

66 J. Díaz, L. R. Pizzio, G. Pecchi, C. H. Campos, L. Azócar, R. Briones, R. Romero, A. Henríquez, E. M. Gaigneaux and D. Contreras, *Catalysts*, , DOI:10.3390/catal12050507.

67 K. Yajima, K. Yamaguchi and N. Mizuno, *Chem. Commun.*, 2014, **50**, 6748–6750.

68 K. I. Matveev, V. F. Odyakov and E. G. Zhizhina, *J. Mol. Catal. A Chem.*, 1996, **114**, 151–160.

69 C. Li, K. Suzuki, K. Yamaguchi and N. Mizuno, *New J. Chem.*, 2017, **41**, 1417–1420.

70 A. W. Stobbe-kreemers, R. B. Dielis and M. S. J. F. Makkee, *J. Catal.*, 1995, **154**, 175–186.

71 K. Kamata, K. Yonehara, Y. Nakagawa, K. Uehara and N. Mizuno, *Nat. Chem.*, 2010, **2**, 478–483.

72 I. D. Ivanchikova, N. V. Maksimchuk, R. I. Maksimovskaya, G. M. Maksimov and O. A. Kholdeeva, *ACS Catal.*, 2014, **4**, 2706–2713.

73 Y. A. Rodikova, E. G. Zhizhina and Z. P. Pai, *Appl. Catal. A Gen.*, 2018, **549**, 216–224.

74 Y. A. Rodikova and E. G. Zhizhina, *Catal. Ind.*, 2019, **11**, 179–190.

75 T. Konishi, K. Kodani, T. Hasegawa, S. Ogo, S. X. Guo, J. F. Boas, J. Zhang, A. M. Bond and T. Ueda, *Inorg. Chem.*, 2020, **59**, 10522–10531.

76 Donald T.Sawyer, *Oxygen Chemistry*, 1993, vol. 41.

77 H. Borsook, H. W. Davenport, C. E. P. Jeffreys and R. C. Warner, *J. Biol. Chem.*, 1937, **117**, 237–279.

78 Y. J. Tu, D. Njus and H. B. Schlegel, *Org. Biomol. Chem.*, 2017, **15**, 4417–4431.

79 J. K. Lee, J. Melsheimer, S. Berndt, G. Mestl, R. Schlögl and K. Köhler, *Appl. Catal. A Gen.*, 2001, **214**, 125–148.

80 J. J. Altenau, M. T. Pope, R. A. Prados and H. So, *Inorg. Chem.*, 1975, **14**, 417–421.

81 and E. I. NOBUYUKI TANAKA,* KEI UNOURA, *Inorg. Chem.*, 1982, **4**, 1662–1666.

82 E. A. Nagul, I. D. McKelvie, P. Worsfold and S. D. Kolev, *Anal. Chim. Acta*, 2015, **890**, 60–82.

83 I. Csöregh, P. Kierkegaard and R. Norrestam, *Acta Crystallogr. Sect. B Struct. Crystallogr. Cryst. Chem.*, 1975, **31**, 314–317.

84 I. Persson, J. E. Penner-Hahn and K. O. Hodgson, *Inorg. Chem.*, 1993, **32**, 2497–2501.

85 A. D. Leu and D. A. Armstrong, *J. Phys. Chem.*, 1986, **90**, 1449–1454.

86 M. Kim, M. Chamack, Y. V. Geletii and C. L. Hill, *Inorg. Chem.*, 2018, **57**, 311–318.

87 Y. V. Geletti, A. J. Bailey, E. A. Boring and C. L. Hill, *Chem. Commun.*, 2001, **1**, 1484–1485.

88 Y. V. Geletii, C. L. Hill, R. H. Atalla and I. A. Weinstock, *J. Am. Chem. Soc.*, 2006, **128**, 17033–17042.

89 Y. V. Geletii, C. L. Hill, A. J. Bailey, K. I. Hardcastle, R. H. Atalla and I. A. Weinstock, *Inorg. Chem.*, 2005, **44**, 8955–8966.

90 S. Aksu, *J. Electrochem. Soc.*, , DOI:10.1149/1.3215996.

91 H. C. Mruthyunjaya and A. R. Vasudeva Murthy, *J. Electroanal. Chem.*, 1968, **18**, 200–204.

92 I. M. Dimucci, J. T. Lukens, S. Chatterjee, K. M. Carsch, C. J. Titus, S. J. Lee, D. Nordlund, T. A. Betley, S. N. MacMillan and K. M. Lancaster, *J. Am. Chem. Soc.*, 2019, **141**, 18508–18520.

93 W. Keown, J. B. Gary and T. D. P. Stack, *J. Biol. Inorg. Chem.*, 2017, **22**, 289–305.

94 P. M. Skitał and P. T. Sanecki, *Russ. J. Electrochem.*, 2012, **48**, 797–803.

95 P. M. Skitał, P. T. Sanecki and K. Gibała, *Electrochim. Acta*, 2014, **138**, 383–391.

96 I. A. Weinstock, *Chem. Rev.*, 1998, **98**, 113–170.

97 Y. V. Geletii and I. A. Weinstock, *J. Mol. Catal. A Chem.*, 2006, **251**, 255–262.

98 D. C. Duncan and C. L. Hill, *J. Am. Chem. Soc.*, 1997, **119**, 243–244.

99 A. M. Khenkin, I. Efremenko, J. M. L. Martin and R. Neumann, *Phys. Chem. Chem. Phys.*, 2018, **20**, 7579–7587.

100 R. Neumann and M. Levin, *J Am Chem Soc*, 1992, **114**, 7278–7286.

101 I. A. Weinstock, R. E. Schreiber and R. Neumann, *Chem. Rev.*, 2018, **118**, 2680–2717.

102 A. M. Khenkin, L. Weiner, Y. Wang and R. Neumann, *J. Am. Chem. Soc.*, 2001, **123**, 8531–8542.

103 Alexander M. Khenkin and Ronny Neumann*, *Angew. Chemie - Int. Ed.*, 2000, **39**, 4088–4090.

104 L. Pettersson, I. Andersson, A. Selling and J. H. Grate, *Inorg. Chem.*, 1994, **33**, 982–993.

105 S. R. Bajpe, C. E. A. Kirschhock, A. Aerts, E. Breynaert, G. Absillis, T. N. Parac-Vogt, L. Giebeler and J. A. Martens, *Chem. - A Eur. J.*, 2010, **16**, 3926–3932.

106 M. Inamo, N. Kamiya, Y. Inada, M. Nomura and S. Funahashi, *Inorg. Chem.*, 2001, **40**, 5636–5644.

Chapter 3:

Role of multiple vanadium centers on redox buffering and rates of polyvanadomolybdate-Cu(II)-catalyzed aerobic oxidations

Abstract

A recent report established that the tetrabutylammonium (TBA) salt of hexavanadopolymolybdate $TBA_4H_5[PMo_6V_6O_{40}]$ (**PV_6Mo_6**) serves as the redox buffer with Cu(II) as a co-catalyst for the aerobic deodorization of thiols in acetonitrile. Here, we document the profound impact of vanadium atom number (x = 0-4, and 6) in TBA salts of $PV_xMo_{12-x}O_{40}^{(3+x)-}$ (**PVMo**) on this multicomponent catalytic system. The **PVMo** cyclic voltammetric peaks from 0 to -200mV vs Fc/Fc^+ under catalytic conditions (acetonitrile, ambient T) have been assigned and clarify that the redox buffering capability of the **PVMo**/Cu catalytic system derives from the number of steps, the number of electrons transferred each step and the potential ranges of each step. All **PVMo** are reduced by varying numbers of electrons, from 1-6, in different reaction conditions. Significantly, **PVMo** with x≤3 not only have much lower activity than when x>3 (for example, the turnover frequency (TOF) of **PV_3Mo_9** and **PV_4Mo_8** are 8.9 and 48 s^{-1}, respectively), but unlike the latter, cannot maintain steady reduction states when the Mo atoms in these POMs are also reduced. Stopped-flow kinetics measurements reveal that Mo atoms in the Keggin **PVMo** exhibit much slower electron transfer rates than the V atoms. Two kinetic arguments: (a) in acetonitrile, the first formal potential of **PMo_{12}** is more positive than that of **$PVMo_{11}$** (-236 mV and -405 mV vs Fc/Fc^+); however, the initial reduction rates are 0.0013 s^{-1} and 0.036 s^{-1} for **PMo_{12}** and **$PVMo_{11}$** respectively; and (b) in aqueous sulfate buffer (pH=2), two-step kinetics are observed for **$PVMo_{11}$** and **PV_2Mo_{10}**, where the first and second steps are assigned to reduction of the V and Mo centers, respectively. Since fast and reversible electron transfers are key for the redox buffering behavior, the slower electron transfer kinetics of Mo preclude these centers functioning in redox buffering that maintains the solution potential. We conclude that **PVMo** with more vanadium

atoms allows the POM to undergo more and faster redox changes, which enables the POM to function as a redox buffer dictating far higher catalytic activity.

3.1 Introduction

Polyoxometalate (POM) research continues with applications of this large and growing class of complexes in catalysis,[1–5] biology,[6–10] environment[11,12] and energy.[13–16] Of particular importance are catalytic O_2-based oxidations that have been studied over decades with some processes commercialized.[1–4,17,18] The phosphovanadomolybdates, $H_{3+x}PV_xMo_{12-x}O_{40}^{(3+x)-}$ (x = 1-6), have been particularly well studied in context with oxidation of organic substrates.[2,17–19] This class of POMs can undergo multi-electron transfer[20,21] and reversible oxygen atom transfer processes,[22–25] and function as radical scavengers.[23,26] Their oxidations can proceed by different mechanisms including electron transfer (ET)[27,28] proton-coupled electron transfer (PCET) and electron transfer-oxygen transfer (ET-OT).[22–25] They function well in Pd(II)-based two-component Wacker-type oxidation reactions.[2,18,29–32] Noble metal-POM two-component catalytic systems other than those containing Pd(II),[33] have been studied, and those containing Pt(II) have been reported to oxidize methane.[34,35] Complementing these studies are reports of POM-stabilized noble-metal(0) nanoparticles catalyzing other oxidation reactions including epoxidation, dehydrogenation and the conversion of alkanes to alkenes.[36–41] However, these two-component systems are all based on noble-metals. Catalytic systems based on first-row transition metals are desired due to their abundance and low cost. Recently, our group found that Cu(II) catalyzes the reoxidation of reduced Keggin POMs.[42–44] In addition, a few groups synthesized heteropolyacids (HPAs) with Cu^{2+} counterions and studied their catalytic behaviors.[45–47] Some studies focused on POMs with different transition metal ions on certain supports as heterogeneous catalysts.[45,47] Others focused on the effect of metal ion substitution on solution acidity and potential.[46] In previous recent work,

we found that Cu(II) and the TBA salts of **PV_6Mo_6** exhibit high synergy in the air-based oxidation of thiols in acetonitrile.[48] Unique to this latter study, the **PV_6Mo_6** behaves as a catalyst for several steps involving multielectron redox buffering[49,50] which controls the ratio and speciation of Cu(II)/Cu(I) complexes and maintains the solution potential in narrow ranges based on different POM redox couples.

In this dissertation chapter, we study the effect of number of vanadium atoms, x, in TBA salts of phosphovanadomolybdates, $PV_xMo_{12-x}O_{40}^{(3+x)-}$ (**PVMo**, x = 0-4 and 6) on the redox buffering properties of the **PVMo**/Cu homogeneous catalytic system for aerobic thiol (RSH) oxidation, eq 3.1. To do this, we measure the potentials and the number of electrons in the reduced **PVMo** intermediates as well as the greatly different electron transfer rates for V versus Mo in the POMs, and show how these properties correlate with catalytic activity and redox self-buffering.

$$2\ RSH + ½\ O_2 \rightarrow RSSR + H_2O \qquad (3.1)$$

3.2 Experimental

3.2.1 General Materials and Methods

All chemicals were purchased from commercial sources and used without further purification. The acetonitrile (Sigma-Aldrich HPLC grade ≥ 99.9%, ≤ 0.02% water) was used for catalytic reactions, kinetics measurements and electrochemistry outside the glovebox and is referred to subsequently as *reaction acetonitrile*). The acetonitrile from ThermoFisher (Extra Dry, ≤ 0.001%) was used for cyclic voltammograms (CVs) conducted in a MBRAUN LABmater 130 glovebox and referred to subsequently as *dry acetonitrile*. UV−vis spectra were measured with an Agilent 8453 spectrophotometer equipped with a diode array detector using a 1.0 cm optical path length quartz cuvette. ^{31}P nuclear magnetic resonance (NMR) spectra were acquired on a Varian INOVA

400 spectrometer. The kinetics were followed using a SF-61 stopped-flow instrument (Hi-Tech Scientific, U.K.).

3.2.2 Electrochemistry

Cyclic voltammograms (CVs) and bulk electrolysis (BE) data were obtained using a BAS CV-50W electrochemical analyzer. CVs were conducted in a standard three-electrode electrochemical cell with a glassy carbon disk working electrode and a platinum wire counter electrode. For experiments in acetonitrile, a Ag/Ag^+ (0.01 M $AgNO_3$ in CH_3CN) reference electrode with 0.1 M tetrabutylammonium hexafluorophosphate (*n*-Bu_4NPF_6) as the supporting electrolyte were used. The measured potential was converted to the Fc/Fc^+ scale using data measured from CV for 1.0 mM ferrocene (Fc). For experiments in aqueous buffer, Ag/AgCl was used as reference electrode with 0.1 M KNO_3 as supporting electrolyte. For bulk electrolysis experiments, a reticulated vitreous carbon working electrode was used as a working electrode. The working and counter electrode were separated by a porous glass sinter. The desired constant potential was applied in each electrolysis until the current dropped to <10% of the initial value, then aliquots were withdrawn, and the UV-Vis spectra were recorded under Ar. The electrolysis was then resumed at the more negative potential.

Rotating disk electrode (RDE) voltammetry and square pulse wave voltammetry (SWV) were conducted on a Wavedriver 10 potentiostat/galvanostat (Pine Research Instrumentation). For both experiments, the standard three electrode setup was used with a 3-mm diameter glassy carbon disk working electrode, a Ag/Ag^+ (0.01 M $AgNO_3$ in CH_3CN) reference electrode, and a platinum wire counter electrode. The rotation speed from 500-3000 RPM was controlled by a Model AFMSRCE ring-disk electrode system (Pine Research Instrumentation).

3.2.3 ^{31}P NMR of TBA salts of $PV_xMo_{12-x}O_{40}^{(3+x)-}$ (x = 0-4 and 6)

All the TBA salts of the POMs, $TBA_3PMo_{12}O_{40}$ (**PMo_{12}**); $TBA_4PVMo_{11}O_{40}$ (**$PVMo_{11}$**); $TBA_4HPV_2Mo_{10}O_{40}$ (**PV_2Mo_{10}**); $TBA_4H_2PV_3Mo_9O_{40}$ (**PV_3Mo_9**); $TBA_4H_3PV_4Mo_8O_{40}$ (**PV_4Mo_8**) and $TBA_4H_5PMo_6V_6O_{40}$ (**PV_6Mo_6**), were synthesized according to literature methods[51–54] and characteried by UV-vis, ATR FT-IR and thermogravimetric (TGA) as in in previous work.[48] Here ^{31}P NMR spectra of **PVMo** in acetonitrile-d_3 with respect to 85% H_3PO_4 (0 ppm) are given in Figure 3.0.

For ^{31}P NMR spectra, **$PVMo_{11}$** has a single peak at -4.31 ppm that proves its purity. **PV_2Mo_{10}** has a peak at -4.31 ppm indicating the **$PVMo_{11}$** component and a broad peak that split to -4.54 and -4.60 ppm which is assigned to **PV_2Mo_{10}** and **PV_3Mo_9** components. For **PV_3Mo_9**, in addition to the peaks that have essentially the same chemical shifts as for **PV_2Mo_{10}**, multiple peaks more positive than -4ppm may be assigned to **PV_4Mo_8** components. **PV_4Mo_8** and **PV_6Mo_6** all show multiple peaks that cannot be clearly assigned indicating the many components and positional isomers present. It is well-established that heteropolyacids, $H_{3+x}PV_xMo_{12-x}O_{40}^{(3+x)-}$, when x>1, are mixtures of positional isomers and components with different x.[55] The ^{31}P NMR data in this work shows that the TBA salts of **PVMo** in acetonitrile are isomeric mixtures.

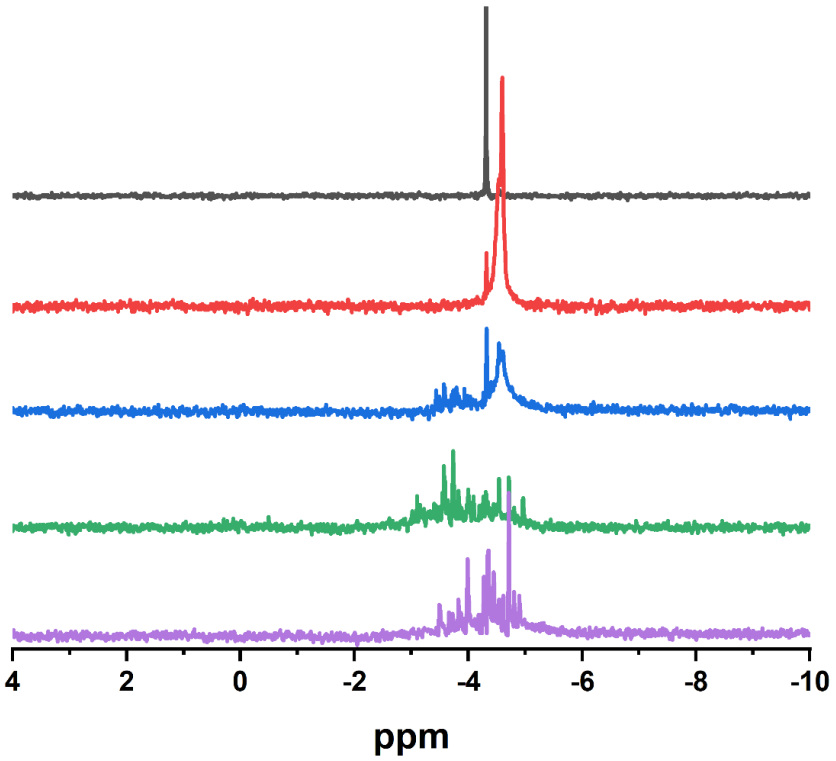

Figure 3.0. ^{31}P NMR spectra in acetonitrile-d_3 relative to 85% H_3PO_4 (0 ppm) of **$PVMo_{11}$**, black; PV_2Mo_{10}, red; **PV_3Mo_9**, blue; **PV_4Mo_8**, green; **PV_6Mo_6**, purple.

3.2.4 RSH Oxidation and Measurement of The Varying PVMo Reduction States

2-Mercaptoethanol was used as an exemplary substrate for probing the aerobic thiol oxidation, eq 3.1 in the text, where RSH is 2-mercaptoethanol. The mechanism of the **PV_6Mo_6**/Cu system was thoroughly studied in previous work.[48] This article focuses on the impact of the number of vanadium atoms (x = 0-4, and 6) in $PV_xMo_{12-x}O_{40}^{(3+x)-}$ (**PVMo**). The RSH concentration was quantified using Ellan's reagent (5,5-dithiobis(2-nitrobenzoic acid) (DTNB)).[56] In a typical reaction, 0.1 mL of DTNB solution (5 mg/mL in methanol) was added to a 5 mL pH = 7.4 phosphate buffer solution (50 mM). This solution was first used as the blank for UV-vis measurements. Then, a 10 µL aliquot of the reaction solution was added and the absorbance at 412 nm was followed and the RSH concentration calculated.

In a typical RSH oxidation reaction, POM (0.1 mM), $Cu(ClO_4)_2$ (0.8 mM) and 2-mercaptoethanol (30 mM) were stirred in acetonitrile in a heavy-wall glass pressure vessel in an air-conditioned room at 25±2 ºC. Aliquots of the solution were withdrawn every several minutes and monitored by UV-vis spectra as described above.

In a typical **PVMo** reduction state measurement, **PVMo** (0.1 mM) and $Cu(ClO_4)_2$ (0.5 mM) were stirred in acetonitrile in a 1.0 cm optical path length quartz cuvette purged with air at 25±2 ºC. After adding the 2-mercaptoethanol (30 mM), the UV-vis spectra of the solution in the course of the reaction were monitored. The absorption was then converted to the apparent extinction coefficient using the Beer–Lambert law. The average number of electrons transferred to the POM was calculated from the calibration curve using different titration methods. For experiments in acetonitrile, ascorbic acid and Ce(IV) were used for titration of **PV_4Mo_8** and **PV_6Mo_6**; $SnCl_2$ and Ce(IV) were used for titration of **$PVMo_{11}$**, **PV_2Mo_{10}** and **PV_3Mo_9**. Bulk electrolysis titration was used to confirm certain results. For experiments in aqueous condition, bulk electrolysis titration was performed for $[PVMo_{11}]^{4-}$, $[PV_2Mo_{10}]^{5-}$ and $[PVW_{11}]^{5-}$.

3.2.5 Stopped-Flow Measurements

A stopped-flow UV-vis spectrometer was used to monitor the rates of $PV_nMo_{12-n}O_{40}^{(3+n)-}$ reduction by 2-mercaptoethanol at different concentrations of $Cu(ClO_4)_2$ under argon. In a typical measurement, one feeding syringe was filled with the de-aerated stock acetonitrile or aqueous buffer solution of POM and $Cu(ClO_4)_2$. The second feeding syringe was filled with the de-aerated acetonitrile or aqueous buffer solution of 2-mercaptoethanol. In all stopped-flow kinetic measurements, the concentrations of all components, POM, $Cu(ClO_4)_2$ and 2-mercaptoethanol in the reaction were two times lower than concentrations in the feeding syringes.

3.3 Results and Discussion

3.3.1 Catalytic Activity

The kinetics of RSH consumption catalyzed by the **PVMo**/Cu system are shown in Figure 3.1. The activity of **PVMo** decreases as the number of vanadium centers decreases from x=6 to x=1. We note that the **PVMo** where x=4 and 6 are dramatically more active than for **PVMo**, where x≤3 (data summarized in Table 3.1). The effect of the substituted vanadium addenda atoms on catalytic activity has been documented in several studies.[27,46,47,57–60] Two mechanisms have been advanced to explain the trend in activity. The first involves the intact POM polyanion as the catalytically-active unit, and the second involves vanadate, VO_2^+, that has dissociated from the polyanion, as the active unit.[27,46,61,62] In the former case, the activity is controlled by V(V/VI) redox potential and POM structure.[57,59] We note that in some H_2O_2-based oxidations catalyzed by divanadium-substituted polyoxotungstates that peroxo-vanadium intermediates have been proposed.[63,64] In previous work,[48] we conducted a series of experiments to show that free vanadium has little effect on PV_6Mo_6/Cu catalytic system in acetonitrile. Thus, we assume that in our system, the intact POM is the catalytically significant unit, and we explain the activity tendency from two vantages: 1. the redox buffer effect of **PVMo**. The difference in electrochemical properties dictates different potential buffer ranges. 2. The difference in electron transfer rates of V and Mo in the **PVMo** Keggin complexes.

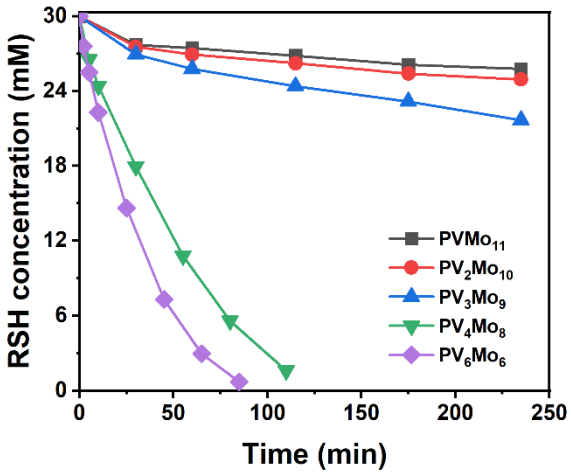

Figure 3.1. RSH consumption catalyzed by **PVMo**/Cu under air at room temperature. Conditions: POM: 0.1 mM, Cu(II): 0.8 mM, RSH: 30 mM in 5 mL acetonitrile.

Table 3.1: Air-based Oxidation of 2-Mercaptoethanol Catalyzed by **PVMo**/Cu Systems[a]

Catalyst	Conversion[b], %	TON×10^{-2}[c]	TOF×10^{3}, s^{-1} [d]
$PVMo_{11}$	10	0.30	5
PV_2Mo_{10}	12	0.36	6
PV_3Mo_9	16	0.48	8
PV_4Mo_8	90	2.7	45
PV_6Mo_6	100	3.0	56
PV_4Mo_8[e]	0.8	0.024	0.4
PV_6Mo_6[e]	1	0.03	0.5
$Cu(ClO_4)_2$[f]	10	0.04	0.6

[a] Conditions: POM (0.1 mM), $Cu(ClO_4)_2$ (0.8 mM), 2-mercaptoethanol (30 mM), acetonitrile (5 mL) at room temperature under air. [b] Conversion was measured after 100 min. [c] Turnover number (TON = moles of 2-mercaptoethanol consumed per mol of POM) was measured after 100 min. [d] Turnover Frequency, TOF = TON/(Reaction time). [e] POM (0.1 mM) without $Cu(ClO_4)_2$. [f] TON and TOF based on $Cu(ClO_4)_2$ concentration.

3.3.2 Electrochemistry of $PV_xMo_{12-x}O_{40}^{(3+x)-}$ (PVMo)

Effect of water on cyclic voltammograms in acetonitrile. In previous work we have found that **PV_6Mo_6** can accept up to 6 electrons in the Cu/**PVMo** catalytic system for air-based thiol

oxidation.[48] Thus, the redox properties of **PVMo** in acetonitrile at very negative potentials are important. However, trace amounts of water in acetonitrile can have a significant effect on the electrochemical behavior of reduced POMs.[65,66] Therefore, we compared the CVs of **PVMo** in reaction acetonitrile and dry acetonitrile. Since acetonitrile can pick up small quantities of water from ambient air during laboratory manipulations, including argon purging, the dry acetonitrile CVs were conducted in the glovebox. Figure 3.2 compares the CVs of **PVMo** in reaction acetonitrile and dry acetonitrile. The assignment of peaks is given below.

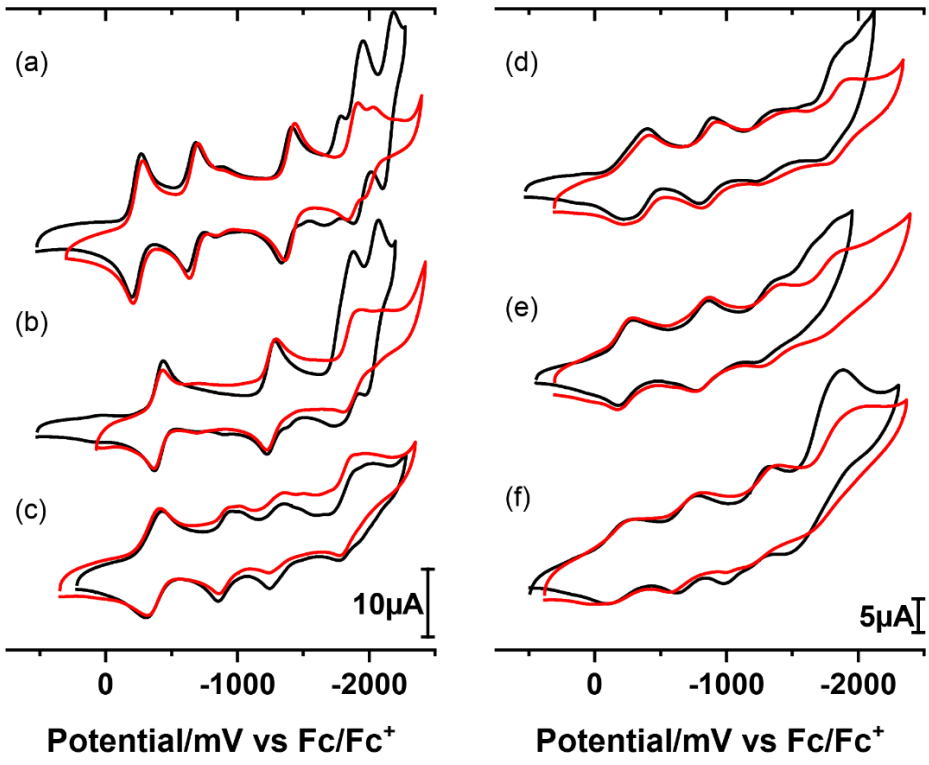

Figure 3.2. Comparison CVs in reaction acetonitrile (black) and CVs in glovebox with dry acetonitrile (red). (a) $\mathbf{PMo_{12}}$, (b) $\mathbf{PVMo_{11}}$, (c) $\mathbf{PV_2Mo_{10}}$, (d) $\mathbf{PV_3Mo_9}$, (e) $\mathbf{PV_4Mo_8}$, (f) $\mathbf{PV_6Mo_6}$. 0.5 mM POM on glassy carbon electrode. 100 mM n-Bu_4NPF_6. v = 100 mV s^{-1}, T = 298 K.

Figure 2a, b (black) shows that the replacement of a single molybdenum atom with vanadium (**$PVMo_{11}$**) dramatically changes the shape of CV curves. Instead of three peaks, only two are seen

for x=1 in the range 0 to -1500 mV. The first peak arises from the V^{V}/V^{IV} redox couple and is one-electron. This result is consistent with the previous work.[67,68] and is confirmed by BE at potentials -780 mV and -1500 mV, each of which involve a transfer of one electron (Figure 3.3 and Table 3.2). At potentials more negative than -1500 mV, two peaks transform to two-electron ones and are very similar to those seen for **PMo12**. The small shoulder peak on **PMo12** comes from the electrochemical instability of **PMo12** when scanned to very negative potential (< -1800 mV) (Figure 3.4).

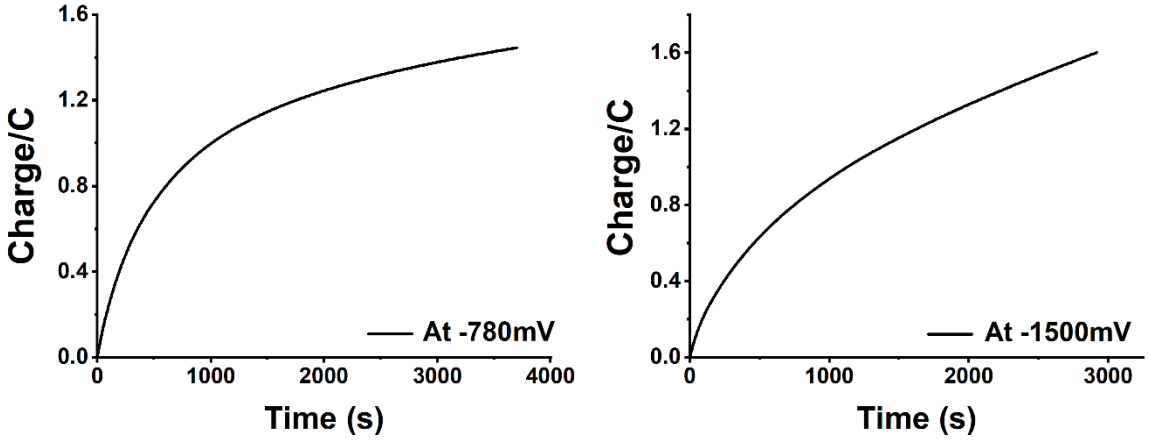

Figure 3.3. Charge vs time curves from the bulk electrolysis of **PVMo11**. Conditions: **PVMo11** (0.5 mM), *n*-Bu_4NPF_6 (100 mM) in acetonitrile (30 mL), at 25 ± 2 °C under argon. See Table 3.2 below.

Table 3.2. The results of bulk electrolysis of **PVMo11** at constant potential in acetonitrile.[a]

Potential/mV vs Fc/Fc^+	Number of Coulombs	Number of electrons[b]	Ending current ratio[c]/%
-780	1.48	1.0	3
-1500	1.6	1.1	5.5

[a] Conditions: **PVMo11** (0.5 mM), *n*-Bu_4NPF_6 (100 mM), acetonitrile (30 mL), at room temperature under argon. [b] Number of electrons transferred to the POM (polyanion) unit, calculated according to Faraday's law of electrolysis. [c] Ending current ratio is defined as the final current at the end of the bulk electrolysis over the initial current at the beginning of the bulk electrolysis at the specific potential.

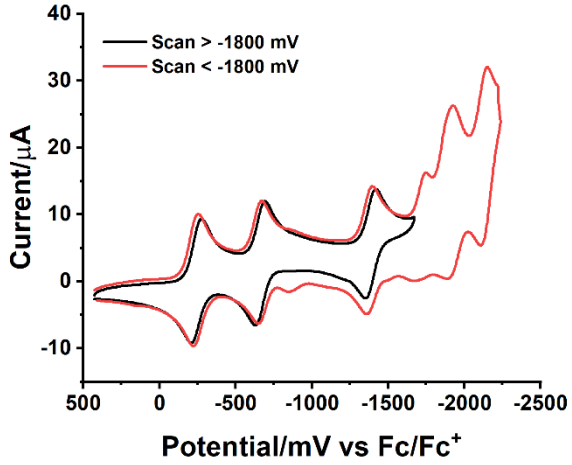

Figure 3.4. Electrochemical instability of **PMo_{12}** when scanned negative of -1800 mV.

To confirm the number of electrons of the peaks at potentials negative of -1500 mV, RDE voltammetry was conducted, however, since the two peaks are quasi-reversible and too close to each other, the plateau current of the RDE scans is relatively hard to define. The approximate relative ratio of limiting currents at 500 rpm is I: II: III: IV = 1: 1.3: 2.3: 1.9 (Figure 3.5a). Plots of $E\ vs \log[(i_d - i)/i]$ are linear for all four processes (Figure 3.5b).[69] The slopes for the first and second confirmed one-electron processes are 75 mV and 86 mV respectively which are larger than the 59 mV for a theoretical reversible one-electron process. This is consistent with relatively slow electron transfer in acetonitrile. The third and fourth two-electron processes have slopes (93 mV) close to the one-electron process but not half of it. This is consistent with the processes III and IV being two proton-coupled one-electron processes at different potentials, but not a two-electron Nernstian process.[70] On comparing the CVs of **PMo_{12}** and **$PVMo_{11}$** in reaction acetonitrile and dry acetonitrile, we can confirm that the two-electron transfer peaks are due to the proton-coupled electron transfer (PCET)[66,71,72] processes facilitated by the trace water present in the reaction acetonitrile, while in the glovebox samples (dry acetonitrile), the two-electron peaks change to one-electron peaks (Figures 3.2a, b).

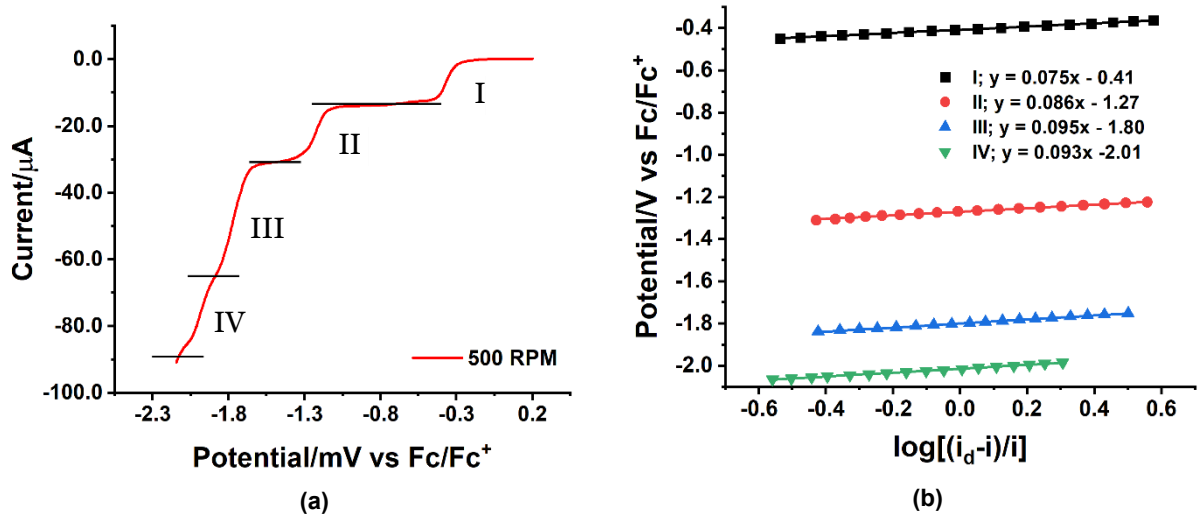

Figure 3.5. (a) Rotating disk electrode (RDE) voltammetry of **PVMo$_{11}$** at 500 RPM. (b) E vs log [(i_d-i)/i] curves for four processes at the RDE. Conditions: **PVMo$_{11}$** (0.5 mM), *n*-Bu_4NPF_6 (100 mM), acetonitrile (20 mL), at room temperature under argon, scan rate 5 mV s^{-1}.

The CV of **PV_2Mo_{10}** shows 3 peaks before -1500 mV (Figure 3.2c). Bulk electrolysis shows that the first peak is one-electron, while the second and third peaks share one electron with an electron ratio of 0.44: 0.56 (Figure 3.6 and Table 3.3). UV-Vis spectra after bulk electrolysis at each potential were collected. The spectra were compared with those from ascorbic acid titration and confirm that second and third peak in total constitute the transfer of one electron during bulk electrolysis (Figure 3.9).

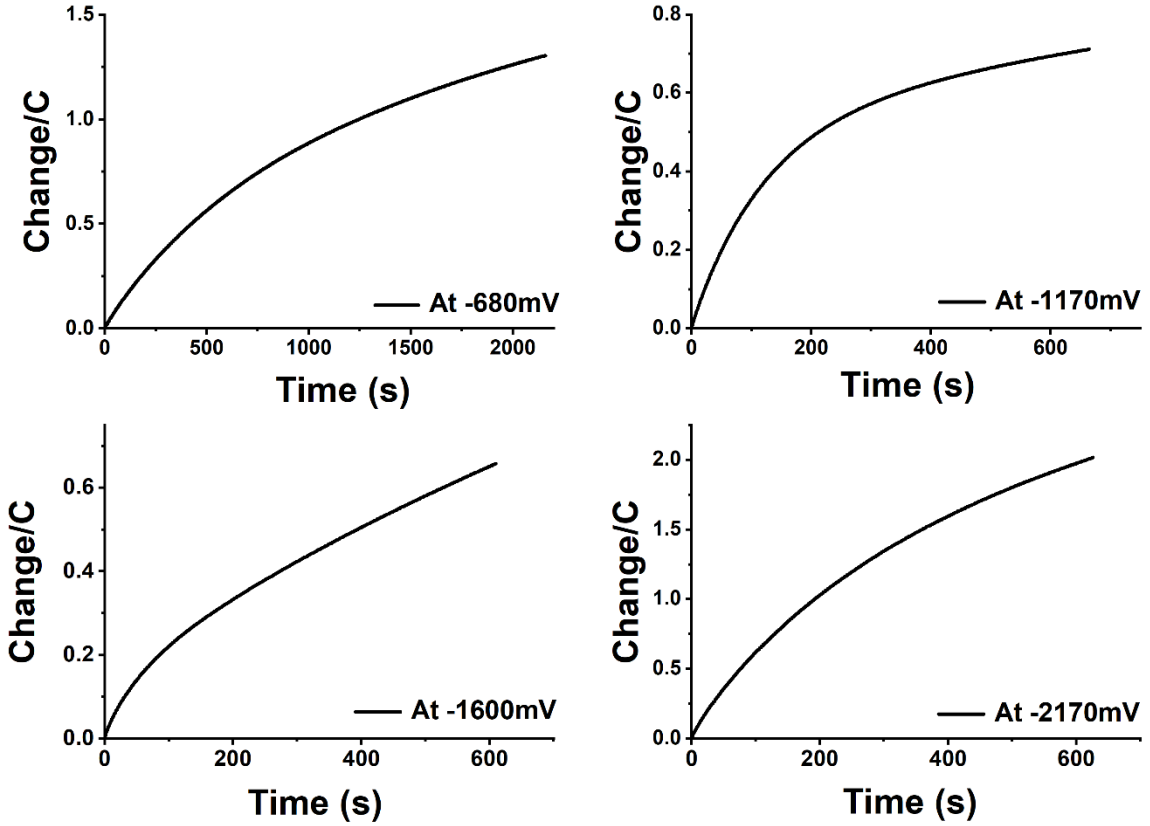

Figure 3.6. Charge vs time curves from the bulk electrolysis of $\mathbf{PV_2Mo_{10}}$. Conditions: $\mathbf{PV_2Mo_{10}}$ (0.5 mM), *n*-Bu_4NPF_6 (100 mM) in acetonitrile (30 mL), at 25 ± 2 ºC under argon. See Table 3.3 below.

Table 3.3: The results of bulk electrolysis of $\mathbf{PV_2Mo_{10}}$ at constant potential in acetonitrile.[a]

Potential/mV vs Fc/Fc^+	Number of Coulombs	Number of electrons	Ending current ratio/%
-680	1.3	0.9	8.2
-1170	0.6	0.4	3.7
-1600	0.75	0.5	8.9
-2170	2.2	1.6	11

[a] Conditions: $\mathbf{PV_2Mo_{10}}$ (0.5 mM), *n*-Bu_4NPF_6 (100 mM), acetonitrile (30 mL), at room temperature under argon.

The Levich plots (i_L vs $\omega^{1/2}$) from the RDE voltametric data for all four processes are linear, indicating mass transport control (Figure 3.7a, b). The relative ratio of limiting currents is I: II: III= 1: 0.59: 0.70, which confirms the bulk electrolysis results. That two peaks share one electron

is attributed to the presence of two families of isomers with different free energies. This is consistent with the computational result from Neumann and Shaik, et al.[73] The two-electron reduced isomers of $[PV_2Mo_{10}]^{7-}$ with the distal vanadium centers have different free energies than the isomers with vicinal vanadium centers. According to the calculation in acetonitrile, if we assume the $[PV_2Mo_{10}]^{7-}$ is a singlet,[74] the average energy difference between two different groups of isomers is 13 kcal/mol = 5.4×10^4 J/mol. This is roughly consistent with the data from CV that the potential difference between the second and the third peak is 386 mV = 3.7×10^4 J/mol. The relative current ratio of the two peaks should equal to the ratio of degeneracies of the two isomer families.[75] Computational results indicate that the distribution of these positional isomers and their associated degeneracies will change with solvent,[73] therefore, we do not discuss these features further here. Comparing the CVs of the glovebox samples reveals that the fourth peak does not obviously change and can be assigned as two one-electron processes close to each other, a result confirmed by the BE data that gives an approximate coulomb ratio of I: IV = 1: 1.7.

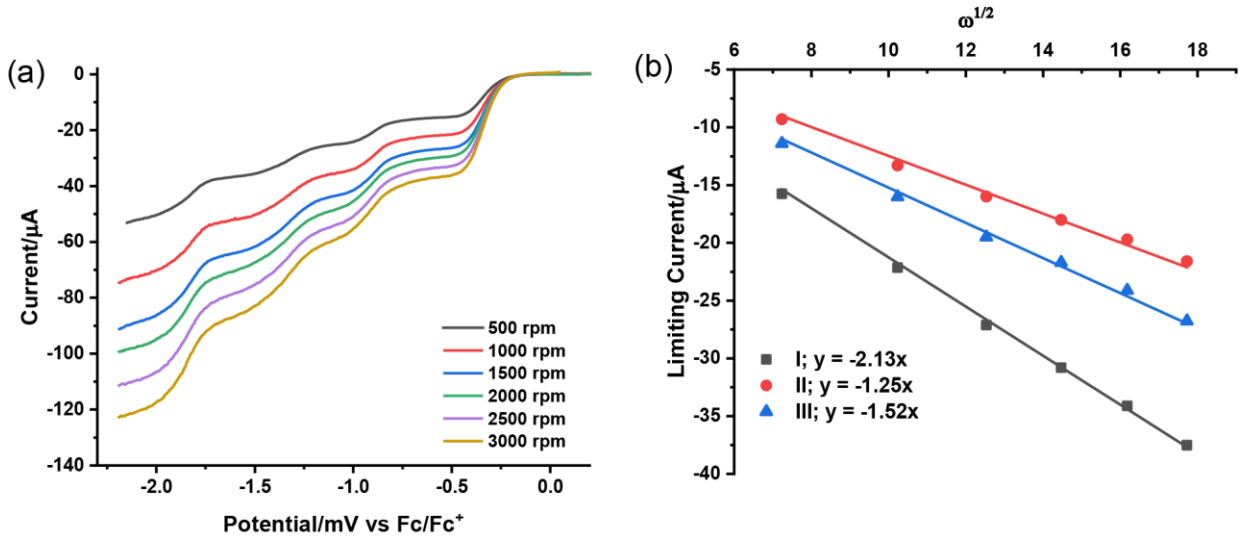

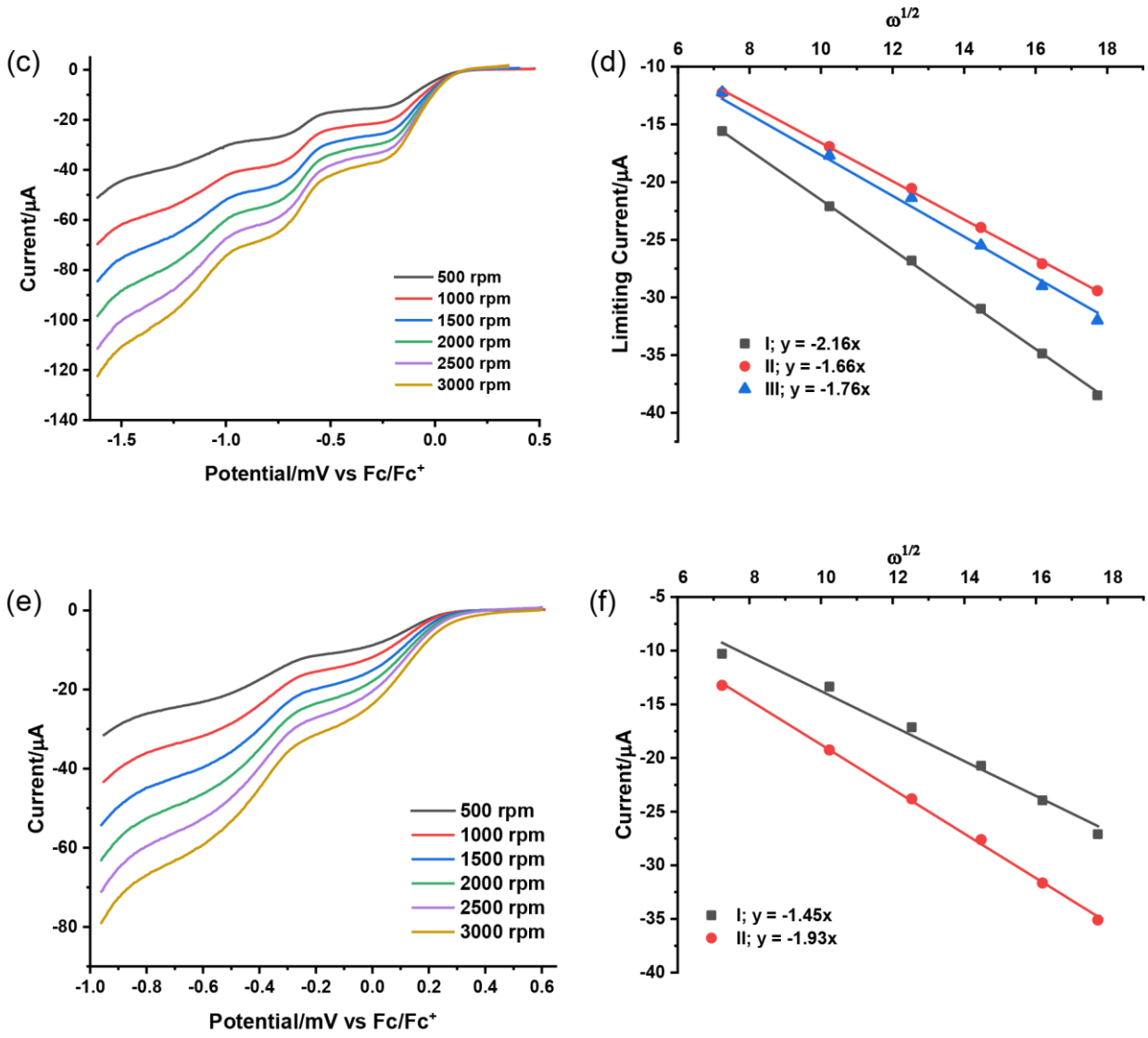

Figure 3.7. Rotating disk electrode (RDE) voltametric data and the corresponding Levich plots (limiting current, i_L vs $\omega^{1/2}$). Conditions: POM (0.5 mM), *n*-Bu_4NPF_6 (100 mM), acetonitrile (20 mL), at room temperature under argon, scan rate 5 mV s^{-1}. (a, b) $\mathbf{PV_2Mo_{10}}$; (c, d) $\mathbf{PV_3Mo_9}$; (e, f) $\mathbf{PV_4Mo_8}$.

The CVs of $\mathbf{PV_3Mo_9}$ and $\mathbf{PV_4Mo_8}$ are very similar. The first three peaks have approximately the same height, which are slightly lower than the first peak of $\mathbf{PVMo_{11}}$. They are broader not only from the presence of several $\mathbf{PV_3Mo_9}$ and $\mathbf{PV_4Mo_8}$ isomers but also because they exist as a statistical distribution.[75] BE shows that the first three peaks of $\mathbf{PV_3Mo_9}$ are one-electron reductions of vanadium (Figure 3.8 and Table 3.4), a finding that is confirmed by the relative ratio of limiting currents, I: II: III = 0.95: 1: 1.21. RDE voltammetry

of the fourth peak does not have a well-defined plateau current due to some irreversibility (Figures 3.7c, d). RDE voltammetry of **PV_4Mo_8** shows the first two peaks are one-electron and the relative ratio of limiting currents is I: II = 1:1.3 (Figure 3.7e, f). Since the third and fourth peaks of **PV_4Mo_8** are irreversible, BE and RDE cannot provide useful information on them.

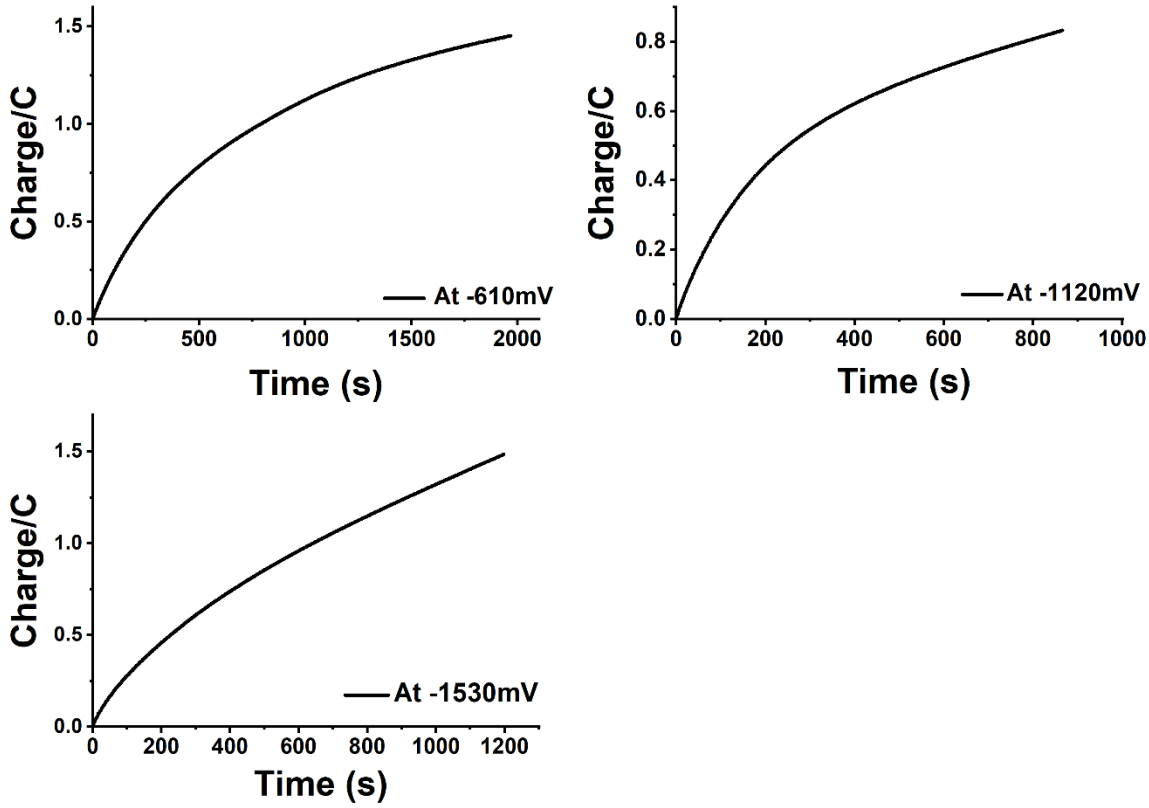

Figure 3.8. Charge vs time curves from the bulk electrolysis of **PV_3Mo_9**. Conditions: **PV_3Mo_9** (0.5 mM), *n*-Bu_4NPF_6 (100 mM) in acetonitrile (30 mL), at 25 ± 2 °C under argon. See Table 3.4 below.

Table 3.4: The results of bulk electrolysis of **PV_3Mo_9** at constant potential in acetonitrile.[a]

Potential/mV vs Fc/Fc^+	Number of Coulombs	Number of electrons	Ending current ratio/%
-610	1.45	1.0	5.2
-1120	0.82	0.6	5.5
-1530	1.4	1.0	10

[a] Conditions: **PV_3Mo_9** (0.5 mM), *n*-Bu_4NPF_6 (100 mM), acetonitrile (30 mL), at room temperature under argon. The CVs of **PV_3Mo_9** in the dry acetonitrile (Figure 3.2d) shows four unequivocal one-electron peaks.

Thus, the fourth peak in reaction acetonitrile can be assigned as a two-electron PCET process. The dry acetonitrile CVs of **PV_4Mo_8** also show four distinct one-electron peaks, while the fourth peak in reaction acetonitrile changes potential slightly and becomes less reversible. Therefore, we assign all four peaks of **PV_4Mo_8** as one-electron peaks in reaction acetonitrile. Finally, in the previous study we assigned the first three peaks of **PV_6Mo_6** to one-electron processes while the fourth peak was assigned as a 3-electron process from the RDE data. Figure 3.2f shows that this fourth peak of **PV_6Mo_6** in reaction acetonitrile is also a PCET process.

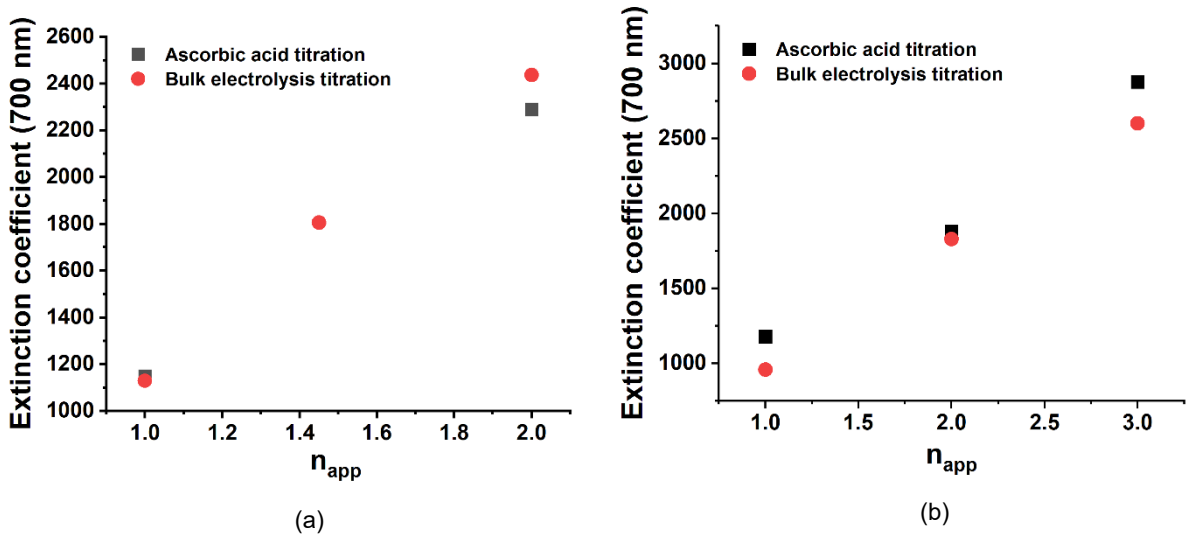

Figure 3.9. Calibrations by ascorbic acid and bulk electrolysis titration: the extinction coefficient at 700 nm versus number of electrons transferred, n_{app}. (a) **PV_2Mo_{10}**; (b) **PV_3Mo_9**.

Since a trace amount of water has large effect on electrochemical behavior of the reduced POMs, and RSH oxidation generates water during the reaction itself, the role of added water and its role on the electrochemistry must be addressed. In these studies, water concentration ranges from 25-50 mM, therefore, less than 25 mM water at a maximum is generated by the end of the reaction. Here we use **$PVMo_{11}$** to probe and discuss the water concentration effect. Figure 3.10a shows that when up to 30 mM H_2O is added to the reaction acetonitrile, the CV peaks positive of

-1.5 V do not change and the peaks negative of -1.5 V shift only slightly positive relative to those in the CVs run in the reaction acetonitrile without addition of any water. As a result, the effect of water concentration can be neglected under the conditions in this work. Figure 3.10b shows that by adding more H_2O (up to 300 mM), the first vanadium peak barely changes, however, the second peak becomes less reversible. The peaks more negative than -1.5 V shift to more positive potentials as H_2O concentration increases; moreover, a third multi-electron peak at *ca.* -1.9 V appears. Finally, many studies show that in acetonitrile the addition of an excess of a strong acid, such as trifluoromethanesulfonic acid, POMs undergo reduction by two-electron transfer PCET processes and all the peaks shift to more positive potentials.[65,68,76,77] In this work, an excess of RSH (2-mercaptoethanol) was used to probe the oxidation reaction. Since the pK_a of 2-mercaptoethonal is 9.6 in water and the H^+ dissociation is significantly less favorable in acetonitrile,[78] RSH cannot perform as an acid to facilitate PCET processes under the conditions in this work.

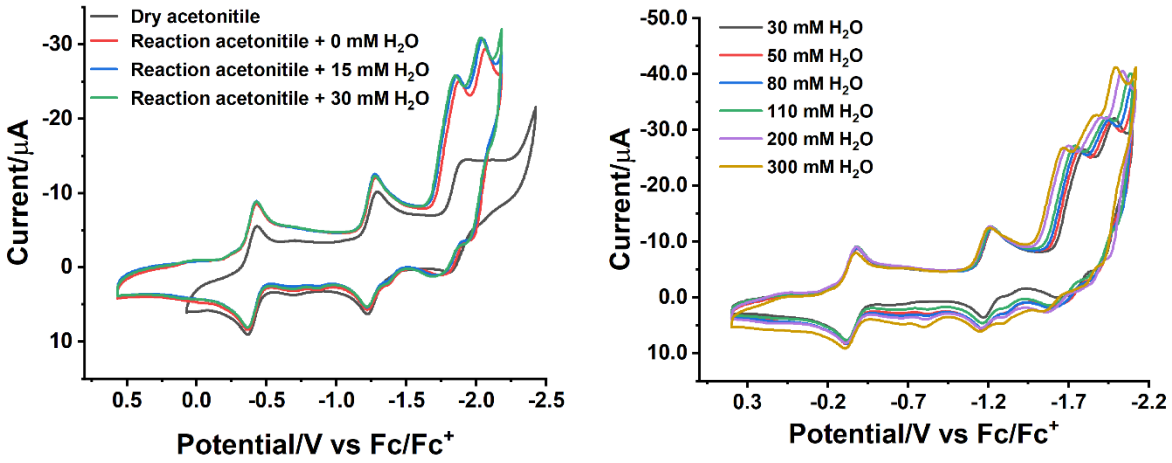

(a) (b)

Figure 3.10. CVs of **$PVMo_{11}$** in different concentrations of water. (a) CVs in dry acetonitrile, reaction acetonitrile and reaction acetonitrile with small amount of water that the RSH oxidation reaction generates. (b) CVs with larger quantities of added water.

Since all the reactions in this work are run in the reaction acetonitrile, we focus on the electrochemical properties of **PVMo** under these conditions, and do not consider the impact of

higher H_2O and acid concentrations. We summarize the **PVMo** peak assignments in reaction acetonitrile in Table 3.5. We should note that, for **PVMo** (x > 1), the peaks more negative than -1500 mV are quasi-reversible, therefore, the number of electrons (n) and corresponding redox atoms are estimated from electrochemical and titration spectra information.

Table 3.5. **PVMo** Formal potentials ($E_{1/2}$) and number of electrons transferred on corresponding process (n) calculated from cyclic voltammetry in acetonitrile

	First peak		Second peak		Third peak		Fourth peak	
	$E_{1/2}$/ mV	n	$E_{1/2}$/ mV	n	$E_{1/2}$/ mV	n	$E_{1/2}$/ mV	n
PMo_{12}	-236	1 (Mo)	-654	1 (Mo)	-1372	1 (Mo)	-1924	2 (Mo)
$PVMo_{11}$	-405	1 (V)	-1260	1 (Mo)	-1828	2 (Mo)	-2025	2 (Mo)
PV_2Mo_{10}	-367	1 (V)	-916	0.4 (V)	-1302	0.6 (V)	-1854	2 (Mo)
PV_3Mo_9[a]	-318	1 (V)	-847	1 (V)	-1306	1 (V)	-1805	1 (Mo)
PV_4Mo_8[a]	-229	1 (V)	-815	1 (V)	-1300	1 (V)	-1801	1 (V)
PV_6Mo_6[b]	-202	1 (V)	-721	1 (V)	-1285	1 (V)	-1810	3 (V)

[a] $E_{1/2}$ measured by square pulse wave voltammetry (SWV) because the quasi-reversibility of the third and fourth peak hinders the calculation $E_{1/2}$ from CV (see Figure 3.11). [b] $E_{1/2}$ measured by rotating disk electrode (RDE) voltammetry from previous work.

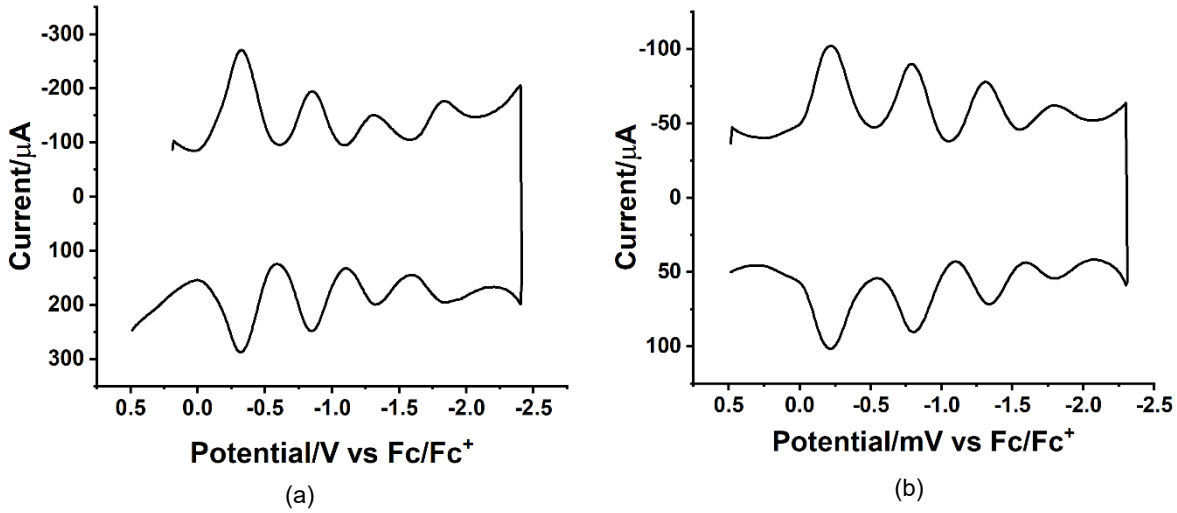

Figure 3.11. Square pulse wave voltammetry (SWV) of (a) **PV_3Mo_9** and (b) **PV_4Mo_8**. Conditions: POM (0.42 mM), *n*-Bu_4NPF_6 (250 mM), amplitude 100 mV, period 10 ms, increment 10 mV and sampling width 1 ms.

Effect of vanadium centers, x, on the charge of PVMo in solution. It has been reported that, the first and second formal potential, $E_{1/2}$, denoted as E_1^0 and E_2^0 respectively, for Keggin POMs with different heteroatoms, depends linearly on the POM charge with a slope of 430-530 mV per unit charge in aprotic solvents.[76,79,80] In our case, the overall charge of POM depends on the number of vanadium atoms and on their reduction state. The difference in potential between the first and second vanadium redox couples for each POM is around 500 mV, which is in the same range as that for Keggin POMs with different heteroatoms (Figure 3.12). This indicates that the charge of POM increases by one unit upon one-electron reduction. On the contrary, the E_1^0 and E_2^0 values for all **PVMo** become more negative with the number of vanadium atoms, with a slope only 46 mV per number of vanadium, x (Figure 3.12a). This is consistent with the interpretation that the initial charge of all studied POMs is the same but increases by one unit after accepting one electron. The number of TBA cations in all **PVMo** was confirmed by TGA in previous work:[48] all **PVMo** have four TBA counterions but have different numbers of protons associated with the polyanion: $[PVMo_{11}]^{4-}$; $[HPV_2Mo_{10}]^{4-}$; $[H_2PV_3Mo_9]^{4-}$; $[H_3PV_4Mo_8]^{4-}$ and $[H_5PV_6Mo_6]^{4-}$. The electrochemistry data indicated that none of the POM protons dissociate in acetonitrile, thus a series of **PVMo** has the same number of negative charges overall.

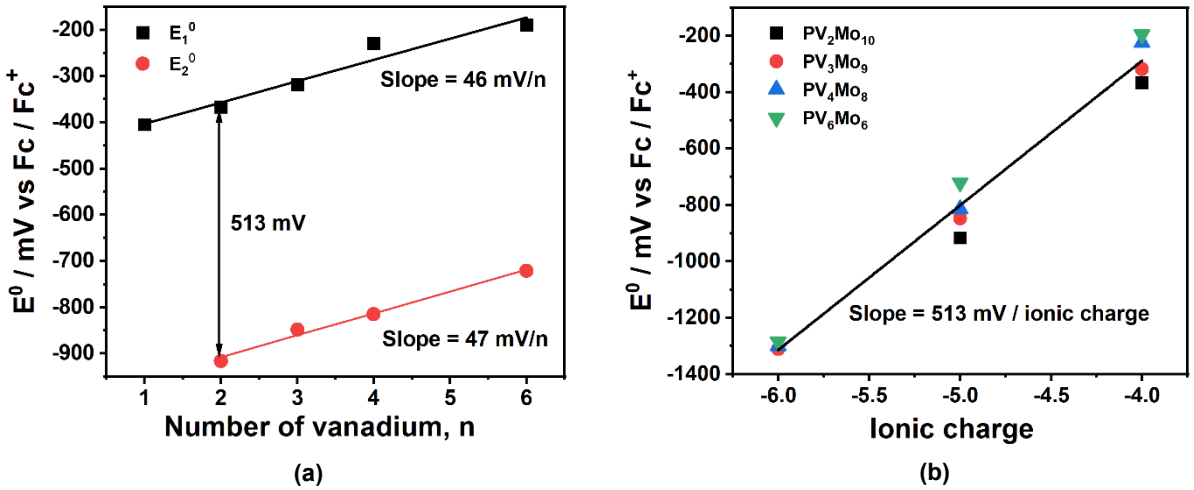

Figure 3.12. (a) First and second formal potentials (E_1^0 and E_2^0) of **PVMo** versus the number of vanadium atoms on them. (b) Formal potentials of V redox peaks (E^0) versus the ionic charges on POM.

This is further proved by the CVs as a function of POM concentration. Figure 3.13 shows the CVs of 0.5-2.0 mM solutions of **PV_6Mo_6** ($[H_5PV_6Mo_6]^{4-}$). If the **PV_6Mo_6** dissociates protons in acetonitrile, then intramolecular proton transfer from POM to the reduced POM ions could happen,[81] thus changing the POM concentration would change the acidity of the acetonitrile solution and therefore the voltametric behavior of the POMs dissolved therein. However, the potential of all the peaks remains constant for all the concentrations consistent with the series of **PVMo** *not dissociating protons in acetonitrile*.

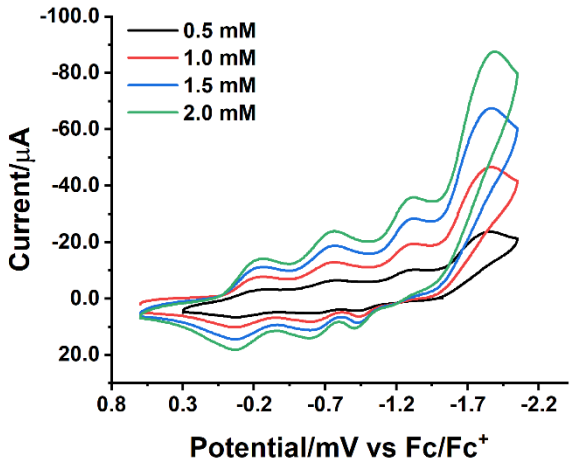

Figure 3.13. The effect of analyte (**PV_6Mo_6**) concentration on the CV behavior.

By plotting the E_1^0, E_2^0 and E_3^0 (the formal potential of the third vanadium-based voltametric peak) versus ionic charge, i, a line with slope of 513 mV / i results, which agrees very well with other studies (Figure 3.12b).[76,79,80] Finally, the 46 mV / x potential shift from x = 1 to 6 can be explained by the bond valence[82–84] difference of different **PVMo**. Eda and Osakai et al.[83,84] correlated the bond valence of Keggin polyanion ($[XW_{12}O_{40}]^{n-}$), with the bond length of μ_4-O−W. We had previously correlated μ_4-O−W and other bond lengths with Keggin polyanion isomer energies.[85] Due to the large electronegativity of oxygen, the shorter the μ_4-O−W bond the greater the electron depopulation on the W atoms, inducing a commensurate increase in the bond length and positive shifts in E_1^0 potential. The properties of **PVMo** in this study depend on the length of the μ_4-O−V (d), and since the **PVMo** have different number of isomers, where d represents an average of these bond lengths. The **PVMo** potential shift to more positive values from x = 1 to 6, which corresponds to the decrease in the average value of d from x = 1 to 6.

3.3.3 Reduction State Measurement and Buffer Range Determination

The apparent reduction state, n_{app}, was defined as the average number of electrons in the reduced POM and was monitored by UV-Vis. POMs can be stoichiometrically reduced by ascorbic acid or $SnCl_2$ and oxidized back by Ce(IV). After adding the desired equivalents of the reducing (or oxidizing) agent, the UV-Vis were recorded and analyzed. The absorbances at 550 and 700 nm appeared to be linearly increasing with a number of reducing equivalents added to the system. This approach has been used for **PV_6Mo_6** in our previous study.[48] The V^{IV}-to-Mo^{VI} intervalence charge transfer (IVCT) band at 550 nm[71,86] was used to calibrate the extinction coefficient versus the number of electrons in the reduced states of **PV_4Mo_8** (Figure 3.14). We found that ascorbic acid has limited electron transfer ability in acetonitrile: it can only reduce the vanadium atoms but not the molybdenum atoms in **PVMo**. Therefore, $SnCl_2$ was used as a reducing agent to reach higher reduction states of **PVMo**.

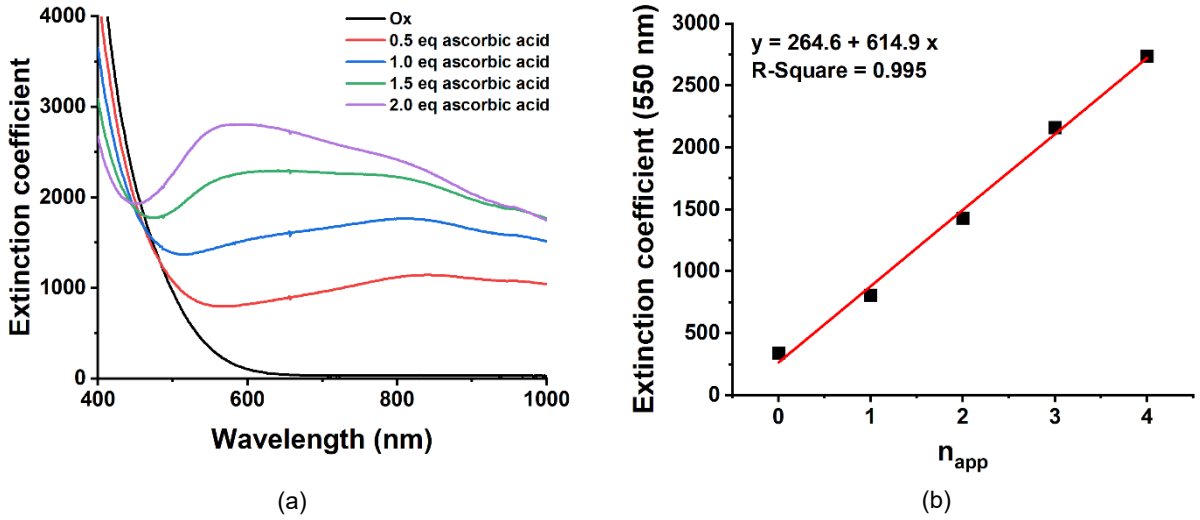

(a) (b)

Figure 3.14. (a) Ascorbic acid titration of **PV_4Mo_8** followed by UV-Vis spectra. For each data point, 0.5 equivalent of ascorbic acid, a two-electron reductant under these conditions, is added. (b) Calibration curve: extinction coefficient at 550 nm versus the number of electrons transferred by ascorbic acid, n_{app}.

Ce(IV) was used subsequently to reoxidize the reduced POMs to confirm the calibration at 700 nm which results primarily from the Mo^{VI}-to-Mo^{V} IVCT band.[87] The spectra for initial reduction

and subsequent reoxidation of **PVMo**, x≤3 and the corresponding calibration curves are shown in Figures 3.15a-f. For a typical titration, POM (0.1 mM) was reduced by 2.5 equivalents of $SnCl_2$ by direct addition of solid $SnCl_2$, followed by oxidative titration via addition of 1 equivalent Ce(IV). Each UV-Vis spectrum was recorded when the reduced POM was fully reoxidized back to its initial state (Ox). The Ce(IV) stock solution was prepared by dissolving ammonium cerium (IV) nitrate (Ce(IV)) in 0.1 M aqueous $HClO_4$ and using 50 µL stock solution per equivalent of reduced **PVMo**.

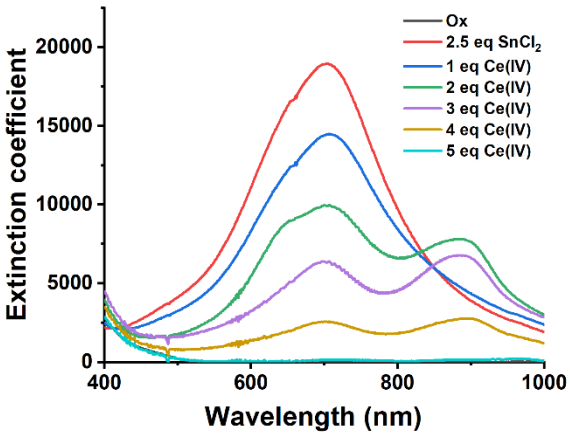

(a)

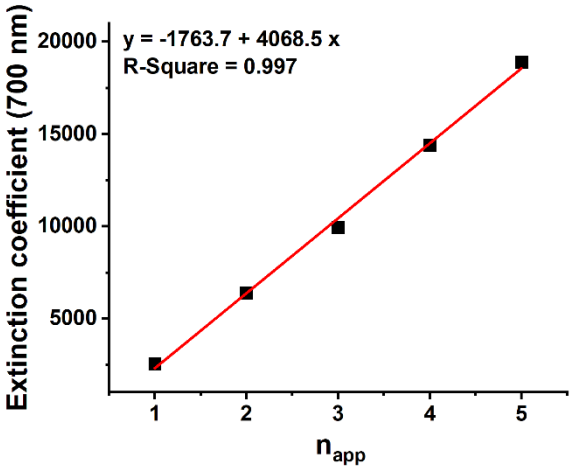

(b)

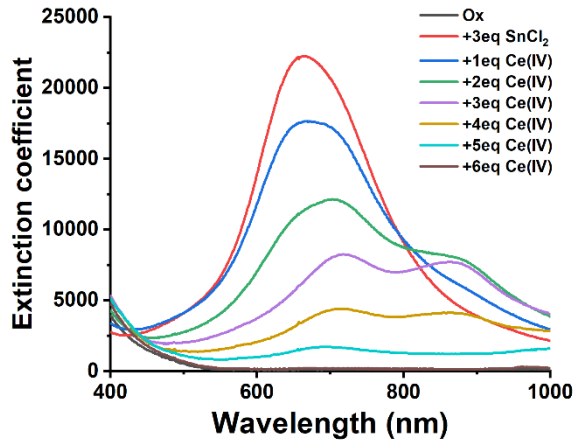

(c)

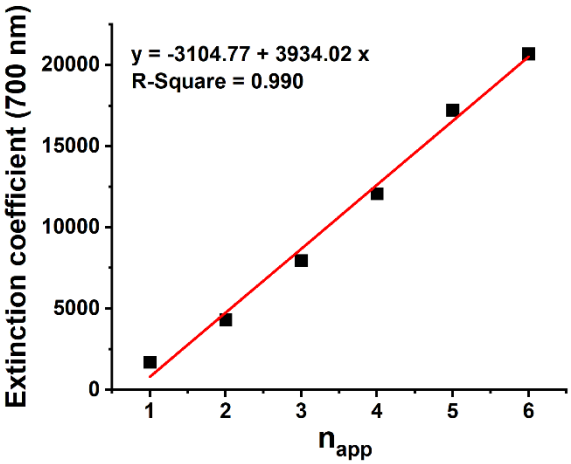

(d)

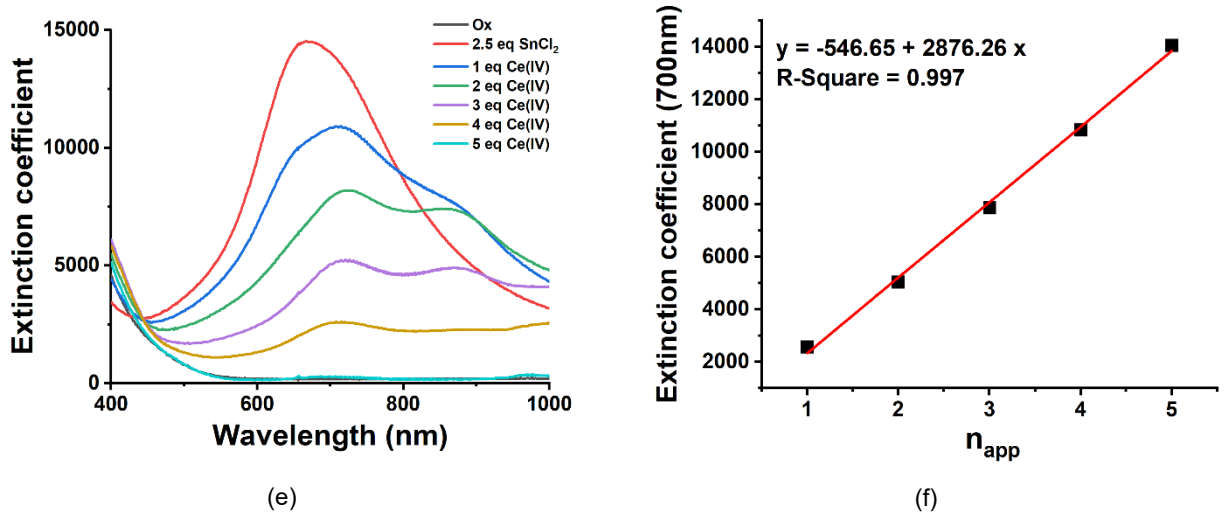

(e) (f)

Figure 3.15. Reductive ($SnCl_2$) and subsequent oxidative Ce(IV) titrations of **PVMo**, and corresponding linear calibration curve of extinction coefficient versus number of electrons transferred to the polyanion, n_{app}, evaluated at 700 nm. (a, b) **$PVMo_{11}$**; (c, d) **PV_2Mo_{10}**; (e, f) **PV_3Mo_9**.

A new peak around 850 nm appears after adding Ce(IV) to the $SnCl_2$-reduced POM solution. Figure 3.16a, b shows the titration spectra using **PV_3Mo_9** as an example. The new peak around 850 nm very likely reflects the interaction between Ce(III) cation and the reduced POM. This was confirmed by the addition of Ce(III) salt to the reduced **PV_3Mo_9** solution (Figure 3.16c).[87] However, the peak at 850 nm does not have a significant effect on the extinction coefficient at 700 nm (Figure 3.16d), thus, the calibration curve for Ce(IV) oxidative titration is also reliable.

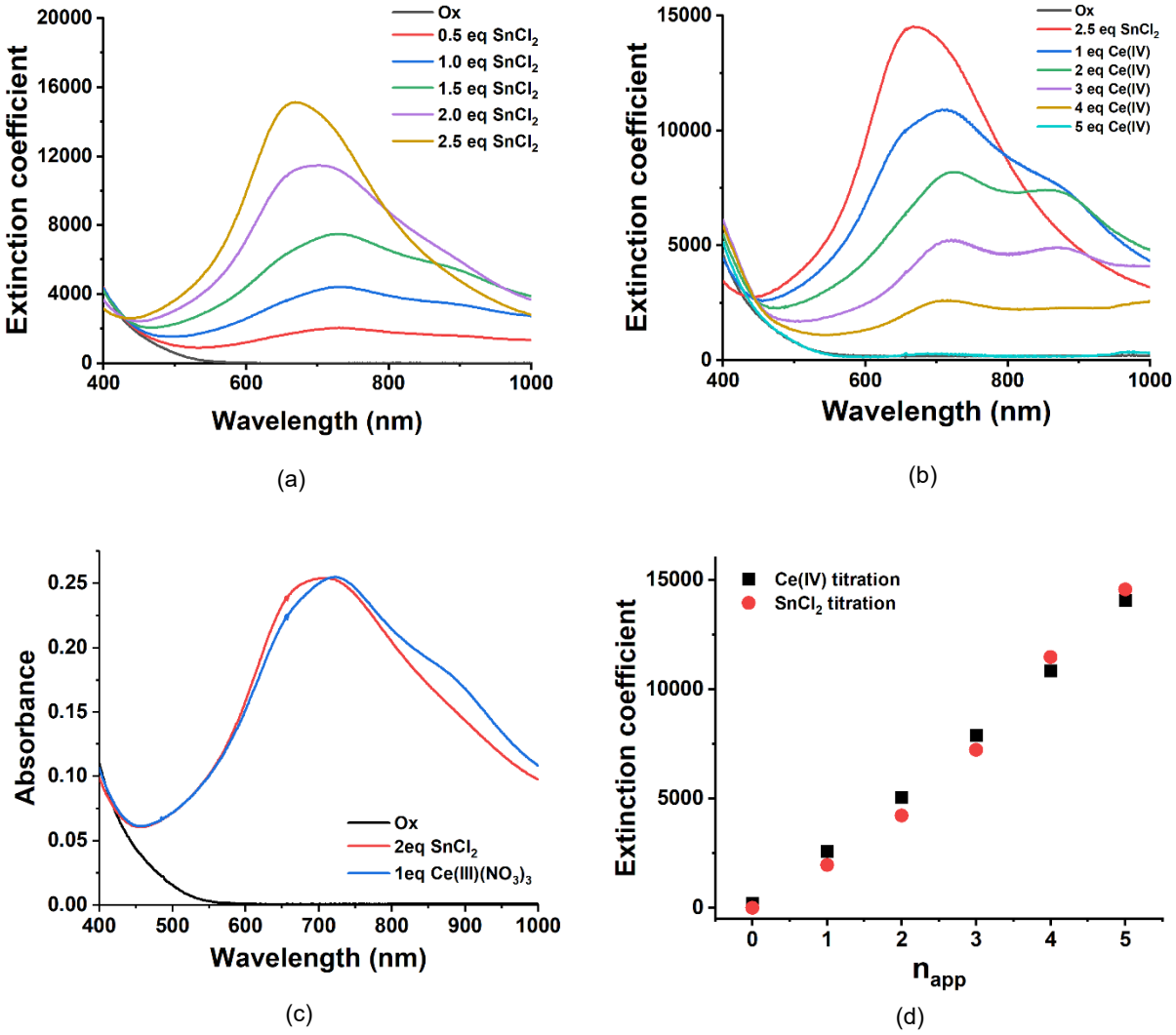

Figure 3.16. (a) **PV_3Mo_9** reductive titration by $SnCl_2$. (b) Five-electron-reduced **PV_3Mo_9** from addition of 2.5 equivalent of $SnCl_2$ then oxidative titration by Ce(IV). (c) Comparison of spectra before and after adding $Ce(III)(NO_3)_3$ to four-electron-reduced **PV_3Mo_9**. (d) Calibration curves at 700 nm for $SnCl_2$ reductive titration followed by Ce(IV) oxidative titration of **PV_3Mo_9**.

The curves of solution potential, E, as a function of reduction state, n_{app}, define the redox buffering of this system: the number of steps, the number of electrons transferred per step and the potential range of each step.[49,50] The curves can be calculated according to the electrochemical information that given above. Figure 3.17a shows the results for **PV_4Mo_8** and **PV_6Mo_6**, and the

PVMo, x≤3, are shown in Figure 3.17b-d. n_{app} under turnover conditions were measured experimentally, thus the solution potential under those reaction conditions can be estimated by fitting the experimental results to the redox buffering curves. For example, under reaction conditions in Figure 3.1, the n_{app} of both **PV_4Mo_8** and **PV_6Mo_6** were measured and shown as icons in Figure 3.18a. There is no measured reduction states for **PVMo**, x≤3 because they cannot maintain a steady reduction state (see below).

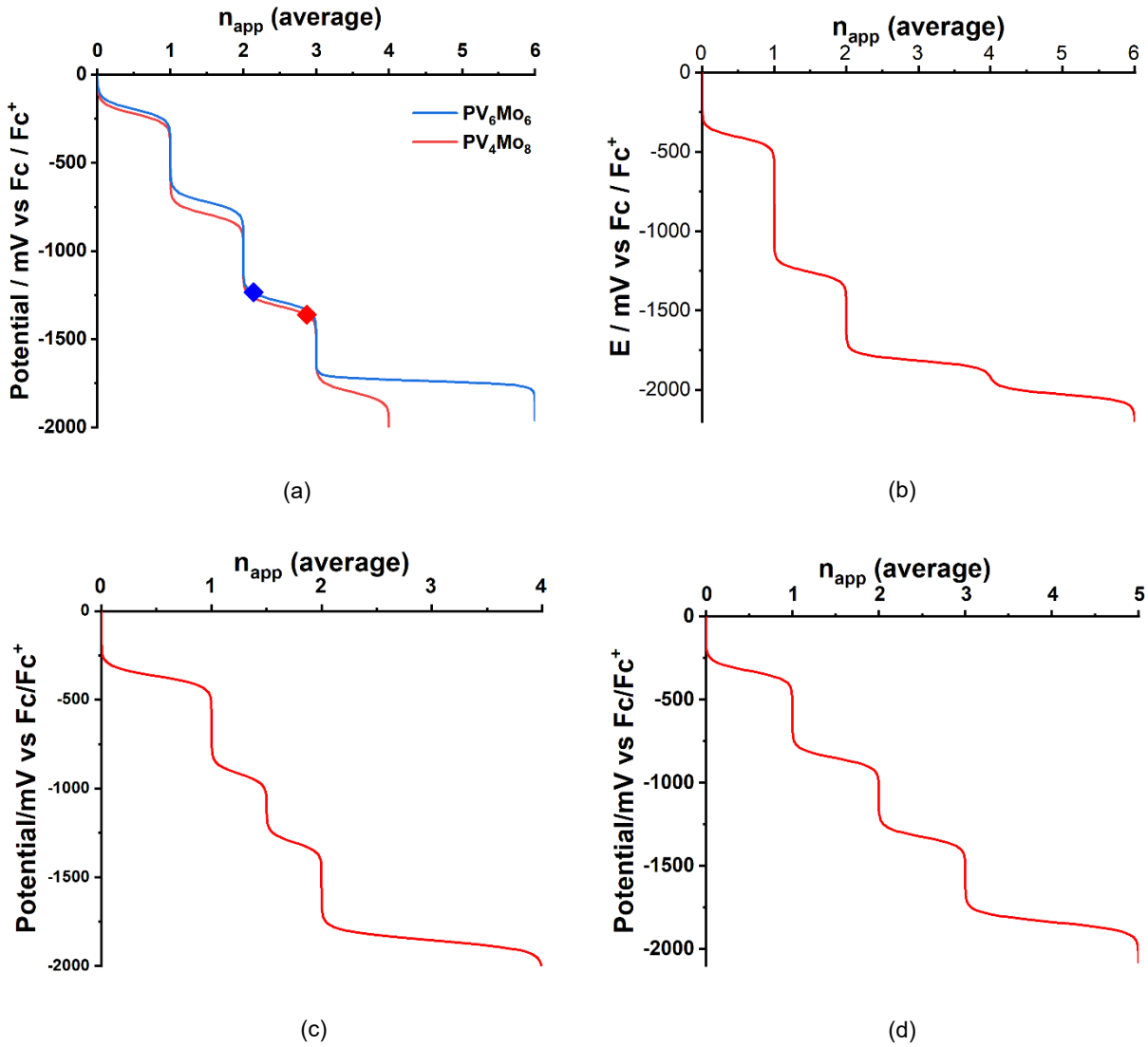

Figure 3.17. The theoretical values of chemical solution potentials as function of the average number of electrons transferred to (a) **PVMo** (x = 4, 6). The diamond icons are experimental data indicating the steady reaction states. (b) **$PVMo_{11}$**; (c) **PV_2Mo_{10}**; (d) **PV_3Mo_9**.

The reduction states of all **PVMo** depend on the concentrations of RSH, Cu(II) and POM, which correspond to the change of solution chemical potential. Figure 3.18a shows that under the turnover condition in Figure 3.1, the maximum n_{app} decreases as the number of V, x, on **PVMo** increases, however unlike **PV_4Mo_8** and **PV_6Mo_6**, when x≤3, **PVMo** cannot maintain a steady reduction state during the course of reaction. Figure 3.18b shows the exemplary comparison between **PV_6Mo_6** and **PV_3Mo_9**. **PV_6Mo_6** keeps steady n_{app} around 2 to the end of conversion**,** however **PV_3Mo_9** are quickly reduced to maximum reduction state around 3.5 and gradually drop back to low reduction state around 1.

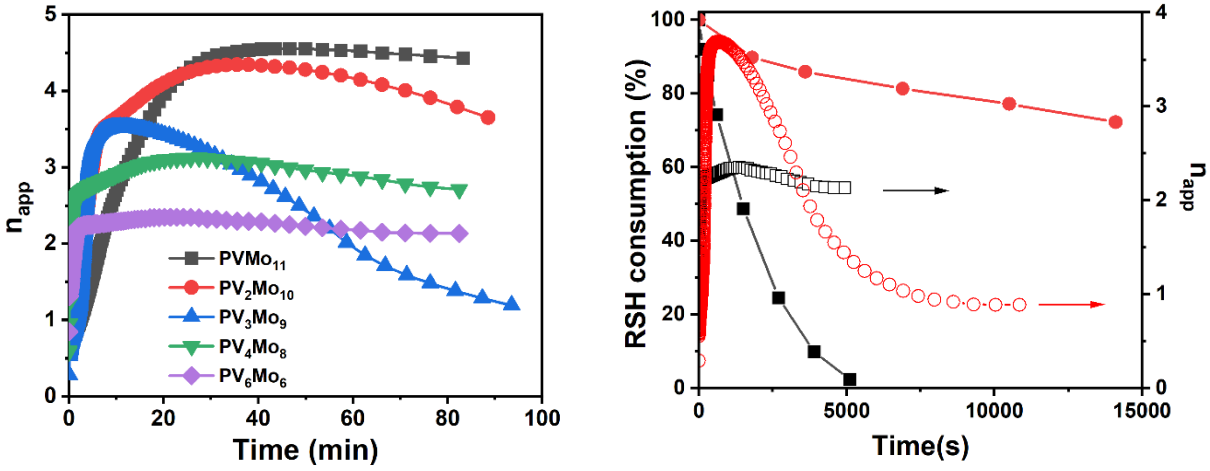

Figure 3.18. (a) n_{app} comparison of **PVMo**, 30 mM RSH and 0.1 mM POM and 0.8 mM Cu(II). (b) RSH consumption (solid-symbol curves) and apparent reduction states, n_{app} (open circle-symbol curves) under turnover conditions: POM: 0.1 mM, Cu(II): 0.8 mM and RSH: 30 mM. **PVMo** x = 3, red; x = 6, black.

Figure 3.19 shows the n_{app} of all **PVMo** changes according to Cu(II) concentration. **PV_4Mo_8** and **PV_6Mo_6** can maintain n_{app} from 1 to 6 (maximum n_{app} 4 and 6, for **PV_4Mo_8** and **PV_6Mo_6** respectively), while **PVMo**, x≤3 are reduced to high reduction states then drop back to ca. 1 electron. An important feature of **PVMo**, x≤3, is that not only V atoms, but also Mo atoms are reduced in reactions where **PVMo** cannot maintain steady reduction states. The drop in n_{app} corresponds to the reoxidation of Mo and finally keeps a steady state value of n_{app} of 1-2 which

corresponds to reduced V centers only. Therefore, a key conclusion is that all vanadium centers are reduced before Mo centers, and only V but not Mo can maintain a steady reduction state.

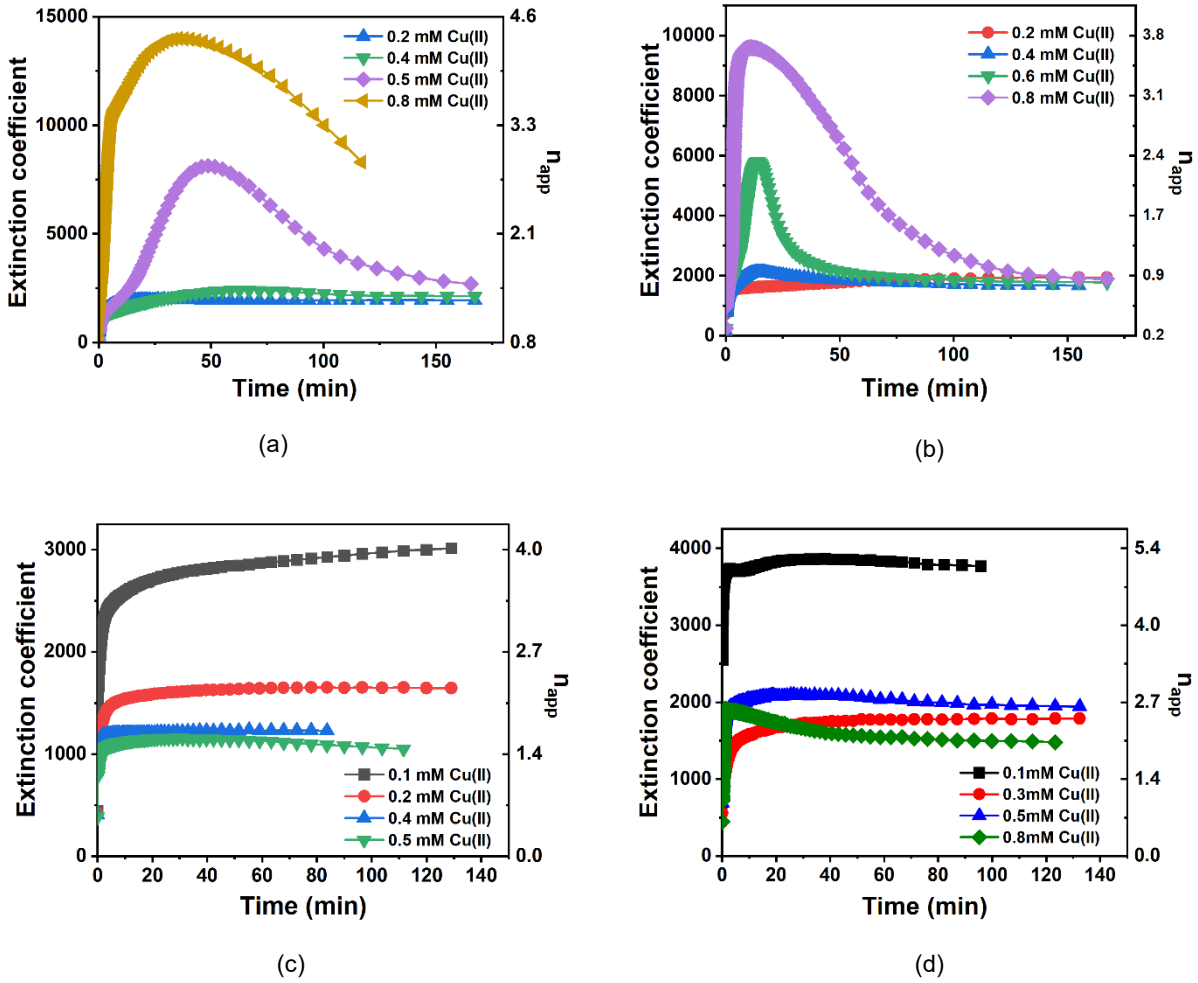

Figure 3.19. n_{app} of **PVMo** as function of Cu(II) concentration with 30 mM RSH and 0.1 mM POM. (a) **PV_2Mo_{10}**; (b) **PV_3Mo_9**;(c) **PV_4Mo_8**; (d) **PV_6Mo_6**.

3.3.4 Difference of Electron Transfer Rates Between V and Mo to Substrates

The overall mechanism of eq 3.1 was proposed in previous work.[48] The key step of POM as redox buffering catalyst is the fast and reversible electron transfer reaction in eq 3.2, where n is number of electrons in the reduced POM.

$$Cu(II)(RS^-)_2 + POM(n) \rightleftarrows Cu(I)(RS\bullet)_2 + POM(n+1),\ n = 0\text{-}5 \qquad (3.2)$$

The observation that the V but not Mo atoms can keep the steady reduction state may be due to the electron transfer rate difference between vanadium versus molybdenum to the reactant in eq 3.2, $Cu(II)(RS^-)_2$. Therefore, we focused on the reduction of POM by RSH catalyzed by Cu(II) under Ar. Figure 3.20 shows the reductions of 0.5 mM **PMo_{12}**, **$PVMo_{11}$** and **PV_2Mo_{10}** by 50 mM RSH catalyzed by 0.1 mM Cu(II) under Ar. **PV_2Mo_{10}** accepts 2 electrons within 30s and **$PVMo_{11}$** accepts 1 electron in less than 45s, while **PMo_{12}** accepts negligible electrons under these conditions. The calculated initial rates ($-d[n_0]/dt$, where n_0 is initial number of electrons in the reduced POM) are 0.184, 0.036 and 0.0013 s^{-1} for **PV_2Mo_{10}**, **$PVMo_{11}$** and **PMo_{12}** respectively.

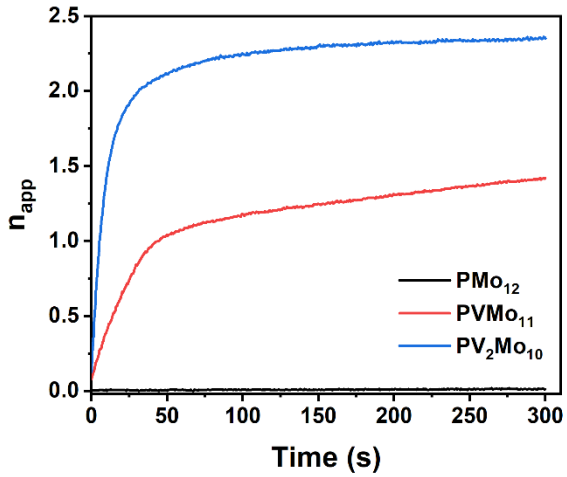

Figure 3.20. Kinetics of 0.5 mM **PMo_{12}**, **$PVMo_{11}$** and **PV_2Mo_{10}** reduction by 50 mM RSH under Ar catalyzed by 10 μM Cu(II) in acetonitrile.

Unlike **PVMo** reduction by RSH that is catalyzed by micromolar levels of Cu(II), **PMo_{12}** is only slightly reduced by RSH even at high concentrations of Cu(II) (Figure 3.21). The first CV peak of **PMo_{12}** is more positive ($E_{1/2}$ = -236 mV) than that of **$PVMo_{11}$** ($E_{1/2}$ = -405 mV; Figure 3.2). This suggests that the reduction rate of **$PVMo_{11}$** and **PMo_{12}** is dominated by kinetic factors. The electron transfer rate between substrate, $Cu(II)(RS^-)_2$, and vanadium is much faster than between the $Cu(II)(RS^-)_2$ and molybdenum in the same Keggin POM in acetonitrile. This point is further

strengthened by the fact that ascorbic acid as another substrate cannot further reduce Mo atoms in **PVMo** as presented above.

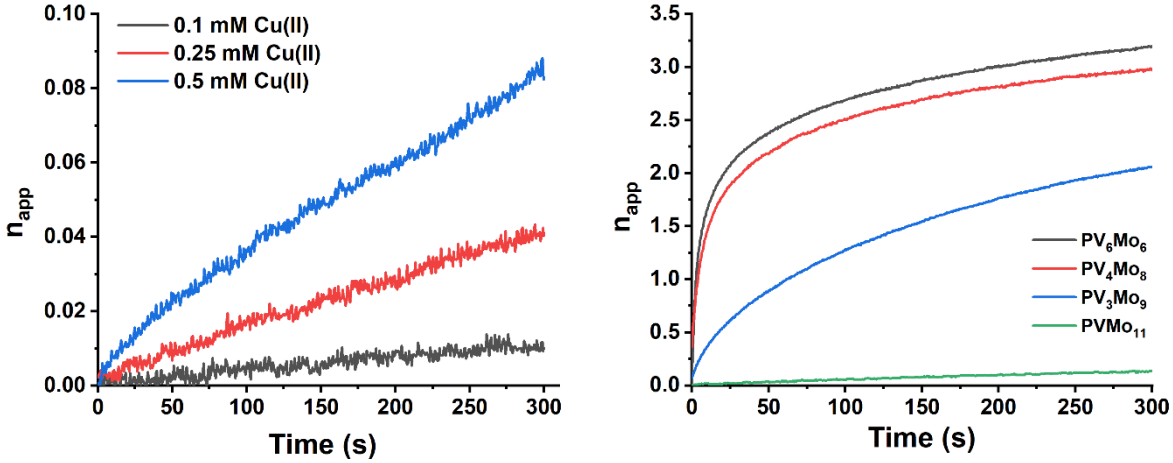

Figure 3.21. (a) Kinetics of 0.5 mM **PMo_{12}** reduction by 50 mM RSH: dependence on Cu(II) concentration under Ar. (b) Kinetics of 0.5 mM **PVMo** reduction by 25 mM RSH catalyzed by 2µM Cu(II) under Ar.

Control reactions for RSH reduction of $Na_4PVMo_{11}O_{40}$, $[PVMo_{11}]^{4-}$ and $Na_5PV_2Mo_{10}O_{40}$, $[PV_2Mo_{10}]^{5-}$ catalyzed by Cu(II) in pH=2 phosphate buffer were conducted. Figure 3.22 shows the Cu(II) concentration dependence of $[PVMo_{11}]^{4-}$ and $[PV_2Mo_{10}]^{5-}$ reductions. Interestingly, they show two-step kinetic curves with turning points at one- and two-electron reduction for $[PVMo_{11}]^{4-}$ and $[PV_2Mo_{10}]^{5-}$, respectively. Bulk electrolysis at fixed potential and the corresponding UV-Vis spectra (Figure 3.23, Table 3.6-3.7) enabled correlation of the extinction coefficient (ε) at 650nm for V^{V}-V^{IV} intervalence charge transfer (IVCT) band in aqueous media[80] with the apparent reduction state of POM, n_{app}. Figure 3.22 shows that the POM reduction rate increases with increasing Cu(II) concentration; however, the point of change was fixed at one and two electrons for $[PVMo_{11}]^{4-}$ and $[PV_2Mo_{10}]^{5-}$ respectively independent of Cu(II) concentration.

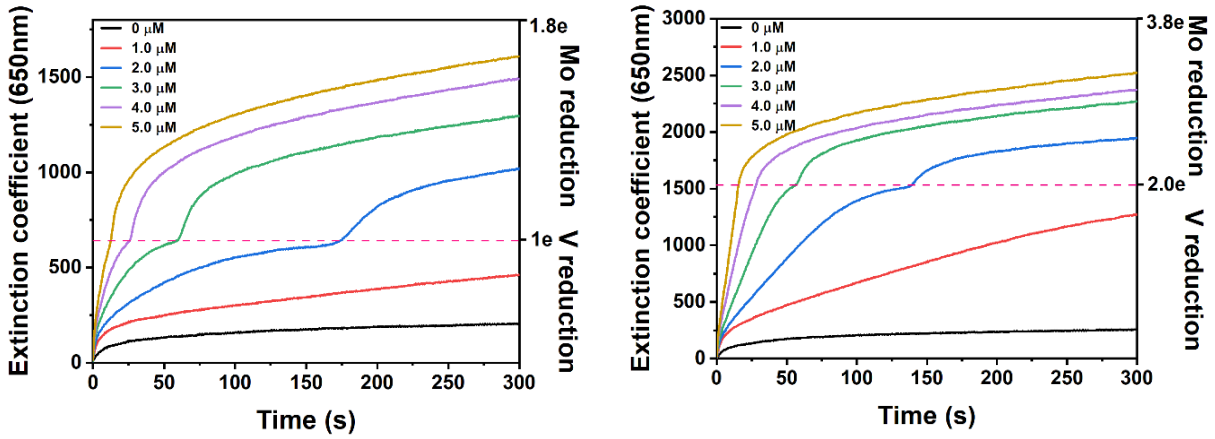

(a) (b)

Figure 3.22. Kinetics of 0.1 mM (a) $[PVMo_{11}]^{4-}$; (b) $[PV_2Mo_{10}]^{5-}$ reduction by 50 mM RSH under Ar catalyzed by Cu(II) in water at pH = 2 phosphate buffer.

The reduction kinetics change with POM and RSH concentration, but the turning point position does not depend on the concentration of either (Figure 3.24). This two-step kinetics suggests two important points: 1. The electrons in reduced POMs are highly localized on V atoms (one and two for $[PVMo_{11}]^{4-}$ and $[PV_2Mo_{10}]^{5-}$), which agrees with the previous computational results.[73,80] 2. The reduction of Mo atoms happens following the depletion of the oxidized V atoms, and the presence of the turning point indicates the electron transfer rate difference between V and Mo centers and the $Cu(II)(RSH)_2$ substrate is large.

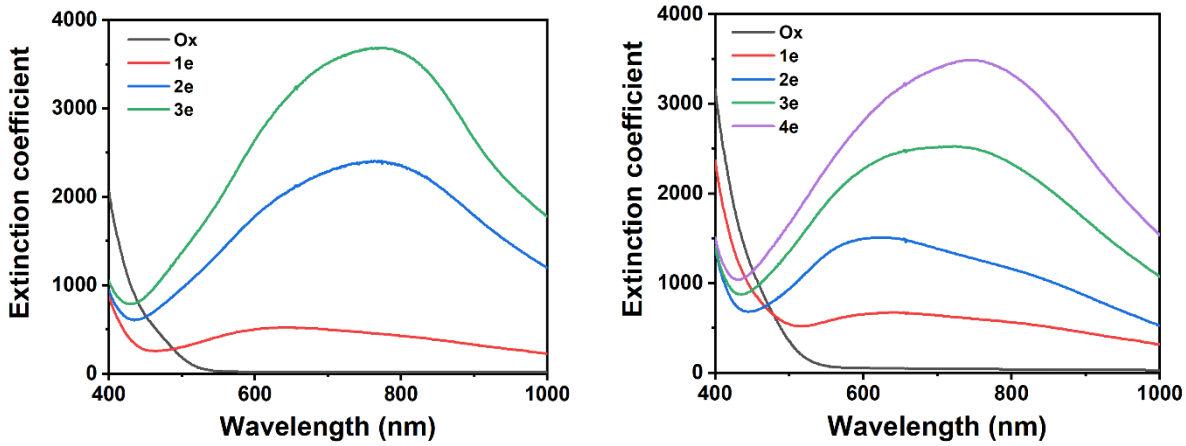

Figure 3.23. UV-Vis spectra for bulk electrolysis titration of (a) $[PVMo_{11}]^{4-}$; (b) $[PV_2Mo_{10}]^{5-}$ in pH = 2 phosphate buffer. The bulk electrolysis results show in Table 3.6 and 3.7.

Table 3.6: The results of bulk electrolysis of $[PVMo_{11}]^{4-}$ at constant potential in pH = 2 phosphate buffer.[a]

Potential/mV vs Ag/AgCl	Number of Coulombs	Number of electrons	Ending current ratio/%
450	2.9	1.0	5
150	2.95	1.0	10
-50	3.05	1.0	10

[a] Conditions: $[PVMo_{11}]^{4-}$ (1 mM), KNO_3 (100 mM), pH = 2 phosphate buffer (30 mL), at room temperature under argon.

Table 3.7: The results of bulk electrolysis of $[PV_2Mo_{10}]^{5-}$ at constant potential in pH = 2 phosphate buffer.[a]

Potential/mV vs Ag/AgCl	Number of Coulombs	Number of electrons	Ending current ratio/%
350	2.88	1.0	5
50	2.93	1.0	10
-50	2.98	1.0	10
-150	3.01	1.0	12

[a] Conditions: $[PV_2Mo_{10}]^{5-}$ (1 mM), KNO_3 (100 mM), pH = 2 phosphate buffer (30 mL), at room temperature under argon.

Figure 3.25c shows the $[PMo_{12}]^{3-}$ has a very slow reduction rate in this reaction even in the presence of high concentrations of Cu(II) catalyst. We note here that previous work proved the TBA salt of polyvanadotungstate (**PVW**) does not exhibit redox buffering in this reaction system. In this work, Figure 3.25a,b shows that $[PVW_{11}]^{4-}$ in aqueous buffer does not have two kinetics steps and only one V atom is reduced independent of concentrations. Therefore, redox buffering is a special property for **PVMo** and not shown by **PVW** in either acetonitrile or aqueous media.

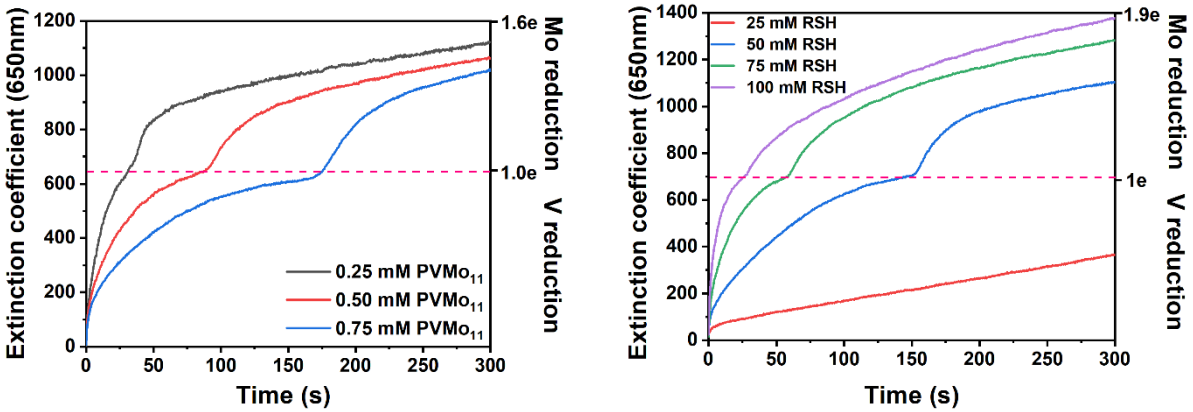

Figure 3.24. (a) Kinetics of $[PVMo_{11}]^{4-}$ reduction by 50 mM RSH under Ar catalyzed by 2μM Cu(II) depend on POM concentration in pH = 2 phosphate buffer. (b) Kinetics of 0.1 mM $[PVMo_{11}]^{4-}$ reduction by RSH under Ar catalyzed by 2μM Cu(II) concentration in pH = 2 phosphate buffer.

The data in acetonitrile and aqueous buffer collectively prove that there is an electron transfer rate difference between V and Mo atoms in Keggin vanadopolymolybdates, $PV_xMo_{12-x}O_{40}^{(3+x)-}$. Since the electron transfer rate from Mo to substrate is slow, it cannot meet the requirement of a fast and reversible electron transfer reaction that enables the redox buffering phenomenon. As a result, in acetonitrile, when Mo is reduced in **PVMo**, $x \leq 3$, a constant reduction state cannot be maintained. In summary, only the V atoms in **PVMo** facilitate redox buffering, thus the more V atoms that are present in **PVMo**, the wider the potential range in which redox buffering is possible.

The multistep and multielectron redox buffering potential ranges facilitate the catalytic activity by compensating the solution electrochemical potential shift due to the consumption of substrate.

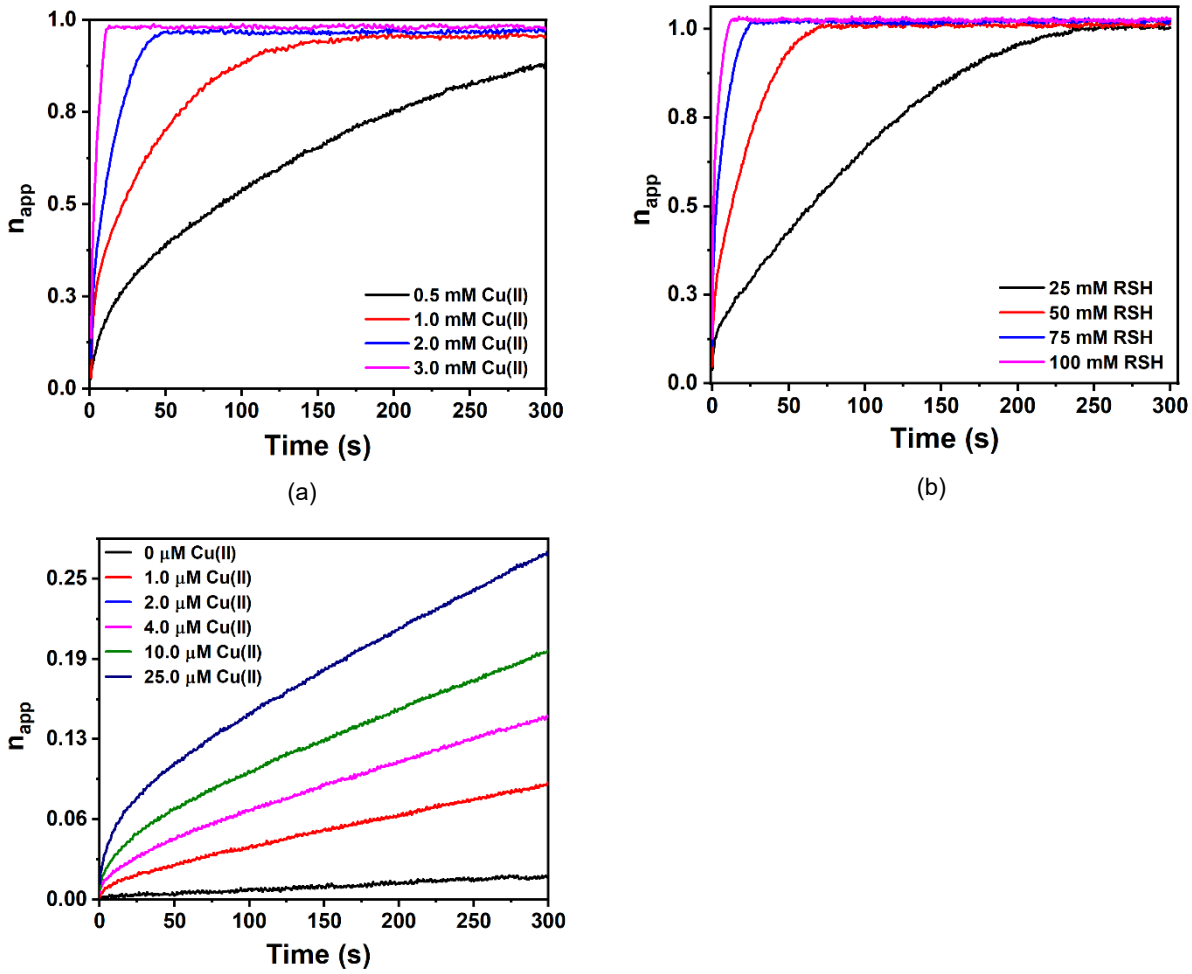

Figure 3.25. Kinetics of $[PVW_{11}]^{4-}$ reduction by RSH catalyzed by Cu(II) under Ar in pH = 2 phosphate buffer. (a) Cu(II) concentration dependence with 0.1 mM POM and 50 mM RSH; (b) RSH concentration dependence with 0.1 mM POM and 2 μM Cu(II); (c) Kinetics of 0.1 mM $[PMo_{12}]^{3-}$ reduction by 50 mM RSH under Ar catalyzed by Cu(II) in pH = 2 phosphate buffer.

3.4 Conclusions

(1) The catalytic activity of $PV_xMo_{12-x}O_{40}^{(3+x)-}$ (**PVMo**, x = 0-4 and 6) for aerobic thiol deodorization (2 RSH + ½ O_2 → RSSR + H_2O) increases with increasing number of vanadium

atoms, x in the polyanion. We explain this trend by both redox buffer thermodynamics and electron transfer kinetics between V and Mo. The catalytic rates are much higher when redox buffering is a dominant effect (turnover frequency: 8 and 45 s^{-1} for **PV_3Mo_9** and **PV_4Mo_8** respectively, Table S6).

(2) The cyclic voltammetric peaks of Keggin vanadopolymolybdates, $PV_xMo_{12-x}O_{40}^{(3+x)-}$ (**PVMo**) under the above catalytic conditions reveal that the redox buffering capability derives from the number of steps, the number of electrons transferred each step and the potential ranges of each step.

(3) The reduction of Mo centers is much slower than reduction of V centers in the same Keggin vanadopolymolybdates under these ambient catalytic conditions: acetonitrile, thiol, ambient T, air. As a result, the rapid multielectron redox processes that facilitate redox buffering are effective when molybdenum-based redox processes are not important. In contrast, the redox processes are effective in vanadopolymolybdates that contain 3 or greater vanadium centers.

(4) While many O_2-based organic substrate oxidation processes catalyzed by vanadopolymolybdates, $PV_xMo_{12-x}O_{40}^{(3+x)-}$ (**PVMo**) are well-studied and some commercialized, none of these studies have noted the self-redox-buffering phenomenon. This dynamic redox self-buffering chemistry might lead to faster rates for other POM-catalyzed organic-compound selective oxidation reactions.

3.5 References

1 S. S. Wang and G. Y. Yang, *Chem. Rev.*, 2015, **115**, 4893–4962.

2 I. A. Weinstock, R. E. Schreiber and R. Neumann, *Chem. Rev.*, 2018, **118**, 2680–2717.

3 C. L. Hill, L. Delannoy, D. C. Duncan, I. A. Weinstock, R. F. Renneke, R. S. Reiner, R. H.

Atalla, J. W. Han, D. A. Hillesheim, R. Cao, T. M. Anderson, N. M. Okun, D. G. Musaev and Y. V. Geletii, *Comptes Rendus Chim.*, 2007, **10**, 305–312.

4 C. L. Hill and C. M. Prosser-McCartha, *Coord. Chem. Rev.*, 1995, **143**, 407–455.

5 N. I. Gumerova and A. Rompel, *Nat. Rev. Chem.*, 2018, **2**, 112.

6 M. Aureliano, N. I. Gumerova, G. Sciortino, E. Garribba, A. Rompel and D. C. Crans, *Coord. Chem. Rev.*, 2021, **447**, 214143.

7 A. Bijelic, M. Aureliano and A. Rompel, *Angew. Chemie - Int. Ed.*, 2019, **58**, 2980–2999.

8 M. Aureliano, N. I. Gumerova, G. Sciortino, E. Garribba, C. C. McLauchlan, A. Rompel and D. C. Crans, *Coord. Chem. Rev.*, 2022, **454**, 214344.

9 A. Bijelic, M. Aureliano and A. Rompel, *Chem. Commun.*, 2018, **54**, 1153–1169.

10 J. T. Rhule, C. L. Hill, D. A. Judd and R. F. Schinazi, *Chem. Rev.*, 1998, **98**, 327–357.

11 J. Zhong, J. Pérez-Ramírez and N. Yan, *Green Chem.*, 2021, **23**, 18–36.

12 V. G. Snider and C. L. Hill, *J. Hazard. Mater.*, 2023, **442**, 130015.

13 N. Li, J. Liu, B. X. Dong and Y. Q. Lan, *Angew. Chemie - Int. Ed.*, 2020, **59**, 20779–20793.

14 S. M. Lauinger, Q. Yin, Y. V. Geletii and C. L. Hill, *Polyoxometalate Multielectron Catalysts in Solar Fuel Production*, Elsevier Inc., 1st edn., 2017, vol. 69.

15 Y. Zhang, J. Liu, S. L. Li, Z. M. Su and Y. Q. Lan, *EnergyChem*, 2019, **1**, 100021.

16 H. Lv, Y. V. Geletii, C. Zhao, J. W. Vickers, G. Zhu, Z. Luo, J. Song, T. Lian, D. G. Musaev and C. L. Hill, *Chem. Soc. Rev.*, 2012, **41**, 7572–7589.

17 R. Neumann, *Inorg. Chem.*, 2010, **49**, 3594–3601.

18 I. V. Kozhevnikov, *Chem. Rev.*, 1998, **98**, 171–198.

19 I. V. Kozhevnikov, *J. Mol. Catal. A Chem.*, 1997, **117**, 151–158.

20 M. T. Pope and A. Müller, *Angew. Chemie Int. Ed. English*, 1991, **30**, 34–48.

21 Noritaka Mizuno and Makoto Misono*, *Chem. Rev.*, 1998, **98**, 199–217.

22 Alex M.Khenkin and Craig L.Hill, *J Am Chem Soc*, 1993, **115**, 8178–8186.

23 A. M. Khenkin, L. Weiner, Y. Wang and R. Neumann, *J. Am. Chem. Soc.*, 2001, **123**, 8531–8542.

24 A. M. Khenkin and R. Neumann, *J. Am. Chem. Soc.*, 2008, **130**, 14474–14476.

25 Alexander M. Khenkin and Ronny Neumann*, *Angew. Chemie - Int. Ed.*, 2000, **39**, 4088–4090.

26 A. M. Khenkin and R. Neumann, *J. Am. Chem. Soc.*, 2001, 123, 6437–6438.

27 O. A. Kholdeeva, A. V. Golovin, R. I. Maksimovskaya and I. V. Kozhevnikov, *J. Mol. Catal.*, 1992, **75**, 235–244.

28 R. Neumann and M. Levin, *J. Org. Chem.*, 1991, 56, 5707–5710.

29 T. Yokota, A. Sakakura, M. Tani, S. Sakaguchi and Y. Ishii, *Tetrahedron Lett.*, 2002, **43**, 8887–8891.

30 M. Čihova, M. Hrušovsky, J. Voitko and K. I. Matveev, *React. Kinet. Catal. Lett.*, 1981, **16**, 383–386.

31 G. U. Mennenga, A. I. Rudenkov, K. I. Matveev and I. V. Kozhevnikov, *React. Kinet. Catal. Lett.*, 1976, **5**, 401–406.

32 Y. Obora, Y. Okabe and Y. Ishii, *Org. Biomol. Chem.*, 2010, **8**, 4071–4073.

33 R. Neumann, *Poly oxlometalate Complexes in Organic Oxidation Chemistry*, 1998, vol. 47.

34 Y. V Geletii and A. E. Shilov, *Kinet. Catal.*, 1983, 24, 413–416.

35 I. Bar-Nahum, A. M. Khenkin and R. Neumann, *J. Am. Chem. Soc.*, 2004, **126**, 10236–10237.

36 M. De Bruyn and R. Neumann, *Adv. Synth. Catal.*, 2007, **349**, 1624–1628.

37 M. Zhang, J. Hao, A. Neyman, Y. Wang and I. A. Weinstock, *Inorg. Chem.*, 2017, **56**,

2400–2408.

38 L. S. Ott and R. G. Finke, *Coord. Chem. Rev.*, 2007, **251**, 1075–1100.

39 Y. Wang and I. A. Weinstock, *Chem. Soc. Rev.*, 2012, **41**, 7479–7496.

40 A. Troupis, A. Hiskia and E. Papaconstantinou, *Angew. Chemie - Int. Ed.*, 2002, **41**, 1911–1914.

41 G. Maayan and R. Neumann, *Chem. Commun.*, 2005, 4595–4597.

42 Y. V. Geletii, C. L. Hill, R. H. Atalla and I. A. Weinstock, *J. Am. Chem. Soc.*, 2006, **128**, 17033–17042.

43 M. Kim, I. A. Weinstock, Y. V. Geletii and C. L. Hill, *ACS Catal.*, 2015, **5**, 7048–7054.

44 M. Kim, M. Chamack, Y. V. Geletii and C. L. Hill, *Inorg. Chem.*, 2018, **57**, 311–318.

45 G. Zhou, X. Yang, J. Liu, K. Zhen, H. Wang and T. Cheng, *J. Phys. Chem. B*, 2006, **110**, 9831–9837.

46 K. I. Matveev, V. F. Odyakov and E. G. Zhizhina, *J. Mol. Catal. A Chem.*, 1996, **114**, 151–160.

47 A. W. Stobbe-kreemers, R. B. Dielis and M. S. J. F. Makkee, *J. Catal.*, 1995, **154**, 175–186.

48 X. Lu, T. Cheng, Y. V. Geletii and C. L. Hill, *Inorg. Chem.*, 2023, **5**, 2404–2414.

49 D. W. King, *J. Chem. Educ.*, 2002, **79**, 1135–1140.

50 R. De Levie, *J. Chem. Educ.*, 1999, **76**, 574–577.

51 G. A. Tsigdinos and C. J. Hallada, *Inorg. Chem.*, 1968, **7**, 437–441.

52 T. Yokota, S. Fujibayashi, Y. Nishiyama, Y. Ishii and S. Sakaguchi, *J. Mol. Catal. A Chem.*, 1996, **114**, 113–122.

53 M. Hamamoto, K. Nakayama, Y. Nishiyama and Y. Ishii, *J. Org. Chem.*, 1993, **58**, 6421–6425.

54 G. A. Tsigdinos, *Ind. Eng. Chem. Prod. Res. Dev.*, 1974, **13**, 267–274.

55 I. V. Kozhevnikov, *Chem. Rev.*, 1998, **98**, 171–198.

56 B. Botar, Y. V. Geletii, P. Kögerler, D. G. Musaev, K. Morokuma, I. A. Weinstock and C. L. Hill, *J. Am. Chem. Soc.*, 2006, **128**, 11268–11277.

57 W. Guo, Z. Luo, H. Lv and C. L. Hill, *ACS Catal.*, 2014, **4**, 1154–1161.

58 J. Díaz, L. R. Pizzio, G. Pecchi, C. H. Campos, L. Azócar, R. Briones, R. Romero, A. Henríquez, E. M. Gaigneaux and D. Contreras, *Catalysts*, , DOI:10.3390/catal12050507.

59 K. Yajima, K. Yamaguchi and N. Mizuno, *Chem. Commun.*, 2014, **50**, 6748–6750.

60 C. Li, K. Suzuki, K. Yamaguchi and N. Mizuno, *New J. Chem.*, 2017, **41**, 1417–1420.

61 Y. A. Rodikova, E. G. Zhizhina and Z. P. Pai, *Appl. Catal. A Gen.*, 2018, **549**, 216–224.

62 Y. A. Rodikova and E. G. Zhizhina, *Catal. Ind.*, 2019, **11**, 179–190.

63 K. Kamata, K. Yonehara, Y. Nakagawa, K. Uehara and N. Mizuno, *Nat. Chem.*, 2010, **2**, 478–483.

64 I. D. Ivanchikova, N. V. Maksimchuk, R. I. Maksimovskaya, G. M. Maksimov and O. A. Kholdeeva, *ACS Catal.*, 2014, **4**, 2706–2713.

65 S. X. Guo, A. W. A. Mariotti, C. Schlipf, A. M. Bond and A. G. Wedd, *Inorg. Chem.*, 2006, **45**, 8563–8574.

66 J. B. Cooper, D. M. Way, A. M. Bond and A. G. Wedd, *Inorg. Chem.*, 1993, **32**, 2416–2420.

67 T. Konishi, K. Kodani, T. Hasegawa, S. Ogo, S. X. Guo, J. F. Boas, J. Zhang, A. M. Bond and T. Ueda, *Inorg. Chem.*, 2020, **59**, 10522–10531.

68 J. I. Nambu, T. Ueda, S. X. Guo, J. F. Boas and A. M. Bond, *Dalt. Trans.*, 2010, **39**, 7364–7373.

69 A. J. Bard, *ELECTROCHEMICAL METHODS*, 2019, vol. 2.

70 † Peter J. S. Richardt,† Robert W. Gable,† Alan M. Bond,‡ and Anthony G. Wedd*, *Inorg. Chem.*, 2001, **4**, 703–709.

71 D. P. Smith and M. T. Pope, *Inorg. Chem.*, 1973, **12**, 331–336.

72 M. T. Pope and G. M. Varga, *Inorg. Chem.*, 1966, **5**, 1249–1254.

73 H. Hirao, D. Kumar, H. Chen, R. Neumann and S. Shaik, *J. Phys. Chem. C*, 2007, **111**, 7711–7719.

74 N. Casañ-Pastorf and L. C. W. Baker, *J. Am. Chem. Soc.*, 1992, **114**, 10384–10394.

75 Michael T. Pope* Thomas F. Scully, *Inorg. Chem.*, 1975, **14**, 1974–1975.

76 K. Maeda, S. Himeno, T. Osakai, A. Saito and T. Hori, *J. Electroanal. Chem.*, 1994, **364**, 149–154.

77 S. Himeno and M. Takamoto, *J. Electroanal. Chem.*, 2002, **528**, 170–174.

78 E. Rossini, A. D. Bochevarov and E. W. Knapp, *ACS Omega*, 2018, **3**, 1653–1662.

79 K. Maeda, H. Katano, T. Osakai, S. Himeno and A. Saito, *J. Electroanal. Chem.*, 1995, **389**, 167–173.

80 J. J. Altenau, M. T. Pope, R. A. Prados and H. So, *Inorg. Chem.*, 1975, **14**, 417–421.

81 J. M. Mayer, *Annu. Rev. Phys. Chem.*, 2004, **55**, 363–390.

82 I. M. Mbomekallé, X. López, J. M. Poblet, F. Sécheresse, B. Keita and L. Nadjo, *Inorg. Chem.*, 2010, **49**, 7001–7006.

83 K. Eda and T. Osakai, *Inorg. Chem.*, 2015, **54**, 2793–2801.

84 K. Nakajima, K. Eda and S. Himeno, *Inorg. Chem.*, 2010, **49**, 5212–5215.

85 K. M. Sundaram, W. A. Neiwert, C. L. Hill and I. A. Weinstock, *Inorg. Chem.*, 2006, **45**, 958–960.

86 P. Sami, T. D. Anand, M. Premanathan and K. Rajasekaran, *Transit. Met. Chem.*, 2010, **35**, 1019–1025.

87 E. A. Nagul, I. D. McKelvie, P. Worsfold and S. D. Kolev, *Anal. Chim. Acta*, 2015, **890**, 60–82.

Chapter 4:

Reactivity and stability synergism directed by the electron transfer between polyoxometalates and metal−organic frameworks

Abstract

The synergism between polyoxometalates (POM) and Cu(II) ion in homogeneous aerobic thiol oxidative deodorization has been realized in a more utilitarian heterogeneous catalyst: a multi-electron-capable POM captured in the pores of a metal-organic framework (MOF), HKUST-1 (POM@HKUST). The synergism between POM and the Cu(II) nodes in the MOF depends on the type of POM. $PV_xMo_{12-x}O_{40}^{(3+x)-}$ (x = 1-3) (**PVMo**) but not transition-metal-substituted polytungstates **XPW$_{11}$** (X = V, Co, Zn and Co) result in POM@MOF materials that exhibit synergy relative to the individual structural components, the POM or MOF alone, not only for catalytic reactivity, but also for catalyst structural stability. The **PVMo**@HKUST-catalyzed reaction proceeds to essentially 100% conversion and the material is recoverable and unchanged based FTIR spectroscopy, powder XRD data and other observations after reaction. The **XPW$_{11}$**@HKUST materials have limited conversion and decompose to white powders after reaction. X-ray photoelectron spectroscopy reveals that all the Cu(II) sites on the HKUST-1 become Cu(I) sites that are stable in air. Further kinetics studies show that **PVMo** undergo fast multielectron transfer with intermediate Cu/RSH complexes, while **PVW$_{11}$** and other **XPW$_{11}$** show far slower and limited electron transfer ability with these Cu/RSH complexes. Limited electron transfer between Cu nodes and the encapsulated POM units not only hinders reactivity but also leads to MOF framework distortion and subsequent decomposition induced by reduction of Cu(II) sites to Cu(I) sites.

4.1 Introduction

POM@MOF composites comprising polyoxometalates (POMs) residing in metal-organic framework (MOF) pores.[1–4] have been reported as catalysts for oxidative, electrocatalytic, photocatalytic and other reactions.[3–6] A central point of interest is that they can combine the

attractive properties of POMs and also those of MOFs. POMs have been investigated as catalysts for years,[7–10] resulting from one or more of their following attributes: strong acidity,[11,12] facile redox chemistry,[13–15] photoactivity[16–20] and multielectron transfer ability.[16,21,22] POMs in conventional solid phases, not pseudo-liquid phases,[23] have small surface areas but are soluble in aqueous and many organic solvents. Thus, the immobilization of POMs on porous materials, including polymers,[24] covalent organic frameworks (COFs),[25] zeolites[26] and MOFs,[27–30] is attractive because it converts these homogeneous catalysts into more utilitarian heterogeneous ones with substantial surface area. Among all POM supports, MOFs, such as MIL-101,[31–33] MOF-199 (HKUST-1),[4,34–36] NU-1000,[37–40] UIO-66 [41–44] and ZIF-8 [45–47] are highly attractive host materials because they offer high porosity and sufficient pore (cage) size to encapsulate POMs, including Keggin,[35] Wells-Dawson[41] and sandwich structural families,[48] as guest materials forming POM@MOF composites.

Recent work in our group[49,50] reveals strong synergism effect between Cu(II) ion and phosphovanadomolybdates, $PV_xMo_{12-x}O_{40}^{(3+x)-}$ (x = 1-6) (**PVMo**) for catalysis of air-based oxidative removal of odorous thiols, facilitated by the redox buffering effect of **PVMo**. Moreover, the redox buffering and synergism are only operative for **PVMo** and not phosphovanadotungstates, $PV_xW_{12-x}O_{40}^{(3+x)-}$ (x = 1, 3, 6) (**PVW**). Triggered by this, we sought formulation of a solid and thus more useful catalyst for aerobic thiol deodorization by combining Cu(II) and POM together as a heterogeneous catalyst. Here, we use the POM, HKUST-1 with Cu-containing nodes to bring Cu(II) and reversible multi-electron POM centers into proximity (POM@HKUST). HKUST-1, in addition to providing well-ligated Cu(II), contains large pores that accommodate Keggin POMs with their accompanying counter-cations in the smaller pores. Various Keggin POMs have been incorporated into HKUST-1 for oxidation,[34,51–57] esterification,[58,59] hydrolysis[35] and other

organocatalytic reactions.[60] Many efforts have been made to increase the catalytic activity such as tuning the nanocrystal size,[51] modifying the morphology,[58] designing the hierarchical structure[55] and regulating the pore size.[61] Incorporating Keggin POMs into HKUST-1 not only increases the thermal[62] and hydrolytic[34] stability of the MOF but also increases the reactivity of the POM with a marked synergy between POM and MOF framework.[34,51–53] However, almost all the synergism reported previously is due to the MOF framework confinement effect that enhances the absorption, selectivity, and conversion of organic substrates, while POM is the real catalytic center of the reaction.[51–53] In this work, we show that the aerobic thiol oxidation mechanism involves both the Cu(II) nodes in the MOF framework and multi-electron redox processes of the POM polyanion. In addition, we show that the synergistic electron transfer between MOF and POM maintains the overall POM@MOF framework.

4.2 Experimental

4.2.1 General Materials and Methods

All the polyoxometalates (POM) including $[PVMo_{11}]^{4-}$, $[PV_2Mo_{10}]^{5-}$, $[PV_3Mo_9]^{6-}$, $[PVW_{11}]^{5-}$, $[PV_2W10]^{5-}$, $[CoPW_{11}]^{5-}$, $[NiPW_{11}]^{5-}$ and $[CuPW_{11}]^{5-}$ were synthesized according to literature methods.[63–68] **PVMo**-HKUST ($PV_nMo_{12-n}O_{40}^{(3+n)-}$, $[PMo_{12}]^{3-}$, $[PVMo_{11}]^{4-}$, $[PV_2Mo_{10}]^{5-}$ and $[PV_3Mo_9]^{6-}$, in HKUST-1) and **PW_{12}**-HKUST were prepared following literature methods.[56,69] All other chemicals and solvents were purchased from commercial sources without further purification. The FT-IR spectra were collected on a Nicolet TM 600 FT-IR spectrometer by the attenuated total reflectance (ATR) sampling technique. Powder XRD data were collected on a D8 Discover Powder Instrument using monochromatic Cu Kα (λ = 1.54060 Å) radiation. The signal crystal XRD data were collected on a Bruker D8 SMART APEX CCD single-crystal diffractometer using Mo Kα (0.71073 Å) radiation. SEM-EDX data were collected on a HITACHI SU8230 FE-SEM.

The POM-MOF samples were coated with gold using a Hummer 6 sputterer. UV−vis spectra were collected with an Agilent 8453 spectrophotometer using a 1.0 cm optical path length quartz cuvette. The kinetics were followed by an SF-61 stopped-flow instrument (Hi-Tech Scientific, U.K.) 1H nuclear magnetic resonance (NMR) spectra were acquired on a Varian INOVA 400 spectrometer. The thermogravimetric (TGA) data were collected on a Mettler Toledo TGA instrument. X-ray photoelectron spectroscopy (XPS) were conducted on a thermos K-ALPHA XPS instrument.

4.2.2 Synthesis of POM@HKUST

PVW and XPW@HKUST ($[PVW_{11}]^{5-}$, $[CoPW_{11}]^{5-}$ and $[NiPW_{11}]^{5-}$ in HKUST-1) were synthesized by modified methods as previously reported for $CuPW_{11}$@HKUST.[34] In a typical experiment, $Cu(NO_3)_2 \cdot 2.5H_2O$ (240 mg) and POM (200 mg) were added to a flask with 10 mL of distilled water and stirred for 20 min. Trimesic acid (210 mg) and $(CH_3)_4NOH$ (180 mg) were then added sequentially and stirred for 10 min after each addition. The solution was stirred until a uniform dispersion was achieved. The resulting solution (pH ~ 2 for $[PVW_{11}]^{5-}$, pH ~ 4 for $[CoPW_{11}]^{5-}$ and $[NiPW_{11}]^{5-}$) was transferred to a Teflon-lined Parr bomb, programmatically heated up to 200 °C for 16 h, then cooled down and maintained at 100 °C for another 4 h. Finally, the reactor was allowed to cool to ambient temperature. Blue or dark green crystals were obtained and separated from the solution. The products were washed 3 times with distilled water, 3 times with 50% v/v ethanol at 50 °C, then dried in vacuo overnight to remove solvent molecules. The crystal structures were characterized by single crystal X-ray diffraction. Their purity was confirmed by Fourier transform infrared (FT-IR) and powder X-ray diffraction (XRD) analyses. The new materials in this work are PVW_{11}@HKUST, $CoPW_{11}$@HKUST and $NiPW_{11}$@HKUST. The number of TMA counterions were characterized by TGA (Figure S25), and their chemical formulas are given as: $[Cu_3(C_9H_3O_6)_2]_4[\{(CH_3)_4N\}_4HPVW_{11}O_{40}] \cdot 23H_2O$,

$[Cu_3(C_9H_3O_6)_2]_4[\{(CH_3)_4N\}_4HCoPW_{11}O_{39}]\cdot 31H_2O$ and $[Cu_3(C_9H_3O_6)_2]_4[\{(CH_3)_4N\}_4HNiPW_{11}O_{39}]\cdot 34H_2O$. The presence of the d-electron transition metal in the PXW@HKUST materials was assessed using SEM-EDX.

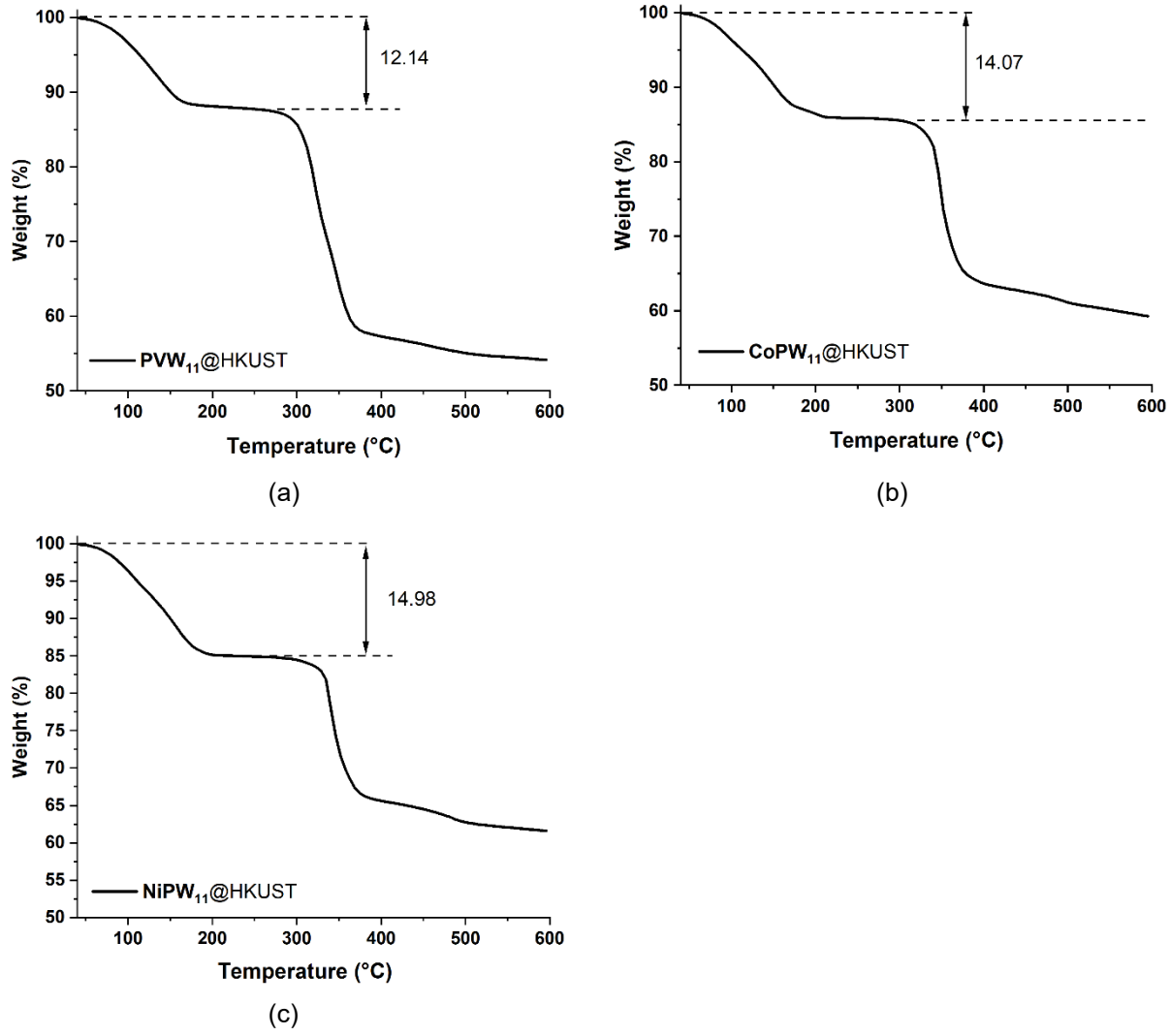

Figure 4.0. Thermogravimetric analyses of the POM@MOFs. The calculated weight percentages of water + tetramethylammonium cations is (a) 12.14 % (PVW_{11}@HKUST); (b) 12.07% ($CoPW_{11}$@HKUST); (c) 14.98% ($NiPW_{11}$@HKUST).

4.2.3 Thiol (RSH) oxidation

An exemplary substrate, 2-mercaptoethanol, was used for probing the aerobic thiol oxidation mechanism, eq 4.1, where RSH is 2-mercaptoethanol. The product (bis(2-hydroxyethyl) disulfide (RSSR)) was formed in nearly quantitative yield.

$$2\ RSH + ½\ O_2 \rightarrow RSSR + H_2O \quad (4.1)$$

In a typical RSH oxidation catalyzed by the heterogeneous POM-HKUST systems, 0.77 mM catalyst, 28.6 mM RSH and 5 mL dichloroethane were stirred in a heavy-wall glass pressure vessel at 50 °C. Aliquots were withdrawn every hour, and the RSH concentration was determined using Ellman's reagent, 5,5-dithiobis(2-nitrobenzoic acid (DTNB). The product was confirmed by ^{1}H NMR. The POM-HKUST catalysts were collected by centrifugation and dried under vacuum overnight then evaluated to quantify stability. The IR spectrum and powder XRD were measured and compared with those data before RSH oxidation. Reaction kinetics were followed by UV-vis spectroscopy or stopped-flow spectroscopy and described previously.[49]

4.2.4 Electrochemistry

Electrochemical data were obtained using a Pine WaveDiver 10 potentiostat. Cyclic voltammograms (CVs) were recorded in a standard three-electrode electrochemical cell with a glassy carbon disk working electrode, a platinum wire counter electrode, an Ag/AgCl (3M KCl) reference electrode and 0.1 M KNO_3 as the supporting electrolyte. For heterogeneous POM-MOF materials, CVs were collected by immobilizing them on glassy carbon electrode. The measured potential was converted to the reversible hydrogen electrode (RHE). For bulk electrolysis, a reticulated vitreous carbon working electrode was used as a working electrode. UV-vis spectra of the aliquots that after bulk electrolysis at desired constant potential were collected under Ar.

4.3 Results and discussion

4.3.1 POM-MOF materials and characterization

We tried to incorporate $PV_xMo_{12-x}O_{40}^{(3+x)-}$ (x = 0-6) (**PVMo**) and $PV_xW_{12-x}O_{40}^{(3+x)-}$ (x = 0-6) (**PVW**) into the HKUST-1 using the well-established hydrothermal synthetic method,[35,36] but only **PVMo** with n≤3 could be successfully inserted into the pores of HKUST-1. **PVMo** with n>3 have higher negative charges (>6-) and thus more counter-cations which prevents successful POM incorporation into HKUST: there is no space for the additional TBA counter-cations in the smaller HKUST pores for the Keggin polyanions with these higher charges. We note that there are other synthetic methods to synthesize POM-HKUST materials.[51,59,70,71] This paper does not explore various synthetic methods but only focuses on the hydrothermal approach. As a result, for **PVMo** in HKUST-1, we only discuss **PVMo**@HKUST (x = 0-3, **$PVMo_{11}$**@HKUST, **PV_2Mo_{10}**@HKUST and **PV_3Mo_9**@HKUST) in this work, and they have been reported before.[35,56] The phase purity of **PVMo**@HKUST were established by FT-IR spectra and powder X-ray diffraction (PXRD) patterns (Figures 4.1-4.2).

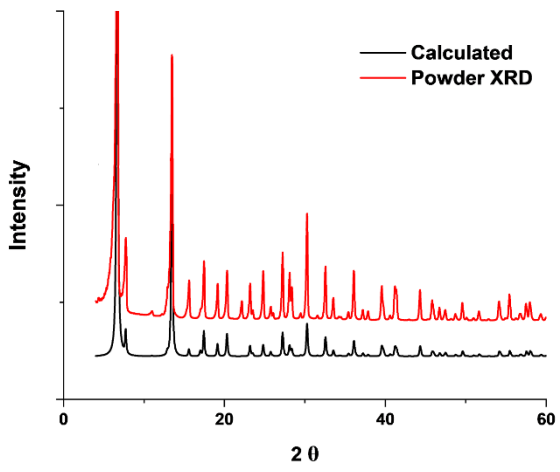

(a)

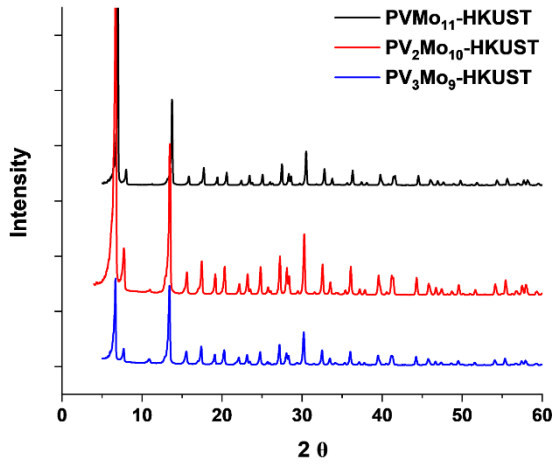

(b)

Figure 4.1. (a) **PV_2Mo_{10}**@HKUST calculated XRD pattern from single-crystal refinement data compare with the experimental powder XRD pattern. (b) Powder XRD pattern of **$PVMo_{11}$**@HKUST ($Cu_3(C_9H_3O_6)_2]_4[\{(CH_3)_4N\}_4PVMo_{11}O_{40}$), **$PV_2Mo_{10}$**@HKUST ($Cu_3(C_9H_3O_6)_2]_4[\{(CH_3)_4N\}_5PV_2Mo_{10}O_{40}$) and **$PV_3Mo_9$**@HKUST ($Cu_3(C_9H_3O_6)_2]_4[\{(CH_3)_4N\}_6PV_3Mo_9O_{40}$).

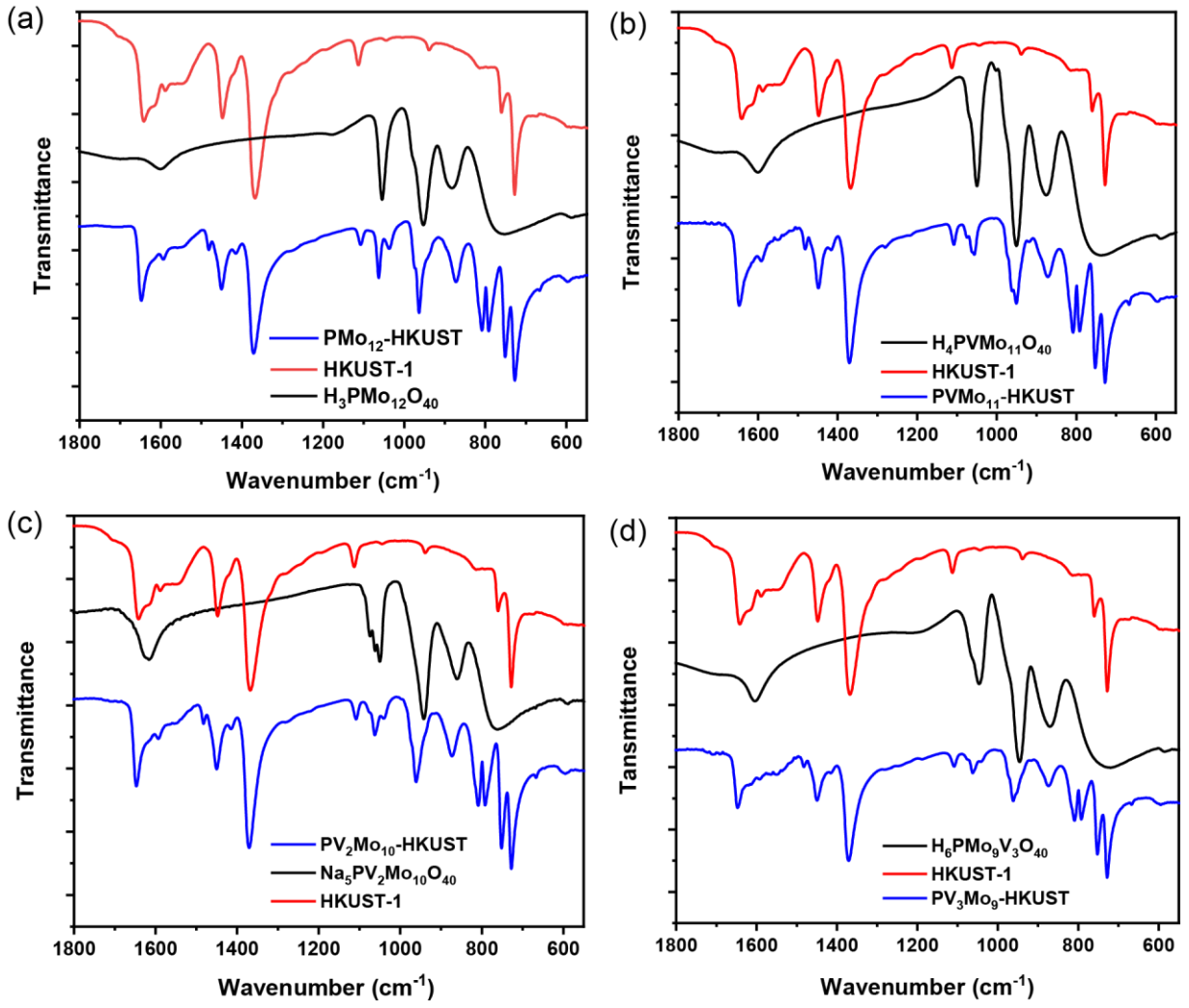

Figure 4.2. FT-IR of POM, HKUST-1 and corresponding POM@HKUST (a) **PMo_{12}**@HKUST; (b) **$PVMo_{11}$**@HKUST; (c) **PV_2Mo_{10}**@HKUST; (d) **PV_3Mo_9**@HKUST.

The PXRD patterns were compared with the calculated patterns from the single crystal X-ray diffraction of **PV_2Mo_{10}**@HKUST (Figures 4.3, Table 4.1).

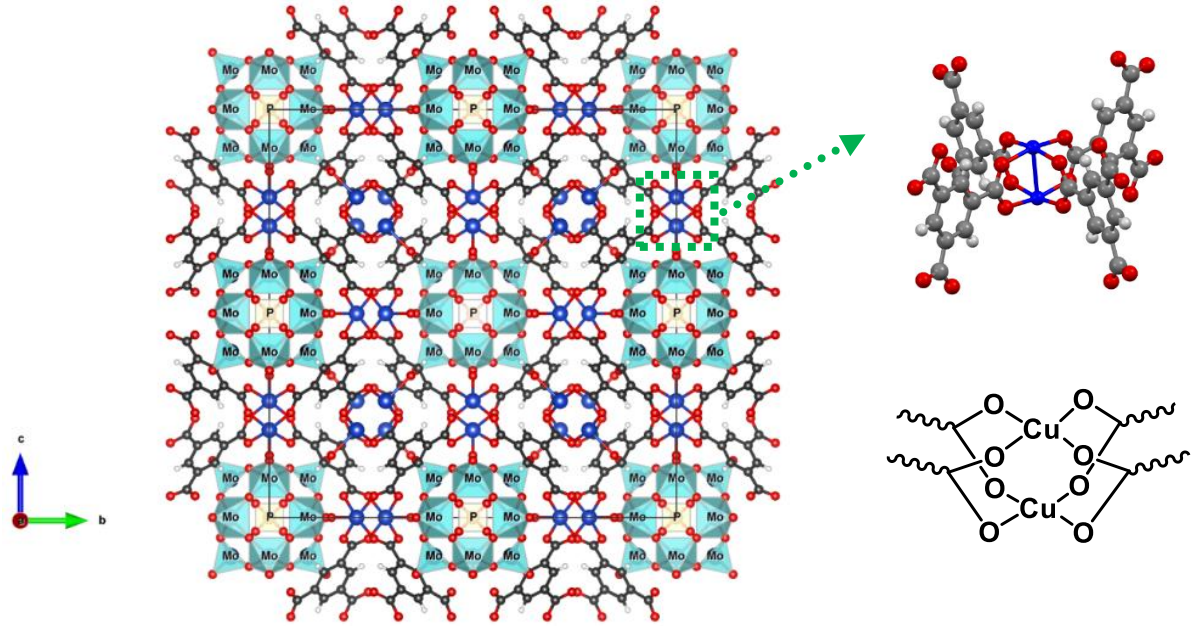

Figure 4.3. X-ray signal-crystal structure of **PV_2Mo_{10}**@HKUST. The blue polyhedra represent the MoO_6 units in the POM, which are orientationally disordered. The HKUST-1 framework is represented in ball-and-stick form. C is black, O is red, Cu is blue, and H is white. The tetramethylammonium (TMA) cations, which are disordered, reside in the smaller pores and are omitted here for clarity. The green box shows the zoom in chemical formular of di-copper node.

For the **PVW**, only x=0, 1 can be inserted into HKUST-1 (PW_{12}@HKUST and PVW_{11}@HKUST). This likely derives from the fact that unlike the corresponding Mo-based Keggin POMs, the Keggin polytungstates are more rigid and far less hydrolytically labile. As a consequence, the HKUST-1 pores can only accommodate Keggin polytungstates with charges <6-. We succeeded in incorporating a series of transition-metal-substituted polytungstates (**PXW_{11}**, X = Cu, Co and Ni) into HKUST-1 (XPW@HKUST: $CuPW_{11}$@HKUST, $CoPW_{11}$@HKUST and $NiPW_{11}$@HKUST).

Table 4.1. Crystal data and structure refinement for **PV_2Mo_{10}**@HKUST

Empirical formula	$C_{72}H_{24}Cu_{12}Mo_{12}O_{102}P$
Formula weight	4465.64
Temperature/K	106(9)
Crystal system	cubic
Space group	Fm-3m
a/Å	26.2445(2)
b/Å	26.2445(2)
c/Å	26.2445(2)
α/°	90
β/°	90
γ/°	90
Volume/$Å^3$	18076.5(4)
Z	4
ρ_{calc} g/cm^3	1.641
μ/mm^{-1}	8.900
F(000)	8556.0
Crystal size/mm^3	0.139 × 0.091 × 0.068
Radiation	CuKα (λ = 1.54184)
2Θ range for data collection/°	5.832 to 153.05
Index ranges	$-28 \leq h \leq 16$, $-32 \leq k \leq 32$, $-25 \leq l \leq 25$
Reflections collected	10446
Independent reflections	974 [R_{int} = 0.0426, R_{sigma} = 0.0176]
Data/restraints/parameters	974/0/54
Goodness-of-fit on F^2	1.118
Final R indexes [I>=2σ (I)]	R_1 = 0.0537, wR_2 = 0.1662
Final R indexes [all data]	R_1 = 0.0563, wR_2 = 0.1686
Largest diff. peak/hole / e $Å^{-3}$	0.78/-1.05

The PXRD patterns of **PVW$_{11}$**@HKUST, **CoPW$_{11}$**@HKUST and **NiPW$_{11}$**@HKUST were compared with the calculated pattern from the single crystal data of **CuPW$_{11}$**@HKUST from previous work (Figure 4.5).[34] PXRD and FT-IR establish the phase purity of these materials Figures 4.4-4.5.

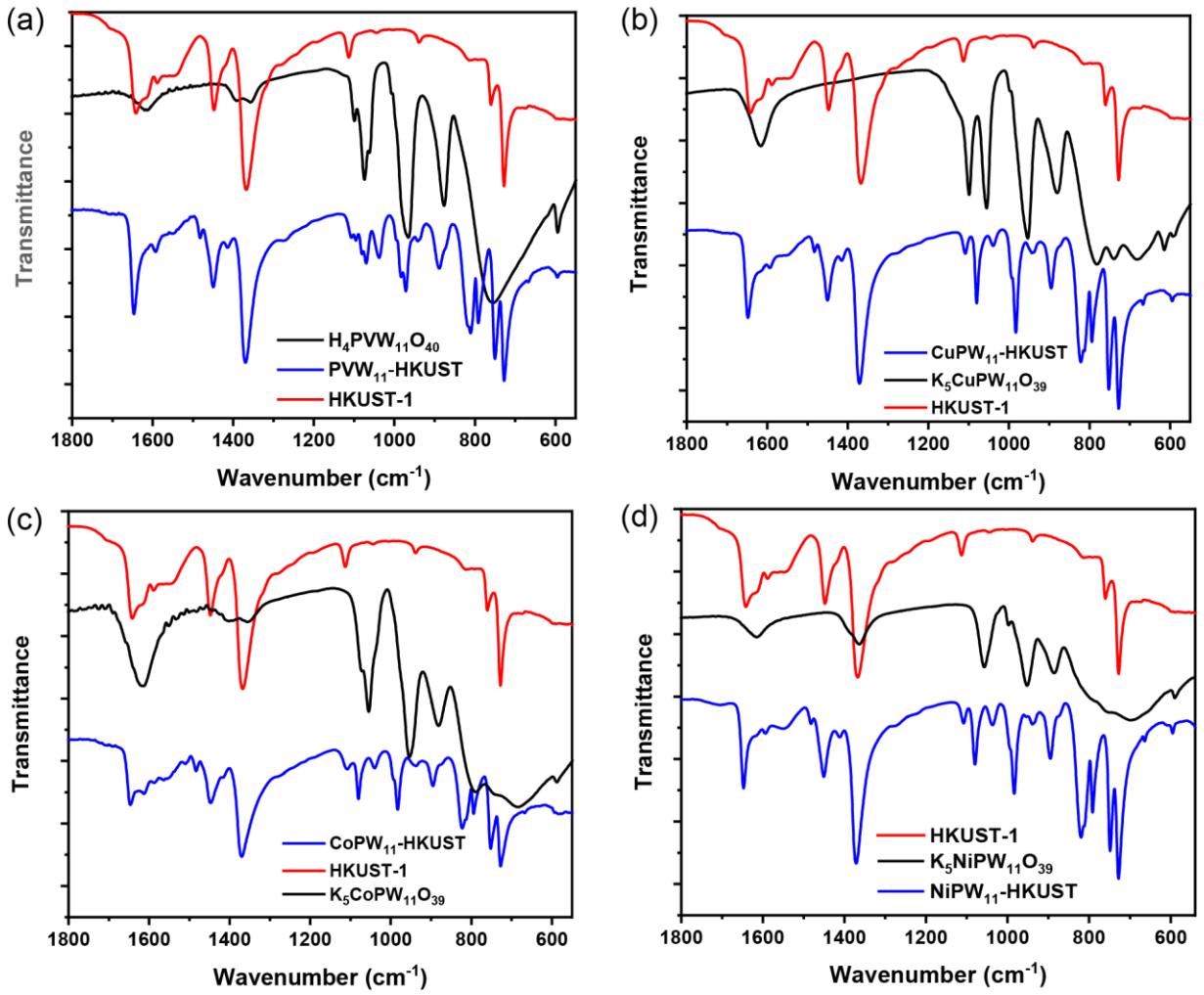

Figure 4.4. FT-IR of POM alone, HKUST-1 and the corresponding POM-HKUST. (a) **PVW$_{11}$**@HKUST; (b) **CuPW$_{11}$**@HKUST; (c) **CoPW$_{11}$**@HKUST; (d) **NiPW$_{11}$**@HKUST.

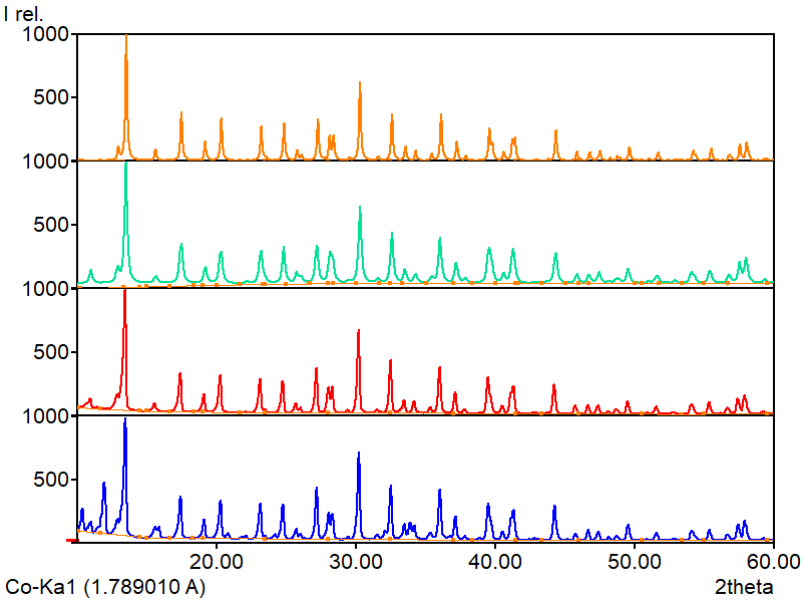

Figure 4.5. Powder XRD patterns of **CoPW$_{11}$**@HKUST ($Cu_3(C_9H_3O_6)_2]_4[\{(CH_3)_4N\}_5CoPW_{11}O_{39}$), blue; **NiPW$_{11}$**@HKUST ($Cu_3(C_9H_3O_6)_2]_4[\{(CH_3)_4N\}_5NiPW_{11}O_{39}$), red; **PVW$_{11}$**@HKUST ($Cu_3(C_9H_3O_6)_2]_4[\{(CH_3)_4N\}_5PVW_{11}O_{39}$), green. The calculated pattern from single crystal data of **CuPW$_{11}$**@HKUST ($[Cu_3(C_9H_3O_6)_2]_4[\{(CH_3)_4N\}_4CuPW_{11}O_{39}H]$ is in orange.

The incorporated transition metal, M, in the POM was established using SEM-EDX (Figures 4.6-4.8).

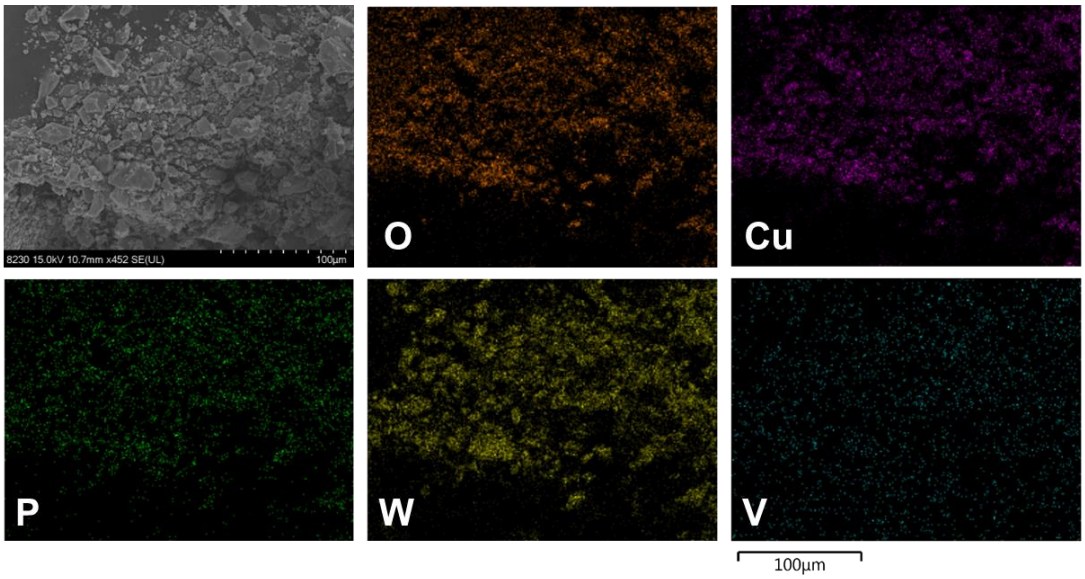

Figure 4.6. **PVW_{11}**@HKUST SEM image and EDX element mapping.

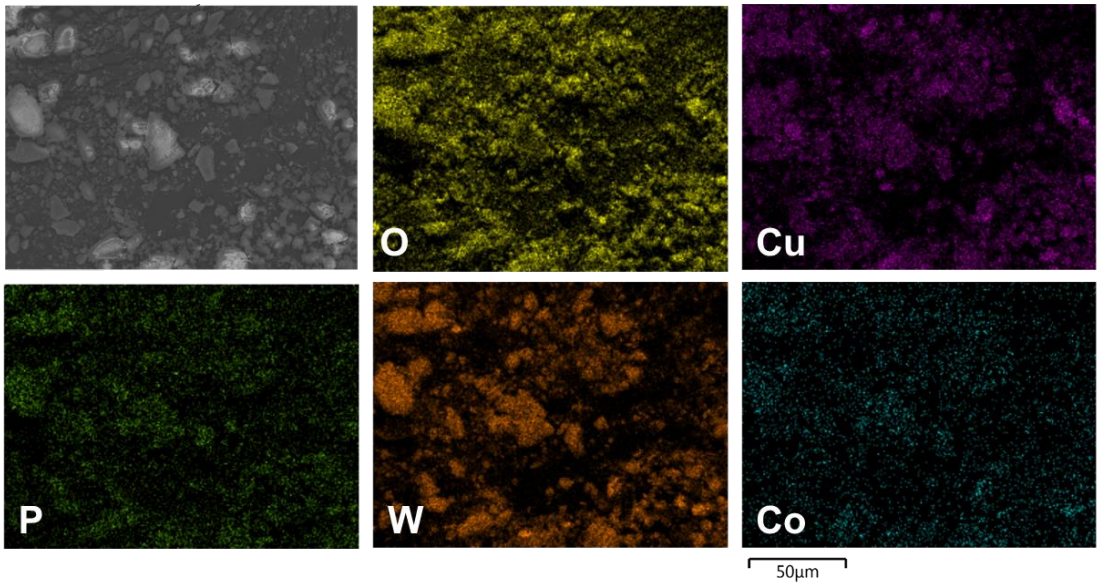

Figure 4.7. **$CoPW_{11}$**@HKUST SEM image and EDX element mapping.

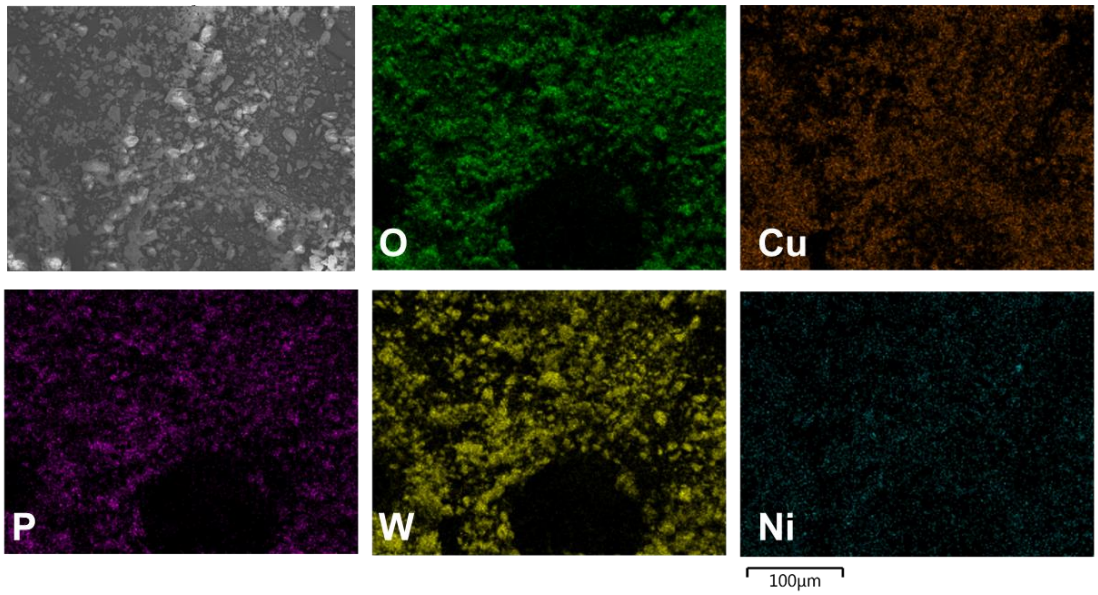

Figure 4.8. **$NiPW_{11}$**@HKUST SEM image and EDX element mapping.

4.3.2 POM leaching and solvent selection

The leaching of POM from MOF pores during the reaction is a potential issue for POM-MOF materials.[3,4] Figure 4.9a shows the thiol (RSH) oxidation reactivity of **PV_2Mo_{10}**-HKUST in different organic solvents. Auto-catalytic behavior is seen in acetonitrile (AN) and dimethylacetamide (DMA). This is because POM is leached into the solution during reaction in these polar POM-solubilizing solvents, and the dominant mode of catalysis switches from heterogeneous to homogeneous by POM in solution. To further address POM leaching from MOF pores in these catalytic studies, we developed a colorimetric method to detect whether POM is extracted into the solution. Supernatants were filtered after the oxidation reaction, then $SnCl_2$, a strong reducing agent, was added to the Ar-purged, filtered solution. Since the Mo(VI)-Mo(V) intervalence charge transfer band has very high extinction coefficient around 600-800 nm,[72] even a trace amount of POM that leaks into the solution is rapidly reduced and quantified by UV-Vis spectroscopy. Figure 4.9b shows the UV-Vis results. When ethanol is used as a solvent, a slight

absorbance due to reduced POM in solution is observed; when AN and DMA are used, large absorbances are observed. When solvents less polar than ethanol are used, no absorbances around 600-800 nm are generated. Here we use dielectric constant (ε) to differentiate and quantify the polarity of the organic solvents. The reactivity increases as ε increases (Figure 4.9a), however, when ε is too large (ethanol, 24.6), the POM starts to leach from the MOF pores. As a consequence, we chose dichloroethane for all the catalytic studies.

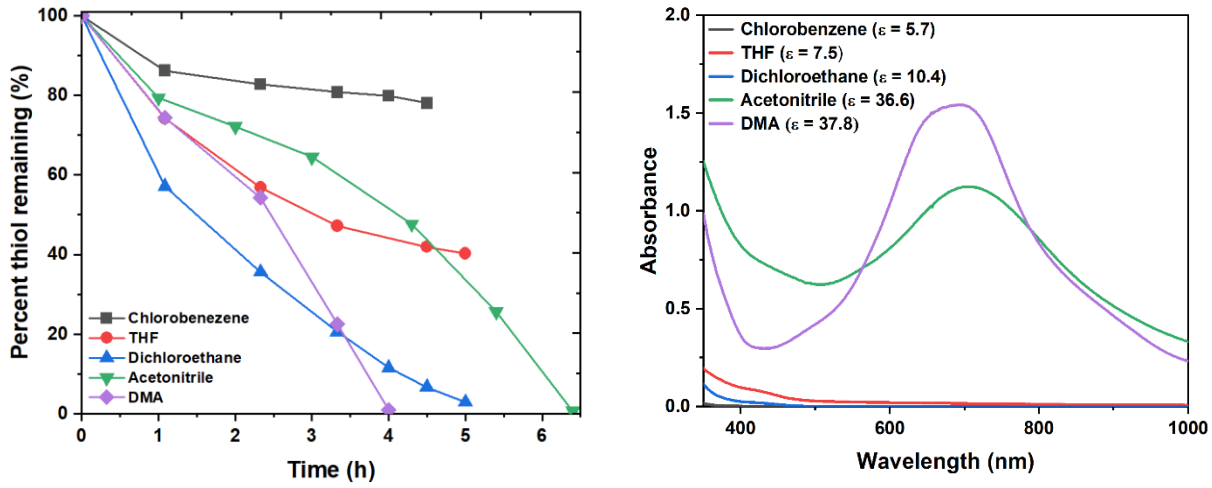

(a) (b)

Figure 4.9. (a) RSH consumption catalyzed by **PV_2Mo_{10}**@HKUST in different solvents. Conditions: dichloroethane (5 mL), 2-mercaptoethanol (28.6 mM), catalyst (0.774 mM), reaction at 50 °C. (b) UV-Vis absorbance of the reduced supernatant solution after addition of $SnCl_2$ under argon after reaction.

4.3.3 Activity and stability synergism

A core thrust of this study is to determine whether the synergism between **PVMo** and Cu(II) in homogeneous solution can still exist while both parts are confined without free diffusion. The aerobic oxidation of RSH catalyzed homogeneously by **PVMo** and Cu(II) in dichloroethane (30% acetonitrile for POM solubility) was evaluated (Figure 4.10). The same results obtain in pure acetonitrile were obtained,[49,50] i.e. catalytic activity increases with increasing number of V centers

in the POM. Notably, neither Cu(II) ion nor POM alone (**PVMo** (x = 1-3, but not x = 0) have significant activity which proves a synergy exists between these two catalytic components.

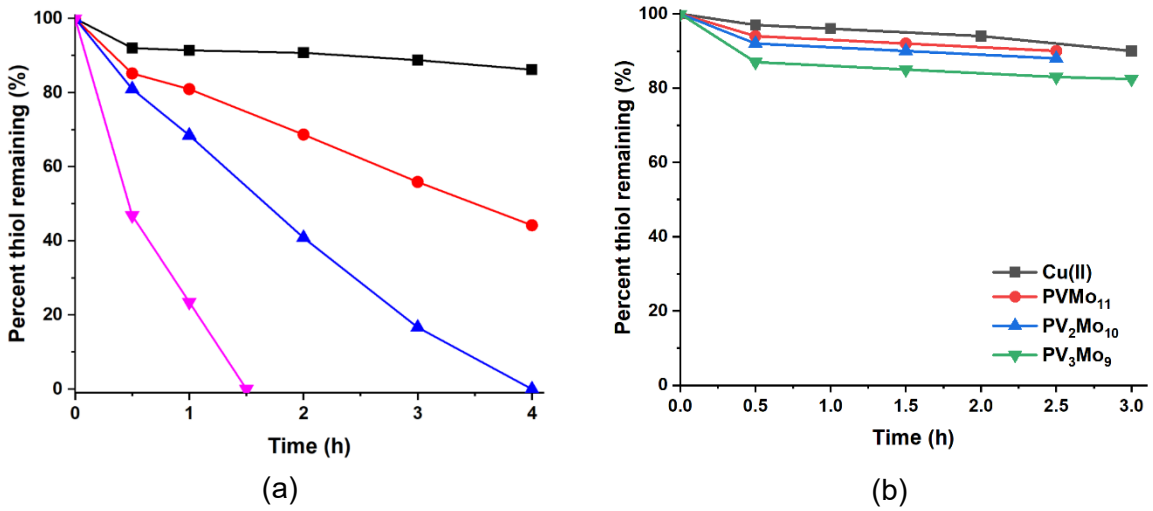

Figure 4.10. (a) Aerobic RSH (30 mM) oxidation catalyzed by 0.2 mM POM with 1.0 mM Cu(II) at room temperature in a dichloroethane / acetonitrile 30%(v/v) solvent system. Black: $H_3PMo_{12}O_{40}$ (**PMo_{12}**); red: $H_4PVMo_{11}O_{40}$ (**$PVMo_{11}$**); blue: $H_5PV_2Mo_{10}O_{40}$ (**PV_2Mo_{10}**); pink: $H_6PV_3Mo_9O_{40}$ (**PV_3Mo_9**). (b) Aerobic RSH (30 mM) oxidation activity in the presence of 0.5 mM Cu(II) alone or 0.5 mM POM alone.

The conversion and turnover frequency (TOF) data of all POM@HKUST catalyze aerobic RSH oxidation are summarized in Table 4.1. The consumption curves of **PVMo**@HKUST (x = 0-3) are shown in Figure 4.11a. The catalytic activity, as for the homogeneous **PVMo**/Cu catalytic systems, increases with increasing number of vanadium centers in **PVMo**. Nearly 100% conversion is achieved in 3h, 6h and 15h by **PV_3Mo_9**@HKUST, **PV_2Mo_{10}**@HKUST and **$PVMo_{11}$**@HKUST, respectively. **PMo_{12}**@HKUST does not achieve 100% after 24h and HKUST-1 alone converts only 45% after 20h (Figure 4.11b). **PVW_{11}**@HKUST and **XPW**@HKUST (X = Cu, Co and Ni) have much lower catalytic activity than **PVMo**@HKUST, Figure 4.11b. The biphasic thiol consumption kinetics in the polytungstate@HKUST systems reflects initial rapid uptake of the thiol into the POM-MOF pores, followed continued but slower thiol uptake that parallels the time-

dependent decomposition of the polytungstate@HKUST systems (see discussion below). Changing the transition metal in the POM does not have a significant effect on activity. **PVW$_{11}$**@HKUST and **XPW**@HKUST do not achieve 100% conversion after 24h.

Table 4.1. Air-based oxidation of 2-mercaptoethanol catalyzed by different POM@HKUST systems[a]

	Conversion[b] %	TON[c]	TOF×10^3, s^{-1} [d]
HKUST-1	45	16.6	0.20
PMo$_{12}$-HKUST	90	30	0.45
PVMo$_{11}$-HKUST	>99	37	1.0
PV$_2$Mo$_{10}$-HKUST	>99	37	2.1
PV$_3$Mo$_9$-HKUST	>99	37	4.1
CuPW$_{11}$-HKUST	63	23.3	0.32
CoPW$_{11}$-HKUST	75	27.7	0.38
NiPW$_{11}$-HKUST	71	26.2	0.36
PVW$_{11}$-HKUST	68	25.1	0.35

[a] Conditions: POM@HKUST (0.774 mM), 2-mercaptoethanol (28.6 mM), dichloroethane (5 mL), at 50 °C under air. [b] Conversion was measured at 20 h. [c] Turnover number (TON = moles of 2-mercaptoethanol consumed per mol of HKUST-POM) was measured at 20 h. [d] Turnover Frequency, TOF = TON/(reaction time).

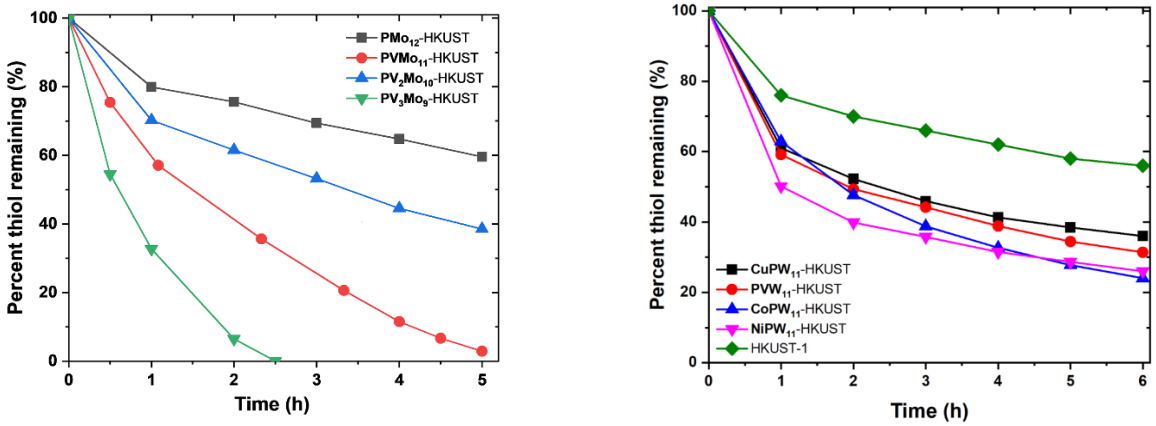

Figure 4.11. (a) RSH consumption catalyzed by **PVMo**@HKUST (n= 0-3). (b) RSH consumption catalyzed by HKUST-1 alone and by **PXW**@HKUST (X = Cu, V, Ni and Co). Conditions: Dichloroethane

(5 mL), 2-mercaptoethanol (28.6mM), catalyst (0.774 mM) at 50 °C under air. The POM@HKUST structure averages four HKUST-1 crystal units per POM, therefore, the molecular unit of HKUST-1 alone is taken as four times that implied by its chemical formula: $Cu_3(C_9H_3O_6)_2$.

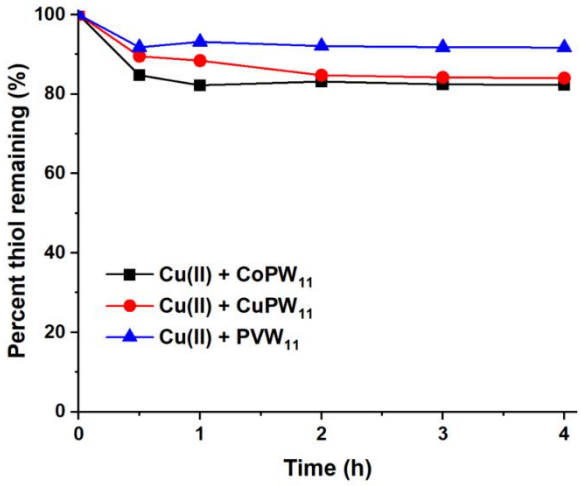

Figure 4.12. RSH (30 mM) catalyzed by 0.2 mM POM with 1.0 mM Cu(II) under room temperature in mix solvent of dichloroethane with 30%(v/v) acetonitrile. Black: $Na_5CoPW_{11}O_{39}$ (**$CoPW_{11}$**); Red: $Na_5CuPW_{11}O_{39}$ (**$CuPW_{11}$**); Blue: $H_5PVW_{11}O_{40}$ (**PVW_{11}**).

A homogeneous aerobic catalytic RSH oxidation investigation reveals no synergistic effect between phosphotungstate POMs and Cu(II) ion (Figure 4.12). The same Keggin POMs were incorporated into the Cu-free large-pore MIL-101 MOFs (Figure 4.13).[31,32,73–76] The resulting POM@MIL-101 binary materials have very little activity implicating a direct role of the HKUST-1 Cu(II) centers in catalytic aerobic thiol oxidation (Figure 4.14).

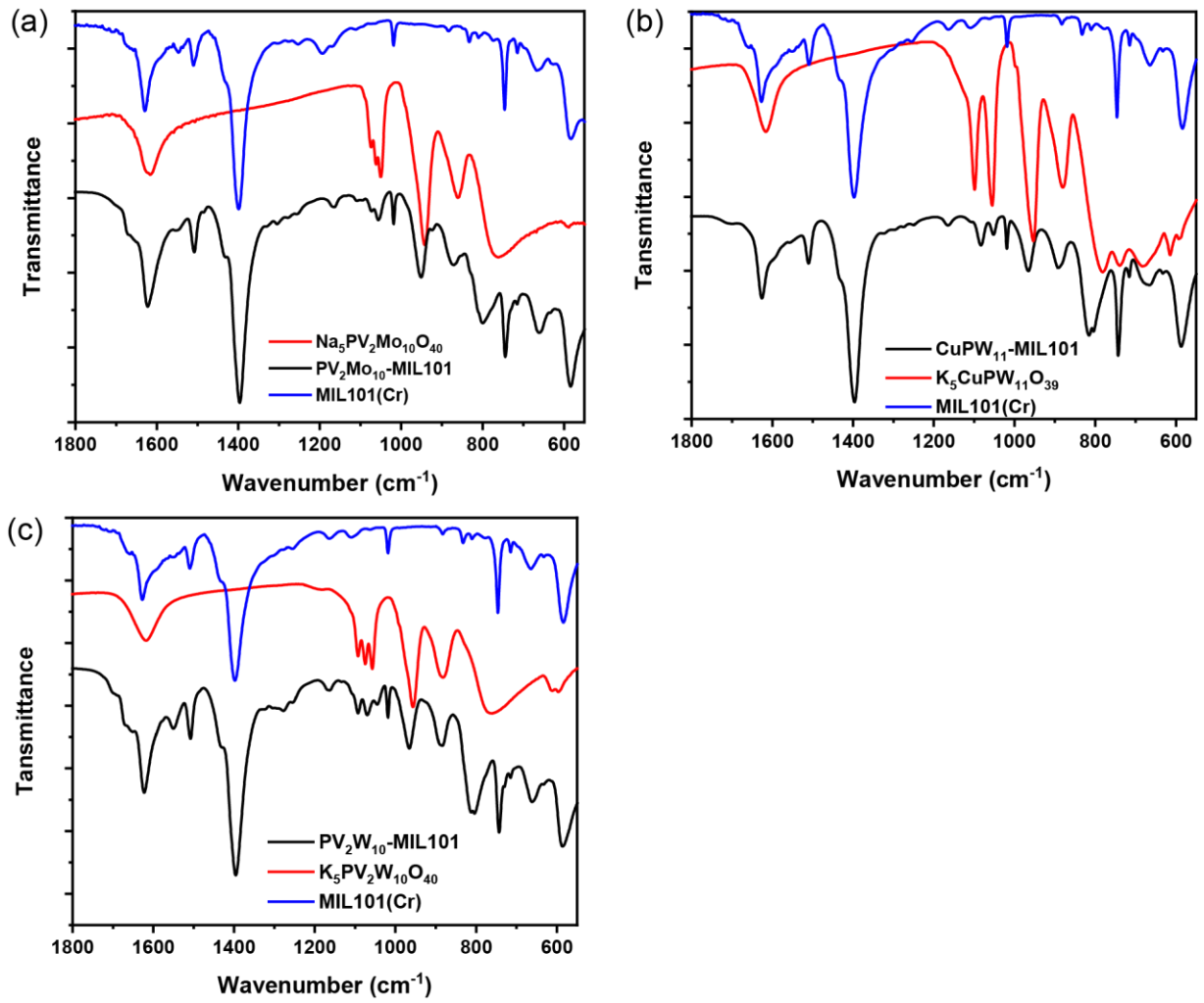

Figure 4.13. FT-IR of POM, MIL-101(Cr) and corresponding POM@MIL-101 materials: (a) **PV_2Mo_{10}**-MIL-101; (b) **$CuPW_{11}$**@MIL-101; (c) **PV_2W_{10}**@MIL-101.

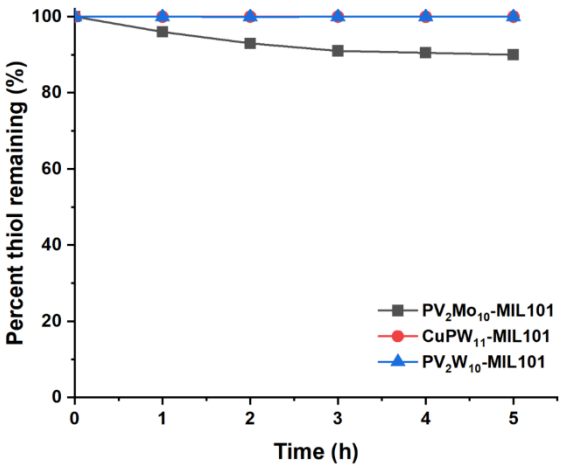

Figure 4.14. POM@MIL101-catalyzed RSH oxidation activity. Conditions: catalyst (20 mg), 2-mercaptoethanol, RSH (30 mM), dichloroethane (5 mL), at 50 °C under air.

Interestingly, the Cu-MOF synergy is not limited to catalytic activity: it also extends to catalyst stability. **PVMo**@HKUST are stable during the oxidation reactions. Figures 4.15a, b show that both the FT-IR spectra and PXRD patterns of **PV_3Mo_9**@HKUST are the same before and after reaction consistent with structural integrity of both the POM and MOF components. Before and after reaction FT-IR spectra for **$PVMo_{11}$** and **PV_2Mo_{10}**@HKUST are given in Figure 4.16.

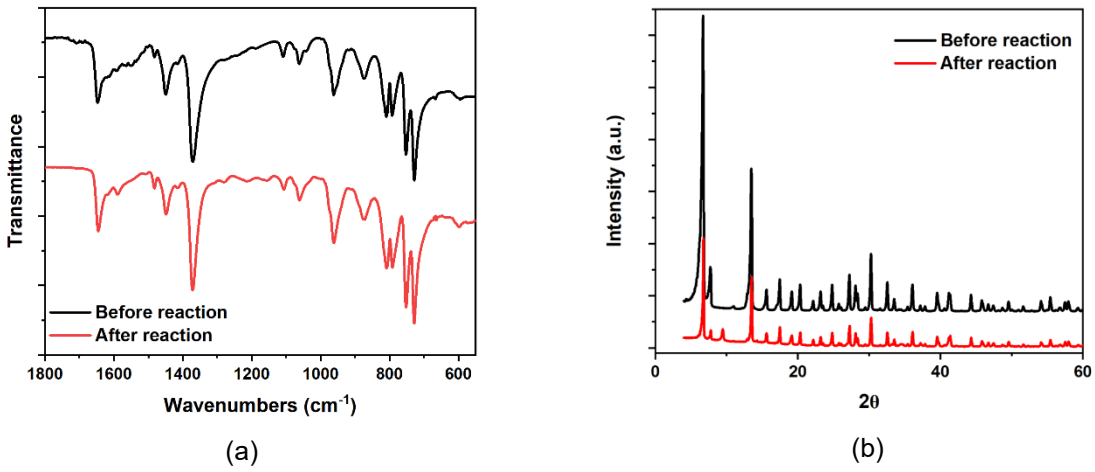

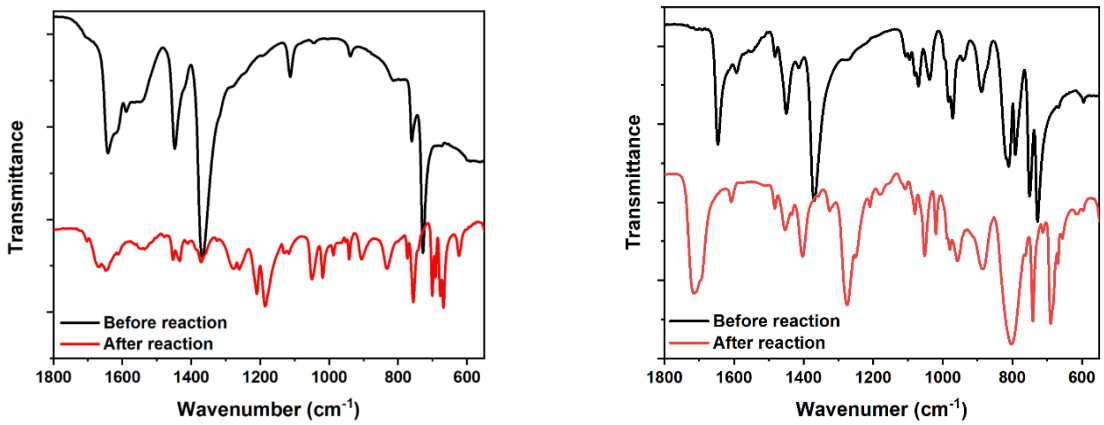

Figure 4.15. (a) FT-IR and (b) PXRD spectra of **PV_2Mo_{10}**@HKUST before and after reaction. FT-IR spectra of (c) HKUST-1 and (d) **PVW_{11}**@HKUST before and after reaction.

In contrast, the FT-IR of HKUST-1 shows that this MOF is destroyed after oxidation (Figure 4.15c). Thus, there is a dramatic oxidative stabilization of the MOF framework when these Keggin POMs are incorporated into the MOF pores. Significantly, all the **PVW_{11}**@HKUST and **XPW**@HKUST materials decompose to white powders after reaction (Figure 4.17).

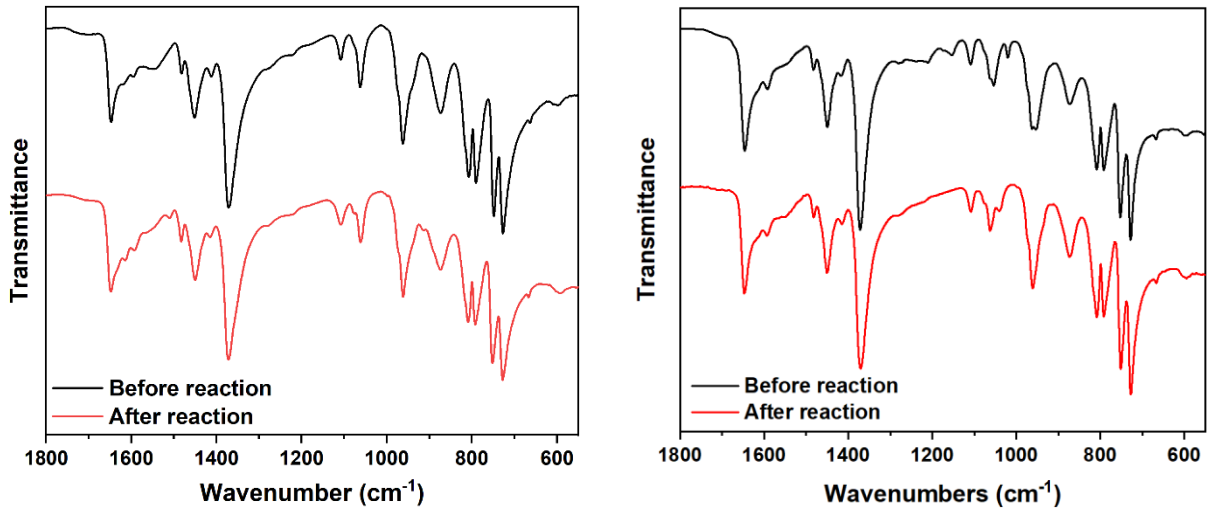

Figure 4.16. FT-IR of (a) **$PVMo_{11}$**@HKUST; (b) **PV_2Mo_{10}**@HKUST before and after RSH oxidation.

Figure 4.15d shows the FT-IR of **PVW$_{11}$**@HKUST. The C=O stretches (1644 cm^{-1}) and C-O stretches (1368 cm^{-1}) shift indicating changes in the MOF structures. This POM stabilization of the POM@MOF framework during the oxidation reaction, is POM selective: only phosphomolybdates but not phosphotugstates facilitate MOF stabilization. These data collectively indicate that the reactivity synergism between Cu(II), the MOF framework and the POM is crucial for stability of these hybrid materials.

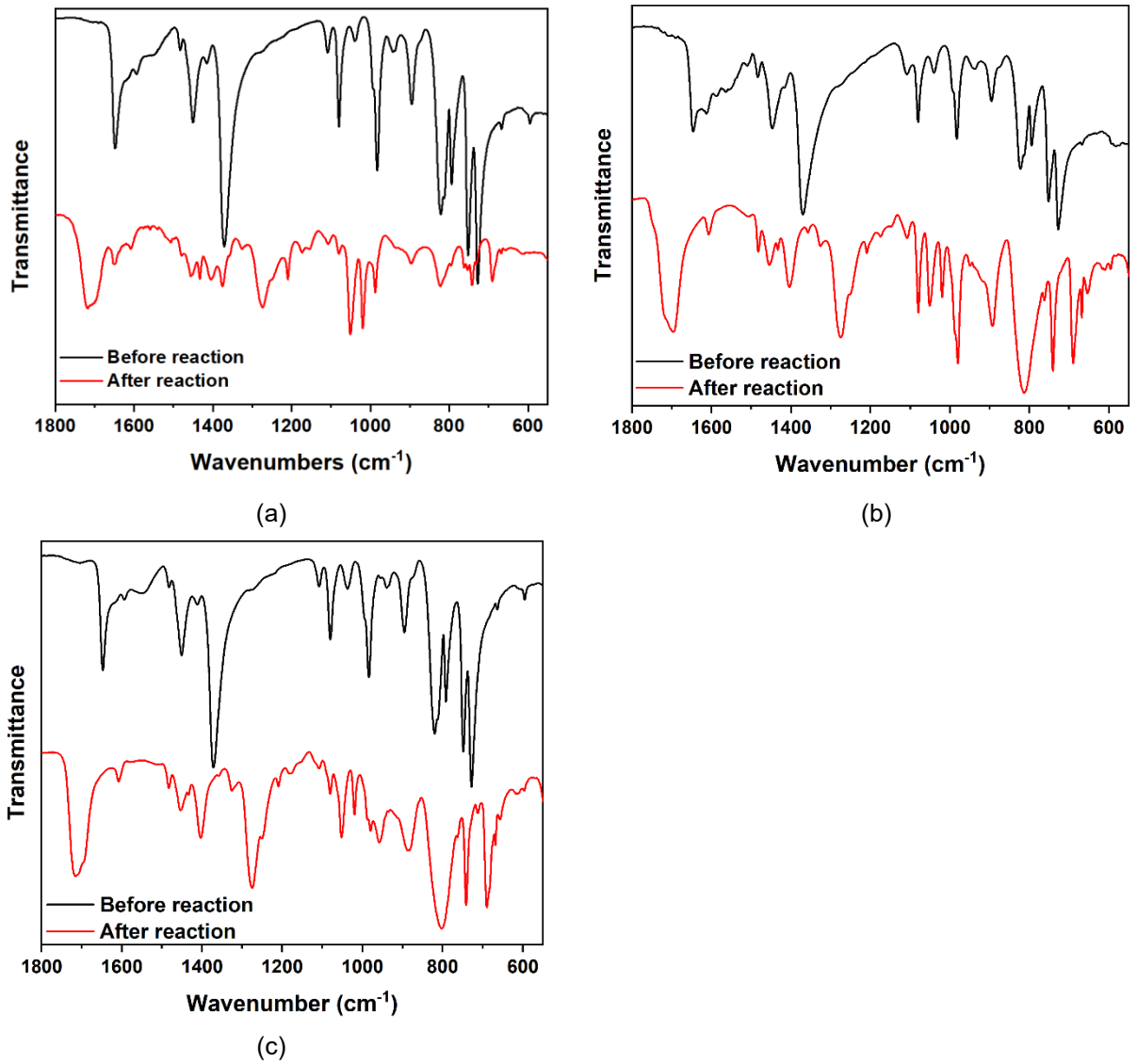

Figure 4.17. FT-IR POM@HKUST before and after RSH oxidation. (a) **CuPW$_{11}$**@HKUST; (b) **CoPW$_{11}$**@HKUST; (c) **NiPW$_{11}$**@HKUST.

We turn to X-ray photoelectron spectroscopy (XPS) to further probe decomposition of the **XPW**@HKUST materials. The spectra of POM@HKUST before and after reaction were collected. Figure 4.18a shows the Cu 2p spectra of **PV_3Mo_9**@HKUST. Peaks at 935.1 eV and 955.1 eV belong to Cu^{2+} $2p_{3/2}$ and $2p_{1/2}$, and are accompanied by satellite peaks at 944.5 and 940.5 eV.[77–79] There are no detectable peaks due to Cu^{1+} indicating all Cu has been reoxidized back to its initial oxidation state after reaction.

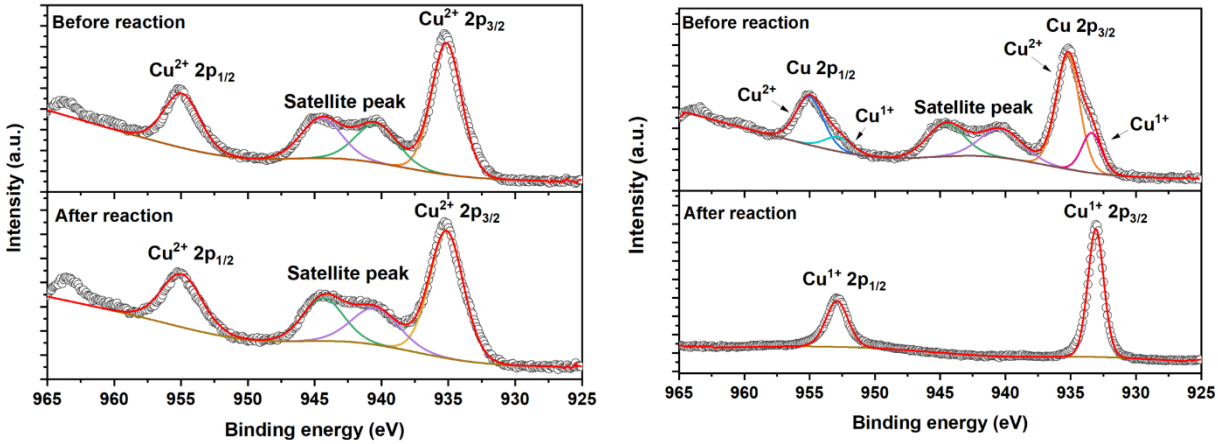

Figure 4.18. Cu 2p XPS spectra of POM@MOF before and after reaction (a) **PV_3Mo_9**@HKUST; (b) **$CuPW_{11}$**@HKUST.

Figure 4.18b shows **$CuPW_{11}$**@HKUST before the reaction, beside the Cu^{2+} 2p peaks, it contains Cu^{1+} $2p_{3/2}$ and $2p_{1/2}$ at 933.0 and 952.9 eV, respectively. This indicates charge transfer between Cu^{2+} nodes and POM during the synthesis.[78–83] Here, we found that under the hydrothermal synthesis conditions, the transition-metal-substituted phosphotugstates prefer to undergo electron transfer with HKUST-1 (Figure 4.19) than **PVMo** (Figure 4.20). Since even perfect HKUST-1 crystals have Cu^{1+} defects,[82] all the POM@MOF materials may contained certain percents of Cu^{1+} in their nodes.

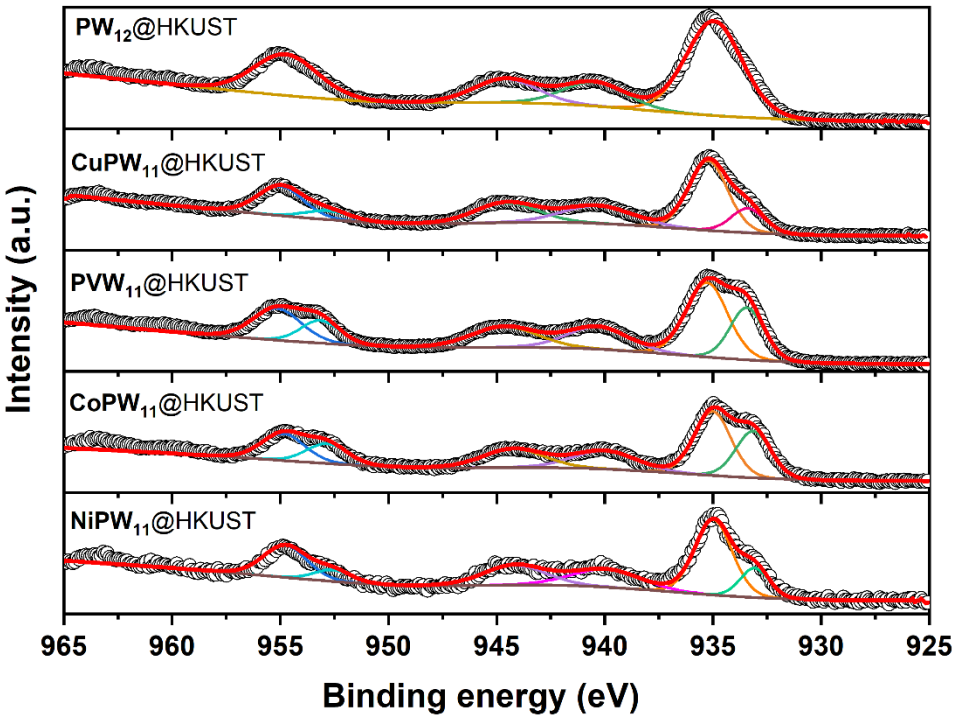

Figure 4.19. **XPW**@HKUST (X = Cu, V, Co and Zn) XPS spectra of Cu 2p.

Moreover, Figure 4b shows that after reaction, the Cu^{2+} 2p peak and corresponding satellite peaks disappear, and only Cu^{1+} 2p peaks are evident. This indicates that the HKUST-1 framework breaks down and generates a Cu^{1+}-based structure that is stable when exposed to ambient air. This also directly implicates a redox role for the Cu centers in the MOF nodes. Its structural distortion results from a lack of reoxidation of Cu^{1+} to Cu^{2+}.

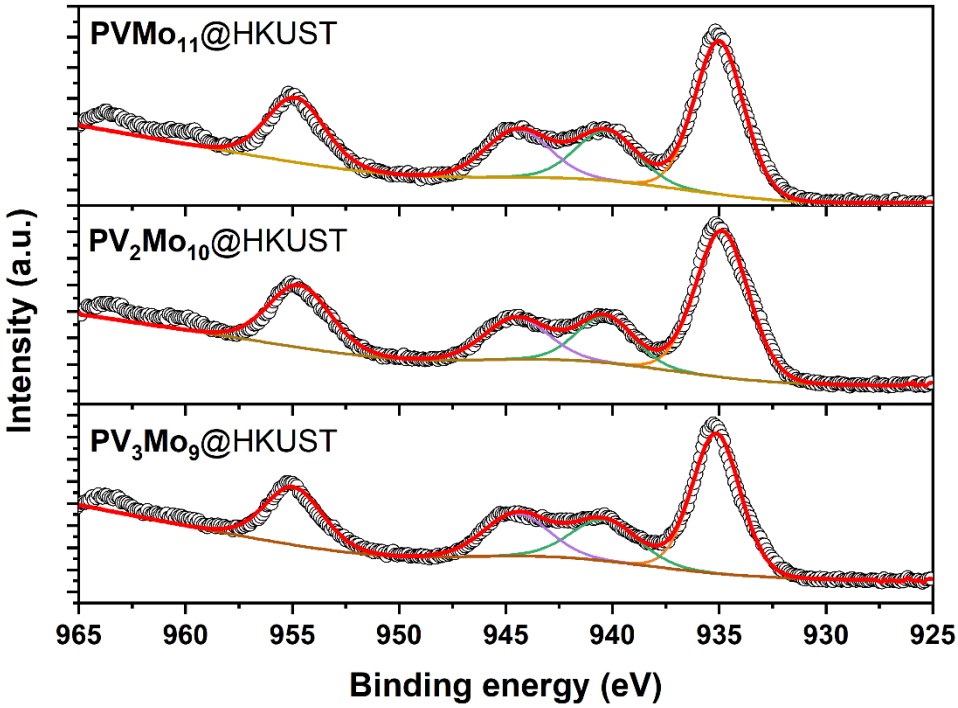

Figure 4.20. **PVMo**@HKUST (n= 0-3) XPS spectra of Cu 2p.

The mechanism of RSH oxidation catalyzed by the homogeneous **PVMo**/Cu system was recently reported.[49] The heterogeneous POM@MOF requires a modified mechanism relative to freely-diffusing copper and phosphovanadomolybdate due to the confinement of Cu(II) and POM locations. The crystal structure of POM@MOF is given in Figure 4.3. Each POM is in proximity, on average, of two di-copper(II) groups. Cu, on average, binds two RSH and forms a polymeric network.[84,85] The $Cu^{II}(RSH)_2$ complex is a strong reducing agent in acetonitrile, and when POM is present, the former reduces the latter by one electron to form $Cu^{I}(RS\cdot)_2$ which then decomposes to Cu^{I} and RSSR products.[49] In the POM@MOF, each di-copper(II) site reduces the proximal POM by two electrons and generate a di-copper(I) site (Figure 4.21, eq 1). One possibility for the reoxidation process is that the di-copper(I) reacts with O_2 forming a peroxo-Cu^{II} intermediate, then the peroxo group is reduced to water after receiving two electrons from a reduced POM (eq 2.)[86] However, for the **PVW_{11}** and **XPW_{11}**@HKUST materials, the decomposition to stable Cu^{I} sites

indicates a lack of electron transfer between the POM and Cu nodes. Cu alone can catalyze the RSH oxidation in alkaline aqueous conditions,[87–91] and the mechanism is given in eq 3. Without a POM catalyst, the di-copper sites may result in Cu^{I}/RSH complexes.[84,85] The XPS data suggest that the Cu^{I}/RSH complex is inert to O_2.

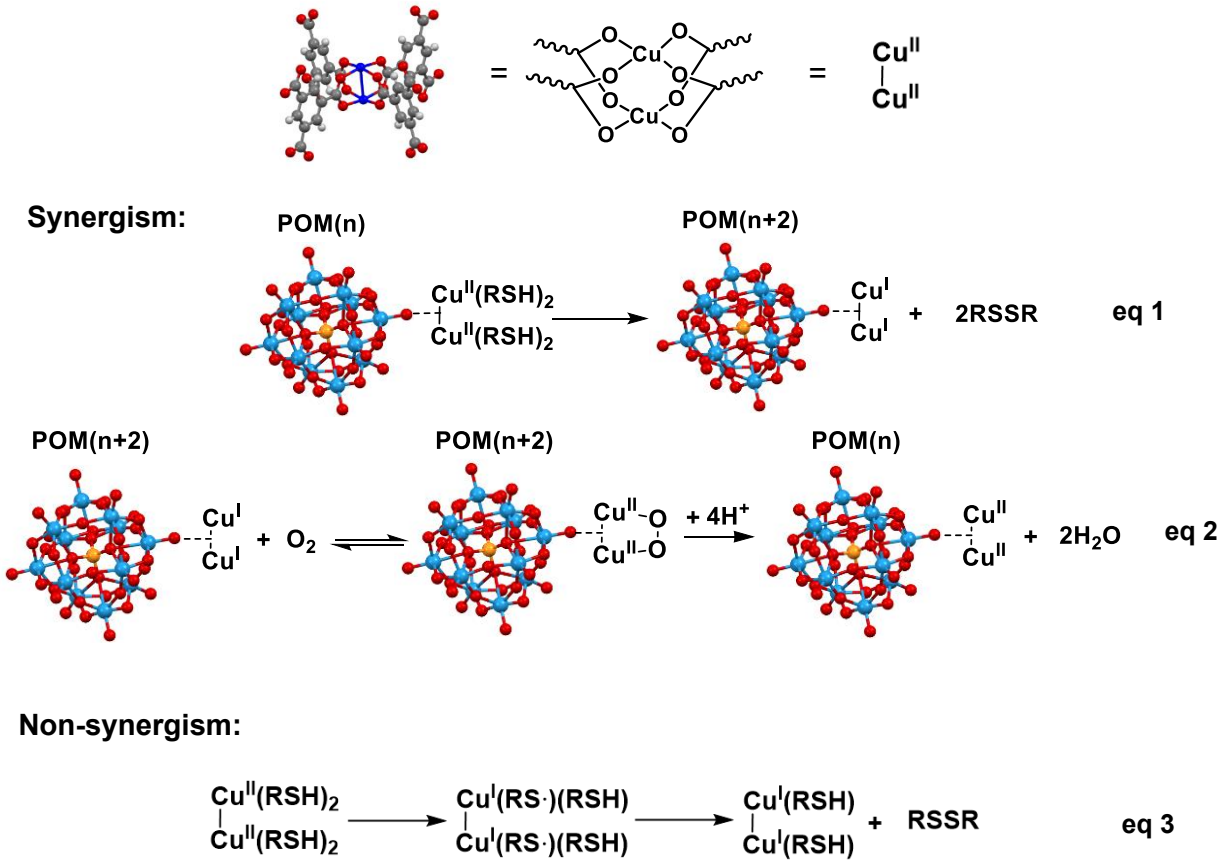

Figure 4.21. The proposed mechanism of POM@MOF catalyzed RSH aerobic oxidation.

The XPS survey spectra of **$CuPW_{11}$**@HKUST after RSH oxidation shows in Figure 4.22, compared to **PV_3Mo_9**@HKUST after reaction, S 2p peak at 163.5 eV can be observed. For **$CuPW_{11}$**@HKUST, the calculated atomic content (%) of Cu and S is 6.29 and 7.35 respectively (Table 4.2). Their ratio is close to 1: 1, and the slightly larger of S could be due to the trapped

unreacted RSH and product RSSR in MOF pores. The XPS results suggest the stable Cu^{I} site is di-Cu^{I}RSH complex

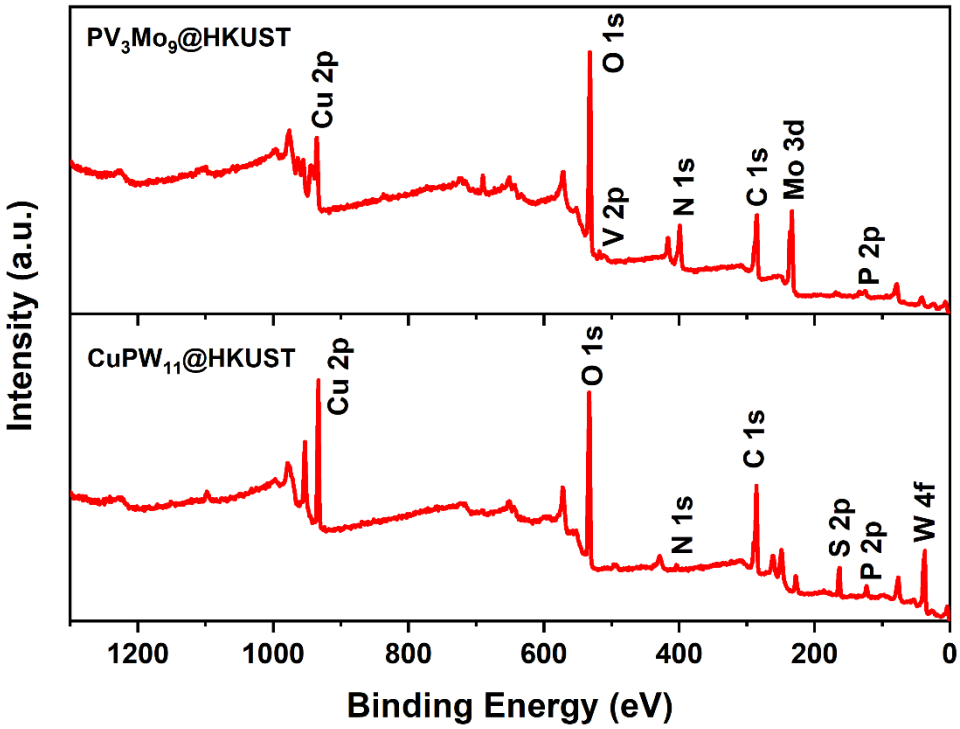

Figure 4.22. XPS survey spectra of **PV_3Mo_9**@HKUST and **$CuPW_{11}$**@HKUST after RSH oxidation.

Table 4.2. XPS survey peak table of **$CuPW_{11}$**@HKUST after RSH oxidation

Name	Start BE	Peak BE	End BE	Height CPS	FWHM eV	Area (P) CPS.eV	Atomic %
Cu2p	942.08	933.26	925.58	125500.7	2.62	391377.72	6.29
O1s	537.58	533	523.08	157488.52	3.27	552637.25	34.01
C1s	296.08	286.11	279.08	77090.97	2.97	311332.18	47.1
S2p	173.08	163.49	157.58	25725.21	1.76	87427.89	7.35
W4f	48.08	37.8	32.08	55626.81	4.11	244481.85	3.26
N1s	406.08	403.8	394.58	5371.03	3.03	21966.79	2

Homogeneous electron transfer between POM and Cu/RSH complex can be studied by stopped-flow spectroscopy. Previous work in aqueous buffer and acetonitrile shows that **PVMo** (x= 1-6) can transfer multiple electrons involving both V and Mo atoms depending on reaction

conditions, while **PVW** (x= 1, 3 and 6) can only transfer one electron independent of reactant concentrations.

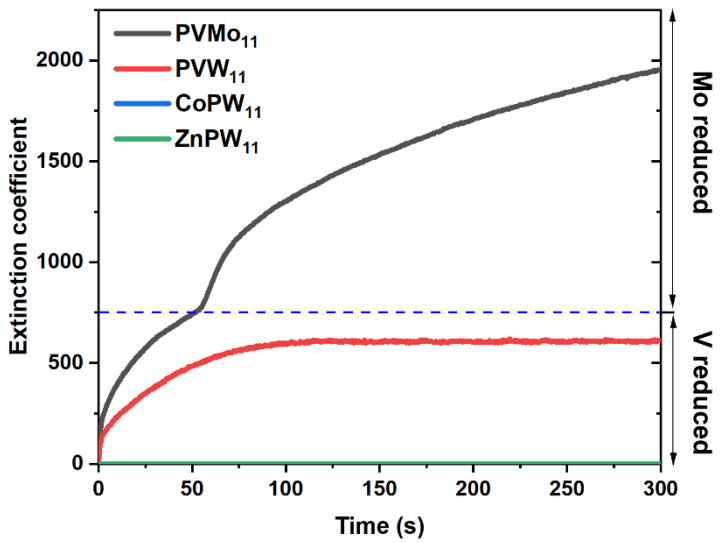

Figure 4.23. Kinetics of 0.5 mM **$PVMo_{11}$** and **PVW_{11}** reduction by 25 mM RSH under Ar catalyzed by 2 µM Cu(II) in pH = 2 H_2SO_4/Na_2SO_4 buffer, and 0.5 mM **$CoPW_{11}$** and **$ZnPW_{11}$** reduction by 25 mM RSH under Ar catalyzed by 10 µM Cu(II) in pH = 5 sodium acetate buffer.

Figure 4.23 shows the stopped-flow kinetics of **$PVMo_{11}$ and PVW_{11}** reduction in pH = 2 H_2SO_4/Na_2SO_4 buffer and **$CoPW_{11}$** and **$NiPW_{11}$** reduction in pH = 5 sodium acetate buffer by RSH catalyzed by µM quantities of Cu(II) under Ar (pH changed according to the stability of POM). **$PVMo_{11}$** exhibits two-stage kinetics that involves the Mo redox couple, while **PVW_{11}** only accepts one electron on a V atom; the W centers are not involved.

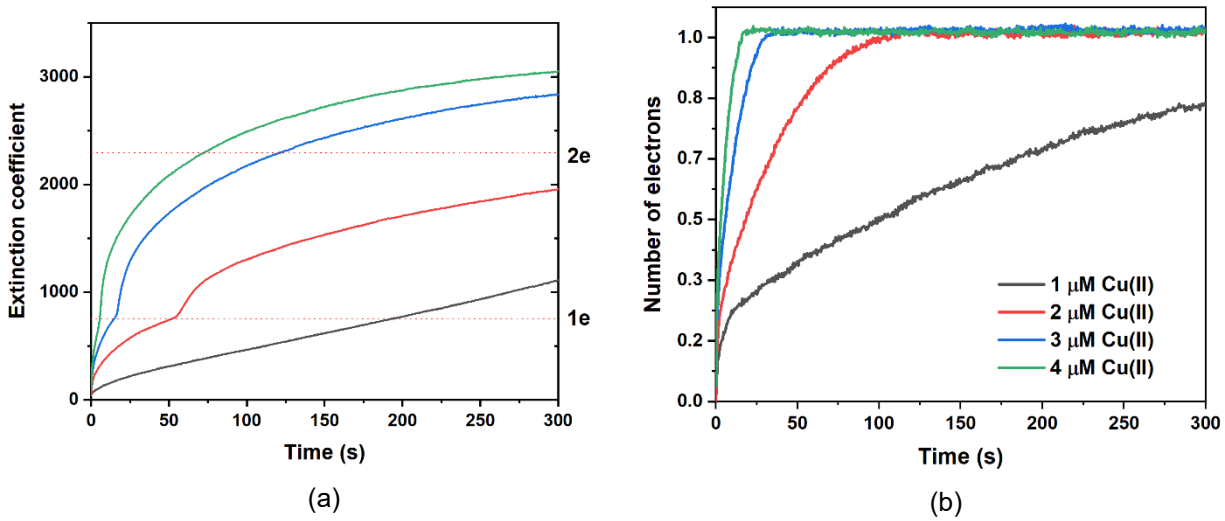

Figure 4.24. Kinetics of 0.5 mM (a) **PVMo$_{11}$** and (b) **PVW$_{11}$** reduction by 25 mM RSH under Ar. Cu(II) concentration dependence of the RSH reduction in pH = 2 H_2SO_4/Na_2SO_4 buffer.

The Cu concentration dependence is given in Figure 4.24. **PVMo$_{11}$** reduced more than two electrons by increasing the Cu concentration, while **PVW$_{11}$** only reduced one electron independent of Cu concentration. The transition metal substitute polytungstates are not reduced by Cu/RSH complex (Figure 4.23). Calibration of the extinction coefficient based on the number of electrons was by UV-vis spectra using bulk electrolysis, Figure 4.25. Based on our proposed mechanism above, POM should have multielectron transfer ability with di-copper thiol complexes. Therefore, the synergistic effects of **PVMo**@HKUST materials come from the fast and multielectron transfer between POM and Cu nodes on MOF.

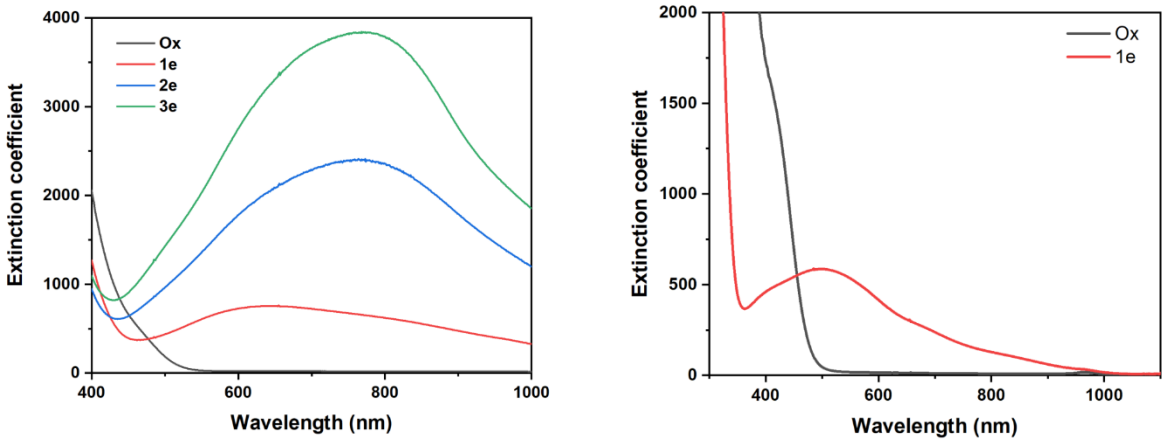

Figure 4.25. Bulk-electrolysis titration UV-vis spectra. (a) **PVMo$_{11}$**; (b) **PVW$_{11}$** in pH = 2 H_2SO_4/Na_2SO_4 buffer.

Cyclic voltammograms (CVs) show that **PVMo$_{11}$** and **PVW$_{11}$** have similar V redox potentials in both aqueous and acetonitrile solutions (4.26-4.27, Table 4.3-4.4). The Mo peaks have more positive potential than W peaks.[92]

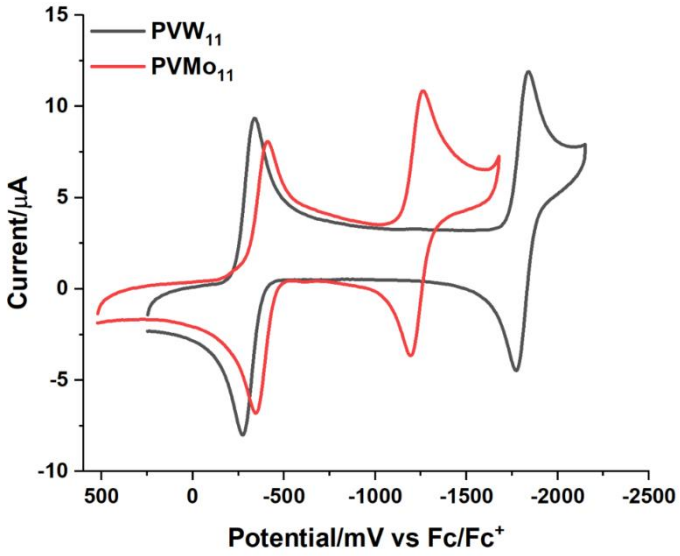

Figure 4.26. Black: cyclic voltammograms (CV) of 0.5 mM $TBA_4PVMo_{11}O_{40}$. Red: CV of 0.5 mM $TBA_4PVW_{11}O_{40}$. Conditions: acetonitrile, 0.1 M n-Bu_4NPF_6, scan rate = 100 mV s^{-1}, T = 298 K.

Table 4.26. Formal potentials ($E_{1/2}$) of V centers in the POM.

	PVW_{11}	**$PVMo_{11}$**
$E_{1/2}^1$ (V)	-338.6	-380.3
$E_{1/2}^2$ (Mo)	-1809.3	-1227.8

Data from figure 4.26. E (mV) vs Fc/Fc^+

$PVMo_{11}$@HKUST and **PVW_{11}**@HKUST cyclic voltammograms (CVs) were collected by immobilizing the materials on glassy carbon working electrodes (Figure 4.27). The observed V peaks in both POM@MOFs have potentials close to those of their homogeneous vanadium-containing POM counterparts.[41,57,93]

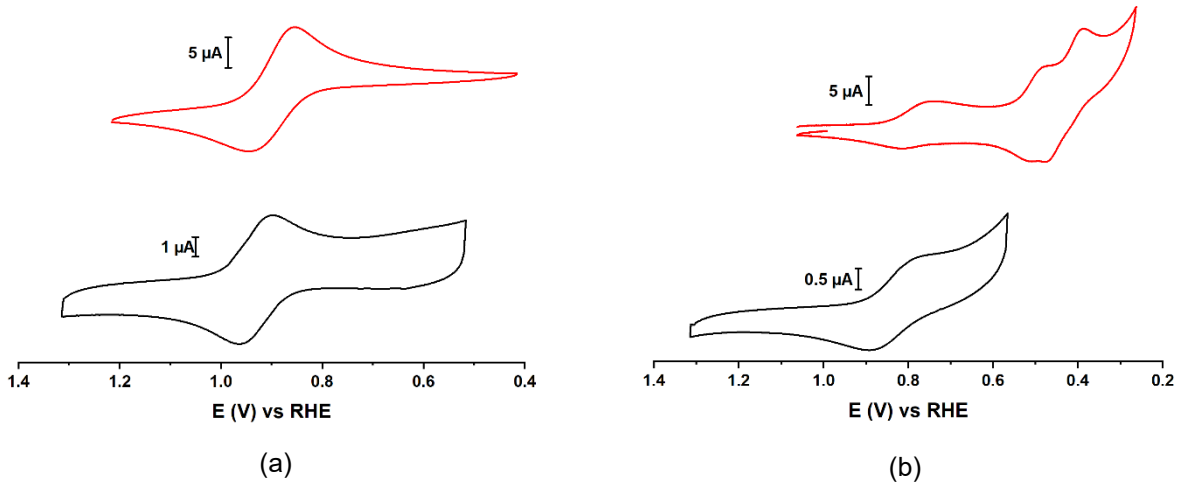

Figure 4.27. (a) Black: cyclic voltammograms (CV) of 0.5 mM homogeneous $H_3PVW_{11}O_{40}$ on glassy carbon (GC) electrode. Red: CV of **PVW_{11}**@HKUST immobilized on GC electrode. (b) Black: CV of 0.5 mM homogeneous $H_3PVMo_{11}O_{40}$ on GC electrode. Red: CV of **$PVMo_{11}$**@HKUST immobilized on GC electrode Conditions: pH =2 H_2SO_4/Na_2SO_4 buffer, 0.1 M KNO_3, scan rate, v = 100 mV s^{-1}, T = 298 K. The immobilization can be proved by the linear relationship of I vs v in figure 4.28.

Thermodynamically, Mo centers are much easier to reduce than W centers in the same POM structure, thus the former centers are more likely to engage in redox processes than the latter. This agrees with the fact that **PVMo** can transfer multiple electrons including both V and Mo centers;

whereas, **PVW** under identical experimental conditions, can only transfer one electron to a V center.

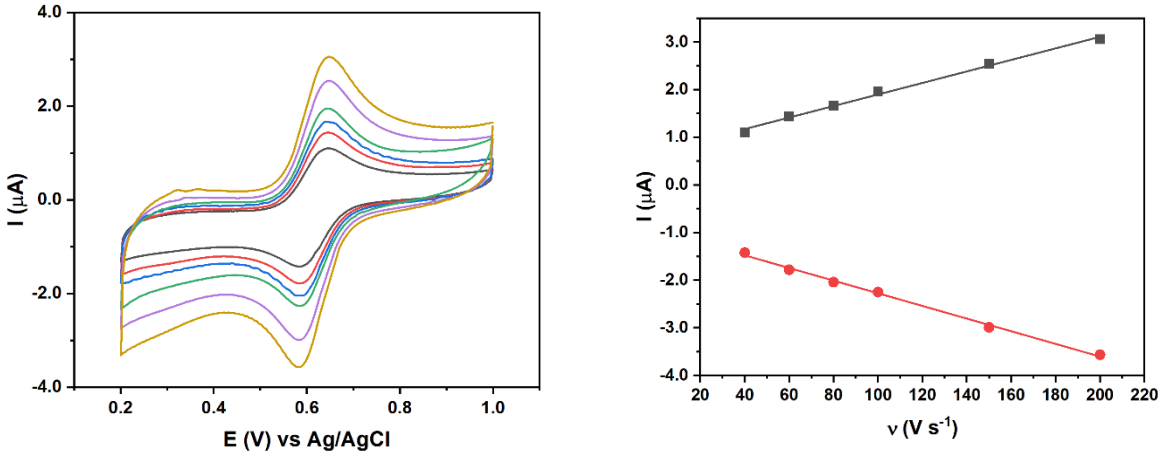

Figure 4.28. (a) Cyclic voltammograms (CV) of **PVW_{11}**@HKUST immobilized on the glassy carbon (GC) electrode at different scan rate. (b) Plots of i_{pc} and i_{pa} vs scan rate, v. Conditions: pH =2 H_2SO_4/Na_2SO_4 buffer, 0.1 M KNO_3.

Figure 4.29 shows the CVs of $CoPW_{11}$ and $NiPW_{11}$ in pH = 5 acetate buffer. Both POM have two redox peaks at negative potential (vs RHE). Transition metal redox peaks are mixed with W redox peaks thus give weak oxidative ability than PVW_{11}.[68]

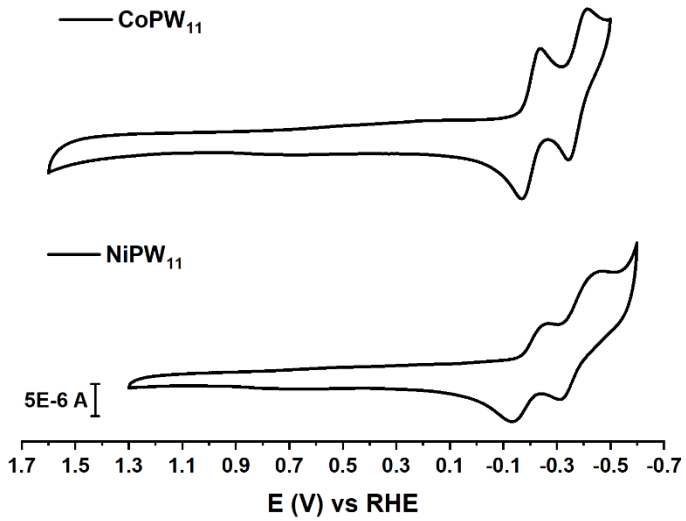

Figure 4.29. Cyclic voltammograms (CVs) of 0.5 mM $K_5CoPW_{11}O_{39}$ and $K_5NiPW_{11}O_{39}$. Conditions: pH = 5 acetate buffer, 0.1 M KNO_3, scan rate, v = 100 mV s^{-1}, T = 298 K.

4.4 Conclusions

In this work, we show compelling evidence of synergistic electron transfer between POM and MOF framework in a host-guest structure for **PVMo**@HKUST materials. The kinetic and thermodynamic results indicate that **XPW11** and **PVW11** have limited electron transfer ability with Cu, thus when all the Cu(II) is reduced to Cu(I) through eq 3, no Cu(II) sites remain in the MOF. As a result, the aerobic thiol removal reaction has limited conversion. The Cu(I) sites in the MOF nodes cannot been reoxidized back to Cu(II) through eq 2, resulting in MOF framework distortion. Therefore, POM@MOF synergism regarding activity parallels this synergism for POM@MOF stability.

4.5 References

1 J. X. Liu, X. B. Zhang, Y. L. Li, S. L. Huang and G. Y. Yang, *Coord. Chem. Rev.*, 2020, **414**, 213260.

2 D. Y. Du, J. S. Qin, S. L. Li, Z. M. Su and Y. Q. Lan, *Chem. Soc. Rev.*, 2014, **43**, 4615–4632.

3 J. Sun, S. Abednatanzi, P. Van Der Voort, Y. Y. Liu and K. Leus, *Catalysts*, 2020, **10**, 578.

4 M. Samaniyan, M. Mirzaei, R. Khajavian, H. Eshtiagh-Hosseini and C. Streb, *ACS Catal.*, 2019, **9**, 10174–10191.

5 M. Genovese and K. Lian, *Curr. Opin. Solid State Mater. Sci.*, 2015, **19**, 126–137.

6 Y. Liu, C. Tang, M. Cheng, M. Chen, S. Chen, L. Lei, Y. Chen, H. Yi, Y. Fu and L. Li, *ACS Catal.*, 2021, **11**, 13374–13396.

7 M. T. Pope and A. Müller, *Angew. Chemie Int. Ed. English*, 1991, **30**, 34–48.

8 C. L. Hill and C. M. Prosser-McCartha, *Coord. Chem. Rev.*, 1995, **143**, 407–455.

9 C. L. Hill, L. Delannoy, D. C. Duncan, I. A. Weinstock, R. F. Renneke, R. S. Reiner, R. H. Atalla, J. W. Han, D. A. Hillesheim, R. Cao, T. M. Anderson, N. M. Okun, D. G. Musaev and Y. V. Geletii, *Comptes Rendus Chim.*, 2007, **10**, 305–312.

10 S. S. Wang and G. Y. Yang, *Chem. Rev.*, 2015, **115**, 4893–4962.

11 I. V. Kozhevnikov, *Chem. Rev.*, 1998, **98**, 171–198.

12 I. V. Kozhevnikov, *J. Mol. Catal. A Chem.*, 1997, **117**, 151–158.

13 R. Neumann, *Inorg. Chem.*, 2010, **49**, 3594–3601.

14 I. A. Weinstock, R. E. Schreiber and R. Neumann, *Chem. Rev.*, 2018, **118**, 2680–2717.

15 Noritaka Mizuno and Makoto Misono*, *Chem. Rev.*, 1998, **98**, 199–217.

16 J. J. Walsh, A. M. Bond, R. J. Forster and T. E. Keyes, *Coord. Chem. Rev.*, 2016, **306**, 217–234.

17 T. Yamase, *Chem. Rev.*, 1998, **98**, 307–325.

18 E. Papaconstantinou, *Chem. Soc. Rev.*, 1989, **18**, 1–31.

19 C. Streb, *Dalt. Trans.*, 2012, **41**, 1651–1659.

20 J. M. Cameron, D. J. Wales and G. N. Newton, *Dalt. Trans.*, 2018, **47**, 5120–5136.

21 I. A. Weinstock, *Chem. Rev.*, 1998, **98**, 113–170.

22 M. Sadakane and E. Steckhan, *Chem. Rev.*, 1998, **98**, 219–237.

23 Noritaka Mizuno and Makoto Misono, *Chem. Rev.*, 1998, **98**, 199–217.

24 V. G. Snider and C. L. Hill, *J. Hazard. Mater.*, 2023, **442**, 130015.

25 H. Ma, B. Liu, B. Li, L. Zhang, Y. G. Li, H. Q. Tan, H. Y. Zang and G. Zhu, *J. Am. Chem. Soc.*, 2016, **138**, 5897–5903.

26 L. Vilà-Nadal and L. Cronin, *Nat. Rev. Mater.*, , DOI:10.1038/natrevmats.2017.54.

27 H. Furukawa, K. E. Cordova, M. O'Keeffe and O. M. Yaghi, *Science (80-.).*

28 Q. Wang and D. Astruc, *Chem. Rev.*, 2020, **120**, 1438–1511.

29 Q. L. Zhu and Q. Xu, *Chem. Soc. Rev.*, 2014, **43**, 5468–5512.

30 J. L. C. Rowsell and O. M. Yaghi, *Microporous Mesoporous Mater.*, 2004, **73**, 3–14.

31 N. V. Maksimchuk, O. A. Kholdeeva, K. A. Kovalenko and V. P. Fedin, *Isr. J. Chem.*, 2011, **51**, 281–289.

32 J. Juan-Alcañiz, E. V. Ramos-Fernandez, U. Lafont, J. Gascon and F. Kapteijn, *J. Catal.*, 2010, **269**, 229–241.

33 G. Férey, C. Mellot-Draznieks, C. Serre, F. Millange, J. Dutour, S. Surblé and I. Margiolaki, *Science (80-.).*, 2005, **309**, 2040–2042.

34 J. Song, Z. Luo, D. K. Britt, H. Furukawa, O. M. Yaghi, K. I. Hardcastle and C. L. Hill, *J. Am. Chem. Soc.*, 2011, **133**, 16839–16846.

35 C. Y. Sun, S. X. Liu, D. D. Liang, K. Z. Shao, Y. H. Ren and Z. M. Su, *J. Am. Chem. Soc.*, 2009, **131**, 1883–1888.

36 L. Yang, H. Naruke and T. Yamase, *Inorg. Chem. Commun.*, 2003, **6**, 1020–1024.

37 S. Ahn, S. L. Nauert, C. T. Buru, M. Rimoldi, H. Choi, N. M. Schweitzer, J. T. Hupp, O. K. Farha and J. M. Notestein, *J. Am. Chem. Soc.*, 2018, **140**, 8535–8543.

38 C. T. Buru, A. E. Platero-Prats, D. G. Chica, M. G. Kanatzidis, K. W. Chapman and O. K. Farha, *J. Mater. Chem. A*, 2018, **6**, 7389–7394.

39 C. T. Buru, P. Li, B. L. Mehdi, A. Dohnalkova, A. E. Platero-Prats, N. D. Browning, K. W. Chapman, J. T. Hupp and O. K. Farha, *Chem. Mater.*, 2017, **29**, 5174–5181.

40 C. T. Buru, M. C. Wasson and O. K. Farha, *ACS Appl. Nano Mater.*, 2020, **3**, 658–664.

41 W. Salomon, C. Roch-Marchal, P. Mialane, P. Rouschmeyer, C. Serre, M. Haouas, F. Taulelle, S. Yang, L. Ruhlmann and A. Dolbecq, *Chem. Commun.*, 2015, **51**, 2972–2975.

42 W. Xie and F. Wan, *Chem. Eng. J.*, 2019, **365**, 40–50.

43 Y. L. Peng, J. Liu, H. F. Zhang, D. Luo and D. Li, *Inorg. Chem. Front.*, 2018, **5**, 1563–1569.

44 L. Zeng, L. Xiao, Y. Long and X. Shi, *J. Colloid Interface Sci.*, 2018, **516**, 274–283.

45 R. Li, X. Ren, J. Zhao, X. Feng, X. Jiang, X. Fan, Z. Lin, X. Li, C. Hu and B. Wang, *J. Mater. Chem. A*, 2014, **2**, 2168–2173.

46 Q. Y. Li, L. Zhang, Y. X. Xu, Q. Li, H. Xue and H. Pang, *ACS Sustain. Chem. Eng.*, 2019, **7**, 5027–5033.

47 S. Mukhopadhyay, J. Debgupta, C. Singh, A. Kar and S. K. Das, *Angew. Chemie - Int. Ed.*, 2018, **57**, 1918–1923.

48 G. Paille, M. Gomez-Mingot, C. Roch-Marchal, B. Lassalle-Kaiser, P. Mialane, M. Fontecave, C. Mellot-Draznieks and A. Dolbecq, *J. Am. Chem. Soc.*, 2018, **140**, 3613–3618.

49 X. Lu, T. Cheng, Y. V. Geletii and C. L. Hill, *Inorg. Chem.*, 2023, **5**, 2404–2414.

50 C. L. Lu, X; Geletii, Y. V.; Cheng, T;Hill, Role of multiple vanadium centers on redox buffering and rates of polyvanadomolybdate-Cu(II)-catalyzed aerobic oxidations, 10.1021/acs.inorgchem.3c00469.

51 Y. Liu, S. Liu, S. Liu, D. Liang, S. Li, Q. Tang, X. Wang, J. Miao, Z. Shi and Z. Zheng, *ChemCatChem*, 2013, **5**, 3086–3091.

52 X. Zhong, Y. Lu, F. Luo, Y. Liu, X. Li and S. Liu, *Chem. - A Eur. J.*, 2018, **24**, 3045–3051.

53 J. Zhu, P. C. Wang and M. Lu, *Catal. Sci. Technol.*, 2015, **5**, 3383–3393.

54 J. Zhu, M. N. Shen, X. J. Zhao, P. C. Wang and M. Lu, *Chempluschem*, 2014, **79**, 872–878.

55 X. Xu, S. Chen, Y. Chen, H. Sun, L. Song, W. He and X. Wang, *Small*, 2016, **12**, 2982–2990.

56 H. Yang, J. Li, L. Wang, W. Dai, Y. Lv and S. Gao, *Catal. Commun.*, 2013, **35**, 101–104.

57 E. Rafiee and N. Nobakht, *J. Mol. Catal. A Chem.*, 2015, **398**, 17–25.

58 Y. Liu, S. Liu, D. He, N. Li, Y. Ji, Z. Zheng, F. Luo, S. Liu, Z. Shi and C. Hu, *J. Am. Chem. Soc.*, 2015, **137**, 12697–12703.

59 L. H. Wee, S. R. Bajpe, N. Janssens, I. Hermans, K. Houthoofd, C. E. A. Kirschhock and J. A. Martens, *Chem. Commun.*, 2010, **46**, 8186–8188.

60 Z. Wang and Q. Chen, *Green Chem.*, 2016, **18**, 5884–5889.

61 L. H. Wee, C. Wiktor, S. Turner, W. Vanderlinden, N. Janssens, S. R. Bajpe, K. Houthoofd, G. Van Tendeloo, S. De Feyter, C. E. A. Kirschhock and J. A. Martens, *J. Am. Chem. Soc.*, 2012, **134**, 10911–10919.

62 D. Mustafa, E. Breynaert, S. R. Bajpe, J. A. Martens and C. E. A. Kirschhock, *Chem. Commun.*, 2011, **47**, 8037–8039.

63 D. P. Smith and M. T. Pope, *Inorg. Chem.*, 1973, **12**, 331–336.

64 A. G. MacDiarmid, *Inorganic Syntheses(BOOK)*, 2007, vol. 17.

65 G. A. Tsigdinos and C. J. Hallada, *Inorg. Chem.*, 1968, **7**, 437–441.

66 C. M. Tourné, G. F. Tourné, S. A. Malik and T. J. R. Weakley, *J. Inorg. Nucl. Chem.*, 1970, **32**, 3875–3890.

67 T. J. R. Weakley and S. A. Malik, *J Inorg Nucl Chem*, 1967, **29**, 2935–2944.

68 J. H. Choi, J. K. Kim, D. R. Park, T. H. Kang, J. H. Song and I. K. Song, *J. Mol. Catal. A*

Chem., 2013, **371**, 111–117.

69 F. Ma, S. Liu, C. Sun, D. Liang, G. Ren and F. Wei, *J Am Chem Soc*, 2011, **133**, 4178–4187.

70 C. R. W. and M. Dincă, *Dalt. Trans.*, 2012, **41**, 7782–7791.

71 S. R. Bajpe, C. E. A. Kirschhock, A. Aerts, E. Breynaert, G. Absillis, T. N. Parac-Vogt, L. Giebeler and J. A. Martens, *Chem. - A Eur. J.*, 2010, **16**, 3926–3932.

72 E. A. Nagul, I. D. McKelvie, P. Worsfold and S. D. Kolev, *Anal. Chim. Acta*, 2015, **890**, 60–82.

73 N. Maksimchuk, M. Timofeeva, M. Melgunov, A. Shmakov, Y. Chesalov, D. Dybtsev, V. Fedin and O. Kholdeeva, *J. Catal.*, 2008, **257**, 315–323.

74 N. V Maksimchuk, K. A. Kovalenko, S. S. Arzumanov, Y. A. Chesalov, M. S. Melgunov, A. G. Stepanov, V. P. Fedin and O. A. Kholdeeva, *Inorg. Chem.*, 2010, **49**, 2920–2930.

75 N. V. N. Maksimchuk, M. N. Timofeeva, M. S. Melgunov, A. N. A. Shmakov, Y. A. Chesalov, D. N. D. Dybtsev, V. P. Fedin and O. A. Kholdeeva, *J. Catal.*, 2008, **257**, 315–323.

76 N. V. N. Maksimchuk, M. N. Timofeeva, M. S. Melgunov, A. N. A. Shmakov, Y. A. Chesalov, D. N. D. Dybtsev, V. P. Fedin and O. A. Kholdeeva, *J. Catal.*, 2008, **257**, 315–323.

77 M. Yin, C. K. Wu, Y. Lou, C. Burda, J. T. Koberstein, Y. Zhu and S. O'Brien, *J. Am. Chem. Soc.*, 2005, **127**, 9506–9511.

78 C. Chen, T. Wu, D. Yang, P. Zhang, H. Liu, Y. Yang, G. Yang and B. Han, *Chem. Commun.*, 2018, **54**, 5984–5987.

79 T. Wei, M. Zhang, P. Wu, Y. J. Tang, S. L. Li, F. C. Shen, X. L. Wang, X. P. Zhou and Y. Q. Lan, *Nano Energy*, 2017, **34**, 205–214.

80 P. Zhu, X. Yang, X. Li, N. Sheng, H. Zhang, G. Zhang and J. Sha, *Dalt. Trans.*, 2019, **49**, 79–88.

81 H. Liu, L. G. Gong, C. X. Wang, C. M. Wang, K. Yu and B. Bin Zhou, *J. Mater. Chem. A*, 2021, **9**, 13161–13169.

82 P. St. Petkov, G. N. Vayssilov, J. Liu, O. Shekhah, Y. Wang, C. Wöll and T. Heine, *ChemPhysChem*, 2012, **13**, 2025–2029.

83 C. Chen, T. Wu, D. Yang, P. Zhang, H. Liu, Y. Yang, G. Yang and B. Han, *Chem. Commun.*, 2018, **54**, 5984–5987.

84 A. D. Leu and D. A. Armstrong, *J. Phys. Chem.*, 1986, **90**, 1449–1454.

85 V. Vortisch, P. Kroneck and P. Hemmerich, *J. Am. Chem. Soc.*, 1976, **98**, 2821–2826.

86 R. Trammell, K. Rajabimoghadam and I. Garcia-Bosch, *Chem. Rev.*, 2019, **119**, 2954–3031.

87 G. A. Bagiyan, I. K. Koroleva, N. V. Soroka and A. V. Ufimtsev, *Russ. Chem. Bull.*, 2003, **52**, 1135–1141.

88 G. Scrivens, B. C. Gilbert and T. C. P. Lee, *J. Chem. Soc. Perkin Trans. 2*, 1995, **9**, 955–963.

89 M. G. Gantman, I. G. Tarkhanova and Y. G. Kolyagin, *J. Sulfur Chem.*, 2016, **37**, 501–514.

90 P. W. Albro, J. T. Corbett and J. L. Schroeder, *J. Inorg. Biochem.*, 1986, **27**, 191–203.

91 G. A. Bagiyan, I. K. Koroleva, N. V. Soroka and A. V. Ufimtsev, *Kinet. Catal.*, 2004, **45**, 372–380.

92 J. J. Altenau, M. T. Pope, R. A. Prados and H. So, *Inorg. Chem.*, 1975, **14**, 417–421.

93 † Diana M. Fernandes,† André D. S. Barbosa,† João Pires,‡ Salete S. Balula,† Luís Cunha-Silva,*,† and Cristina Freire*, *ACS Appl. Mater. Interfaces*, 2013, **5**, 13382–13390.

Chapter 5

$Na_4W_{10}O_{32}$-stabilized Pt(0) nanoparticles for the conversion of light to chemical energy via alkane dehydrogenation

Abstract

The development of cost-effective systems for alkane dehydrogenation to alkenes has been of widespread scientific and commercial interest the past few decades. Despite plenty of research in the field of thermal dehydrogenation of alkanes, relatively little progress has been made in photochemical alkane dehydrogenation. Here, we report the photochemical synthesis of $Na_4W_{10}O_{32}$-stabilized (~20 nm) Pt(0) nanoparticles (NPs) that efficiently catalyze the photodehydrogenation of alkanes at room temperature, a process that is endothermic and endoergic in the dark, and for which $W_{10}O_{32}^{4-}$ salts or Pt(0) particles alone are completely inactive. These hybrid $Na_4W_{10}O_{32}$-stabilized Pt(0) nanoparticles (W_{10}-PtNPs) exhibit high efficiency (quantum yields ~0.10 and turnover numbers ~100) and high selectivity (~80%) for alkene and can be isolated and reused.

5.1 Introduction

The dehydrogenation of alkanes to alkenes is one of the most investigated areas in organic synthesis and has received considerable attention from the petrochemical industry because of the increasing global demand for light alkenes.[1,2] The majority of research has focused on thermal alkane dehydrogenation with metal and metal oxide catalysts, which suffer from harsh reaction conditions and low conversion rate. For example, the Pt/TiO_2-Al_2O_3 catalyst for propane dehydrogenation operates at 873 K and results in only a ca. 50% conversion to propene.[3] Homogenous catalysts such as iridium pincer complexes, i.e., (^{t}Bu4PCP)Ir, drive reactions at lower temperature and are more efficient for alkene production, but these processes require a sacrificial alkene reagent, M, as the hydrogen acceptor (eq 1).[4–7] The direct photocatalytic dehydrogenation

of hydrocarbons, eq 5.2, is highly desirable, but the unfavorable thermodynamics and kinetics (cleavage of unactivated C-H bonds) makes it as difficult to achieve as it is attractive. There are reports of photocatalytic alkane dehydrogenation, but these have limitations. One system uses Vaska-type rhodium complexes $[RhCl(CO)(PR_3)_2]$ (R = Me, Et, and Ph) as the alkane photodehydrogenation catalyst.[8–10] However, the recyclability of these photocatalysts is poor and key features of the mechanisms remain unclear.

$$\text{alkane} + M \rightarrow \text{alkene} + MH_2 \quad (5.1)$$

$$\text{alkane} + h\nu \rightarrow \text{alkene} + H_2 \quad (5.2)$$

We reported that polyoxometalates (POMs), metal-oxo clusters of high-valent early-transition metals (V, Mo, W, Nb, and Ta),[11–14] including decatungstate, $W_{10}O_{32}^{4-}$, photocatalyze alkane C-H bond cleavage under some conditions,[15,16] a process that has been recently used by several groups in C-H bond functionalization chemistry.[17–21] Decatungstate has also been combined with cobaloxime pyridine chloride to achieve cooperative hydrogen atom transfer for photochemical alkane dehydrogenation,[22] which demonstrates the important role of decatungstate in alkane dehydrogenation.

While POMs in the absence of a hydrogen evolution catalyst are very poor at evolving H_2, we reasoned that having intimate and molecular communication between the photocatalyst (light-absorber and hydrogen-atom abstractor, namely, $W_{10}O_{32}^{4-}$) and a hydrogen evolution catalyst (HEC) would significantly facilitate eq 5.2. This process constitutes an alternative route to solar fuel (H_2) complementing conventional artificial photosynthesis (photoreduction of H_2O and/or CO_2) given that eq 5.2 is thermodynamically uphill. It is endothermic and endogenic by up to 40

kcal mol^{-1} depending on the hydrocarbon reactant, and thus requires light to proceed and converts light to chemical energy.

We report here that $Na_4W_{10}O_{32}$-stabilized Pt(0) nanoparticles (NPs) (20 nm), **W_{10}-PtNPs**, can be prepared by a facile one-pot photochemical synthesis, and that this hybrid nanosystem photodehydrogenates alkanes, eq 5.2, at ambient temperature with near-UV light and can be re-used.

5.2 Experimental

5.2.1 General Materials and Methods

All chemical reagents were purchased from Sigma-Aldrich Chemical Co. (St. Louis, MO) and were used directly without further purification. UV-Vis spectra were recorded with an Agilent 8453 spectrophotometer equipped with a diode array detector using a 1.0-cm optical path length quartz cuvette. Infrared spectra (2% sample in KBr pellet) were recorded on a Nicolet TM 6700 Fourier transform infrared (FT-IR) spectrometer. Transmission electron microscopy (TEM) measurements were conducted on a Hitachi H-7500 transmission electron microscope at an accelerating voltage of 80 kV in the Robert P. Apkarian Integrated Electron Microscopy Core at Emory University. Dynamic light scattering (DLS) data were acquired on a NanoPlus DLS Particle Size Analyzer instrument (Particulate Systems, Norcross, GA). ^{1}H nuclear magnetic resonance (NMR) spectra were acquired on a Varian INOVA 400 spectrometer using deuterated chloroform (δ 7.24) as an external standard. Product distributions and gas phase samples were analyzed by gas chromatography (GC) using an Agilent 7890 gas chromatograph with a 5 Å molecular sieve column and argon carrier gas.

5.2.2 Synthesis of $Na_4W_{10}O_{32}$-stabilized Pt Nanoparticles

Synthesis of $Na_4W_{10}O_{32}$-stabilized Pt nanoparticles (**W_{10}-PtNPs**): $Na_4W_{10}O_{32}$ was synthesized according to previous reports.[23–25] A 5 mL aqueous solution of 0.7mM $Na_4W_{10}O_{32}$, 10 mM H_2PtCl_6, and 0.5 M 2-propanol was put into a 1-cm pathlength cell deareated with argon and covered with a plastic cap. The solution was stirred and irradiated with 365 nm LED light; the intensity incident on the cell, measured by a digital light meter, was 5.0 mW/cm^2. The color of the solution quickly turned dark blue and then gradually changed to dark brown. The dark brown solution was centrifuged at 5,000 rpm for 10 min, the resulting supernatant decanted via pipette, and the remaining solids redissolved in water.

5.2.3 Photocatalytic Alkane Dehydrogenation

W_{10}-PtNPs (5 mg) were dispersed in 5 mL of CH_3CN containing 50 mM alkane in a 1 cm pathlength cell which was then deareated with argon and covered with a plastic cap. The solution was stirred and irradiated with 365 nm LED light, the intensity of which on the cell was measured to be 5.0 mW/cm^2. Control experiments were conducted using (a) $Na_4W_{10}O_{32}$ and platinum black mixture with light, (b) only $Na_4W_{10}O_{32}$(s) with light, (c) only platinum black with light, and (d) **W_{10}-PtNPs** without light. The ratio of $Na_4W_{10}O_{32}$ to platinum black equaled that in **W_{10}-PtNPs**. The reaction conversion and selectivity for alkene product were determined by nuclear magnetic resonance (NMR) spectroscopy. The amount of the hydrogen gas was quantified by gas chromatography (GC). The difference between the moles of alkene and hydrogen was within 5% throughout the experiment, thus validating equation 2. The quantum efficiency (QE) was measured using the following equation: QE = 2 ^{x} N(alkene) / N(photons). To assess the recyclability of **W_{10}-PtNPs**, the solution after the initial catalytic photodehydrogenation was centrifuged at 5000 rpm

for 10 minutes; the **W_{10}-PtNPs** were collected and re-dispersed in a fresh 5-mL CH_3CN solution 50 mM in alkane for subsequent runs.

5.3 Results and Discussion

5.3.1 Characterization of $Na_4W_{10}O_{32}$-stabilized Pt Nanoparticles

The binary nanosystem was prepared using a one-pot photoredox reaction and characterized by a range of physical methods under heterogeneous conditions. No $Na_4W_{10}O_{32}$ dissociates from the Pt NPs. The synthesis involves mixing hexachloroplatinic acid, sodium decatungstate, and 2-propanol in a deaerated aqueous solution and irradiating with 365 nm LED light. The decatungstate excited state is first reduced by 2-propanol and the resulting dark-blue, reduced POM then reduces Pt(IV) to Pt(0). The decatungstate molecules rapidly bind to the surfaces of the nascent Pt(0) NPs forming the **W_{10}-PtNPs**.[26] The UV-Vis spectra of reduced $Na_4W_{10}O_{32}$ and the $Na_4W_{10}O_{32}$-stabilized Pt nanoparticles, **W_{10}-PtNPs**, are shown in Figure 5.1.

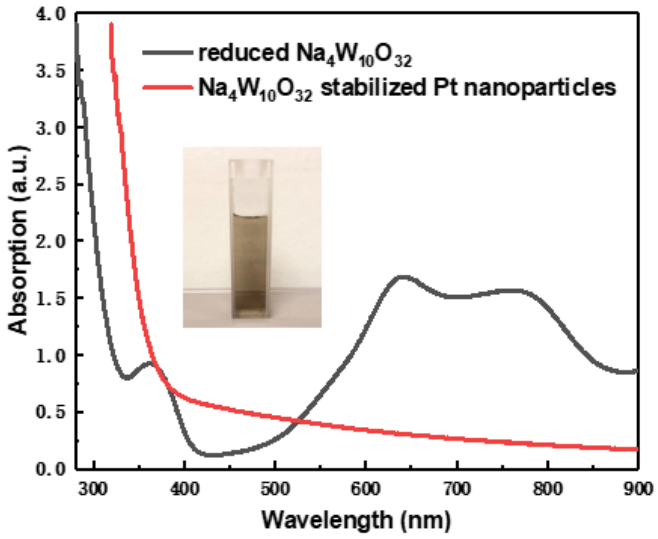

Figure 5.1. UV-Vis spectra of reduced $Na_4W_{10}O_{32}$ and the **W_{10}-PtNPs**. Inset: Photograph of the **W_{10}-PtNPs** in a 1-cm quartz cuvette.

The final solution is dark-brown which is in good agreement with previously reported Pt nanoparticle solution. It is worth noting here that a similar preparation using $(TBA)_4W_{10}O_{32}$ instead of $Na_4W_{10}O_{32}$ in an organic solvent failed. The sterically large tetra0n-butylammonium counter-cations of decatungstate likely prevent the close POM-Pt interaction seen in the case of the **W_{10}-PtNPs**. The **W_{10}-PtNPs** solution could be centrifuged, the supernatant decanted to to remove unreacted $W_{10}O_{32}^{4-}$ and $PtCl_6^{2-}$, and then redissolved in water. This process was repeated several times to prepare fresh **W_{10}-PtNP** powder and the corresponding solutions for subsequent characterization and photocatalytic reactions.

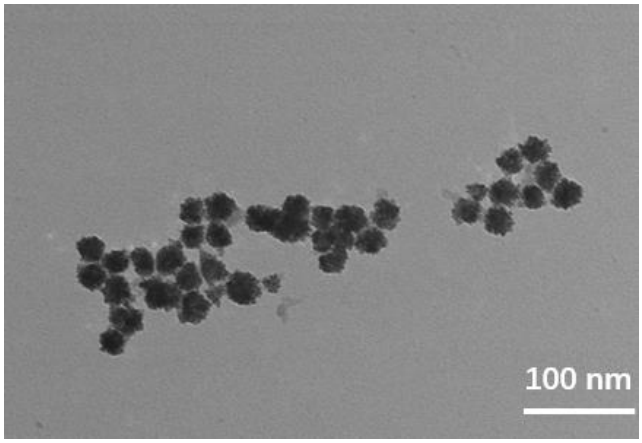

Figure 5.2. Transmission electron microscopy (TEM) image of the **W_{10}-PtNPs**.

The transmission electron microscopy (TEM) image (Figure 5.2) shows that the **W_{10}-PtNPs** have a spherical morphology, and dynamic light scattering (DLS) data (Figure 5.3) reveal that the average size of **W_{10}-PtNPs** is ca. 20 nm.

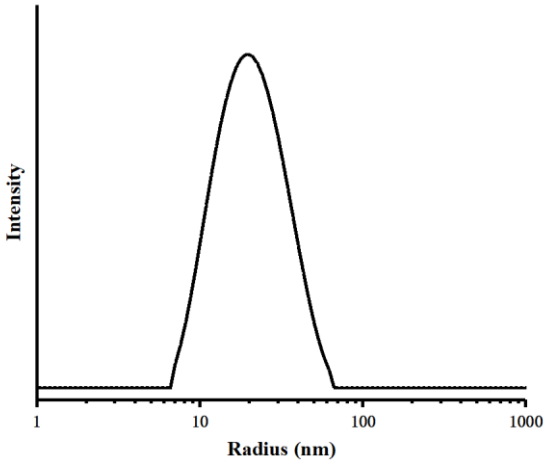

Figure 5.3. Dynamic light scattering (DLS) data of **W_{10}-PtNPs**.

5.3.2 Reactivity and Stability of the W_{10}-PtNPs

The photodehydrogenation of alkanes by the **W_{10}-PtNPs** is conducted with these nanoparticles suspended in a solution of acetonitrile and alkane in which $Na_4W_{10}O_{32}$ is insoluble. This prevents dissociation of $W_{10}O_{32}^{4-}$ from the Pt(0) surfaces. This lack of $W_{10}O_{32}^{4-}$ dissociation is readily detected by UV-Vis spectroscopy because decatungstate has a very high absorbance in the UV region (see Figure 5.1). In contrast, $Na_4W_{10}O_{32}$ does dissociate from Pt when **W_{10}-PtNPs** are dissolved in an acetonitrile/water mixed solvent. **W_{10}-PtNPs** dissolve in a 9/1 v/v, CH_3CN/H_2O solvent system and catalyze alkane dehydrogenation as described in the experimental section. Under these conditions, $W_{10}O_{32}^{4-}$ is fairly effective at preventing rapid aggregation of Pt(0) particles to microscale or macroscale ones. However, $W_{10}O_{32}^{4-}$ does dissociate form the Pt(0) surfaces generating the POM in solution after the catalytic reaction. This is proved by the zeta potential of the solution, which changes from -36.2 mV before the reaction to -9.5 mV after the

reaction. Since the anionic polyoxometalates contribute to most of the zeta potential, the notable change suggests that a significant number of POMs dissociate from the Pt(0) NP surfaces. It is worth noting here that the average size of **W_{10}-PtNPs** doesn't change much after the reaction because the ~20 nm Pt nanoparticles are remain protected by the remaining decatungstate molecules. As a consequence, all **W_{10}-PtNPs**-catalyzed reactions are conducted in pure acetonitrile where $Na_4W_{10}O_{32}$ is insoluble preventing any detectable dissociation of the POM from the Pt surfaces.

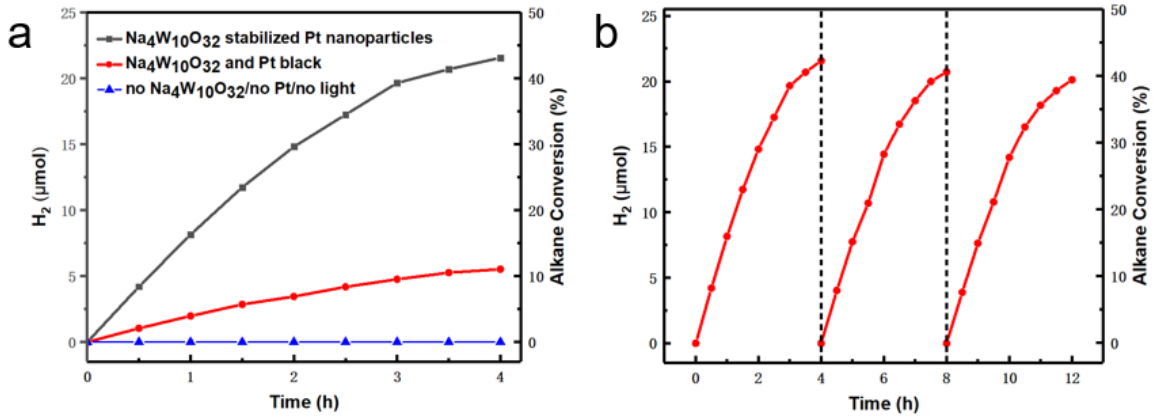

Figure 5.4. (a) Time course for dehydrogenation of 50 mM 2,3-dimethylbutane photocatalyzed by the **W_{10}-PtNPs** (black) and a mixture of $Na_4W_{10}O_{32}$ and Pt black (red). An CH_3CN solution of Pt with no $Na_4W_{10}O_{32}$ upon irradiation yields no reaction (blue). (b) Three sequential runs of 2,3-dimethylbutane dehydrogenation photocatalyzed by the **W_{10}-PtNPs**.

Figure 5.4 shows the reactivity and recyclability of **W_{10}-PtNPs** for the dehydrogenation of 2,3-dimethylbutane to 2,3-dimethylbutene and hydrogen gas. As shown in Figure 2a, $Na_4W_{10}O_{32}$-stabilized Pt nanoparticles achieve over 40% alkane conversion while $Na_4W_{10}O_{32}$ and platinum

black mixture under otherwise indentical conditions only transforms ~10% alkane. Alkene and hydrogen are not detected for experiments without either $Na_4W_{10}O_{32}$ or platinum or light. These results demonstrate the superior alkane dehydrogenation activity of **W_{10}-PtNPs** and the indispensable role of $Na_4W_{10}O_{32}$, platinum, and light in the photocatalysis. The specific mechanism of the reaction is discussed in the next section.

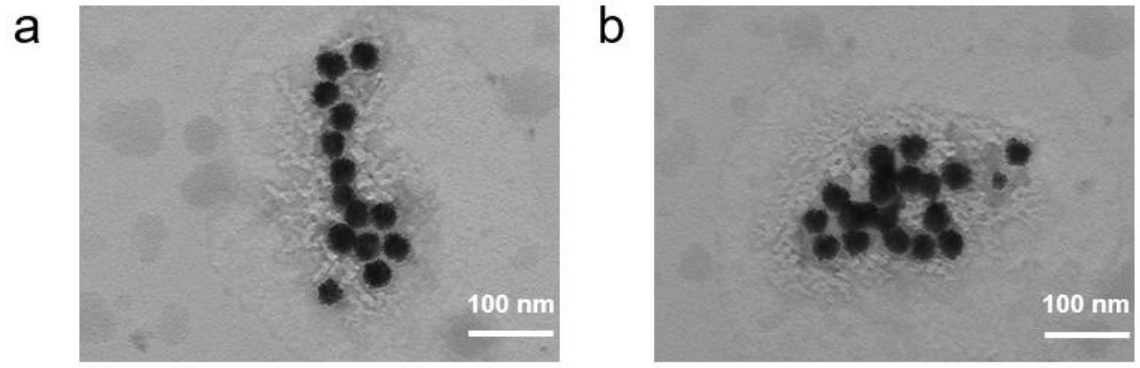

Figure 5.5. TEM images of the **W_{10}-PtNPs** (a) before and (b) after alkane dehydrogenation. Give specific conditions here (that gets us closer to what we need in the figure for the manuscript).

The **W_{10}-PtNP** solution appeared to be completely stable to aggregation for several months, thus to further assess stability, we evaluated the recyclability of these solutions after sequential photochemical alkane dehydrogenation reactions. Figure 2b shows that after over 10 hours of continuous reaction, the activity of **W_{10}-PtNPs** remains almost the same. The small diminution in activity can be ascribed to catalyst loss during recycling. The stability of **W_{10}-PtNPs** is also indicated by their TEM images (Figure 5.5) and fourier-transform infrared (FT-IR) spectra (Figure 5.6) as the particle sizes and the characteristic IR peaks of decatungstate before and after the photocatalytic alkane dehydrogenation are unchanged.

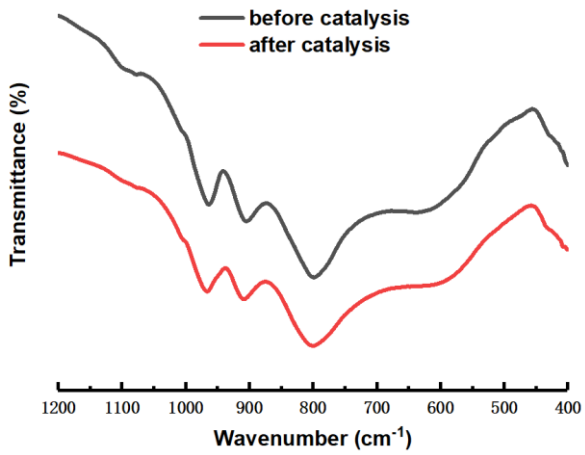

Figure 5.6. FT-IR spectra of **W_{10}-PtNPs** before (black) and after (red) alkane dehydrogenation.

We further explored other alkane substrates for dehydrogenation catalyzed by **W_{10}-PtNPs** and Table 1 summarizes the results. The alkene products are quantified by nuclear magnetic resonance (NMR) spectroscopy. Figure 5.7 shows 2,3-dimethylbutane dehydrogenation as an example. The quantum efficiency and yield are calculated accordingly as described above. As shown in Table 1, the major products of alkane dehydrogenation are the non-thermodynamic 1-alkenes. The logical explanation for these products is a kinetically-controlled alkane radical disproportionation reaction.[27] Other mechanisms, including oxidation of intermediate freely-diffusing alkyl radicals to carbocations, all preferentially produce the thermodynamic product, the most substituted alkene, 2,3-dimethyl-2-butene. The quantum efficiencies and yields decrease in the order 2,3-dimethylbutane > cycloolefins > n-alkanes which is consistent with the relative homolytic C-H bond dissociation energies and rate-limiting hydrogen atom abstraction (HAT) by the excited decatungstate.

Table 5.1. Photodehydrogenation of different alkanes at ambient temperature with 365-nm light.

Substrate	Product	Quantum Efficiency	Yield
2,3-dimethylbutane	2,3-dimethyl-1-butene	0.20	42%
cyclohexane	cyclohexene	0.07	15%
cyclooctane	cyclooctene	0.10	21%
n-heptane	1-heptene	0.02	4%
n-octane	1-octene	0.02	4%

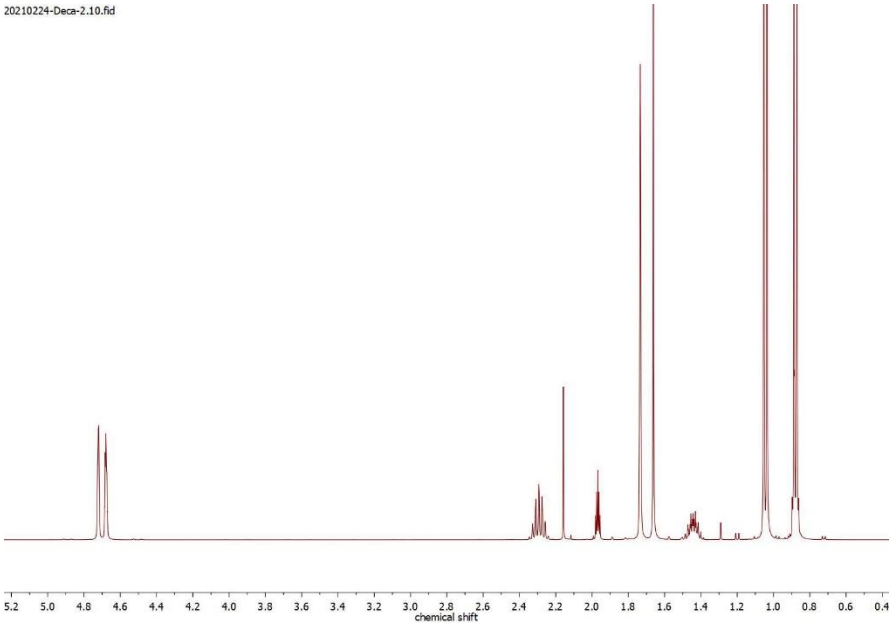

Figure 5.7. ^{1}H NMR of 2,3-Dimethylbutane dehydrogenation catalyzed by **W_{10}-PtNPs** after 2h.

5.4. Conclusions

$Na_4W_{10}O_{32}$-stabilized (~20 nm) Pt(0) nanoparticles (**W_{10}-PtNPs**) have been synthesized through a photochemical method and characterized by UV-Vis spectroscopy, FT-IR spectroscopy, transmission electron microscopy and dynamic light scattering. These **W_{10}-PtNPs** work as photocatalysts for alkane dehydrogenation at room temperature and are quite stable under turnover

conditions. **W_{10}-PtNPs** exhibit higher quantum efficiency and higher yield than a simple combination of $Na_4W_{10}O_{32}$ and platinum black. This better performance is attributed, in part, to smaller size and consequently higher specific surface area of **W_{10}-PtNP** relative to the POM and Pt(0) particles alone in the same molar concentrations. The superior catalytic activity of **W_{10}-PtNPs** opens up potential future applications of this photocatalytic and light-to-chemical-energy-converting chemistry involving other organic substrates.

5.5. References

1 S. R. Docherty, L. Rochlitz, P. A. Payard and C. Copéret, *Chem. Soc. Rev.*, 2021, 50, 5806–5822.

2 S. Chen, X. Chang, G. Sun, T. Zhang, Y. Xu, Y. Wang, C. Pei and J. Gong, *Chem. Soc. Rev.*, 2021, 50, 3315–3354.

3 F. Jiang, L. Zeng, S. Li, G. Liu, S. Wang and J. Gong, *ACS Catal.*, 2015, **5**, 438–447.

4 M. B. Alan S. Goldman, Amy H. Roy, Zheng Huang, Ritu Ahuja, William Schinski, *Science (80-.).*, 2006, 257–261.

5 R. Ahuja, B. Punji, M. Findlater, C. Supplee, W. Schinski, M. Brookhart and A. S. Goldman, *Nat. Chem.*, 2011, **3**, 167–171.

6 Y. Wang, Z. Huang, X. Leng, H. Zhu, G. Liu and Z. Huang, *J. Am. Chem. Soc.*, 2018, **140**, 4417–4429.

7 W. Yao, Y. Zhang, X. Jia and Z. Huang, *Angew. Chemie - Int. Ed.*, 2014, **53**, 1390–1394.

8 K. Nomura and Y. Saito, *J. Chem. Soc. Chem. Commun.*, 1988, 161–162.

9 J. A. Maguire, W. T. Boese and A. S. Goldman, *J. Am. Chem. Soc.*, 1989, **111**, 7088–7093.

10 A. D. Chowdhury, N. Weding, J. Julis, R. Franke, R. Jackstell and M. Beller, *Angew. Chemie*, 2014, **126**, 6595–6599.

11 L. Cronin and A. Müller, *Chem. Soc. Rev.*, 2012, **41**, 7333–7334.

12 A. Misra, K. Kozma, C. Streb and M. Nyman, *Angew. Chemie - Int. Ed.*, 2020, 59, 596–612.

13 C. L. Hill and C. M. Prosser-McCartha, *Coord. Chem. Rev.*, 1995, **143**, 407–455.

14 I. A. Weinstock, R. E. Schreiber and R. Neumann, *Chem. Rev.*, 2018, **118**, 2680–2717.

15 R. F. Renneke, M. Kadkhodayan, M. Pasquali and C. L. Hill, *J. Am. Chem. Soc.*, 1991, **113**, 8357–8367.

16 R. F. Renneke, M. Pasquali and C. L. Hill, *J. Am. Chem. Soc.*, 1990, **112**, 6585–6594.

17 D. M. Schultz, F. Lévesque, D. A. DiRocco, M. Reibarkh, Y. Ji, L. A. Joyce, J. F. Dropinski, H. Sheng, B. D. Sherry and I. W. Davies, *Angew. Chemie - Int. Ed.*, 2017, **56**, 15274–15278.

18 P. J. Sarver, N. B. Bissonnette and D. W. C. Macmillan, *J. Am. Chem. Soc.*, 2021, **143**, 9737–9743.

19 G. Laudadio, Y. Deng, K. Van Der Wal, D. Ravelli, M. Nunõ, M. Fagnoni, D. Guthrie, Y. Sun and T. Noël, *Science (80-.).*, 2020, **369**, 92–96.

20 P. J. Sarver, V. Bacauanu, D. M. Schultz, D. A. DiRocco, Y. hong Lam, E. C. Sherer and D. W. C. MacMillan, *Nat. Chem.*, 2020, **12**, 459–467.

21 I. B. Perry, T. F. Brewer, P. J. Sarver, D. M. Schultz, D. A. DiRocco and D. W. C. MacMillan, *Nature*, 2018, **560**, 70–75.

22 J. G. West, D. Huang and E. J. Sorensen, *Nat. Commun.*, 2015, **6**, 1–7.

23 R. F. Renneke and C. L. Hill, *Angew. Chemie Int. Ed. English*, 1988, **27**, 1526–1527.

24 R. F. Renneke, M. Pasquali and C. L. Hill, *J. Am. Chem. Soc.*, 1990, **112**, 6585–6594.

25 R. F. Renneke, M. Kadkhodayan, M. Pasquali and C. L. Hill, *J. Am. Chem. Soc.*, 1991,

113, 8357–8367.

26 A. Troupis, A. Hiskia and E. Papaconstantinou, *Angew. Chemie - Int. Ed.*, 2002, **41**, 1911–1914.

27 C. L. Hill, *Synlett*, 1995, **02**, 127–132.